STUDIA UNIVERSITATIS
BABEŞ-BOLYAI

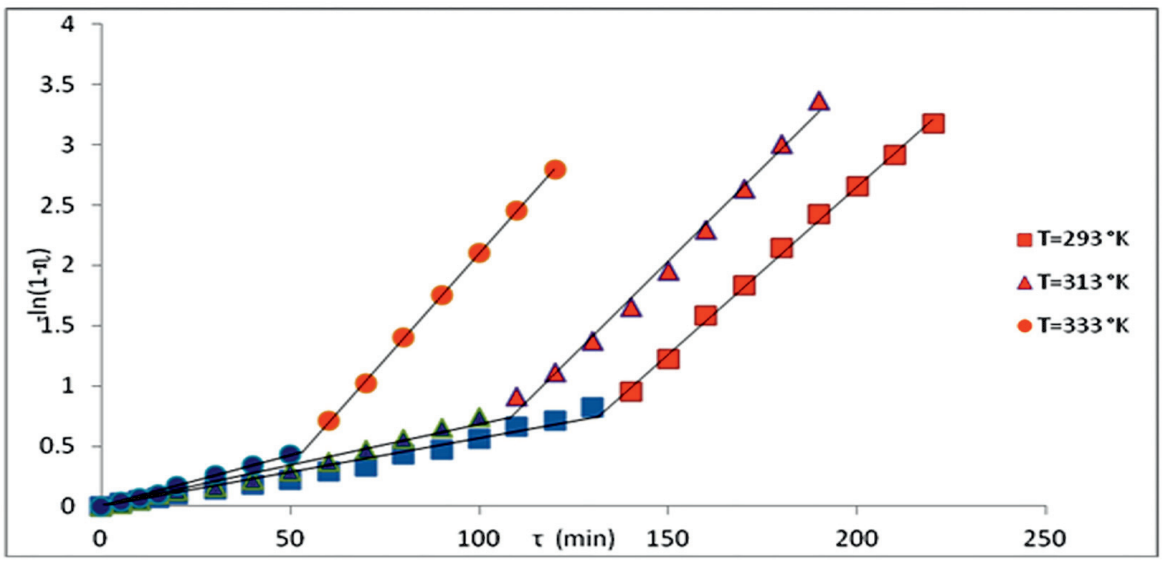

CHEMIA

2/2019
Tom II

STUDIA
UNIVERSITATIS BABEŞ-BOLYAI

CHEMIA

2/2019
Tom II

http://chem.ubbcluj.ro/~studiachemia/; studiachemia@chem.ubbcluj.ro
http://www.studia.ubbcluj.ro/serii/chemia/index_en.html

YEAR **Volume 64 (LXIV) 2017**
MONTH **JUNE**
ISSUE **2**
TOM **II**

S T U D I A
UNIVERSITATIS BABEŞ-BOLYAI
CHEMIA

2

Tom II

ISSUE DOI:10.24193/subbchem.2019.2.II

STUDIA UBB EDITORIAL OFFICE: B.P. Hasdeu no. 51, 400371 Cluj-Napoca, Romania, Phone + 40 264 405352

Dedicated to Professor Ioan Bâldea on the Occasion of His 80th Anniversary

CUPRINS – CONTENT – SOMMAIRE – INHALT

Studia Universitatis Babes-Bolyai Chemia has been selected for coverage in Thomson Reuters products and custom information services. Beginning with V. 53 (1) 2008, this publication is indexed and abstracted in the following:

- Science Citation Index Expanded (also known as SciSearch®)
- Chemistry Citation Index®
- Journal Citation Reports/Science Edition

STUDIA UBB CHEMIA, LXIV, 2, Tom II, 2019 (p. vii)
(RECOMMENDED CITATION)

PROFESSOR IOAN BÂLDEA AT HIS 80TH ANNIVERSARY

A decade ago, Volume 54(3)/2009 of *Studia Universitatis Babeș-Bolyai Chemia*, was dedicated to *Professor Ioan Bâldea* at his 70th birthday, along with wishes of "health in the many years to come as well as the spice of current valuable scientific activity".

And indeed, he shared his passion as well as joy in research and study within his Alma Mater. He continued coordinating PhD students in physical chemistry, chemical technology and pharmacology. He recently rejoined teaching with inspiring liveliness, by initiating a series of plenaries that discuss either novel, sensitive or complex aspects of organic reaction mechanisms and physical chemistry (thermodynamics, kinetics, experimental aspects, etc.) of electron exchange processes.

Our former teacher and colleague continues to inspire the scientific and academic community of Cluj-Napoca. Therefore, this issue of *Studia Universitatis Babeș-Bolyai Chemia* represents a loving express of gratitude of his disciples and younger colleagues from various universities as well as research institutes.

In the eve of at his 80th anniversary, the authors of the papers along with the Editorial Board, wish Professor Ioan Bâldea to continue in health, joy and liveliness the sharing of his valuable knowledge and passion for Chemistry and Science among the younger generations.

On behalf of all his disciples,
Alexandra Ana Csavdári

STUDIA UBB CHEMIA, LXIV, 2, Tom II, 2019 (p. 309-322)
(RECOMMENDED CITATION)
DOI:10.24193/subbchem.2019.2.26

Dedicated to Professor Ioan Bâldea on the Occasion of His 80th Anniversary

THE DEVELOPMENT OF A NEW OPTICAL METHOD TO MEASURE THE DELAY TIME OF SPARK IGNITION

MARIA MITU[a,b], DOMNINA RAZUS[a], DUMITRU OANCEA[b,*]

ABSTRACT. The development of a new optical method to measure the delay time following the spark ignition in gaseous explosive mixtures, based on the measurement of the emitted radiation intensity detected with a photo diode active in visible and near infrared range is presented. Several CH_4-air-inert mixtures were used to test the validity of the method. Our results are comparable with the available literature data. The influence of the different operational factors was investigated to establish the range of the optimum conditions.

Keywords: *spark ignition, ignition delay, emitted radiation intensity, CH_4-air-inert mixtures*

INTRODUCTION

The homogeneous combustion reactions in gas phase are complex reactions involving hundreds of molecular species and coupled elementary reactions. They are generally exothermic reactions and many imply also the participation of chain-branching mechanism. A simplified picture of temperature increase in time was suggestively illustrated in literature [1]. Using a (log T) against time diagram for thermal and chain branching explosions, a straight-line passing through origin or a straight-line intersecting X axis after an induction period, respectively, were found. During a chain-branching explosion, an induction period is necessary for accumulation of a critical concentration of

[a] "*Ilie Murgulescu Institute of Physical Chemistry", Romanian Academy 202 Splaiul Independentei, RO 060021, Bucharest, Romania*
[b] *University of Bucharest, Department of Physical Chemistry, 4-12 Regina Elisabeta Blvd. RO 030018, Bucharest, Romania*
** Corresponding author: doan@gw-chimie.math.unibuc.ro*

active species. When such a system is suddenly brought into a critical state, able to react in an explosive regime, a self-ignition delay time is necessary. The ignition of the explosive regime occurs either as self-ignition, when the whole system reacts simultaneously, or as a forced ignition, starting from a small region where the ignition energy is delivered and propagates through the whole system. The self-ignition is a frequently encountered process with many applications. Consequently, many experimental techniques were dedicated and extensively used. Among these, rapid compression machines (RCM) [2-5], shock tubes (ST) [6-10] or both [11-15] are the most widespread. A qualitative description of the self-ignition delay is given in Figure 1 as a plot pressure *P* or radiation intensity *RI* in time:

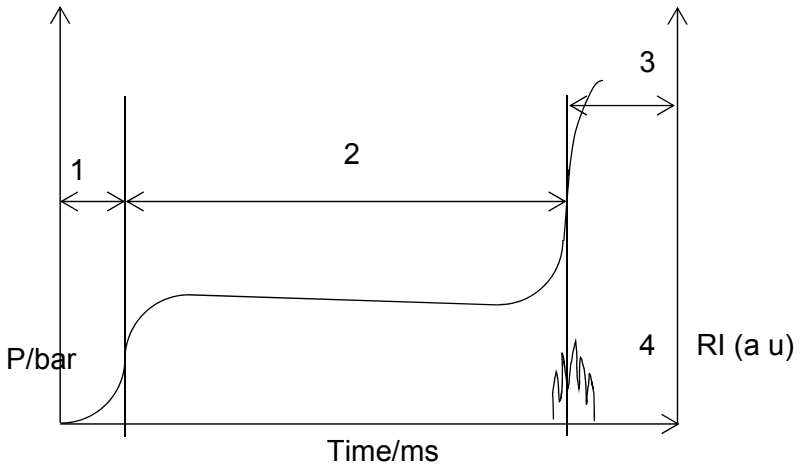

Figure 1. 1-Preignition period; 2-Ignition delay; 3-explosion; 4-Emitted radiation intensity in arbitrary units

The forced ignition, particularly spark ignition, sometimes supplemented with plasma or laser [15-20], was frequently studied using constant volume combustion bombs (CVB). The method presented in this paper relies on the analysis of the radiation intensity variation during the early stages of spark ignition in a CVB.

Due to the numerous applications of delay time in optimization of internal combustion operation, diminution of engine knocking, control of pollutant emission or validation of detailed kinetic models, the literature on these subjects is extremely rich and therefore only selected references were given.

RESULTS AND DISCUSSION

The present paper originates in our previous work regarding the laminar flame propagation in flammable gaseous mixtures using the pressure history and intensity of emitted radiation in closed vessels. It relies on the detailed analysis of the early stages of flame propagation. The use of the third power law of pressure increase during these stages, ΔP, combined with an improved statistical analysis of experimental data, resulted in a new method to evaluate the normal burning velocity and suggested the existence of an ignition delay time, τ, defined as a time interval between the ignition energy deposition and the beginning of steady flame propagation [21-27]:

$$\Delta P=\delta+k_2*(t-\tau)$$

where δ is the base line correction and t is the time.

The method was validated either by comparing the resulted parameters with those reported in literature [21-28], or by analysing also the time evolution of emitted radiation within the same time interval [29].

This analysis relies on the deconvolution of the composite recorded curve of radiant intensity in time. It is composed of the emitted radiation due to spark emission and to flame emission. The first one is given in Figure 2.

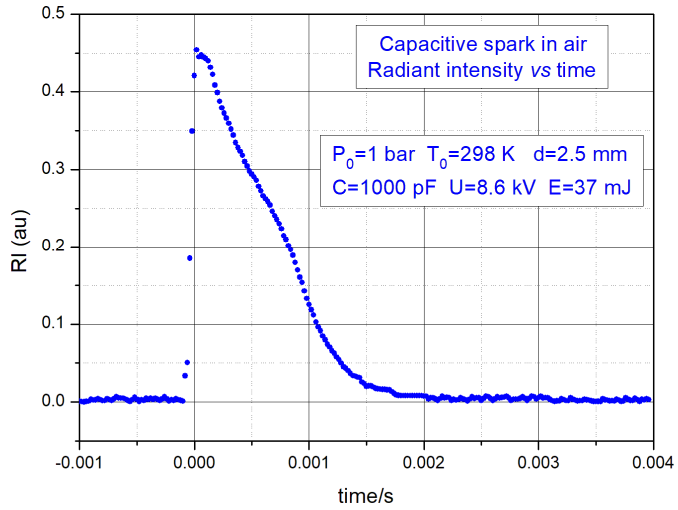

Figure 2. Radiant intensity - time due to spark emission (RI in arbitrary units) for spark gap length d=2.5mm and ignition energy E=37mJ

Even if capacitive sparks with discharging time of ~ 1 μ-second, or inductive sparks with discharging time of ~ 1 m-second were used, the general pattern and characteristics of the discharging emission are similar.

The composite curves, with both spark and flame emission, allow the measurement of the delay times, τ_1, τ_2, and τ_3, defined in Figure 3.

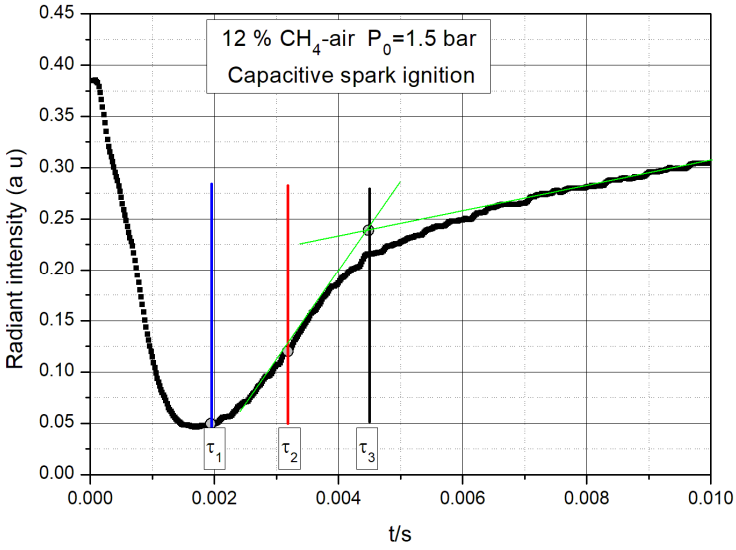

Figure 3. Experimental composite curve RI – time

There are three representative points on this curve: the first one, τ_1, at the end of spark emission and beginning of flame emission, the second one, τ_2, at the first inflection point of the ascending curve and the third one, τ_3.as seen in figure.

These are dependent on the operational conditions and initial mixture composition and can be used to describe the characteristics of the ignition process. Among the most relevant operational parameters are the spark characteristics and the initial mixture pressure and temperature. The mixture composition allows also to take into account the effect of different additives, frequently used in practical applications. As will be seen, the present experimental approach allows the measurements only at normal temperature. However, if mixtures with different fuel/air ratios or explosive mixtures with inert additives are investigated, some temperature dependent properties can be investigated and compared with the data obtained from variation of the same properties by changing the initial mixture temperature.

Spark characteristics effects on ignition delay times

The different ignition delay times can be significantly influenced by spark characteristics. To ensure similar conditions for spark discharge when pressure or composition are changed, an analysis of several operational factors is necessary. For capacitive sparks, these effects are illustrated in Figures 4 and 5.

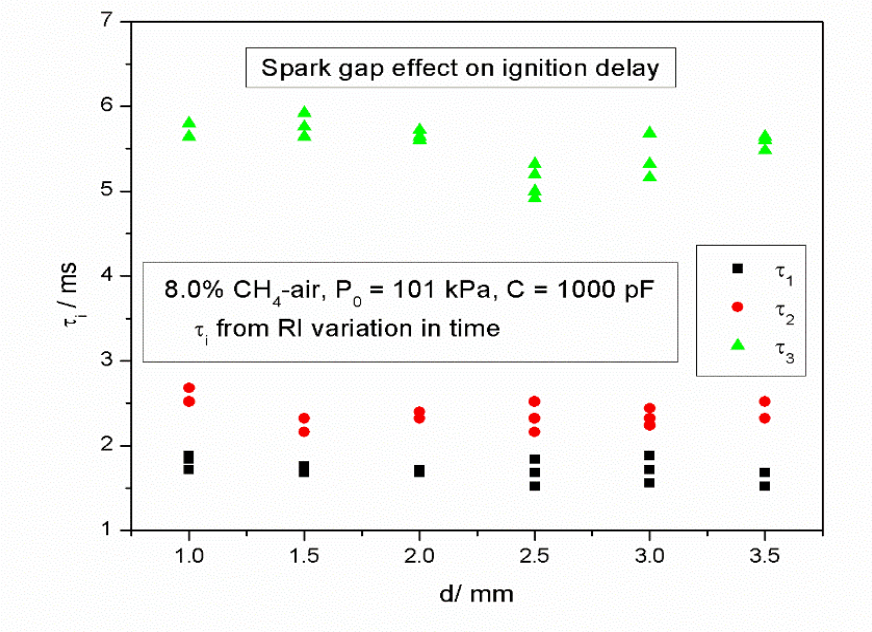

Figure 4. The effect of spark gap length (*d*) on the ignition delay for capacitive sparks with *C*=1000 *p*F

It can be observed that only τ_1 exhibits the best stability within a wide interval of spark gap. The observed differences originate, presumably, from the different stages of the flame development. It can be concluded that τ_1, when the radiant emission from the spark becomes nonsignificant and that from the minimal flame formation starts, is the best choice to be used when other operational parameters are varied. A similar trend was also observed for inductive-capacitive sparks as a function of the spark gap length.

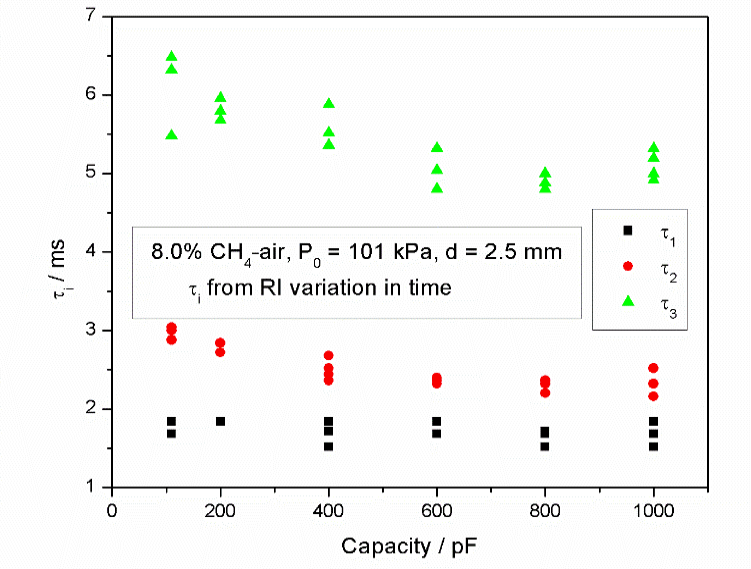

Figure 5. Effect of condenser capacity on the ignition delay for a spark gap length d=2.5 mm

Again, only τ_1 has the best stability within a large interval of capacity.

Effect of initial pressure and temperature on the delay time

The dependence of the ignition delay on the initial pressure and temperature of the flammable mixtures was thoroughly studied in different experimental configurations for both self-ignition and spark ignition. The most frequently, the analytical form of this dependence is of Arrhenius type: exponential with respect to temperature and product of powers with respect to other parameters [13].

$$\tau = a_0 \cdot \prod P_j^{n_j} \cdot P_0^b \cdot \exp(E_a/RT) \quad (1)$$

where a_0, n_j, and *b* are empirical parameters, P_j or P_0 is the partial or total pressure, respectively, *T* is the temperature (K) and *R* = 8.314 J mol^{-1} K^{-1} is the universal gas constant [30, 31]. According to Equation (1), the baric coefficient *b* has the significance of an overall reaction order.

For systems with constant composition and temperature, Equation (1) takes a simpler form:

$$\tau = a_0 \cdot \prod P_j^{n_j} \cdot P_0^b \quad (2)$$

or:

$$\tau = a_1 \cdot P_0^b \tag{3}$$

where a_1 includes the mixture composition.

Effect of initial mixture composition on the delay time

Addition of different inert gases (like Ar, N_2, CO_2, H_2O or exhaust products) allows to modulate the mixture properties, including also the delay time. [32, 33] An illustrative example is given in Figure 6.

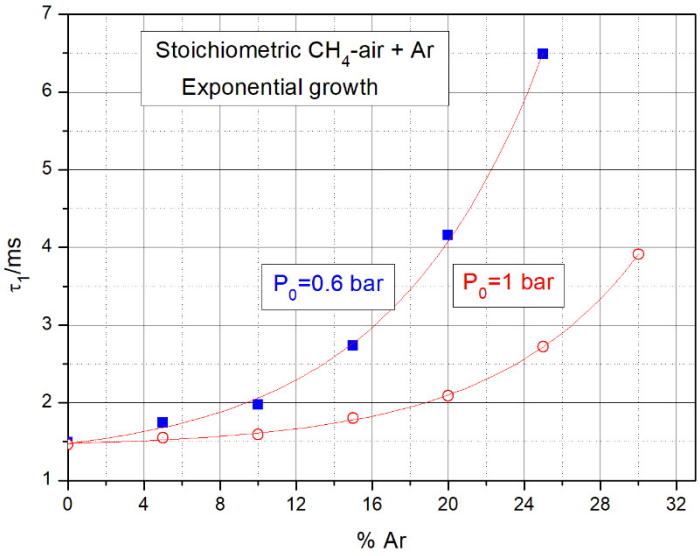

Figure 6. Effect of inert addition on the ignition delay, τ_1

Another possibility to change the mixture properties and implicitly both the ignition delay τ_1 and baric coefficient *b* is to use different fuel/air ratios as given in Figure 7 for different methane-air mixtures.

Sometimes, in many practical conditions, the mixture composition can be changed using both different fuel/air ratios and inert gases addition, keeping the initial temperature constant or changing it. In these cases, the minimal flame temperature, characteristic for the critical ignition properties including the ignition delay, can be obtained only by using numerical calculations. The adiabatic flame temperatures can be calculated with ECHIMAD, the 0D COSILAB package version 3.0.3 and the kinetic modelling with CHEMKIN or 1D COSILAB

package developed by Rogg and Peters [34-39]. Due to an increased interest in this field, numerous other numerical calculations can be found in the pertinent literature [34-40].

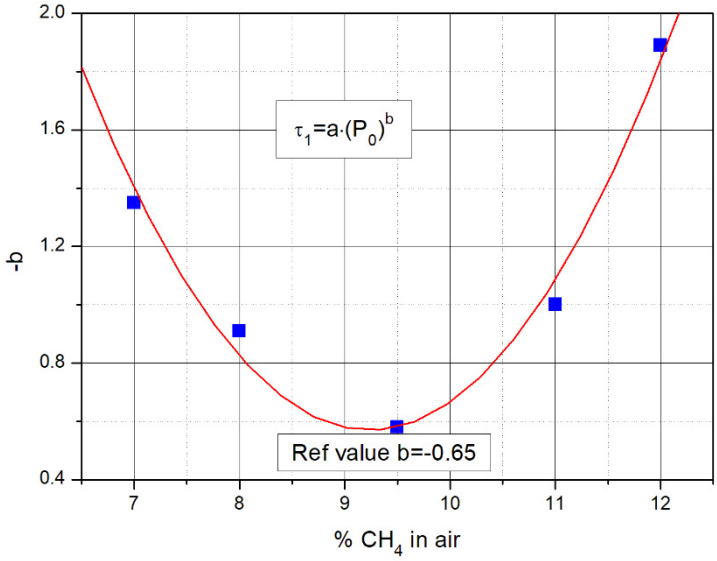

Figure 7. Variation of the baric coefficient *b* from the law (2) with CH_4 content in mixtures with air (ref. [28])

Additionally, taking into account the availability of these numerical calculations, the evaluation of temperature dependent properties becomes possible. In Table 1 the ignition delay τ_1 can be compared to experimental or calculated maximum of pressure rise ΔP_{max} and to calculated or available from other measurements of normal burning velocity S_u.

Table 1. The efficiency of several diluting components on inerting the stoichiometric CH_4-air mixtures containing 10% inert

Inert	$\tau_{1/ms}$	ΔP_{max}/bar	S_u/(cm/s)
-	1.46	5.94	37.40
Ar	1.59	5.60	31.08
N_2	1.79	5.36	28.35
CO_2	2.45	4.68	19.14

Dilution with an inerting component results in a decrease of the ignition delay and of minimal flame temperature. A corresponding activation energy can be evaluated and compared with other reference values [40].

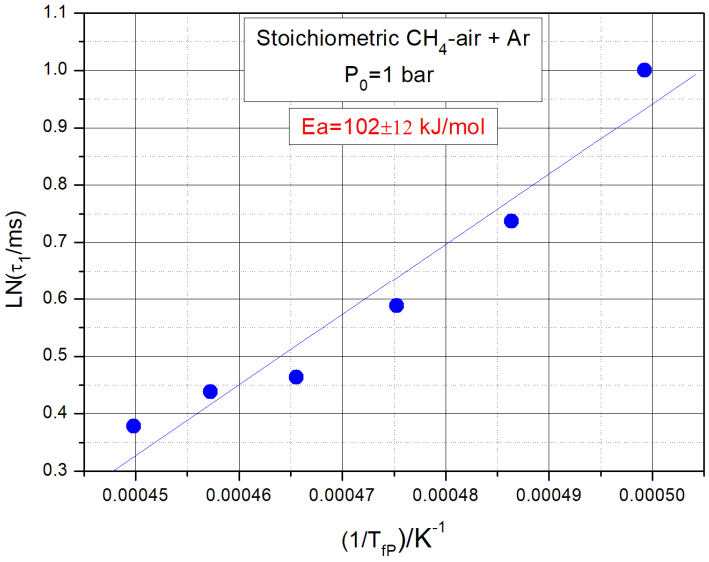

Figure 8. Variation of the ignition delay with flame temperature T_{fP} (calculated here at constant pressure)

To underline the significance of τ_1, its relationships with other properties were examined. Some results are given in Figures 9 and 10:

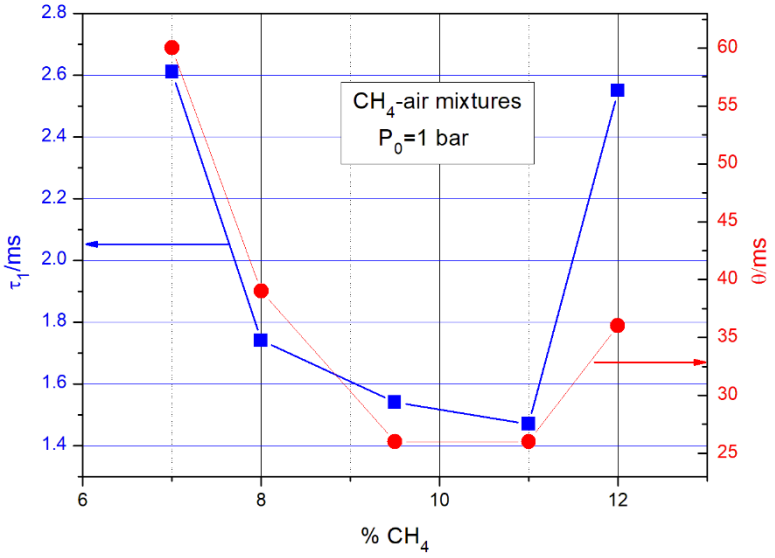

Figure 9. Comparison between the ignition delay τ_1 and the time θ necessary to reach the maximum of the pressure rise ΔP_{max}

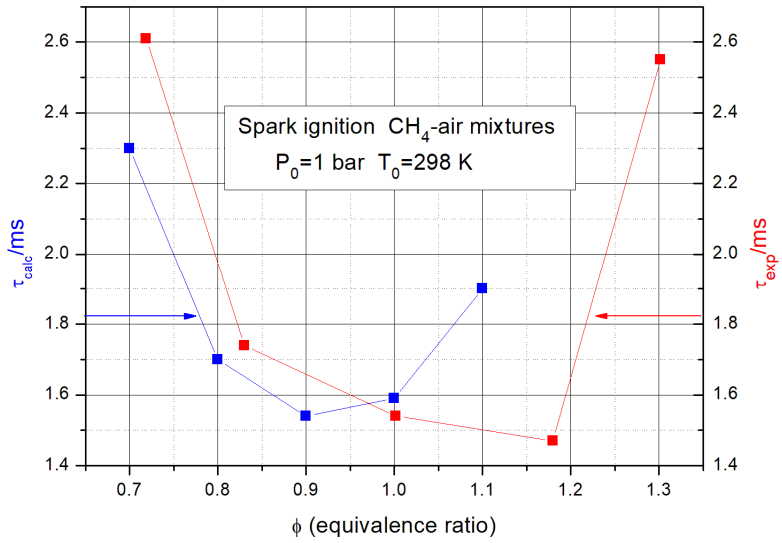

Figure 10. Comparison between experimental and calculated ignition delay.

The calculated ignition delays were obtained by using numerical calculations [34-39].

The adiabatic maximum rate of pressure rise, ΔP_{max}/bar, either calculated or experimental [41], measured explosion violence $(dP/dt)_{max}$/(bar s^{-1}), calculated volumetric rate of heat release, R_{max}/(J s^{-1} m^{-3}) are also properties related to the measured ignition delay times. Some of these correlations will be analysed in a future paper where the effects of other operational parameters will be taken into consideration. The interest for new alternative fuels like methanol and ethanol [42-44] suggest also another direction of research based on the method discussed here.

CONCLUSIONS

Taking into account the increasing interest for the ignition delay measurement when electrical sparks are used, the development of new and simpler techniques is quite beneficial. While the pertinent literature is based preponderantly on the measurement of flame size increase using high-speed time-resolved schlieren recording, our simpler method relies on the deconvolution of the composite recorded curve of radiant intensity in time, measured with a photodiode, in a constant volume combustion bomb. It is

composed from the emitted radiation due to spark emission superposed over of the flame emission. A procedure based on our previous paper allowed the development of this new optical method. The influence of the spark characteristics, initial mixture composition, pressure and temperature was studied and reported. Some relationships with other mixture properties were also discussed. All reported values are highly reproducible and in agreement with both experimental and calculated literature data.

EXPERIMENTAL SECTION

The experimental measurements were carried out in the Laboratory of Chemical Kinetics from the Department of Physical Chemistry, University of Bucharest, using the equipment given schematically in Figure 11.

The gaseous mixtures containing CH_4, air and sometimes inert were prepared in stainless steel cylinders at 4 bar total pressure by partial pressure method using methane 99.99% purity from SIAD and used 24 h after mixing. The experiments were carried out in a stainless-steel cylindrical explosion cell with diameter equal to height: $\Phi = h = 6$ cm ($V_0 = 1.70 \cdot 10^{-4}$ m^3 and with a radius of the equivalent spherical volume $R^*_{cell} = 0.03434$ m). The upper lid has a transparent window made from synthetic glass allowing the observation of the radiation intensity variation with a Si PIN S 123 photodiode (Hamamatsu). The lower lid was fitted with a pressure transducer. The ignition was initiated by high voltage sparks between 1.5 mm diameter stainless steel electrodes with rounded tips within a spark gap of 2.5 mm. The high voltage sparks were either capacitive or inductive. The capacitive sparks were obtained using an adjustable vacuum condenser fed from an adjustable high voltage source (Advanced Energy) interrupted at the end of discharge by an UltraVolt Opto Coupler OC250 (Voltage Multiplier INC.).

The ignition energy was higher than the minimum ignition energy (0.29 mJ) ensuring a safe ignition without important induced turbulence. The inductive sparks were obtained from an automotive ignition coil having the primary winding with an inductance L = 9.5 mH, fed from a dc stabilized power supply. The pressure variation during the explosion process was monitored with a Kistler piezoelectric pressure transducer type 601A coupled with a charge amplifier type 5011B and recorded using a Tektronix TDS 210 oscilloscope.

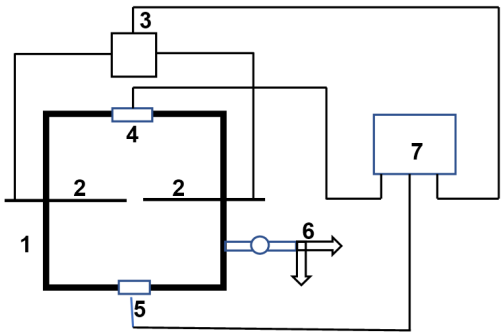

Figure 11. A simplified scheme of the experimental setup: 1. Explosion cell; 2. Spark electrodes; 3. Adjustable high voltage generator; 4. Photodiode; 5. Piezoelectric pressure transducer and charge amplifier. 6. Connections to vacuum and mixing systems; 7. Oscilloscope connected to spark generator (3), photodiode (4) and pressure transducer (5)

ACKNOWLEDGEMENTS

The authors acknowledge the financial support of CNCSIS during the whole period.

REFERENCES

1. J. Warnatz, U. Maas, R. W. Dibble, "Combustion" 2nd Edition, Springer, **1999**, pg.144.
2. X. Nan, W. Yingtao, T. Chenglong, Z. Peng, H. Xin, W. Zhi, H. Zuohua, *Proceedings of the Combustion Institute*, **2017**, *36*, 323.
3. H. Liu, H. Zhang, Z. Shi, H. Lu, G. Zhao, B. Yao, *Energies*, **2014**, *7*, 6083.
4. S. Gersen, N. B. Anikin, A. V Mokhov, H. B. Levinsky, *International Journal of Hydrogen Energy*, **2008**, *33*, 1957.
5. P. Park, J. C. Keck, *SAE Transactions*, **1990**, *99*, 11.
6. B. Koroglu, O.M. Pryor, J. Lopez, L. Nash, S. S. Vasu, *Combustion and Flame*, **2016**, *164*, 152.
7. C. Zhang a, J. He, Y. Li, X. Li, P. Li, *Fuel*, **2015**, *154*, 346.
8. S. Li, A. Campos, D. F. Davidson, R. K. Hanson, *Fuel*, **2014**, *118*, 398.
9. Y. Zhang, Z. Huang, L. Wei, J. Zhang, C. K. Law, *Combustion and Flame*, **2012**, *159*, 918.
10. S. Saxena, M.S.P. Kahandawala, S. S. Sidhu, *Combustion and Flame*, **2011**, *158*, 1019.
11. J. Bugler, B. Marks, O. Mathieu, R. Archuleta, A. Camou, C. Grégoire, K. A. Heufer, E. L. Petersen, H. J. Curran, *Combustion and Flame*, **2016**, *163*, 138.

12. P. Sabia, M. de Joannon, G. Sorrentino, P. Giudicianni, R. Ragucci, *Chemical Engineering Journal*, **2015**, *277*, 324.
13. U. Burke, K. P. Somers, P. O'Toole, C. M. Zinner, N. Marquet, G. Bourque, E L. Petersen, W. K. Metcalfe, Z. Serinyel, H. J. Curran, *Combustion and Flame*, **2015**, *162*, 315.
14. M. Werler, L.R. Cancino, R. Schiessl, U. Maas, C. Schulz, M. Fikri, *Proceedings of the Combustion Institute*, **2015**, *35*, 259.
15. Z. Hu, X. Zhang, *International Journal of Hydrogen Energy*, **2019**, *44*, 487.
16. L-Q. Wang, H-H. Ma, Z.–W. Shen, *International Journal of Hydrogen Energy*, **2019**, *44*, 6271.
17. L. Zhang, H. Ma, Z. Shen, L. Wang, R. Liu, J. Pan *Experimental Thermal and Fluid Science*, **2019**, *102*, 52.
18. C. Xu, A. Zhong, C. Wang, C. Jiang, X. Li, K. Zhou, Y. Huang, Biofuels *Engineering*, **2017**, *2*, 63.
19. E. Hu, X. Li, X. Meng, Y. Chen, Y. Cheng, Y. Xie, Z. Huang*, Fuel,* **2015**, *158*, 1.
20. D. K. Srivastava, M. Weinrotter, K. Iskra, A. K. Agarwal, E. Wintner, *International* T. Le Cong, P. Dagaut *Journal of Hydrogen Energy*, **2009**, *34*, 2475.
21. D. Razus, D. Oancea, N. I. Ionescu, *Revue Roumaine de Chimie*, **2000**, *45*, 319.
22. D. Razus, D. Oancea, C. Movileanu, *Journal of Loss Prevention in the Process Industries* **2006**, *19*, 334.
23. V. Brinzea, M. Mitu, D. Razus, D. Oancea, *Revue Roumaine de Chimie*, **2010**, *55*, 55.
24. V. Brinzea, M. Mitu, C. Movileanu, D. Razus, D. Oancea, *Revista de Chimie*, **2011**, *62*, 201.
25. C. Movileanu, D. Razus, D. Oancea, *Energy & Fuels*, **2011**, *25*, 2444.
26. D. Razus, V. Brinzea, M. Mitu, *Energy & Fuels*, **2012**, *26*, 901.
27. M. Mitu, D. Razus, V. Giurcan, D. Oancea, *Fuel,* **2015**, *147*, 27.
28. J. Han, H. Yamashita, N. Hayashi, *Combustion and Flame*, **2010**, *157*, 1414.
29. M. Prodan, M. Mitu, D. Razus, D. Oancea, *Revue Roumaine de Chimie*, **2016**, *61*, 299.
30. Y. Cheng, E. Hu, F. Deng, F. Yang, Y. Zhang, C. Tang, Z. Huang, *Fuel,* **2016**, *172*, 263.
31. F. S. Shariatmadar, Sh. Ghanbari Pakdehi, M. A. Zarei, *Iranian Journal of Chemical Engineering*, **2016**, *13*, 84.
32. W. Zeng,H. Ma,Y. Liang, E. Hu, *Journal of Advanced Research*, **2015**, *6*, 189.
33. T. Le Cong, P. Dagaut, *Proceedings of the Combustion Institute*, **2009**, *32*, 427.
34. D. Razus, M. Mitu, V. Giurcan, C. Movileanu, D. Oancea, *Process Safety and Environmental Protection*, **2018**, *114*, 240.
35 M. Mitu, V. Giurcan, D. Razus, D. Oancea, *Revista de Chimie* **2018**, *69*, 196.
36. M. Mitu, V. Giurcan, D. Razus, D. Oancea, *Journal of Hazardous Materials*, **2017**, *321*, 440.
37. C. Movileanu, D. Razus, A. Musuc, D. Oancea, *Fuel*, **2017**, *193*, 401.
38. C. Movileanu, D. Razus, D. Oancea, *Fuel*, **2013**, *111*, 194.
39. E. L. Petersen, M. Röhrig, D. F. Davidson, R. K. Hanson, C. T. Bowman, *Symposium (International) on Combustion*, **1996**, *26*, 799.
40. A. Burcat, K. Scheller, A. Lifshitz, *Combustion and Flame*, **1971**, *16*, 29.

41. D. Oancea, V. Gosa, N. I. Ionescu, D. Popescu, *Revue Roumaine de Chimie*, **1985**, *30*, 767.
42. M. Mitu, E. Brandes, *Fuel*, **2015**, *158*, 217.
43. M. Mitu, E. Brandes, *Fuel*, **2017**, *203*, 460.
44. M. Mitu, E. Brandes, W. Hirsch, *Process Safety and Environmental Protection*, **2018**, *117*, 190.

STUDIA UBB CHEMIA, LXIV, 2, Tom II, 2019 (p. 323-333)
(RECOMMENDED CITATION)
DOI:10.24193/subbchem.2019.2.27

Dedicated to Professor Ioan Bâldea on the Occasion of His 80th Anniversary

STUDY OF S235 STEEL CORROSION PROCESS IN WASTEWATER FROM THE PETROCHEMICAL INDUSTRY

JULIETA DANIELA CHELARU[a], LIANA MARIA MUREŞAN[a*]

ABSTRACT. The aim of this study is to investigate the corrosion behavior of low carbon steel (S235) used in petrochemical industry. The corrosion process was analyzed in simulated wastewater at different values of pH and at different temperatures and also in real wastewater from the exploitation of crude oil from Transylvania, Romania. Two commercial corrosion inhibitors (Nalco 73413 (Nalco Products, USA,) and Galoryl IC20 (ArrMazz Chemicals SAS, USA) were tested at different concentrations. The corrosion behavior was investigated by electrochemical impedance spectroscopy and potentiodynamic polarization measurements. Adsorption of these inhibitors was found to obey Langmuir adsorption isotherm.

Keywords: *electrochemical impedance spectroscopy, polarization curves, steel corrosion, corrosion inhibitors, petroleum industry corrosion.*

INTRODUCTION

Due to the low price, carbon steel is widely used in industry, including the petrochemical industry [1-4]. Because of this, its corrosion has a great impact on the economic environment. Compared to other materials, it has good physical, chemical and mechanical properties, but low corrosion resistance. The main factors contributing to the corrosion of carbon steel in the petrochemical industry are temperature, pressure, but also chemical and microorganism attacks [4-7]. Lately, there are many studies that have focused on finding innovative solutions for the protection against corrosion of carbon steel, with low cost and low environmental impact [3-6]. The most practical method for protecting carbon steel is the use of inhibitors [3, 8-13]. This

[a] *Department of Chemical Engineering, "Babeş-Bolyai" University, 11 Arany Janos St., 400028 Cluj-Napoca, Romania*
** Corresponding author: limur@chem.ubbcluj.ro*

method has proven to be the most economical and efficient. Most commonly used are organic corrosion inhibitors containing heteroatoms, such as nitrogen, sulphur, phosphorus and / or oxygen [8]. There are also studies on the use of green inhibitors [11-13] and commercial inhibitors for the protection of carbon steel [14, 15].

In this context, the purpose of this paper is to investigate the corrosion of low carbon steel (S235) in synthetic solutions simulating wastewater (SWW) from petrochemical industry. The corrosion tests were made at different values of temperature and pH. Also, the corrosion behavior of S235 steel was investigated in wastewater from an exploitation of crude oil (WWCO) from Transylvania, Romania. The tests were made in the absence and in the presence of two commercial inhibitors, Nalco 73413 (Nalco Products, USA) and Galoryl IC20 (produced by ArrMazz Chemicals SAS, USA). The corrosion behavior of S235 steel was investigated by electrochemical methods (electrochemical impedance spectroscopy and polarization measurements).

RESULTS AND DISCUSSION

Corrosion in simulated wastewater

Effect of temperature

In order to determine the corrosion behavior of S235 steel in simulated wastewater (pH 3) at different values of temperature (20 ºC, 30 ºC, 40 ºC), the experiments were started by recording the open circuit potential (OCP) for one hour. Nyquist impedance spectra were recorded immediatly after OCP (results not shown) and the results are presented in Fig. 1.

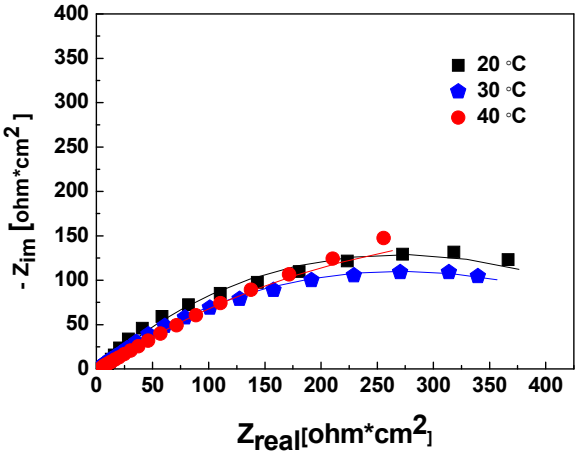

Figure 1. Nyquist plots of the S235 steel dipped in simulated wastewater (pH = 3), at different values of temperature

The spectra ehxibit one depressed capacitive loop. Consequently, the electrical equivalent circuit used to fit the experimental spectra contains besides corrosion solution resistance (R_e), only one R-C couple, presented in Fig. 2. R_{ct} represents the charge transfer resistance and, C_{dl}, the double layer capacity at the steel | electrolyte interface. The data obtained for all samples by using the proposed equivalent electrical circuit are shown in Table 1 (the chi squared (χ^2) values were of order 10^{-4}). The values of C_{dl} were calculated using the equation $C = (R^{1-n}CPE)^{1/n}$, where *CPE* is the constant phase element and *n* reflects the depressed feature of the capacitive loop in Nyquist diagram ($0 < n \leq 1$).

Analyzing the data from Table 1, it can be observed that the polarization resistance (Rp), which is an indicator of corrosion resistance, can be practically assimilated to the charge transfer resistance, and is influenced by temperature. The values of R_p are slightly decreasing with increasing temperature. The highest R_p was observed for T = 20 ºC.

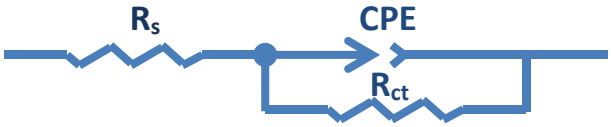

Figure 2. The equivalent electrical circuit used to fit the EIS results

Table 1. The electrochemical impedance data determined by fitting the experimental Nyquist spectra from Figure 1

Temperature [ºC]	Re [Ω·cm²]	R_{ct}[a] [Ω·cm²]	C_{dl}[b] [mF/cm²]	n[c]
20	1.26	537.6	9.078	0.572
30	2.29	533.3	9.433	0.495
40	3.70	418.6	9.544	0.583

a The standard error for Rct values was between 3.24%-5.61%
b The standard error for CPE values was between 2.74%-4.47%
c The standard error for n values was between 0.87%-1.96%

To determine the polarization resistance of the electrodes, linear polarization curves were recorded, in the potential domain of ± 20 mV vs. OCP. The polarization resistance values, for each electrode, were calculated as the inverse of the slope of each curve (Table 2). The largest Rp was observed also at 20 ºC. Potentiodynamic polarization curves were recorded in the potential range of ± 200 mV *vs.* OCP (Fig. 3) in order to determine

the corrosion current density (i_{corr}) and the corrosion potential (E_{corr}). The results obtained by Tafel interpretation of the polarization curves are presented in Table 2. Based on these results, it can be seen that the corrosion of S235 steel increased with the rise of temperature, but not significantly and, as expected, the highest corrosion rate is noticed at 40 ^{0}C. The results are in agreement with EIS measurements.

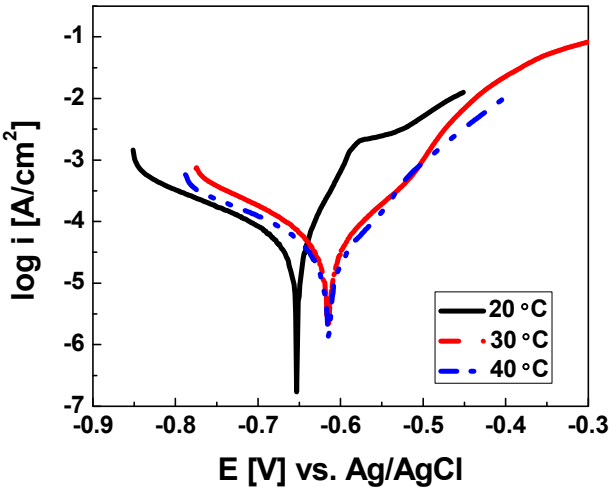

Figure 3. The polarization curves (± 200 mV *vs.* OCP) for the S235 steel immersed in synthetic corrosion solution (pH = 3) at different temperatures; scan rate, 10 mV / min

Table 2. Electrochemical parameters of S235 steel at different temperatures

Temperature	**20 °C**	**30 °C**	**40 °C**
i_{cor} [μA/cm^2]	42.52	49.43	58.04
E_{corr} [mV *vs.* Ag/AgCl/KCl$_{sat}$]	-652	-615	-615
R_p [kΩ cm^2]	0.21	0.19	0.18

Effect of pH

In Fig. 4 are presented the Nyquist plots in case of S235 steel dipped in a simulated wastewater from oil industry at different values of pH (3÷8). The parameters obtained for all samples by using the equivalent electrical circuit from Fig 2 are shown in Table 3. Analyzing the data from Table 3, it can be observed that the corrosion resistance increases at higher pH values. Highest value was obtained at pH 8 (Rp =699.5 [Ω·cm^2]).

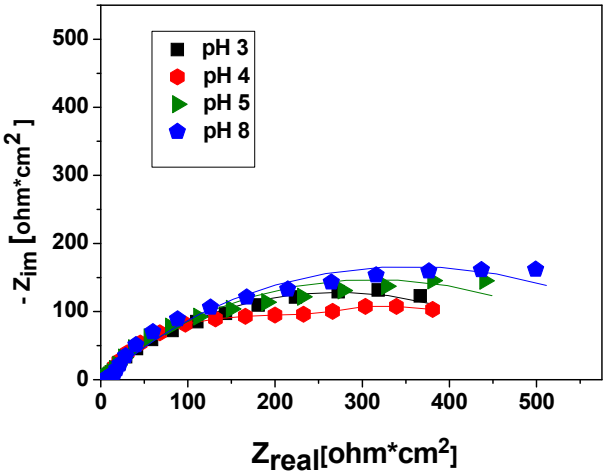

Figure 4. Nyquist plots of the S235 steel dipped in simulated wastewater, at different values of pH

Table 3. The electrochemical impedance parameters estimated by fitting the experimental impedance data from Fig. 6 with the electrical circuit from Fig. 2

pH	R_e [Ω·cm^2]	R_{ct} [Ω·cm^2]	C_{dl} [μF/cm^2]	n
3	1.26	533.3	9.078	0.572
4	2.72	535.3	7.376	0.562
5	3.28	619.9	6.524	0.564
8	5.24	699.5	5.614	0.565

[a] The standard error for Rp values was between 3.40 % - 5.04 %
[b] The standard error for Y_0 values was between 1.68 % - 2.65 %
[c] The standard error for n values was between 1.68 % - 2.65 %

The corrosion currents density and the corrosion potential for the samples studied at different pH values, determined by the Tafel interpretation of the polarization curves from Fig. 5, are shown in Table 4. The results confirm the results obtained through EIS measurements.

Table 4. Electrochemical parameters of S235 steel corrosion at different values of pH

	pH 3	pH 4	pH 5	pH 8
i_{corr} [μA/cm^2]	42.52	37.75	21.73	17.66
E_{corr} [mV *vs.* Ag/AgCl/KCl$_{sat}$]	- 652	- 614	- 535	- 583
Rp [kΩ cm^2]	0.21	0.33	0.48	0.62

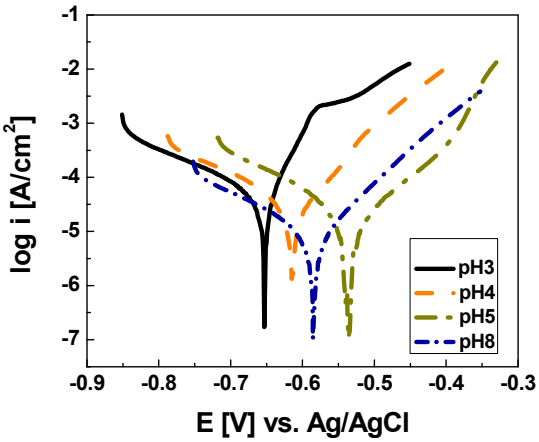

Figure 5. The polarization curves (± 200 mV *vs.* OCP) for the S235 steel immersed in synthetic wastewater at different pH values; scan rate, 10 mV / min

Corrosion in real wastewater

Effect of inhibitors

Fig. 6 shows the Nyquist plots obtained for S235 steel, recorded immediately after OCP monitoring in the real wastewater (pH 8) from an exploitation of crude oil from Transylvania, Romania, without and with different concentrations of two commercial inhibitors (Galoryl IC20, Nalco 73413). It can be seen that all the plots contain depressed semicircles. It was found that the results obtained in the absence and in the presence of inhibitors can be suitably represented using only one time constant circuit. The parameters obtained for all samples are shown in Table 5.

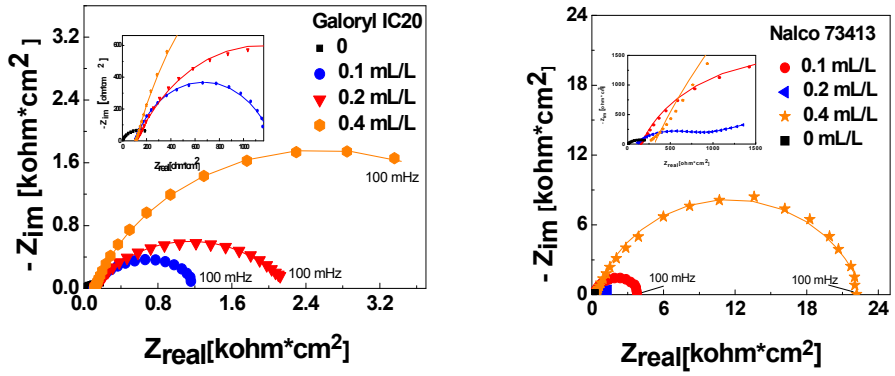

Figure 6. Nyquist plots of the S235 steel dipped in real wastewater (pH 8), from an exploitation of crude oil, at different concentrations of inhibitors; the lines show fitted data

Table 5. The electrochemical impedance parameters estimated by fitting the experimental impedance data from Figure 6

Inhibitor	Conc. [mL / L]	R_e [Ω·cm^2]	R_{ct} [Ω·cm^2]	C_{dl} [μF/cm^2]	n	η [%]
-	0	1.66	280	6.69x10^3	0.611	-
Galoryl IC20	0.1	106	1128	88.06	0.738	75
	0.2	86.35	2626	52.55	0.755	89
	0.4	29.11	9820	44.17	0.398	97
Nalco 73413	0.1	104.60	2143	6.99 x10^3	0.417	90
	0.2	163.70	3756	8.37	0.829	92
	0.4	309.70	22490	2.25	0.800	98

[a] The standard error for *Rp* values was between 1.51 % - 3. 51 %
[b] The standard error for *CPE* values was between 1.19 % - 3.49 %
[c] The standard error for *n* values was between 0.45 % - 1.42 %

Analyzing the data from Table 5, it can be observed that the value of the corrosion resistance depends on the concentrations of inhibitors, which inhibit the corrosion process on the surface of S235 steel. The highest polarization resistance (R_p), was observed at the concentration of 0.4 mL/L in case of both corrosion inhibitors (Table 5).

In Table 5 are presented also the values of the corrosion inhibitors efficiency, determined with the formula: $\eta = \left(\frac{R_p - R_p^0}{R_p} \right) \times 100$ where R_p and R_p^0 are the polarization resistance in presence and in the absence of inhibitors, respectively. As it can be observed, the inhibition is more pronounced in both cases, at higher inhibitors concentration.

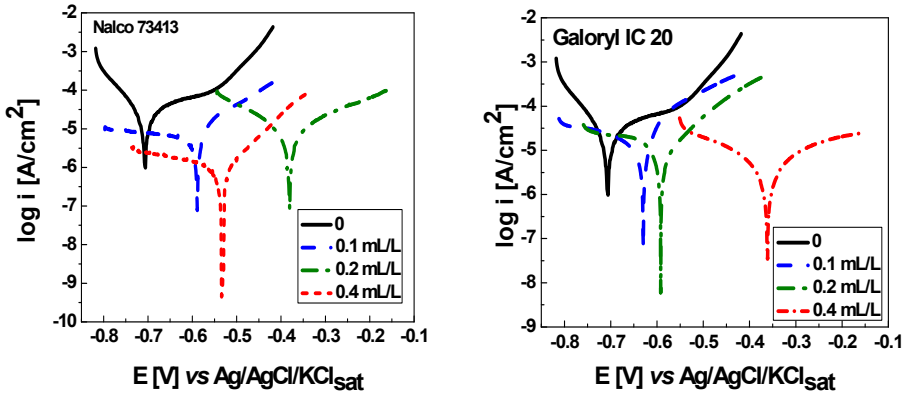

Figure 7. The polarization curves (± 200 mV *vs.* OCP) for the S235 steel immersed in wastewater (pH = 8) at different concentrations of inhibitors; scan rate, 10 mV / min

Table 6. Corrosion process parameters for the examined samples

Inhibitors	Concentrations [mL/L]	E_{corr} [mV vs. Ag/AgCl/KCl$_{sat}$]	i_{corr} [μA/cm^2]	R_p [kΩ*cm^2]	η [%]
-	0	-707	30.33	0.47	-
Nalco 73413	0.1	-596	5.99	2.57	81
	0.2	-385	8.12	3.87	87
	0.4	-533	0.95	30.48	98
Galoryl IC20	0.1	-630	14.38	1.13	58
	0.2	-591	15.95	3.04	84
	0.4	-374	4.49	5.45	91

In order to determine the corrosion currents density and the corrosion potential (E_{corr}), potentiodynamic polarization curves were recorded in the potential range of ± 200 mV *vs.* OCP (Fig. 7). The results are presented in Table 6. The analysis of the data led to the conclusion that in case of both Nalco 73413 and Galoryl IC 20 an increase of corrosion resistance takes place at all inhibitors concentrations.

The highest corrosion resistance and the lowest corrosion current density were noticed at 0.4 mL/L concentration of inhibitors and the best results were noticed in the case of Nalco 73413. This is in agreement with the results obtained from the EIS measurements.

Adsorption isotherm

The efficiencies of the corrosion inhibitors are related to their adsorption ability on the steel surface. The inhibitors reduce the corrosion rate by covering the steel surface with inhibitor molecules. For this purpose, the efficiencies (Table 5 and Table 6), were used to calculate the degree of surface coverage $\theta = \eta / 100$.

In Fig. 8 the linear relationships of C_{in}/θ *versus* C_{in} suggest that the adsorption of both inhibitors (Nalco 73413 and Galoryl IC20) on S235 steel are well described by the Langmuir isotherm: $\frac{C_{in}}{\theta} = \frac{1}{K} + C_{in}$, where K is the adsorption equilibrium constant and C_{in} is the inhibitor concentration (Fig. 8). This kind of isotherm involves the assumption that no interaction between the adsorbed molecules on the electrode surface exists.

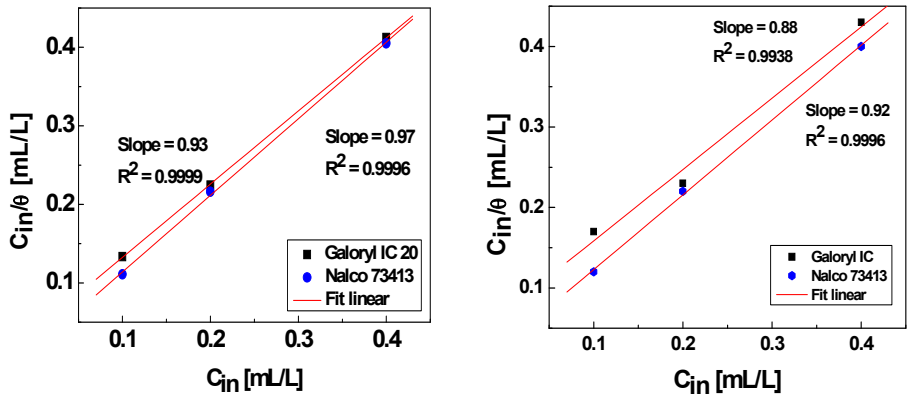

Figure 8. Langmuir adsorption isotherm of the inhibitors by using surface coverage values calculated by a) EIS results and b) Tafel polarization results

CONCLUSIONS

Electrochemical investigations (EIS and potentiodynamic polarization curves measurements) have shown that the corrosion resistance of S235 steel recorded lower values at higher temperature and lower pH values.

When using corrosion inhibitors, the electrochemical results showed that the corrosion resistance improved as their concentration increased. Both used inhibitors exert a good protective effect against steel corrosion in wastewater from petrochemical industry. The best efficiency was noticed when 0.4 mL/L concentration of inhibitors was used (η= 86.61 % for Nalco 73413 and respectively η = 87.07 % for Galoryl IC 20).

Results obtained from EIS and potentiodynamic polarization measurements demonstrated that the adsorption of inhibitors (Nalco 73413, Galoryl IC 20) on S235 steel surface immersed in synthetic and real wastewater from petrochemical industry obeyed Langmuir isotherm and exhibit single-layer adsorption characteristics.

EXPERIMENTAL

Materials and methods

The samples made of S235 steel used for electrochemical tests were disk shaped with 0.8 cm diameter (about 0.5 cm^2 of the surface was exposed to the corrosive solution). Prior tests, the steel samples were

ground using emery papers from # 800 up to # 2000 grades, cleaned with acetone, with distilled water, dried at room temperature, and mounted in Teflon. For electrical contact, a copper road was used.

The commercial corrosion inhibitors used in the experiments were: (i) Nalco 73413 (Nalco Products), (ii) Galoryl IC 20 EU. The inhibitors were dissolved in the corrosive solution at concentrations: 0.1 mL / L, 0.2 mL / L, 0.4mL / L. For corrosion tests, two different solutions were used: (i) an electrolyte that simulated wastewater of high salinity, (pH = 3÷8) and (ii) a wastewater from petroleum industry (pH = 8) containing besides inorganic ions, oils and hydrocarbs. The composition of the synthetic wastewater is presented in Table 7 [14]. For pH correction, NaOH was used.

Table 7. The composition of the electrolyte used in corrosion tests (pH = 3)

Conc.	Fe^{3+}	Ni^{2+}	Cu^{2+}	Na^{+}	K^{+}	SO_4^{2-}	NO_3^{-}	Cl^{-}
g / L	0.02	0.006	$0.1 \cdot 10^{-3}$	50	5.4	6.64	$0.27 \cdot 10^{-3}$	77.09

For the electrochemical corrosion measurements, a PC – controlled electrochemical analyzer PAR 2273 (Princeton Applied Research, USA) connected to a cell containing three electrodes was used: the working electrode (S235 steel), a counter electrode (platinum) and a reference electrode (Ag/ClAg). The open circuit potential (OCP) for steel immersed in the corrosive solution was monitored during one hour. The EIS measurements were performed with a disturbance voltage of ± 10 mV and frequency ranging from 10^3 – 10^{-3} Hz and the results were fited using the ZSimpWin V3.21 software. In order to determine the corrosion parameters, the potentiodynamic polarization curves were recorded by scanning in a potential range of ± 20 mV and of ± 200 mV *vs.* OCP, with a scan rate of 10 mV / min.

REFERENCES

1. M.N. Ilman, Kusmono, *Case Studies in Engineering Failure Analysis*, **2014**, *2*, 1 - 8.
2. W. Geary, *Case Studies in Engineering Failure Analysis*, **2013**, *1*, 249 - 256.
3. G. Sıgırcık, T. Tüken, M. Erbil, *Applied Surface Science*, **2015**, *324*, 232 - 239.
4. T. Liu, Y. F. Cheng, M. Sharma, G. Voordouw, *Journal of Petroleum Science and Engineering*, **2017**, *156*, 451 - 459.
5. W Zhao, Y. Zou, K. Matsuda, *Corrosion Science*, **2015**, *51*, 761 - 768.

6. R. Xiao a, G. Xiao, B. Huanga, J. F. Qionghui, *Engineering Failure Analysis*, **2016**, *68*, 113 - 121.
7. Y. Liu, B. Zhang, Y. Zhang, L. Ma, P. Yang, *Engineering Failure Analysis*, **2016**, *60*, 307 - 315.
8. M. Finšgar, J. Jackson, *Corrosion Science*, **2014**, *86*, 17 - 41.
9. M. Askari, M. Aliofkhazraei, S. Ghaffari, A. Hajizadeh, *Journal of Natural Gas Science and Engineering*, **2018**, *58,* 92 - 114.
10. Y. Zhu, M. L. Free, R. Woollam, W. Durnie, *Progress in Materials Science*, **2017**, *90*, 159 - 223.
11. A. A. Olajire, *Journal of Molecular Liquids*, **2017**, *248*, 775 - 808.
12. K. Haruna, I.B. Obot, N.K. Ankahc, A.A. Sorour, T.A. Saleha, *Journal of Molecular Liquids*, **2018**, *264*, 515 - 525.
13. Gh. Golestani, M. Shahidi, D. Ghazanfari, *Applied Surface Science* **2014**, *308*, 347 – 362.
14. J. D. Chelaru, D. Aylakov, L. M. Mureşan, *Studia UBB Chemia*, **2017**, *62*(4, Tom II), 357 - 368.
15. H. Essom, *Journal of Materials and Environmental Science*, **2015**, *6* (7) 1850 – 1857.

STUDIA UBB CHEMIA, LXIV, 2, Tom II, 2019 (p. 335-343)
(RECOMMENDED CITATION)
DOI:10.24193/subbchem.2019.2.28

Dedicated to Professor Ioan Bâldea on the Occasion of His 80th Anniversary

INTERACTION OF SILVER NANOPARTICLES WITH VANCOMYCIN: AN UV-VIS STUDY

REKA BALINT[a], GERTRUD ALEXANDRA PALTINEAN[a], AURORA MOCANU[a*], OSSI HOROVITZ[a], MARIA TOMOAIA-COTISEL[a]

ABSTRACT. Silver nanoparticles (AgNPs) were synthesized by chemical reduction method, using different reducing systems. The interaction of AgNPs and vancomycin hydrochloride (V) was investigated by UV-Vis spectroscopy, and their tendency to form AgNP@V associations or complexes was identified in colloidal solutions. Moreover their affinity to self-assembly and aggregate is also examined. This behavior is important and decisively influences the antimicrobial effect of AgNP@V complexes.

Keywords: *silver nanoparticles, vancomycin, UV-VIS spectroscopy*

INTRODUCTION

The current need for novel syntheses and functionalization methods of silver nanoparticles (AgNPs) for gaining an enhanced antimicrobial activity represents a great challenge in the development of new antimicrobials.

Many investigations are made nowadays regarding AgNPs, in particular their effect in various combinations with drugs, like antibiotics, leading to new strategies for their therapeutic use [1, 2].

Firstly, AgNPs can be used as antimicrobial agents [2-6]. Further, they can also improve the activity of antibiotics, reducing their secondary effects [7], and even make them active against bacterial strains resistant to those antibiotics. Moreover, the AgNPs and antibiotics were jointly found effective against pathogenic bacteria, which have developed resistance against certain antibiotics, because of the abusive uses of antibiotics [8-12].

[a] *Babeş-Bolyai University, Faculty of Chemistry and Chemical Engineering, Research Center of Physical Chemistry, 11 Arany Janos str., RO-400028, Cluj-Napoca, Romania*
** Corresponding author: mocanu.aurora@gmail.com*

In this regard, the method by which AgNPs were obtained is of major importance. If they are synthesized by chemical reduction method, the reducing agent can also stabilize the colloidal system [13, 14], or other substances are introduced, as capping agents [15]. They may determine the size and shape of the particles. Clearly, the interactions between the drug and silver can be mediated by capping agents.

These interactions can stabilize, but also can destabilize the colloidal system, causing the aggregation of the nanoparticles and finally their precipitation. These interactions can also influence the biological effects of the system, leading to a synergistic, additive effect or antagonistic effect of AgNPs and drug [16]. Even the orientation of drug molecules on the AgNPs can play an important role [11].

The methods to synthesize AgNPs are numerous and varied [2, 17], going from physical approaches, to chemical or electrochemical reduction processes, and to biogenic (green) syntheses [18, 19], often by plant extracts [20-23], fungi and bacteria [16, 24, 25]. Ag^+ ions can be easily reduced even by weak reducing agents, both inorganic and organic [6, 26]. In order to better control the particles size and shape, mixtures of different reducing agents were also used (co-reduction) [17, 27-29]. Of course, the cytotoxicity of AgNPs and also their impact on medium must be taken into account [30].

Vancomycin, $C_{66}H_{75}Cl_2N_9O_{24}$, is a large glycopeptide, noted V, active generally against Gram-positive bacteria. It is mostly used in the form of hydrochloride. Vancomycin is largely used as an alternative to antibiotics for which drug resistance was developed. Unfortunately, even strains resistant to vancomycin already emerged [31]. Therefore, associating vancomycin with silver nanoparticles could be a solution [32].

Consequently, the focus of this work is on syntheses and functionalization of AgNPs with an antibiotic, like vancomycin, to obtain homogeneous colloidal solutions, having narrow sized particles, of high stability.

RESULTS AND DISCUSSION

Silver reduction with citrate ions is frequently used to obtain AgNPs, and also to stabilize them, but that mechanism in not yet fully understood [33]. The spectra of AgNPs obtained by reduction with trisodium citrate (C) and their mixtures with vancomycin hydrochloride (V) solution in different ratios are given in Figure 1. The peak at about 280 nm is due to vancomycin hydrochloride. The characteristic surface plasmon resonance (SPR) band of AgNPs has a maximum at 406 nm, denoting the presence of rather small nanoparticles.

There is a single sharp peak indicating the presence of mostly spherical AgNPs [12]. The full width at half maximum (FWHM) is 76.8 nm, showing a rather narrow distribution of particles size (namely, of low polydispersivity).

By adding increasing volumes of V solution, the maximum decreases, due to the dilution of the AgNPs solution and is shifted toward higher wavelengths (red shift). This significant shift is the result of the interactions between Ag and the drug. The width of the peak (FWHM) also increases with increasing amounts of V, up to 78.5 nm, due to the formation of the AgNP@V complex [11]. After 2 days the spectrum is only slightly modified, so the AgNP@V associations are stable, without a tendency to aggregate. The interaction between vancomycin and citrate capped AgNPs can be assigned to hydrogen bond between the oxygen atoms of citrate anion and the H atom in the amino groups of vancomycin, in total agreement with other similar data [12].

The reduction of Ag^+ with β-cyclodextrin (β-CD) is a green synthesis [34] The UV-Vis spectrum (Fig. 2) is quite similar to that of AgNP-citrate (Fig. 1). From TEM images, an average size of the particles of 13.1 ± 2.1 nm was found [34]. The particle distribution is narrower (FWHM = 69.6 nm) than for the reduction with citrate. The addition of V causes also a red shift of the absorption maximum. But after several days a deformation of the SPR peak occurs, with the apparition of a shoulder at higher wavelengths and a corresponding increase of the FHWM, to over 100 nm. This indicates the beginning of self-assembly of the AgNPs mediated by vancomycin.

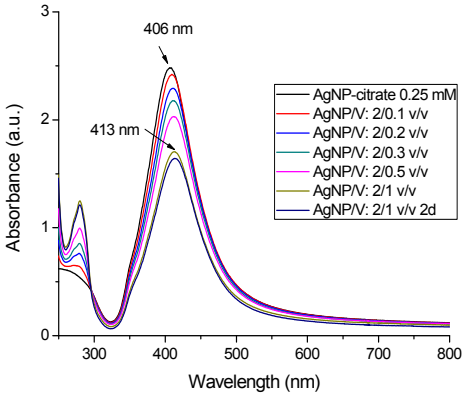

Figure 1. UV-VIS spectra of AgNPs-citrate and V solutions in different ratios and in time

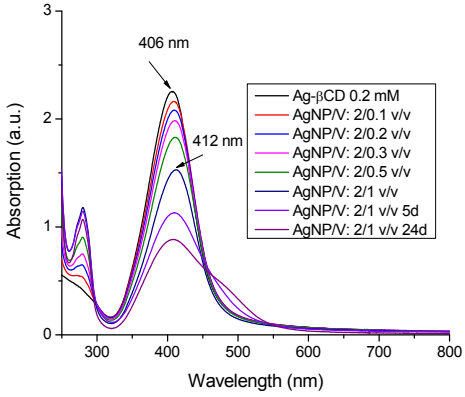

Figure 2. UV-VIS spectra of AgNPs-β-cyclodextrin (β-CD) and V solutions in different ratios and in time

Another green synthesis of AgNPs uses glucose as reducing agent and starch as capping agent [35, 36]. The maximum of the SPR band of the AgNPs is at 406 nm (Fig. 3), and the FWHM is 56.2 nm. The peak is not shifted by adding V, but after 2 days a shoulder appears at about 470 nm, and a new peak appears after 3 days, at 508 nm, while the main peak is much diminished. The new peak corresponds to aggregates of AgNPs resulted by their self-assembly. In presence of starch, the vancomycin mediated self-assembly is more accentuated than for other capping agents.

The synthesis of AgNPs, using also glucose as reducing agent and tetraethyl orthosilicate (TEOS) [37] as capping agent (Fig. 4), produced larger AgNPs. The maximum absorption in the SPR band occurs at about 410 nm, and the band is asymmetrical, outstretched toward higher wavelengths, and FWHM is about 80 nm. This finding means that there is a wider distribution of particles sizes, and larger particles being also present. This asymmetry increases when V is added, and in time. After 4 days the maximum of the SPR band is significantly reduced, and the V band is at 280 nm. The cause is the precipitation of larger aggregated AgNPs.

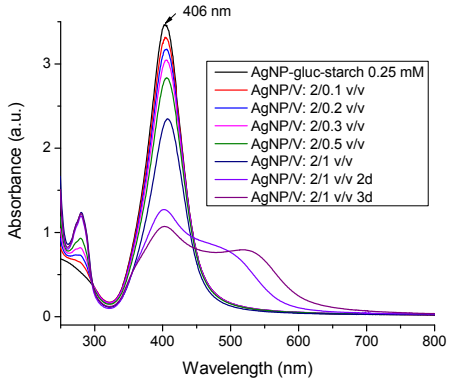

Figure 3. UV-VIS spectra of AgNPs-glucose-starch (gluc-starch) and V solutions in different ratios and in time

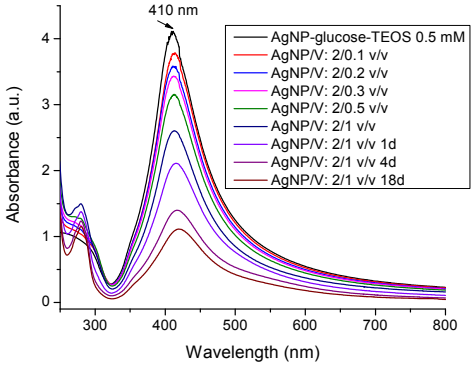

Figure 4. UV-VIS spectra of AgNPs-glucose -TEOS and V solutions in different ratios and in time

Using a mixture of trisodium citrate (C) and tannic acid (T) [17] (Fig. 5) in the molar ratio of 1:7:2 for Ag:C:T, relatively large AgNPs are obtained. In the presence of V, the absorption maximum of the SPR band shifts toward red. The AgNPs are stable, no tendency to aggregation is observed in time. The absorption band of V at 280 nm is not visible, since it is hidden by the strong absorption band of tannic acid.

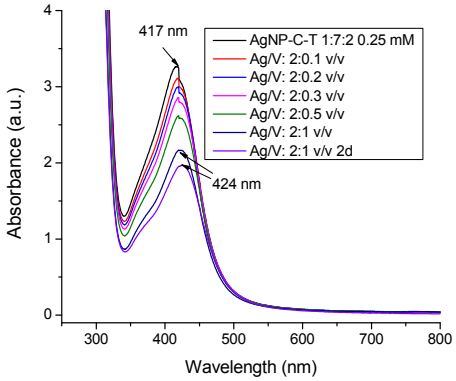

Figure 5. UV-VIS spectra of AgNPs-citrate (C) and tannic acid (T) in the molar ratio 1:7:2 and V solutions in different ratios and in time

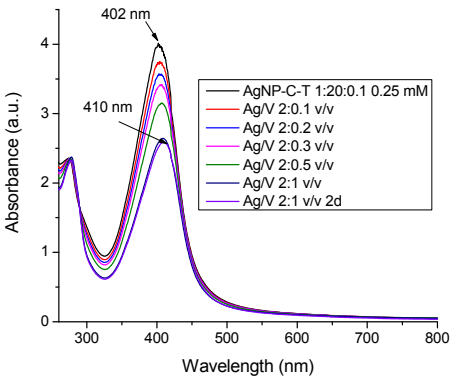

Figure 6. UV-VIS spectra of AgNPs-citrate (C) and tannic acid (T) in the molar ratio 1:20:0.1 and V solutions in different ratios and in time

With a much lower tannic acid concentration (Ag:C:T molar ratio of 1:20:0.1) the AgNPs are much smaller (absorption maximum at 402 nm) and the SPR band is quite narrow (low polydispersivity). The band is red shifted for increasing V addition, which is a sign of vancomycin association to AgNPs (Fig. 6). No significant modifications are observed in time.

The vancomycin-AgNPs complexes are stable, no aggregation and precipitation occur. The V band of 280 nm is here superposed on a stronger tannic acid band at the same position, so its variation with the V content of the solution is no longer visible,

The UV-Vis spectra of V mixtures with silver nitrate solution are compared with the spectra of V and $AgNO_3$ in Fig. 7. $AgNO_3$ presents no absorption in the visible and UV wavelength range investigated, and no SPR band appears.

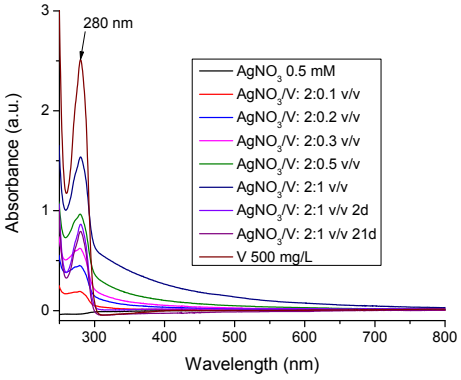

Figure 7. UV-VIS spectra of 0.5 mM $AgNO_3$ and 500 mg/L vancomycin hydrochloride (V) solutions and their mixtures, and in time

Vancomycin can also reduce Ag^+ to AgNPs, but only in basic medium and at higher temperature [unpublished research]. The V band at 280 nm increases with V concentration in that mixture, but in several days a diminution of its intensity is observed. Only after 21 d, traces of a gray deposit are seen (indicating that silver ions are reduced by V).

CONCLUSIONS

UV-Vis measurements enabled us to highlight the various behavior of AgNPs colloidal solutions, obtained using various reduction systems, due to the formation of differently capped AgNPs. Further, the interaction of the capped AgNPs with the antibiotic drug, like vancomycin, is identified.

For some preparations (e.g. AgNPs-citrate or AgNPs-citrate-tannic acid) stable AgNPs-vancomycin associations (complexes) were obtained. For other colloidal solutions (e.g. AgNPs-βCD) less or more advanced vancomycin mediated self-assemblies of AgNPs appeared, and still maintained in colloidal solution. Finally, in other systems (e.g. AgNPs-glucose-starch or AgNPs-glucose-TEOS), the AgNPs slightly precipitated under the influence of vancomycin.

Clearly, the knowledge on the characteristic behavior of AgNPs-vancomycin systems can help in the selection of appropriate systems in order to maximize their antimicrobial effect.

EXPERIMENTAL SECTION

Synthesis of silver nanoparticles

For all syntheses $AgNO_3$ solution was used (high purity silver nitrate from Merck). For the reduction with trisodium citrate [17, 38], 25 mL 1 mM $AgNO_3$ were boiled with 5 mL 1% solution of trisodium citrate, C, ($Na_3C_6H_5O_7 \cdot 2H_2O$, high purity, from Sigma Aldrich) and 70 mL water for 30 min, under continuous stirring, The mole ratio C:Ag was about 7:1. The pale yellow solution obtained (0.25 mM Ag) was cooled on an ice-water mixture at room temperature.

β-Cyclodextrin (Sigma-Aldrich) was used as a 10^{-2} M aqueous solution to reduce a 10^{-2} M $AgNO_3$ solution in the 9:1 volume ratio, at pH 9 (adjusted with K_2CO_3). The colloidal AgNPs solution obtained was diluted to 0.2 mM Ag [34].

AgNPs-glucose-starch solution [35] was prepared from 20 mL 10^{-3} M $AgNO_3$ solution by reduction with 1.36 mL 4% glucose solution (obtained from glucose B. Braun 100 mg/mL, Melsungen AG, Germany) and 50 mL

0.34% starch solution (soluble starch, p.a. from Chempur, Poland) with ultrapure water to a total volume of 80 mL. The solution was heated under continuous stirring until boiling, when the pH was set at 7 with 10% NaOH solution and boiled for other 15 min. The obtained 0.25 mM Ag solution was cooled to room temperature. The glucose:Ag mole ratio was 1.2:1.

The AgNPs-glucose-TEOS solution [37] was obtained from 100 mL 10^{-3} M $AgNO_3$ solution and 100 mL solution prepared from 5.2 mL 4% glucose solution, 1 mL 0.4% TEOS solution in ethanol (from Merck) and ultrapure water. The two solutions were separately heated to 50 ^oC under stirring, and then, they were mixed and 10% NaOH solution was added to reach pH 10. The AgNPs solution with 0.5 mM Ag had a glucose:Ag mole ratio of 2.3:1.

The AgNPs-citrat-tannic acid colloidal solutions with the mole ratios 1:7:2 and 1:20:0.1 for Ag:C:T mole ratios, and a final Ag concentration of 0.25 mM [17, 39] were prepared by heating up the 10^{-2} M $AgNO_3$ solution until boiling, and then adding the solution containing the calculated amount of trisodium citrate and tannic acid (purchased from Merck). The solutions were kept boiling, under continuous stirring, for 15 min.

Interaction of AgNPs with vancomycin

Vancomycin hydrochloride (V, $C_{66}H_{75}Cl_2N_9O_{24}$•HCl) was purchased from Xellia Pharmaceuticals ApS Denmark, and a 500 mg/L aqueous solution (0.336 mM) was prepared and used in the subsequent experiments. In each experiment, 2 mL of AgNPs colloidal solution was used and different volumes of vancomycin solution (up to 1 mL) were successively added.

The *UV-VIS absorption spectra* were measured with a Jasco UV/Vis V650 spectrophotometer, from 800 to 250 nm wavelength for the AgNPs colloidal solution and for the mixtures containing 2 mL AgNP solution and 0.1; 0.2; 0.3; 0.5 and 1 mL V solution. The measurements for the last mixture were repeated after several days. For comparison, the interaction between a 0.5 mM $AgNO_3$ solution with vancomycin solution was investigated in the same conditions.

ACKNOWLEDGMENTS

Authors acknowledge the financial support from Executive Unit for Financing Higher Education, Research, Development and Innovation (*UEFISCDI*) through the research project number 83.

REFERENCES

1. B. Calderón-Jiménez; M. E. Johnson; A. R. M. Bustos; K. E. Murphy; M. R. Winchester; J. R. V Baudrit; *Front. Chem.*, **2017**, *5*, Article 6. doi: 10.3389/ fchem.2017.00006
2. S. U. Khan; T. A Saleh; A. Wahab; M. H. U. Khan; D. Khan; W. U. Khan; A. Rahim; S. Kamal; F. U. Khan; S. Fahad; *Int. J. Nanomedicine*, **2018**, *13*, 733-762
3. M. Rai; A. Yadav; A. Gade; *Biotechnol. Adv.*, **2009**, *27*, 76–83
4. M. K. Rai; S. D. Deshmukh; A. P. Ingle; A. K. Gade; *J. Appl. Microbiol*., **2012**, *112*, 841–852
5. H. H. Lara; N. V. Ayala-Núnez; L. del C. I. Turrent; C. R. Padilla; *World J. Microbiol. Biotechnol*., **2010**, *26*, 615-621
6. L. Ge; Q. Li; M. Wang; J. Ouyang; X. Li; M. M. Q. Xing; *Int. J. Nanomedicine*, **2014,** *9*, 2399–2407
7. A. Coates; Y. Hu; R. Bax; C. Page; *Nat. Rev. Drug Discov*., **2002**, *1*, 895–910
8. W. Q. Shan; J. Jian; F. J. Hong; S. J. Cong; *Sci. China B Chem.*, **2007**, *50*, 418–424
9. Y. E. Hur; Y. Park; *J. Nanosci. Nanotechnol*., **2016**, *16*, 6393-6399
10. N. Xu; H. Cheng; J. Xu; F. Li; B. Gao; Z. Li; C. Gao; K. Huo; J. Fu; W. Xiong; *Int. J. Nanomedicine*, **2017**, *12*, 731-743
11. A. Kaur; D. Goyal; R. Kumar; *Appl. Surf. Sci.*, **2018**, *449*, 23-30
12. A. Kaur; S. Preet; V. Kumar; R. Kumar; R. Kumar; *Colloids Surf. B: Biointerfaces*, **2019**, *176*, 62–69
13. A. Mocanu; R.D. Pasca; Gh. Tomoaia; C. Garbo; P.T. Frangopol; O. Horovitz; M. Tomoaia-Cotisel; *Int. J. Nanomedicine*, **2013,** *8*, 3867-3874
14. G. Furtos; M. Tomoaia-Cotisel; C. Garbo; M. Senila; N. Jumate; I. Vida-Simiti; C. Prejmerean; *Particul. Sci. Technol.,* **2013,** *31*(4), 392-398
15. C. T. Matea; T. Mocan; F. Tabaran; T. Pop; O. Mosteanu; L. Mocan; C. Zdrehus; *Studia UBB Chemia*, **2018**, *63*, 95-102
16. M. Wypij; J. Czarnecka;·M. Świecimska; H. Dahm;·M. Rai; P. Golinska; *World J. Microbiol. Biotechnol*. **2018**, *34*:23. doi.org/10.1007/s11274-017-2406-3
17. S. Rapuntean; R. Balint; G. A. Paltinean; Gh. Tomoaia; A. Mocanu; C. P. Racz; O. Horovitz; M. Tomoaia-Cotisel; *Studia UBB Chemia*, **2018**, *63*, 73-85
18. N. Arjunan; H.L.J. Kumari; C. M. Singaravelu; R. Kandasamy; J. Kandasamy; *Int. J. Biol. Macromol.*, **2016**, *92*, 77–87
19. P. K. Ponnaian; R. Oommen; S. K. C. Kannaiyan; S. Jayachandran; M. Natarajan; A. Santhanam; *J. Environ. Nanotechnol.,* **2015**, *4*, *23-26*
20. S. Ahmed; M. Ahmad; B. L. Swami; S. Ikram; *J. Adv. Res.* **2016**, *7*, 17–28
21. T. A. Abalkhil; S. A. Alharbi; S. H. Salmen; M. Wainwright; *Biotechnol. Biotechnol. Equip.*, **2017**, *31*, 411–417
22. K. S. Siddiqi; A. Husen; R. A. K. Rao; *J. Nanobiotechnol.*, **2018,** *16*:14, https://doi.org/10.1186/s12951-018-0334-5

23. P. Singh; S. Pandit; J. Garnæs; S. Tunjic; V. R. S. S. Mokkapati; A. Sultan; A. Thygesen; A. Mackevica; R. V. Mateiu; A. E. Daugaard; A. Baun; I. Mijakovic; *Int. J. Nanomedicine*, **2018**,*13*, 3571–3591
24. S. Z. H. Naqvi; U. Kiran; M. I. Ali; A. Jamal; A. Hameed; S. Ahmed; N. Ali; *Int. J. Nanomedicine*, **2013**, *8*, 3187–3195
25. B. Momin; S. Rahman; N. Jha; U. S. Annapure; *Bioprocess. Biosyst. Eng*., **2019**, *42*, 541-553
26. M. Tomoaia-Cotisel; *Multifunctional nanostructures formed of gold or silver nanoparticles and different biomolecules with medical applications*, *e-Book*, Cluj University Press, Cluj-Napoca, **2016**, pp. 1-322 http://www.editura.ubbcluj.ro/bd/ebooks/pdf/1976.pdf
27. S. Agnihotri; S. Mukherji; S. Mukherji; *RSC Advances*, **2014**, *4*, 3974-3983
28. K. Ranoszek-Soliwoda; E. Tomaszewska; E. Socha; P. Krzyczmonik; A. Ignaczak; P. Orlowski; M. Krzyzowska; G. Celichowski; J. Grobelny; *J. Nanopart. Res.*, **2017**, *19*, article *273,* https://doi.org/10.1007/s11051-017-3973-9
29. L. Salvioni; E. Galbiati; V. Collico; G. Alessio; S. Avvakumova; F. Corsi; P. Tortora; D. Prosperi; M. Colombo; *Int. J. Nanomedicine*, **2017**, *12*, 2517–2530
30. M. Akter; M. T. Sikder; M. M. Rahman; A. K. M. A. Ullah; K. F. B. Hossain; S. Banik; T. Hosokawa; T. Saito; M. Kurasaki; *J. Adv. Res.*, **2018**, *9*, 1–16
31. B. P. Howden; J. K. Davies; P. D. R. Johnson; T. P. Stinear; M. L. Grayson; *Clin. Microbiol. Rev.*, **2010**, *23*, 99-139
32. M. Esmaeillou; G. Zarrini; M. A. Rezaee; J. S. Mojarrad; A. Bahadori; *Adv. Pharm. Bull.*, **2017**, 7, 479-483
33. Y. L. Mikhlin; S. A. Vorobyev; S. V. Saikova; E. A. Vishnyakova; A. S. Romanchenko; S. M. Zharkov; Y. V. Larichev; *Appl. Surf. Sci.*, **2018**, *427*, 687-694
34. A. Mocanu; O. Horovitz; C. P. Racz; M. Tomoaia-Cotisel; *Rev. Roum. Chim.*, **2015**, *60*, 721-726
35. L. Ortega-Arroyo; E. S. Martin-Martinez; M. A. Aguilar-Mendesz; A. Cruz-Orea; I. Hernandez-Pérez; C. Glorieux; *Starch*, **2013**, *65*, 814-821
36. S. V. Kumar; A. P. Bafana; P. Pawar; A. Rahman; S. A. Dahoumane; C. S. Jeffryes; *Sci. Rep.*, **2018,** *8:5106,* DOI:10.1038/s41598-018-23480-6
37. A. Mocanu; G. Furtos; S. Rapuntean; O. Horovitz; C. Flore; C. Garbo; A. Danisteanu; Gh. Rapuntean; C. Prejmerean; M. Tomoaia-Cotisel; *Appl. Surf. Sci.*, **2014**, *298*, 225-235
38. O. Horovitz; M. Tomoaia-Cotisel; C. Racz; Gh. Tomoaia; L. D. Bobos; A. Mocanu; *Studia UBB Chemia*, **2009**, *54*, 89-96
39. N. G. Bastús; F. Merkoçi; J. Piella; V. Puntes; *Chem. Mater.*, **2014**, *26*, 2836-2846.

STUDIA UBB CHEMIA, LXIV, 2, Tom II, 2019 (p. 345-355)
(RECOMMENDED CITATION)
DOI:10.24193/subbchem.2019.2.29

Dedicated to Professor Ioan Bâldea on the Occasion of His 80th Anniversary

KINETIC STUDY OF SULFUR DIOXIDE ABSORPTION INTO DOLOMITE-BRUCITE SUSPENSIONS

SIMION DRAGAN[a], ADINA GHIRISAN (MICLAUS)[a*]

ABSTRACT. The influence of the dolomite-brucite concentration and temperature on the global process of sulfur dioxide, SO_2, absorption into dolomite-brucite suspensions was established. According to the proposed macro-kinetic model, the chemical reaction between H_2SO_3 and $MeCO_3$ takes place into the adsorbed layer, at the outer surface of the granules. The low values of the activation energies obtained, Ea << 25.1 kJ/mol, confirmed for working conditions, that the global chemisorption process was limited to diffusion stage. At suspension concentrations lower than 5% and high temperatures, the chemisorption was carried out according to the shrinking core model without crust, when the diffusion of H_2SO_3 through the liquid phase is the limitative stage. At concentrations higher than 10% the chemisorption was carried out according to the unreacted core model with crust formation, when the diffusion of H_2SO_3 through the crust of products remains the limitative phenomenon.

Keywords: *dolomite-brucite suspension, sulfur dioxide, chemisorption, activation energy, macro-kinetic mechanism*.

INTRODUCTION

Industrial development has caused emissions of gas pollutants (SO_2, SO_3, NO_x, HCl, HF, etc.) which were released into the atmosphere, thus affecting seriously the quality of the environment. An important case with a major environmental impact is the emission of sulfur dioxide [1-10].

Annual sulfur dioxide emissions have been estimated to be approximately 160 million tons, half being produced by industrial activities [11]. The industrial sectors that contribute to the SO_2 emissions are the metallurgical ore refining and power industry that uses fossil fuels as raw material. Therefore the desulphurization of gaseous emissions from burning fossil fuels is very important.

[a] *Babeş-Bolyai University, Faculty of Chemistry and Chemical Engineering, 11 Arany Janos str., RO-400028, Cluj-Napoca, Romania*
** Corresponding author: ghirisan@chem.ubbcluj.ro*

In the last 30-40 years, a significant number of gas scavenging technologies have developed, amid the consumption of fossil fuels and the continued increase in energy demand [12]. Desulphurization technologies are classified in three main categories: dry, semi-dry and wet [13,14]. The wet desulfurization process achieves one of the highest purification efficiency and reliability, being the most commonly used technology for controlling the emission of SO_2 in the world [3,15-18].

Retention of SO_2 in suspension of calcium carbonate (rock or precipitated) is the most used wet process, due to the low cost [1,4,8,9,19,20]. Desulphurization by this method leads to large amounts of gypsum, which is a storage problem. Nowadays, the research in the desulphurization of flue gas is oriented to develop technologies that lead to compounds which can be completely reused. The wet flue gas desulfurization using dolomite-brucite suspension is of great perspective, reducing at half the amount of the gypsum, and recovering a part of sulfur dioxide as $MgSO_4$, with many practical uses.

The present study investigates the macro-kinetic mechanism of the SO_2 absorption into dolomite-brucite ($CaMg(CO_3)_2.Mg(OH)_2$) suspensions. It was determined experimentally the influence of the temperature and the dolomite-brucite concentration on the global process.

RESULTS AND DISCUSSION

The influence of dolomite-brucite concentration on the SO_2 absorption rate at a temperature range from 293 to 333 K and stirring speed of 200 rpm, was observed. An example, for a temperature of 293 K, is shown in Figure 1.

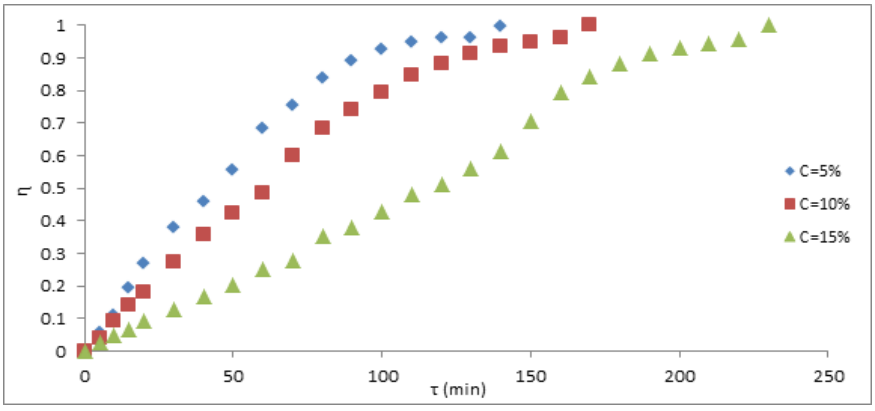

Figure 1. Influence of the suspension concentration on SO_2 absorption rate, T = 293 K

The results indicate that the absorption of SO_2 is strongly influenced by the suspension concentration on the entire studied temperature range, the absorption rate being greater at lower concentrations. This behavior of the absorbent system is determined by two categories of factors:

a) relating to the physical properties of the system, e.g. viscosity and pH. The lower viscosity of diluted suspensions causes higher diffusion rates and therefore the increase of the absorption rate. At higher concentrations of suspension, the viscosity is higher, so that the rate of the diffusion process is lower. At the same time, at lower concentrations of suspension, the value of pH equal 5.0 - 5.5 is quickly reached, and so the absorption process takes place;

b) relating to the mass transformation processes as chemical reaction, dissolution, formation and growth of germs. Reactions between $MeCO_3$ and H_2SO_3 are carried out mainly in the outer surface of the granules, at pH = 6.7 - 7, when the $MeSO_3$ is stable, with very low solubility in water. According to the proposed mechanism, $MeSO_3$ reacts with HSO_3^- resulting $Me(HSO_3)_2$, which is 50 to 100 times more soluble.

In diluted suspensions, the driving force of reaction products dissolution, $\Delta C = C^s - C^v$, is higher, the volume concentration C^v being lower. In these conditions, crust is not formed at the surface of the granule, and the process can be described by the mechanism of granule with contractible core without crust.

The analysis of kinetic curves shows that the induction period depends on operation conditions, concentration and temperature. The induction period increases for the higher suspension concentrations and decreases with the increase of temperature. In the final stage of absorption it was observed a change in slope, suggesting a lower rate of the absorption, determined by the change of macro-kinetic mechanism, when the process is controlled by diffusion through the crust of the reaction products. The obtained results show that the most pronounced influence of suspension concentration on the absorption rate occurs at 293 K. The influence of suspension concentration decreases with the increase of temperature. At 333 K the rate of absorption is the same for the suspension concentrations of 10% and 15%, due to the increase of suspension viscosity and concentration of sulfites in the suspension, the driving force of the dissolution process decreases.

The temperature has a significant and complex influence on the rate of SO_2 absorption into dolomite-brucite suspensions. The increase of the temperature leads to the decrease of suspension viscosity, thus increasing the rate of the diffusion processes. A more pronounced influence of temperature is manifested on mass transformation processes, as reaction, dissolution and germ growth, whose rate increases with temperature. The temperature influence on the absorption rate of SO_2 into the dolomite-brucite suspensions is shown in Figure 2, for the 15% suspension.

The analysis of the experimental data shows that for 5% concentration and temperature of 293 K, the time required to obtain a conversion of 90% is 80 min and 110 min for the suspension concentration of 15%. At the same time, for suspension concentrations of 5% and 10%, the effect of temperature on the absorption process is small. At the suspension concentration of 15% the temperature has a significant influence, determined by the occurrence of the reaction products, when the determinant mechanism is the diffusion of the reactant through the crust.

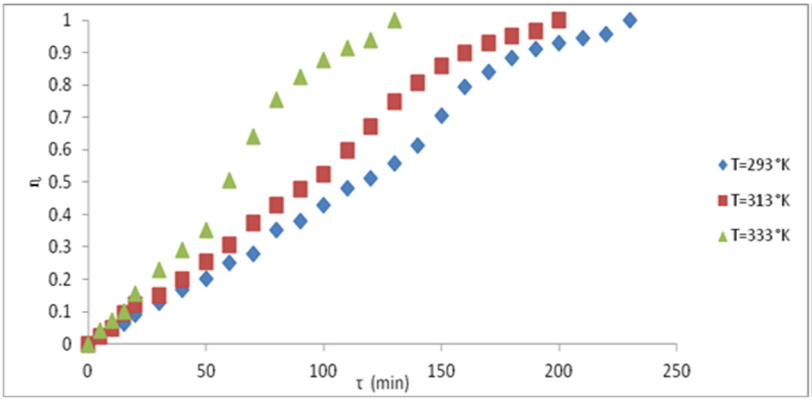

Figure 2. Temperature influence on SO_2 absorption into dolomite-brucite suspension 15%

Processing the data in coordinates -ln(1-η) versus time, specific diagrams as presented in Figures 3-5 are obtained. The analysis of diagrams shows the change of the slopes for investigated temperatures and suspension concentrations. This behavior suggests that the macro-kinetic mechanism of chemisorption process is modified.

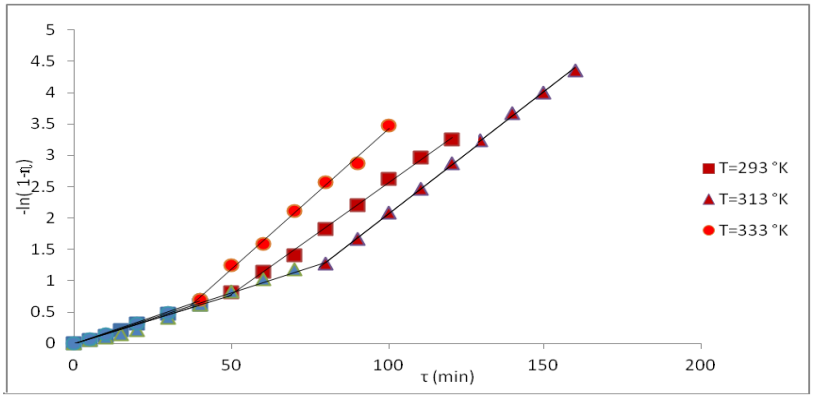

Figure 3. -ln (1-η) vs. time for SO_2 absorption into the dolomite-brucite suspension 5%

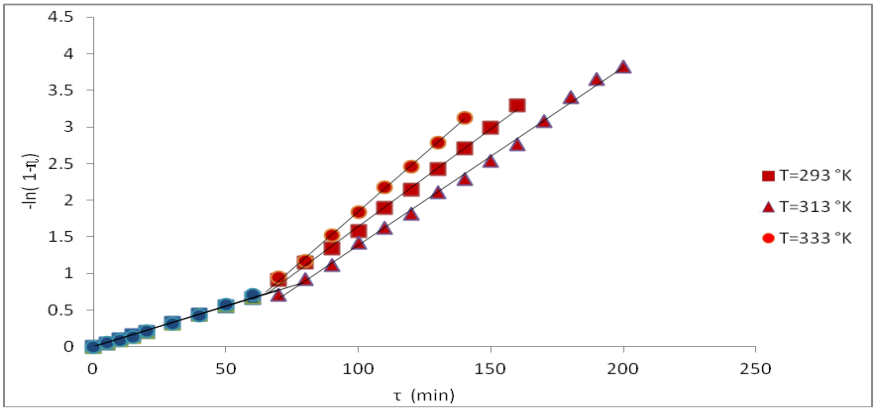

Figure 4. -ln (1-η) vs. time for SO_2 absorption into the dolomite-brucite suspension 10%

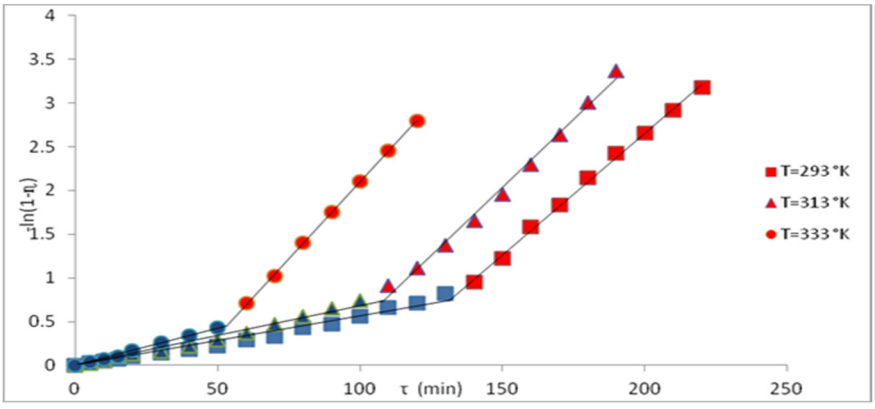

Figure 5. -ln (1-η) vs. time for SO_2 absorption into the dolomite-brucite suspension 15%

To determine the rate limiting step of the global process, the activation energies were calculated. The data are presented as Figure 6 shows for a concentration of 5%.

The obtained results show, for each concentration and temperature, two values of the activation energy, Ea_1 and Ea_2 (Table1). The low values of activation energies, Ea << 25.1 kJ/mol, indicate for the working conditions that the absorption process takes place by diffusion. The transport processes as the mass transport of SO_2 through the liquid phase at the beginning of the process, and the mass transport of SO_2 through the crust of the reaction products at the end of the process, are limitative.

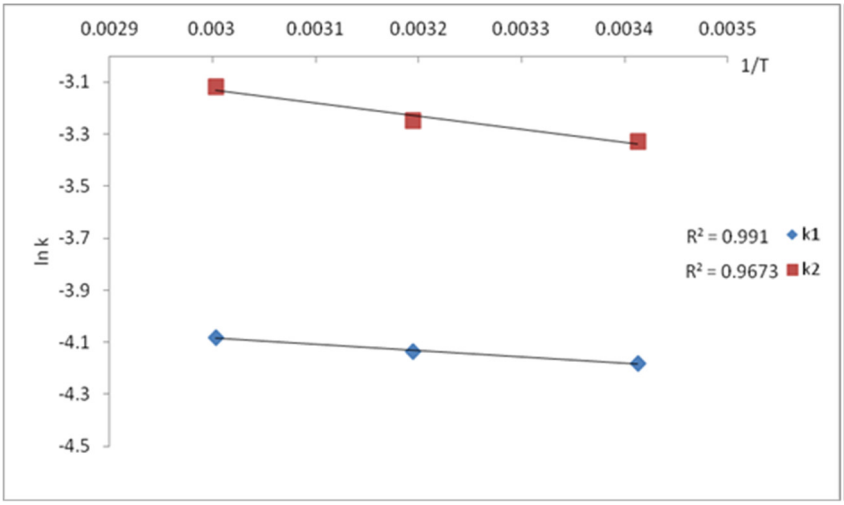

Figure 6. Diagram ln k vs. 1/T for SO_2 absorption into dolomite-brucite suspension 5%

Table 1. The values of the activation energies

Nr. crt.	Suspension conc.	Temp.	Activation energies	
	C(wt.%)	T (K)	Ea_1 (kJ/mol)	Ea_2 (kJ/mol)
1	5	293-333	2.001	4.17
2	10	293-333	4.55	8.37
3	15	293-333	0.544	5.11

Comparing the values of the activation energies at the beginning period of the process, Ea_1, with the corresponding values at the final period, Ea_2, it was found for all concentrations that $Ea_1 < Ea_2$. Thus, at low concentrations, the rate of the reaction products dissolution as $MgSO_3$, $Mg(HSO_3)_2$, $Ca(HSO_3)_2$, is higher, the absorption takes place according to the model of grain without crust formation. In these conditions, the concentration of HSO_3^- ions at the reaction surface (the outer surface of the granule) is sufficiently high so that the rate of chemical reactions (4, 7) is not the limitative stage in the process (see proposed mechanism).

The global rate is determined by the diffusion of HSO_3^- ions through the liquid phase at the outer surface of the granule (external diffusion). Ea_2 is twice higher than Ea_1 for suspension concentrations of 5% and 10%, and Ea_2 is one time higher than Ea_1 for the concentration of 15%, probably due

to the thickness of the reaction products crust. In the second period, corresponding to the final stage of absorption, the concentration of $Mg(HSO_3)_2$ and $Ca(HSO_3)_2$ in the liquid phase increases, the dissolution rate decreases, and the contribution of mass transformation processes increases. In these conditions, the activation energy Ea_2 is higher than Ea_1. At a dolomite-brucite concentration over 10%, the concentration of solids in liquid phase increases too much, so that the reaction products as $Mg(HSO_3)_2$ and $Ca(HSO_3)_2$, are no longer dissolved. The reaction products remain as crust on the outer surface of the granule and the process takes place by the unreacted core model. Through the reaction products crust the access of HSO_3^- ions to the reaction surface decreases, so that the rate of the chemical reaction decreases. Although the contribution of mass transformation processes increases, as emphasized by the higher Ea_2 activation energy, the diffusion phenomenon through the crust (internal diffusion) remains limitative.

Macro-kinetic mechanism of the process

The wet process of SO_2 absorption into calcium and magnesium carbonate suspension (slurry) is a complex process, with two basic stages: a) the mass transport (diffusion) through one of the phases (gas, liquid, solid); and b) the mass transformation as dissolution of reagents, chemical reaction, formation and growth of new phase germs.

Several mechanisms of SO_2 absorption into the slurry of calcium carbonate are presented in the literature [16,21-26]. Figure 7 shows the structure of the global process proposed in the present study. According to this mechanism, the process is carried out in the liquid phase, after the calcium carbonate and sulfur dioxide dissolution. The analysis of the phase equilibrium shows that the solubility of the solid compounds participating in the reaction is very small (Table 2).

Table 2. Solubility data of the compounds [27,28]

	Component				
Solubility (g/100g sol.)	**$CaCO_3$**	**$MgCO_3$**	**$Mg(OH)_2$**	**$CaSO_3$**	**$MgSO_3$**
	0.0069	0.2200	0.0084	0.0054	0.5250

The low solubility of the carbonates (Table 2) correlated with the low dissolution rates, excludes the possibility of full reaction between SO_2 and carbonates in the liquid phase.

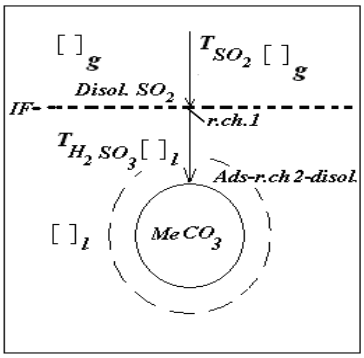

$$-T_{SO_2}[\,]_g \rightarrow -\text{Disol. } SO_2 \rightarrow -\text{r.ch.1} \rightarrow -T_{H_2SO_3}[\,]_l \rightarrow -\text{Ads } HSO_3^- \rightarrow \text{-r.ch 2} \rightarrow -\text{Disol } Me(H_2SO_3)_2 \rightarrow$$

Figure 7. The sequence of elementary stages in the global process

Based on the macro-structural element of the mass reaction, the characteristic equation can be written as:

$$\left[CaCO_3 + MgCO_3 + Mg(OH)_2 + A''\right]_s + \left[H_2SO_3 + SO_2 + H_2O\right]_l \rightarrow$$
$$\left[CaCO_3 + MgCO_3 + Mg(OH)_2 + CaSO_3 + MgSO_3 + A''\right]_s +$$
$$\left[Ca(HSO_3)_2 + Mg(HSO_3)_2 + H_2SO_3 + H_2O\right]_l + \left[CO_2\right]_g$$

The mass transformation processes, in accordance with the characteristic equation, are:

$$SO_{2[]_g} \rightleftarrows SO_{2aq} \quad (1)$$

$$SO_{2aq} + H_2O \rightleftarrows H_2SO_{3aq} \quad (2)$$

$$H_2SO_{3aq} \rightleftarrows H^+ + HSO_{3\,aq}^- \quad (3)$$

$$MeCO_{3[]_s} + HSO_{3\,aq}^- \longrightarrow \mathrm{MeCO_3} * HSO_{3\,ads}^- \quad (4)$$

$$MeCO_3 * HSO_{3\,ads}^- \longrightarrow \mathrm{MeSO_{3[]_s}} + HCO_{3\,aq}^- \quad (5)$$

$$SO_{2aq} + H_2O + HCO_3^- \longrightarrow HSO_3^- + CO_2 + H_2O \quad (6)$$

$$MeSO_{3[]s} + HSO_3^- + H_2O \longrightarrow Me\left(HSO_3\right)_{2[]s} + H^+ \quad (7)$$

$$Me\left(HSO_3\right)_{2[]_s} \longrightarrow Me\left(HSO_3\right)_{2aq} \quad (8)$$

$$H^+ + HCO_3^- \longrightarrow H_2O + CO_2 \quad (9)$$

In the absorption zone, in addition to reactions (1)-(9), secondary reactions (10)-(11) and the oxidation of the sulfites can take place (12)-(13):

$$Ca\left(HSO_3\right)_2 + O_2 \longrightarrow CaSO_{4aq} + H_2SO_4 \quad (10)$$

$$CaSO_{4aq} + 2H_2O \longrightarrow CaSO_4 \cdot 2H_2O_{[]s} \quad (11)$$

$$Mg\left(HSO_3\right)_2 + O_2 \longrightarrow MgSO_{4aq} + H_2SO_4 \quad (12)$$

$$MgSO_{4aq} + 2H_2O + Ca\left(HSO_3\right)_2 \longrightarrow CaSO_4 \cdot 2H_2O_{[]s} + Mg\left(HSO_3\right)_2 \quad (13)$$

The structure of the process can be now illustrated by the diagram shown in Figure 8.

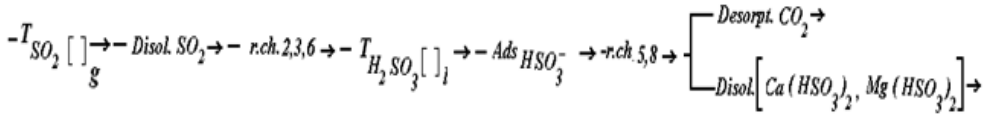

Figure 8. Process structure of the gas desulphurization with dolomite-brucite suspension

According to the process structure above, the reaction between dolomite-brucite particles and sulfurous acid has shown three possible macro-kinetic mechanisms: a) the transport of the reactants into fluid phase; b) the mass transformation processes as chemical reactions in the liquid phase or at the surface of dolomite-brucite particles; and c) the combined model as mass transport into the fluid phase-transformation.

CONCLUSIONS

Based on the study of the sulfur dioxide chemisorption into wet dolomite-brucite suspension, a new macro-kinetic mechanism was proposed according to which the chemical reaction between H_2SO_3 and $MeCO_3$ takes place into the adsorbed layer, at the outer surface of the granules. The influence of the concentration of the dolomite-brucite suspension and of the temperature on the global process was determined.

The process analysis by the activation energies suggests that SO_2 chemisorption in dolomite-brucite suspensions takes place after the macro-kinetic model in which the diffusion is the limitative step. At suspension concentrations lower than 5% and high temperatures, the chemisorption process takes place according to the shrinking core model, without crust,

when the diffusion of H_2SO_3 through the liquid phase is the limitative stage. At concentrations higher than 10% the chemisorption process is carried out according to the unreacted core model with crust formation of reaction products, when the diffusion through the crust of products remains the limitative phenomenon.

EXPERIMENTAL SECTION

The sulfur dioxide absorption was carried out in a laboratory cylindrical batch reactor, as was described in [29]. The evolution of the process was determined by weighing the samples collected with a pipette from the absorption reactor, at each 5 minutes. After weighing, the samples were diluted with about 100-150 mL distilled water. The SO_2 dosing was carried out using iodometric means, with 0.05N iodine solution in the presence of starch.

The dolomite-brucite suspensions used in the research had three concentrations: 5%, 10% and 15%. Working temperatures were 293 K, 313 K and 333 K. The absorbent suspension was prepared using dolomite-brucite solid obtained by grading on Retzsch sieves, with the size less than 125 μm. The analysis with Coulter-Counter device indicates a mean particle size $d_{50\%}$ of 2.75 μm.

Due to the fact that the rate of desulphurization process depends on the reactivity of the suspension, the main textural properties and chemical composition of dolomite-brucite have been determined. Textural properties were investigated with surface area analyzer Qsurf Series M1. The specific surface area of the samples was determined by measuring nitrogen adsorption/desorption isotherms at 77 K, using the Brunauer, Emmett and Teller (BET) relation. The specific surface ($S_{spec.}$) area as the average of three measurements was found to be 1.5 m^2/g.

Table 3. The composition, specific surface area and porosity of the dolomite-brucite rock

Component	**$CaCO_3$**	**$Mg(OH)_2$**	**$MgCO_3$**	**SiO_2**	**H_20**
(wt.%)	62.98	21.35	2.34	3.23	10.03
$S_{spec.}$ (m^2/g)	1.5				
Porosity (cm^3/g)	0.0052				

TG analysis indicates that dolomite-brucite contains three principal compounds, $CaCO_3$, $MgCO_3$ and $Mg(OH)_2$, with a very compact form at the room temperature, which is confirmed by the very low values of the specific surface area and porosity.

REFERENCES

1. J. B. W. Frandsen; S. Kiil; J. E. Johansson; *Chem. Eng. Sci.*, **2001**, *56*, 3275-3287
2. Y. S. Kang, S. K. Sung. S.C. Hong; *J. Ind. Eng. Chem.*, **2015**, *30*, 197-203
3. F. J. Gutierrez Ortiz; F. P. Vidal; L. S. Ollero; V. Cortes; *Ind. Eng. Chem. Res.*, **2006**, *45*, 1466-1477
4. I. Hrastel; M. Gerbec; A. Stergaršek; *Chem. Eng. & Technol.*; **2007**, *30*, 220-233
5. Y. Wu; Q.Li; F. Li; *Chem. Eng. Sci.*, **2007**, *62*, 1814-1824
6. X. Li; C. Zhu; Y. Ma; *Front. Chem. Sci. Eng.,* **2013**, *7*, 185-191
7. G. Muthuraman; Moon Il-Shik; *J. Ind. Eng. Chem,* **2012**, *18*, 1540-1550
8. T. Hlincik; P. Buryan; *Fuel Process. Technol.*; **2013**, 111, 62-67
9. T. Hlincik; P. Buryan; *Fuel*; **2013**, *104*, 208-215
10. R. Valle-Zermeño; J. Formosa; J. M. Chimenos; *Rev. Chem. Eng.*, **2015**, *31*, 303-310
11. S. C. Stultz; J. B. Kitto; *Steam: its generation and use*, Ed. Babcock & Wilcox, Barberton, Ohio, **2005**, Chapter 1, pp. 1-17
12. S. Shafiee; E. Topal; *Energy Policy*, **2008**, *36*, 775-786
13. A. Kohl; R. Nielsen; *Gas purification*, 5th Edition, Gulf Publishing Company, Elsevier, Houston, Texas, **1997,** Chapter 1**,** pp. 466-670
14. N. Karatepe; *Energy Sources*; **2000**, *22*, 197-206
15. A. Gómez; N. Fueyo; A. Tomás; *Comput. Chem. Eng.* **2007**, *31*, 1419-1431
16. C. Brogren; H. T. Karlsson, *Chem. Eng. Sci*, **1997**, *52*, 3085-3099
17. Y. Zhong; X. Gao; W. Huo; Z. Y. Luo; M. J. Ni; K. F. Cen; *Fuel Process. Technol.*, **2008**, *89*, 1025-1032
18. B. Dou; W. Pan; Q. Jin; W. Li; Y. Wang; *Energy Conv. Manage*, **2009**, *50*, 2547-2553
19. P. Taerakul; P. Sun; D. W. Golightly; H. W. Walker; L. K. Weavers; B. Zand; T. Butalia; T. J. Thomas; H. Gupta; L. S. Fan; *Fuel*, **2007**, *86*, 541-553
20. L. E.Kallinikos; E. I. Farsari; D. N. Spartinos; N. G. Papayannakos; *Fuel Process. Technol.*, **2010**, *91*, 1794-1802
21. P. A. Ramachandran; M. M. Sharma; *Chem. Eng. Sci.*,**1969**, *24*, 1681-1686
22. C. Brogren; H. T. Karlsson; *Ind. Eng. Chem. Res.*, **1997**, *36*, 3889-3897
23. S. Y. Liu; W. D. Xiao, *Chem. Eng. Technol.*, **2006**, *29*, 1167-1173
24. B. Dou; Y. C. Byun; J. Hwang; *Energy & Fuel*, **2008**, *22(2)*, 1041-1045
25. S. Kiil; M. L. Michelsen; K. Dam-Johansen; *Ind. Eng. Chem. Res.*, **1998**, *37*, 2792-2806
26. S. Dragan; A. Ozunu; *Central Eur. J. Chem.,* **2012**, *10*, 1556-1564
27. R. H. Perry; *Perry's Chemical Engineering Handbook*, Section 2, Physical and Chemical Data, 8th Edition, McGraw Hill., **2008**, Chapter 2, pp. 121-124
28. M. R. Masson; H. D. Lutz; B. Engelen; *Solubility Data Series, Sulfites, Selenites and Tellurites*, Pergamon Press, Oxford, **1986**, Chapter 26, pp.153-220
29. S. Dragan; *Studia UBB Chemia*, **2017**, *62(4)*, 283-291

STUDIA UBB CHEMIA, LXIV, 2, Tom II, 2019 (p. 357-369)
(RECOMMENDED CITATION)
DOI:10.24193/subbchem.2019.2.30

Dedicated to Professor Ioan Bâldea on the Occasion of His 80th Anniversary

MAXIMIZING ENERGY SAVINGS ATTAINABLE BY DYNAMIC INTENSIFICATION OF BINARY DISTILLATION

LINGQING YAN[a], THOMAS F. EDGAR[a], MICHAEL BALDEA[a,b*]

ABSTRACT. Dynamic intensification of distillation columns has shown significant promise in achieving energy savings with minimal investment in new equipment. Conceptually, it entails making a desired product as a blend of two auxiliary products (one with higher purity, the other with lower purity, but both having lower energy consumption). Practically, dynamic intensification means periodically switching between two operating states corresponding to the aforementioned products. Past work has relied on ad-hoc choices of auxiliary products. In this paper, we introduce a new optimization framework for selecting auxiliary products for dynamic intensification. An extensive case study concerning the separation of a methanol/propanol mixture is then presented. We show that optimizing the choice of auxiliary products can lead to significant energy savings (more than 3.6% compared to a column operated at steady state) derived from dynamic intensification.

Keywords: *process intensification; dynamic intensification; distillation; energy efficiency, optimization*

INTRODUCTION

The chemical industry turns raw materials into value-added products via physical and/or chemical transformations. In most circumstances, the feedstock of chemical plants contains (traces of) impurities. Moreover, most chemical reactors are not designed for complete conversion, and many chemical

[a] *McKetta Dept. of Chemical Engineering, The University of Texas at Austin, Austin, TX 78712, USA*
[b] *Institute for Computational Engineering and Sciences, The University of Texas at Austin, Austin, TX 78712, USA*
** Corresponding author: mbaldea@che.utexas.edu*

reactions produce a (set of) desired product(s) and (several) undesired by product(s). As a consequence, chemical plants comprise reaction and separation units, interconnected via material and energy recycle streams [1]. Separation units account for a significant portion of the capital and operating cost of a chemical plant, with distillation being the dominant approach for separating liquid mixtures. In the United States alone, it was estimated that there are about 40,000 distillation columns in operation, which handle 90-95% of total separation needs [2]. Distillation columns are quite flexible and robust in dealing with fluctuations in feed quality and product constraints [3]. However, distillation is a thermal process that exploits the difference in volatility between the components of the mixture. This requires that the mixture to be separated be brought to a boiling state, which, in turn, entails a significant energy input. The *theoretical* energy use of distillation columns is driven by the nature of the mixture, and increases as the throughput of the system increases. The energy demand (typically described in terms of the amount of steam supplied to the reboiler) of columns used in industry is further increased by inefficiencies related to heat loss, heat transfer, etc. Overall thermal efficiencies as low as 10% may be encountered in practice [4].

Significant research and engineering efforts have been directed at lowering the energy consumption of distillation columns. In the *design* realm, we recall, e.g., thermal integration concepts (whereby a heat source – typically a condenser – within a column or a distillation train is used to meet heat demand in a sink – typically a reboiler), intensification (such as the case of dividing wall columns, whereby the function of two or more distillation columns is combined in a single shell, compartmented by a septum/wall) [5,6,7].

In the *operations* area, work has focused on imposing cyclic operating patterns that segregate liquid and vapor traffic in the column, with the purpose of minimizing energy inefficiencies associated with (re)mixing. The advent of these ideas can be traced back to the 1960s [8], and research continues to date. The implementation of cyclic distillation concepts can lead to significant energy savings (compared to a conventional column of the same capacity) [9] but entails major equipment changes. Separating the movement of the vapor and liquid phases requires special trays and control strategies that can manage frequent (occurring every minute or faster) flow redirection. The capital expenditure is significant for new projects, and can be prohibitive for retrofits.

In several recent publications [10,11], we introduced dynamic process intensification (DPI) as a novel operational approach for lowering energy use in distillation columns. DPI exploits the nonlinearities inherently present in the *static* behavior of distillation columns to create *periodic, dynamic* operating patterns that produce the same output (in terms of time-averaged flow rates and purities of the products) as an equivalent conventional column,

but with lower energy consumption. Importantly, DPI relies on existing distillation hardware and can therefore be deployed on a significant number of columns already in operation.

Our early work in DPI focused on demonstrating the concept empirically; in this paper, we propose a rigorous optimization framework for defining the maximum energy savings attainable by DPI. The paper is organized as follows: in the next section, we introduce the DPI framework and the underlying physics. Next, we define the optimization framework for computing the maximum achievable energy savings. A case study, focused on the separation of an equimolar methanol/propanol mixture is presented, demonstrating considerable energy savings compared to the empirical case. Finally, we draw conclusions and propose potential directions for future work.

DYNAMIC INTENSIFICATION OF BINARY DISTILLATION: CONCEPT

We begin by defining dynamic process intensification (DPI) in the general case, as any "changes to the dynamics, operation strategy, and/or control of a process that lead to a substantially more efficient processing path." [11] This general statement was translated to the intensification of binary distillation columns by exploiting their intrinsically nonlinear behavior. Specifically, early work by Jacobsen and Skogestad [12] (later confirmed experimentally by Koggesbol et al. [13]) revealed an economically interesting output multiplicity. This consists of a nonlinear steady-state characteristic whereby *the same* reboiler duty Q_B (manipulated input and significant contributor to column operating cost) could lead to two *different* values of the distillate purity y_d (controlled variable/ output), as shown in Figure 1.

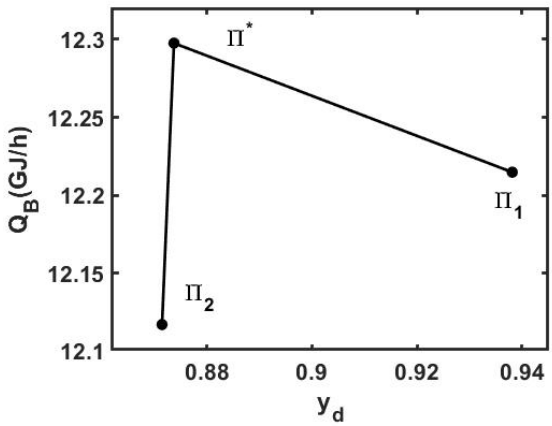

Figure 1. Nonlinear non-monotonic representation of target and two auxiliary products in terms of distillate purity and reboiler duty

This observation served as the basis for formulating the DPI paradigm for binary distillation columns in terms of producing an energy-intensive (i.e., having high reboiler duty Q_B*) product Π*, with target purity y_d*, as a mixture of two auxiliary products Π_1 and Π_2, having purities $y_{d,1}$ (higher than the target purity) and, respectively, purity $y_{d,2}$ (lower than the target purity). The reboiler duties corresponding to the auxiliary products are, respectively, $Q_{B,1}$ and $Q_{B,2}$. Importantly, *both* $Q_{B,1}$ *and* $Q_{B,2}$ are *lower* than Q_B* and, as a consequence, the mixture of the two auxiliary products, chosen in the appropriate proportion, can have the same *average* purity as target purity y_d*, but lower *average energy consumption* than Q_B*.

Of critical importance here is the split coefficient α, defined such that:

$$\alpha \text{ Product Flow Rate } \Pi_1 + (1 - \alpha) \text{ Product Flow Rate } \Pi_2 = \text{Product Flow Rate } \Pi^*$$
$$\alpha \text{ Product Purity } \Pi_1 + (1 - \alpha) \text{ Product Purity } \Pi_2 = \text{Product Purity } \Pi^* \quad (1)$$

That is, α is weighting the product qualities of the auxiliary products, such that the weighted average of the respective values is equal to the desired/target value for the desired product Π^*. From a practical perspective, the implementation of this concept entails operating a single distillation column in a transient, periodic fashion, switching between making products Π_1 and Π_2 with a frequency dictated by α. The desired product Π* is obtained as a time-averaged mixture of the auxiliary products. Naturally, in practice, this requires the installation of holding tanks for the distillate and bottoms products of the distillation column, where the high purity and low purity auxiliary products are mixed and the “time averaging” occurs.

The DPI concept described above is not applicable immediately to binary distillation columns due to an additional complication. Conditions (1) cannot be *simultaneously* met by altering *only* the boilup rate. First, considering, e.g., the case of the distillate product, it is intuitive that, as the distillate purity increases, its flow rate will drop. In turn – based on the column overall and component material balances – the bottoms flow rate will increase, and the purity of the bottoms product (in terms of the heavy component) will drop to accommodate the decrease in the amount of light component that leaves the column as distillate.

In our previous work, we have resolved this problem by defining the auxiliary product in terms of broader *operating states*, characterized as a function of the values of *multiple* manipulated variables. In addition to boilup rate, these include, e.g., reflux rate, column pressure. In this manner, we

demonstrated that, with the appropriate choice of the split coefficient and auxiliary operating states, a periodically operated distillation column can meet, *on average over time,* all the product specifications (purity, flow rate) of a conventional, steady-state column, but with lower energy consumption (defined in terms of reboiler duty or the sum of reboiler and condenser duties).

OPTIMIZING AUXILIARY PRODUCTS FOR DYNAMIC INTENSIFICATION

Our previous work relied on ad-hoc choices of the auxiliary products and related operating states. These were largely based on empirical exploration, via steady-state simulation, of the static nonlinear response of a column to changes in the manipulated variables frequently used in practice. In this section, we aim to set this exploration on a rigorous basis. Below, we describe an optimization problem formulation that captures the search for the *optimal* auxiliary operating states and split coefficient for dynamic intensification.

The inputs of the problem are as follows: we assume that the parameters of the binary feed mixture and target properties of the distillate and bottoms products (flow rate, composition) are known, and that the desired separation is feasible with a finite number of theoretical stages. Further, we assume that a steady-state model of the column is available, reflecting the material and energy balances, as well as relevant constitutive relations (e.g., phase equilibria) of the column operating at the respective state. Finally, we state that the choice of n manipulated variables (MV_i, $i=1,\ldots,n$) to be used in imposing periodic operation is fixed *a priori* (that is, the optimization procedure will not select which column inputs to manipulate; rather, it will set their values within known upper and lower bounds). Implicitly, we assume that a control scheme can be designed to impose the periodic transitions between the two auxiliary operating states.

Under these circumstances, the goal of solving the optimization problem is to identify the values of the split coefficient and the values $MV_{i,1}$ and $MV_{i,2}$ of the manipulated variables at each of the two operating states, such that the weighted average energy consumption of the column $\alpha Q_{B,1} + (1 - \alpha)Q_{B,2}$ is lower than that of the aforementioned steady-state design. The constraints of the problem include, i) ensuring that flow rate and quality constraints (1) are met for distillate and bottoms, ii) that the manipulated variables are within their bounds, and iii) that the material and energy balance equations are satisfied at both auxiliary operating states.

Thus, the problem statement is as follows:

$$\min_{\alpha,\, MV_{i,1},\, MV_{i,2}} \quad \alpha Q_{B,1} + (1 - \alpha) Q_{B,2}$$

s.t.

$$\begin{gathered} \text{quality and flow constraints (1)} \\ MV_{i,min} \le MV_i \le MV_{i,max} \\ \alpha_{\min} \le \alpha \le \alpha_{\max} \\ F(MV_{i,1}) = 0 \\ F(MV_{i,2}) = 0 \end{gathered} \tag{2}$$

where $F(MV_{i,1}) = 0$ and $F(MV_{i,2}) = 0$ reflect the constraint that the material and energy balance equations of the column must be satisfied at both auxiliary operating states.

We note that problem (2) is nonlinear and non-convex, and multiple local minima are to be expected. One of these minima is in fact the original set of operating conditions of the column, where $MV_{i,1} = MV_{i,2} = MV_i^*$. In order to steer the optimization solver away from this trivial solution, additional constraints should be included; these can be of the form

$$\begin{gathered} MV_{i,min,1} \le MV_{i,1} \le MV_{i,max,1} \\ MV_{i,min,2} \le MV_{i,2} \le MV_{i,max,2} \\ MV_{i,max,1} \le MV_{i,min,2} \end{gathered} \tag{3}$$

CASE STUDY: OPTIMAL DYNAMIC INTENSIFICATION OF A METHANOL-PROPANOL BINARY DISTILLATION COLUMN

In this section, we build on the extensive case study of the dynamic intensification of a methanol-propanol binary distillation column, that we presented earlier [11], and identify the optimal (rather than ad-hoc) auxiliary operating states. Figure 2 shows the design and control configurations of the column and lists operating conditions under the reference steady state for the target distillate and bottoms products. The column has a total of 8 stages, including a total condenser and a reboiler, and was modeled in AspenPlus [14]. An equimolar mixture of methanol-propanol enters the column at stage 4 as a saturated liquid at 1.03 bar. The reference steady state operating pressure of the column is 1.00 bar, with 300 kmol/h reflux rate and 11.51 boilup ratio. The target distillate purity is $y_d^* = 87.37\%$, with a distillate flow rate of 34.26 kmol/h. Two blending tanks are used to reflect the needs of dynamic intensification. These tanks were not explicitly modeled and are assumed to be sufficiently large to filter fluctuations in product flow rates and compositions. Six control loops are implemented:

- boilup ratio/rate is adjusted using steam flow rate to the reboiler
- the reflux rate is adjusted using the reflux valve
- column pressure is controlled using coolant flow rate
- the feed flow rate is controlled using the feed valve
- condensate drum and sump levels are stabilized using distillate and bottoms flow rates, respectively.

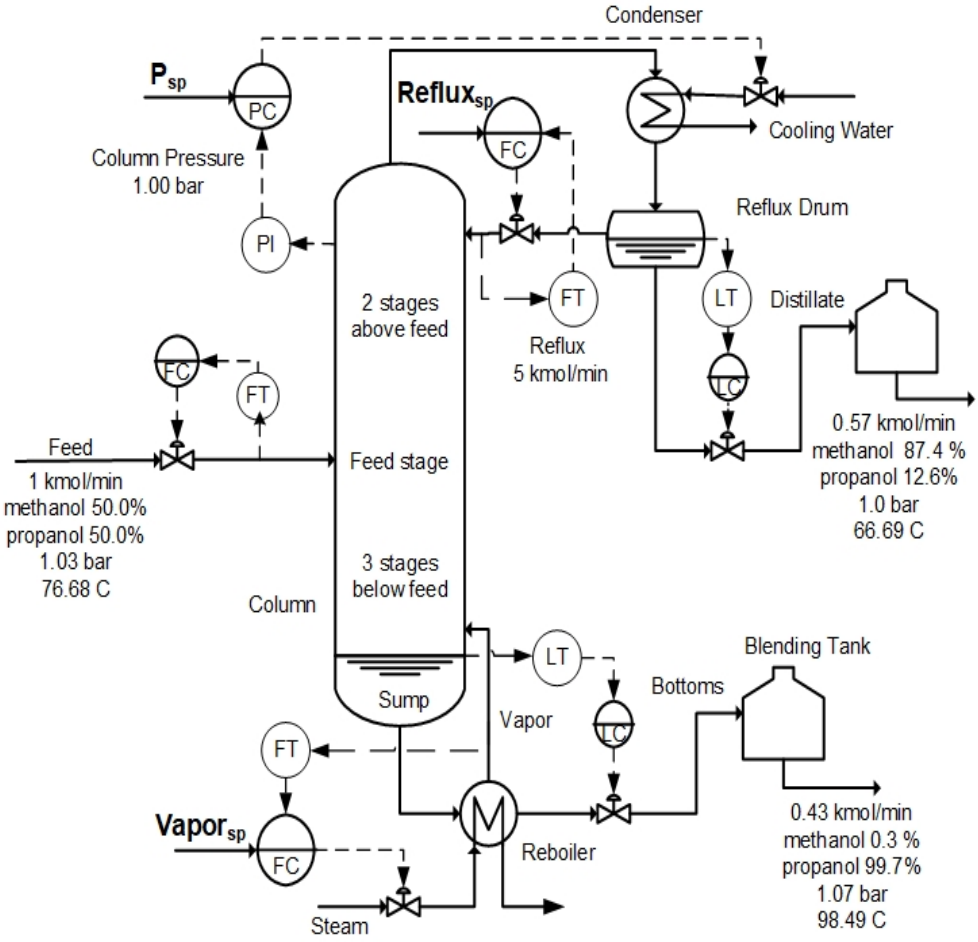

Figure 2. Schematic configuration of methanol-propanol binary column and operation conditions for reference steady state

Four manipulated variables were used to define the auxiliary operating states for dynamic intensification: reflux rate, boilup rate, column pressure and feed stream pressure. Figure 3 a) shows the effect of varying reflux rate

on reboiler duty under fixed pressure. As expected, lower reflux rates require less energy to reach same purity as in the base case, at the cost of a drop in distillate flow rate. Figure 3 b) presents the influence of column pressure on reboiler duty under fixed reflux rate. Somewhat counter-intuitively, higher pressures can save energy while maintaining same purity. The reason is that increasing pressure diminishes the amount of material vaporized.

Figure 4 shows that the pressure of saturated liquid feed has a similar effect on reducing reboiler duty as the column pressure. At the same purity, higher feed pressure is favorable to reducing reboiler energy consumption. This is due to the characteristics of the vapor-liquid equilibrium. As pressure increases, the temperature of the feed increses and therefore less steam is required to reach same bottoms temperature, with minimal impact on separation performance.

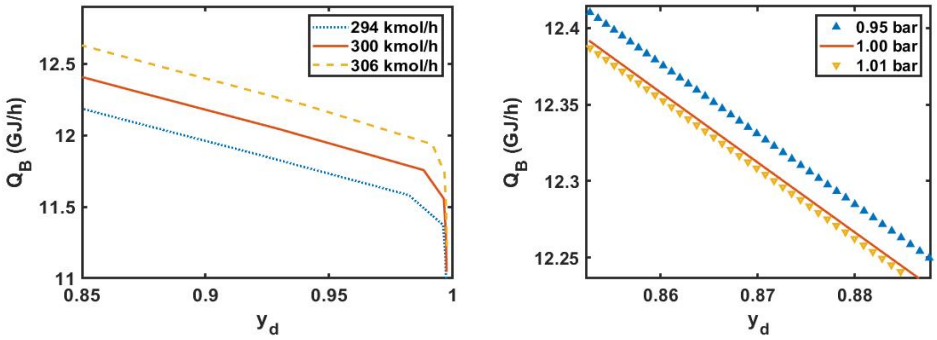

Figure 3. a) Effect of reflux rate on reboiler duty at operating pressure of 1 bar and feed pressure 1.03 bar; b) Effect of operating pressure on reboiler duty under fixed reflux rate 300 kmol/h

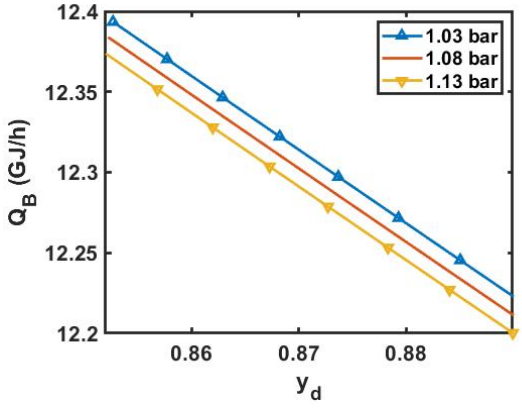

Figure 4. Effect of saturated liquid feed pressure on reboiler duty under operating pressure 1 bar and reflux rate 300 kmol/h

In our previous work [11], we empirically selected two auxiliary operating states, reaching 1.4% energy savings for periodic operation/dynamic intensification compared to the steady-state column. Below, we implement the optimization-based strategy outlined above to maximize these savings.

The optimization problem includes nine decision variables: one defining the overall operation (α) and four for each auxiliary product/operating point, specifically column pressure (P), feed pressure (P_F), boilup ratio (Bratio) and reflux rate (Reflux).

$$\text{Min} \quad \alpha Q_{B,1} + (1 - \alpha) Q_{B,2}$$

Subject to:

$$\begin{aligned}
&\alpha \text{Distillate}_{,1} + (1 - \alpha)\text{Distillate}_{,2} = \text{Distillate}^* \\
&\alpha y_{d,1} + (1 - \alpha)\, y_{d,2} = y_d^* \\
&P_{min,1} \le P_1 \le P_{max,1} \\
&P_{Fmin,1} \le P_{F1} \le P_{Fmax,1} \\
&\text{Bratio}_{min,1} \le \text{Bratio}_1 \le \text{Bratio}_{max,1} \\
&\text{Reflux}_{min,1} \le \text{Reflux}_1 \le \text{Reflux}_{max,1} \\
&P_{min,2} \le P_2 \le P_{max,2} \\
&P_{Fmin,2} \le P_{F2} \le P_{Fmax,2} \\
&\text{Bratio}_{min,2} \le \text{Bratio}_2 \le \text{Bratio}_{max,2} \\
&\text{Reflux}_{min,2} \le \text{Reflux}_2 \le \text{Reflux}_{max,2} \\
&\alpha_{min} \le \alpha \le \alpha_{max}
\end{aligned} \tag{4}$$

Inequality constraints reflect upper and lower bounds for the eight decision variables which are subject to change according to the different auxiliary operating points. The upper and lower bounds for the split coefficient, α, are, respectively, 0.01 and 0.99 to guarantee at least 1% of contribution from one of the auxiliary operating points. The problem was solved for two product purities, y_d^* = 83.37% (Table 1 lists bounds used for this case), and y_d^* = 92.97% (Table 3). We note that quality and flow rate constraints were only set on the distillate product; since this is a binary column, the desired flow rate and composition of the bottoms stream are achieved implicitly by virtue of closing the material balance.

The problem was implemented and solved in AspenPlus V8.8 [14]. The flowsheet (Figure 5) uses *two* column units (represented as RadFrac blocks) to represent the two auxiliary operating states (which correspond to a low purity and, respectively, high purity product). The splitter blocks are used to reflect the effect of the split coefficient, while a mixer block mimics the mixing tank where the final blended product is collected. The optimization problem was solved using the DMO solver. The objective convergence tolerance was set to 1e-6 and residual convergence tolerance to 1e-5. To facilitate the numerical solution, the equality constraints on distillate flow rate and purity in

(4) were reformulated as inequalities, with tolerance 5e-4%. Given a feasible initial solution, the problem could be solved in a matter of seconds on an Intel Core i7 computer with 32GB RAM running Windows 10.

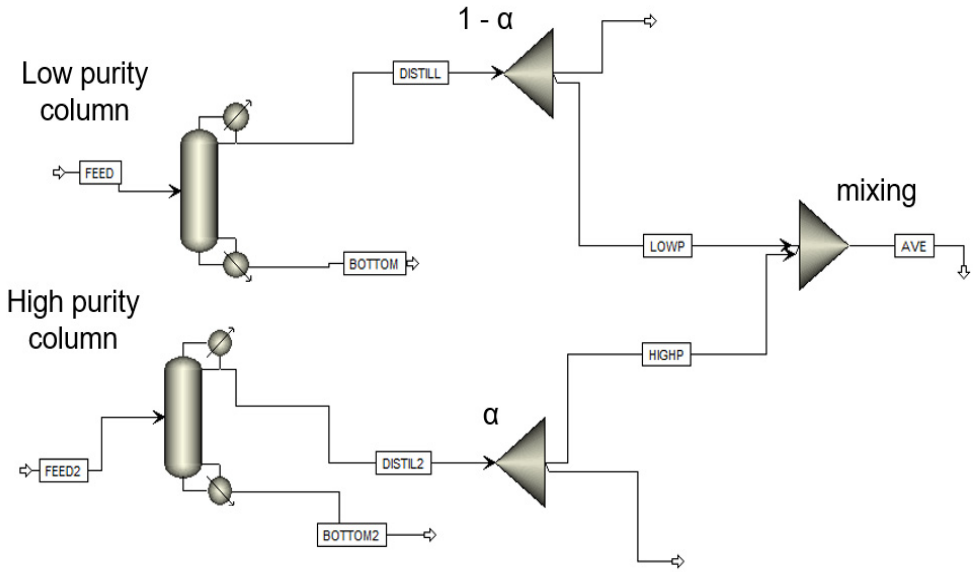

Figure 5. Aspen Plus flowsheet

Table 2 summarizes the results of the optimization calculations for y_d^* = 83.37%. The results show a potential 3.63% energy savings with no impact on product quality. The values of the manipulated variables follow the trends expected based on the discussion above (Figures 3 and 4). Both operating and feed pressure approached their upper limits and the reflux rate reached its lower limit.

The second run of the optimization problem focused on dynamic intensification at a higher purity point, y_d^* = 92.97%. Table 4 lists the corresponding optimized auxiliary operating points, based on the bounds on the manipulated variables defined in Table 3. The optimization results show similar energy savings for the higher purity target, with closely matched average stream qualities.

A couple of remarks are in order. First, the energy savings are quite significant, and achieving them only requires changes in operating strategy with minimal hardware modifications. Second, we note that the implementation of results similar to the ones presented above in the form of a transient, periodic operation strategy was successfully demonstrated via dynamic simulation in our previous papers [10,11].

Table 1. Upper and lower bounds for decision variables, y_d* = 83.37%

	Low purity state Π_2		**High purity state Π_1**	
Decision variables	Lower bound	Upper bound	Lower bound	Upper bound
Bratio	10	12	10	12
Reflux (kmol/h)	287.9	293.9	300.1	306.1
P (bar)	0.96	1.06	1.001	1.101
P_F (bar)	0.99	1.09	1.031	1.131

Table 2. Optimal operating conditions, y_d* = 83.37% with α = 0.01

	Π*	Π_1	Π_2	**Weighted Ave**	**% difference**
y_d	0.8737	0.8765	0.8737	0.8737	-0.0005
$F_{methanol}$ (kmol/h)	29.9339	29.9322	29.9336	29.9336	-0.0010
Distillate (kmol/h)	34.2614	34.1489	34.2624	34.2612	-0.0005
x_b	0.9974	0.9974	0.9974	0.9974	-0.0012
$F_{propanol}$ (kmol/h)	25.6725	25.7833	25.6713	25.6724	-0.0005
Bottoms (kmol/h)	25.7386	25.8511	25.7377	25.7388	+0.0007
P (bar)	1	1.0024	0.9841		
P_F (bar)	1.03	1.131	1.09		
Bratio	11.5102	11.4308	11.0774		
Reflux (kmol/h)	300.0	300.1	287.9		
Q_B (GJ/h)	12.2976	12.2644	11.8464	11.8506	**-3.6347**

Table 3. Upper and lower bounds for decision variables, y_d* = 92.97%

	Low purity state Π_2		**High purity state Π_1**	
Decision variables	Lower bound	Upper bound	Lower bound	Upper bound
Bratio	9	12	9	12
Reflux (kmol/h)	286	286.4	299.9	300.3
P (bar)	0.9	0.92	1.001	1.021
P_F (bar)	0.93	0.95	1.031	1.051

Table 4. Optimal operating conditions, y_d^* = 92.97% with α = 0.01

	New Π^*	Π_1	Π_2	Weighted Ave	% difference
y_d	0.9297	0.9901	0.9291	0.9297	+0.0004
$F_{methanol}$ (kmol/h)	29.8769	29.0328	29.8854	29.8768	-0.0002
Distillate (kmol/h)	32.1362	29.3218	32.1644	32.1360	-0.0006
x_b	0.9956	0.9672	0.9959	0.9956	-0.0002
$F_{propanol}$ (kmol/h)	27.7407	29.7110	27.7209	27.7408	+0.0005
Bottoms (kmol/h)	27.8638	30.6782	27.8356	27.8640	+0.0007
P (bar)	1.00	1.021	0.92		
P_F (bar)	1.03	1.051	0.95		
Bratio	10.3947	9.21501	9.97547		
Reflux (kmol/h)	299.5	299.9	286.0		
Q_B (GJ/h)	12.0251	11.7238	11.5867	11.5881	**-3.6342**

CONCLUSIONS

In this paper, we presented recent developments in maximizing the economic and energy saving benefits derived from dynamic intensification of distillation column operations. Conceptually, this entails making a desired product as a blend of two auxiliary products (one with higher purity, the other with lower purity, but both having lower energy consumption). Practically, dynamic intensification means periodically switching between two operating states corresponding to the aforementioned products. Past work has relied on ad-hoc choices of auxiliary products. Here, we formulated the problem of identifying said products as an optimization problem. An extensive case study concerning the separation of an equimolar methanol/propanol mixture demonstrated that optimizing the choice of auxiliary products can lead to significant energy savings (more than 3.6% compared to a column operated at steady state) with minimal hardware additions. We expect that these concepts can be extended to ternary separations and beyond, and the dynamic intensification of ternary columns constitutes the subject of ongoing work in our group.

ACKNOWLEDGMENTS

Funding from the U.S. Department of Energy through the RAPID Process Intensification Institute under Award DE-EE0007888-05-4 is acknowledged with gratitude.

This report was prepared as an account of work sponsored by an agency of the United States Government. Neither the United States Government nor any agency thereof, nor any of their employees, makes any warranty, express or implied, or assumes any legal liability or responsibility for the accuracy, completeness, or usefulness of any information,

apparatus, product, or process disclosed, or represents that its use would not infringe privately owned rights. Reference herein to any specific commercial product, process, or service by trade name, trademark, manufacturer, or otherwise does not necessarily constitute or imply its endorsement, recommendation, or favoring by the United States Government or any agency thereof. The views and opinions of authors expressed herein do not necessarily state or reflect those of the United States Government or any agency thereof.

DEDICATION

Michael Baldea: with the assent of my co-authors, I dedicate this work to Professor Ioan Baldea. He is an academic researcher par excellence and a teacher whose pedagogic style uniquely blends scientific rigor with a healthy dose of humor. More importantly, he is the father I aspire to be.

REFERENCES

1. M. Baldea, P. Daoutidis, “Dynamics and Nonlinear Control of Integrated Process Systems”, Cambridge University Press, Cambridge, UK, **2012**.
2. J. L. Humphrey, *Chemical Engineering Progress,* **1995**, *91* (10).
3. A. A. Kiss, “Advanced Distillation Technologies”, John Wiley & Sons, Ltd, Chichester, UK, **2013**. https://doi.org/10.1002/9781118543702.
4. J. L. Humphrey, A. F. Seibert, R. A. Koort, *Separation Technologies: Advances and Priorities*, Washington DC, **1991**.
5. S. S. Jogwar, M. Baldea, P. Daoutidis, *Computer & Chemical Engineering,* **2010**, *34* (9), 1457–1466. https://doi.org/10.1016/j.compchemeng.2010.02.005.
6. M. M. Donahue, B. J. Roach, J. J. Downs, T. Blevins, M. Baldea, R. B. Eldridge, *Chemical Engineering and Process: Process Intensification,* **2016**, *107*, 106–115. https://doi.org/10.1016/j.cep.2016.05.013.
7. R. C. Pattison, A. M. Gupta, M. Baldea, *AIChE Journal,* **2016**, *62* (3), 704–716. https://doi.org/10.1002/aic.15060.
8. M. R. Cannon, *Industrial & Engineering Chemistry,* **1961**, *53* (8), 629. https://doi.org/10.1021/ie50620a021.
9. B. V. Maleta, A. Shevchenko, O. Bedryk, A. A. Kiss, *AIChE Journal,* **2015**, *61* (8), 2581–2591. https://doi.org/10.1002/aic.14827.
10. L. Yan, T. F. Edgar, M. Baldea, *AIChE Journal,* **2019**, *65* (4), 1162-1172. https://doi.org/10.1002/aic.16506.
11. L. Yan, T. F. Edgar, M. Baldea, *Industrial & Engineering Chemistry Research*, **2019**, *58* (15), 5830-5837. https://doi.org/10.1021/acs.iecr.8b04852.
12. E. W. Jacobsen, S. Skogestad, *AIChE Journal,* **1991**, *37* (4), 499–511. https://doi.org/10.1002/aic.690370404.
13. A. Koggersbøl, T. R. Andersen, J. Bagterp, S. B. Jørgensen, *Computer & Chemical Engineering,* **1996**, *20* (96), S835–S840. https://doi.org/10.1016/0098-1354(96)00147-0.
14. Aspen Technology Aspen Plus, www.aspentech.com

STUDIA UBB CHEMIA, LXIV, 2, Tom II, 2019 (p. 371-381)
(RECOMMENDED CITATION)
DOI:10.24193/subbchem.2019.2.31

Dedicated to Professor Ioan Bâldea on the Occasion of His 80th Anniversary

ASSESSMENT OF VARIOUS WATER-GAS-SHIFT PROCESS CONFIGURATIONS APPLIED TO PARTIAL OXIDATION ENERGY CONVERSION PROCESSES WITH CARBON CAPTURE

VLAD-CRISTIAN SANDU[a], CALIN-CRISTIAN CORMOS[a], ANA-MARIA CORMOS[a*]

ABSTRACT. The energy conversion systems based on partial oxidation processes (hydrocarbons catalytic reforming, solid fuel gasification) are very promising for integrating carbon capture technologies due to high CO_2 partial pressure in syngas to be treated. In these systems, the water-gas-shift (WGS) reaction has a very important place in concentrating the syngas energy as hydrogen and to convert carbon species as CO_2. This paper is evaluating various WGS process configurations to be applied in catalytic reforming and gasification designs ranging from the conventional designs (multiple catalytic shift reactors) to more innovative reactive gas-solid systems (chemical & calcium looping) for simultaneous syngas conversion and CO_2 capture. As the evaluations show, the reactive gas-solid systems are more promising in reducing energy penalty for CO_2 capture as well as to increase the overall energy efficiency and carbon capture rate. As illustrative examples, the coal gasification for hydrogen and power co-generation with carbon capture were assessed.

Keywords: *Partial oxidation, Water-gas-shift, Carbon capture, Reactive gas-liquid and gas-solid systems.*

INTRODUCTION

The fossil fuel intensive industrial applications are facing increasing pressure from the point of reducing greenhouse gas (GHG) emissions as well as to secure primarily energy supplies [1]. In the last decade, significant research and development efforts were directed to reduce GHG emissions (in combating

[a] *Babeş-Bolyai University, Faculty of Chemistry and Chemical Engineering, 11 Arany Janos str., RO-400028, Cluj-Napoca, Romania*
** Corresponding author: cani@chem.ubbcluj.ro*

global warming and climate change) and also to find promising energy conversion systems with higher energy efficiency. Along this line, a large variety of conceptual methods can be used e.g. replacing fossil fuels (natural gas, coal, lignite) with renewable energy sources (solar, wind, biomass) as energy carriers, increasing the energy efficiency of large scale industrial systems, improving the end-user energy utilization, fuel switching, nuclear energy, large scale deployment of Carbon Capture, Utilization and Storage (CCUS) technologies [2].

Among the most important two energy conversion concepts (based on fuel total and partial oxidation methods), the partial oxidation (PO) systems have significant advantages [3-5] e.g. lower effort to introduce the carbon capture (due to higher CO_2 partial pressure in syngas compared with flue gas), better overall energy efficiencies, poly-generation capabilities (ability of the plant to produce simultaneously various energy carriers e.g. power, hydrogen, methanol, synthetic methane etc.). Two main partial oxidation systems are used: (i) catalytic reforming of hydrocarbons (gas or liquid) and (ii) solid fuel gasification. In PO designs, the conversion of carbon monoxide and steam to carbon dioxide and hydrogen is of paramount importance for a two-fold reason [6]: concentration of syngas energy as hydrogen and converting most of carbon species as CO_2 to be later captured. The reaction of water gas shift (WGS) is the following:

$$CO + H_2O \leftrightarrow CO_2 + H_2$$

The WGS conversion of syngas can be done in various process configurations as evaluated in the present paper [7-9]. The assessments are geared towards the evaluation of process configurations on key plant performance indicators (e.g. overall energy efficiency, ancillary energy consumptions, carbon capture rate, specific CO2 emissions etc.) of various WGS conceptual designs. The assessed WGS process options are:

(i) Conventional catalytic conversion using 2-3 reactors in series either in clean shift conditions (with applications in natural gas reforming technologies) or sour shift conditions (with applications in coal gasification);

(ii) Iron looping (FeL) cycle using three interconnected circulated fluidized bed (CFB) reactors where the following reactions take place [10]:

- Syngas (fuel) reactor:

$$3CO + Fe_2O_3 \rightarrow 3CO_2 + 2Fe$$

$$3H_2 + Fe_2O_3 \rightarrow 3H_2O + 2Fe$$

- Steam reactor:

$$3Fe + 4H_2O \rightarrow Fe_3O_4 + 4H_2$$

- Air reactor:

$$2Fe_3O_4 + 1/2O_2 \rightarrow 3Fe_2O_3$$

(iii) Calcium looping (CaL) cycle using two interconnected circulated fluidized bed (CFB) reactors where calcium-based sorbent is used to move the WGS equilibrium to the right according to the following reactions [10]:

- Carbonation (sorption enhanced water gas shift) reactor:

$$CO + H_2O + CaO \rightarrow CaCO_3 + H_2$$

- Calcination reactor:

$$CaCO_3 \rightarrow CaO + CO_2$$

As can be observed, both above mentioned high temperature looping cycles have as global WGS reaction as for catalytic case.

As illustrative case studies, this paper is assessing coal gasification as partial oxidation energy conversion system in conjunction with the above mentioned WGS configurations for hydrogen and power generation with carbon capture using reactive gas-liquid and gas-solid systems. The main novelty of this paper is relating to the evaluation of WGS systems based on chemical and calcium looping technologies for improved energy efficiency.

PLANT CONFIGURATIONS AND MAIN DESIGN ASSUMPTIONS

The Integrated Gasification Combined Cycle (IGCC) is a power generation technology in which the solid fuel is gasified with oxygen and steam to produce syngas [11]. After desulphurization, the syngas is used in a Combined Cycle Gas Turbine (CCGT) for power generation. When carbon capture step is integrated into an IGCC plant, WGS reaction has the purpose to concentrate the syngas energy as hydrogen as well as carbon species as CO_2 [12-14]. The conceptual design of IGCC plant for hydrogen and power co-generation with carbon capture using conventional catalytic WGS conversion and gas-liquid absorption is presented in Figure 1.

In this design, the mixture of hydrogen and carbon dioxide resulted after WGS conversion is fed to the Acid Gas Removal (AGR) unit where using a reactive gas-liquid absorption (e.g. Methyl-DiEthanol-Amine - MDEA) CO_2 is captured. The resulted hydrogen-rich gas can be either used in a combined cycle block for power generation or / and purified by Pressure Swing Adsorption for producing 99.95% (vol.) hydrogen stream (either for external customers of for energy storage purposes).

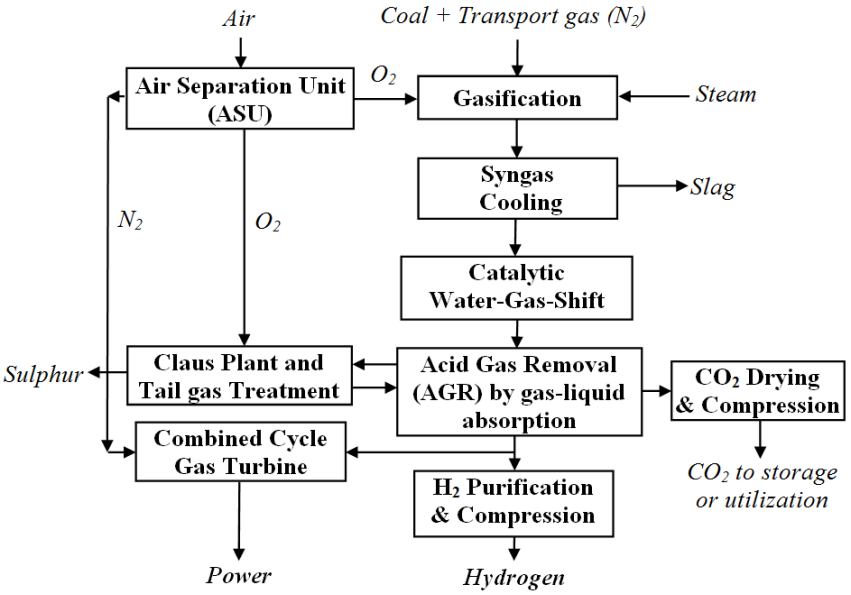

Figure 1. Design of IGCC plant with conventional catalytic WGS conversion

The other two investigated WGS concepts (based on FeL and CaL cycles) are using a more innovative technique - high temperature solid looping - to convert the fuel (syngas) simultaneous with CO_2 capture. For illustration, Figure 2 presents the conceptual design of Sorption Enhanced Water Gas Shift (SEWGS) unit using calcium-based material [15-16].

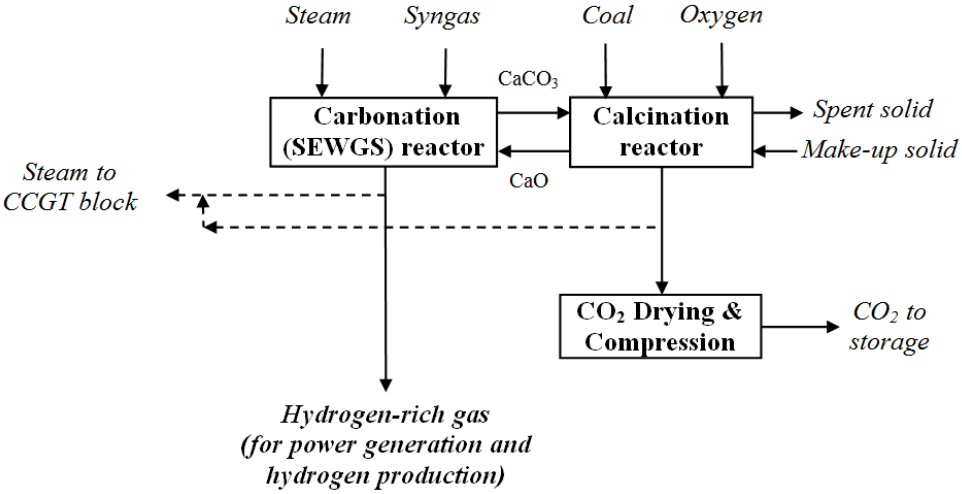

Figure 2. Design of carbon capture unit using CaL - SEWGS cycle

In term of fuel, all cases used an international trade high grade coal sort (Douglas Premium). As gasification reactor considered in all designs, the dry fed syngas boiler configuration was chosen considering the high energy efficiency and low syngas clean-up issues [11]. Also, in term of gas turbine selection, a Mitsubishi Hitachi Power Systems - M701G2 was chosen for all evaluated cases considering its good industrial experience in processing hydrogen-rich gases as well as high energy efficiency and operational flexibility. The following IGCC with carbon capture (based on reactive gas-liquid and gas-solid systems) cases were assessed:

Case 1: IGCC plant with conventional catalytic WGS reactors and MDEA-based gas-liquid absorption for CO_2 capture;
Case 2: IGCC plant with syngas-based iron looping cycle;
Case 3: IGCC plant with syngas-based calcium looping cycle.

The main design assumptions used in the modelling and simulation of the above mentioned concepts are presented in Table 1 [3,13,17-18].

Table 1. Main design assumptions of assessed IGCC case studies (Cases 1 - 3)

Unit	Parameters
Air Separation Unit (ASU)	Oxygen purity (vol.): 95% O_2, 3% Ar, 2% N_2 ASU power consumption: 195 kWh/ton oxygen
Gasification reactor	Oxygen / coal ratio (kg/kg): 0.85 Steam / coal ratio (kg/kg): 0.11 Nitrogen / coal ratio (kg/kg): 0.10 Gasifier pressure: 40 bar Gasifier temperature: ~1450^{o}C Fuel conversion: >99 %
Catalytic WGS conversion	Sulphur tolerant catalyst (sour shift) Two adiabatic catalytic beds Pressure drop: 1 bar / bed
Acid Gas Removal - AGR (all cases - desulphurisation)	Solvent: aqueous MDEA solution (50% mass) Thermal solvent regeneration
Iron looping (FeL) cycle	Fuel reactor: 31.5 bar / 750 - 900^{o}C Steam reactor: 30 bar / 700 - 800^{o}C Air reactor: 29 bar / 800 - 1000^{o}C Gibbs free energy minimization model Pressure drops: 1 bar / reactor
Calcium looping (CaL) cycle	Carbonation reactor: 32 bar / 550 - 600^{o}C Calcination reactor: 31 bar / 900 - 980^{o}C Gibbs free energy minimization model Pressure drops: 1 bar / reactor
CO_2 compression and drying	CO_2 delivery pressure at plant gate: 120 bar Compressor efficiency: 85% Solvent used for drying: Tri-ethylene-glycol

Unit	Parameters
Gas turbine	1 x Mitsubishi Hitachi Power Systems - M701G2 Gas turbine net power output: 334 MW Heat rate: 9110 kJ/kWh (net efficiency: 39.5%) Compressor pressure ratio: 21 Turbine outlet temperature (TOT): 587ºC
Heat Recovery Steam Generator (HRSG) and steam cycle (Rankine)	Three pressure levels: 120 / 35 / 3 bar MP steam reheat Steam turbine isoentropic efficiency: 85% Steam wetness ex. steam turbine: max. 10%
Heat exchangers	ΔTmin. = 10ºC Pressure drop: 2-5 % of inlet pressure

RESULTS AND DISCUSSIONS

The evaluated IGCC plant concepts were modeled and simulated using ChemCAD software, the generated mass and energy balances being used for quantification of main key performance indicators. For overall plant energy efficiency optimization (targeting especially WGS unit), all evaluated designs were thermally integrated using pinch methodology [19-20]. For illustration, Figure 3 presents the hot and cold composite curves for all three investigated WGS configurations along with syngas treatment line.

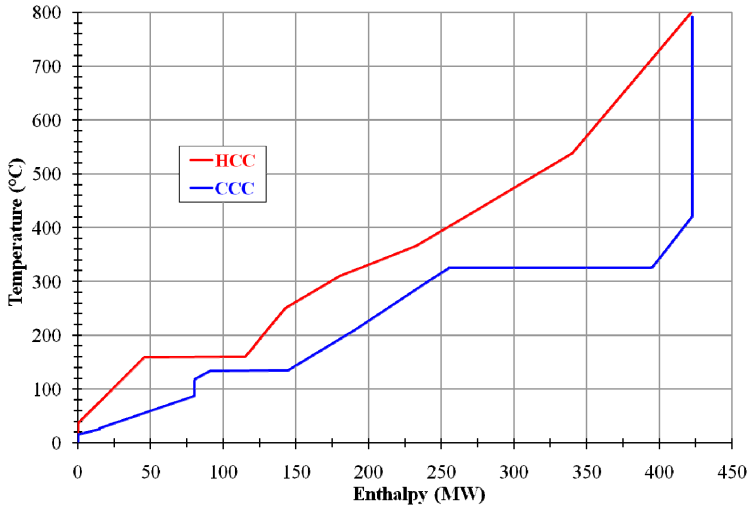

Figure 3.a. Composite curves for catalytic WGS reactors (Case 1)

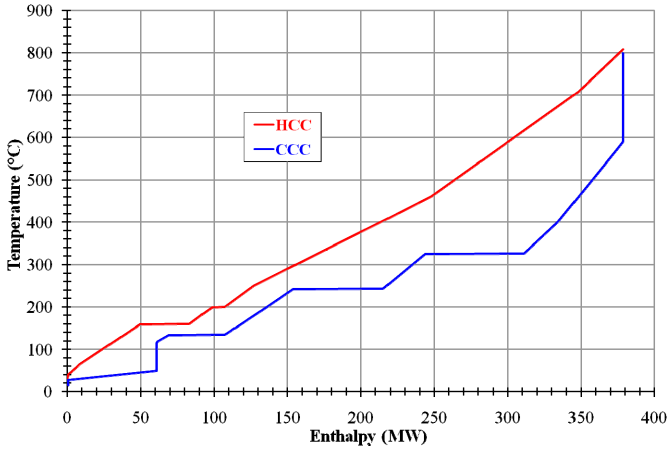

Figure 3.b. Composite curves for iron looping cycle (Case 2)

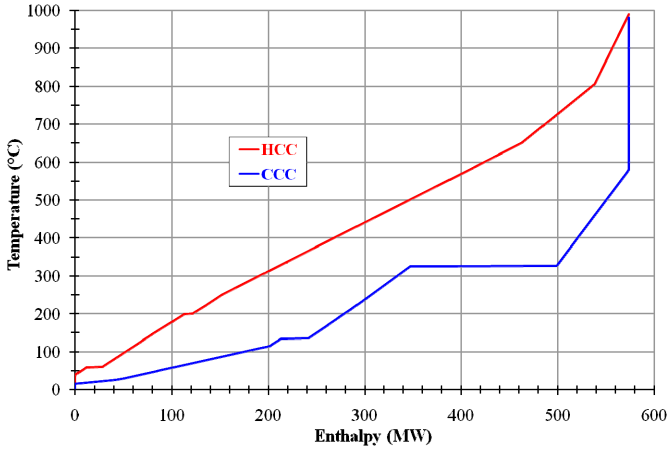

Figure 3.c. Composite curves for chemical looping cycle (Case 3)

An important aspect to be mentioned is that for the chemical looping cases, the operating temperatures of looping reactors are significantly higher than for gas-liquid absorption (operated around atmospheric temperature). As can be observed from Figure 3, for iron looping case (Case 2), more heat is recovered as MP steam compared to Cases 1 and 3. Also, when compare the looping cases, one can noticed that the thermal integration in Case 2 (FeL) is better (hot and cold composite curves are closer) than for Case 3 (CaL). These aspects will have an important influence on overall energy efficiency of the plant as presented below.

Table 2 presents the main performance indicators of evaluated IGCC with carbon capture designs operated in power generation only.

Table 2. Overall plant performance indicators - power generation only

Main Plant Data	Units	Case 1	Case 2	Case 3
Coal flowrate (as received)	t/h	165.00	162.00	225.00
Coal LHV (as received)	MJ/kg		25.353	
Coal thermal energy (A)	MW_{th}	1162.00	1140.88	1584.56
Gas turbine output (M701G2)	MW_e	334.00	334.00	334.00
Steam turbine output	MW_e	201.25	200.00	411.25
Expander power output	MW_e	1.01	1.25	1.40
Gross electric power output (B)	MW_e	536.26	535.25	746.65
Ancillary consumption (C)	MW_e	110.67	95.75	152.82
Net power output (D = B - C)	MW_e	425.59	439.50	593.83
Gross efficiency (B/A * 100)	%	46.15	46.91	47.12
Net efficiency (D/A * 100)	%	36.62	38.52	37.47
Carbon capture rate	%	90.00	99.00	96.00
CO_2 specific emissions	kg/MWh_e	83.24	4.10	33.50

The high temperature looping cases (FeL and CaL) have superior overall net efficiency (by about 0.9 - 1.9 points) and carbon capture rate (90% vs. 96 - 99%) than conventional WGS catalytic conversion coupled with reactive gas-liquid absorption for CO_2 capture. These results show the good potential of chemical looping technology (which simultaneously convert the syngas energy in a decarbonised energy carrier - hydrogen and capture carbon from syngas) to replace in the future the conventional technologies (catalytic WGS conversion and gas-liquid absorption).

Ancillary energy consumption of carbon capture unit is a factor with paramount importance in any CCUS design. In this respect, the reactive gas-liquid systems (as exemplified here by MDEA-based system) have a clear disadvantage by the significant heat duty required to regenerate the solvent (about 3 MJ/kg CO_2). To evaluate in a holistic manner the ancillary energy consumption for CO_2 capture, one can use primary energy consumption for CO_2 avoided (SPECCA) calculated as follow [21]:

$$SPECCA = \frac{Power\ plant\ heat\ rate_{Capture}[\frac{MJ_{LHV}}{MWh_e}] - Power\ plant\ heat\ rate_{No\ capture}[\frac{MJ_{LHV}}{MWh_e}]}{Specific\ CO_2\ emissions_{No\ capture}[\frac{kg\ CO_2}{MWh_e}] - Specific\ CO_2\ emissions_{Capture}[\frac{kg\ CO_2}{MWh_e}]}$$

For an IGCC power plant benchmark case without capture, key literature references (e.g. IEAGHG, NETL reports) were used [14,22]. The SPECCA values calculated for the investigated concepts (Cases 1 to 3) are: 2.75, 1.88 and respectively 2.36 MJ/kg. As also showed by SPECCA indicator, the reactive gas-solid systems (FeL and CaL cycles) have lower energy consumptions for CO_2 capture than the reactive gas-liquid system.

An important feature of gasification plants coupled with pre-combustion CO_2 capture (exhibits here by all investigated concepts) is the ability of hydrogen and power co-generation [23-25]. These plants can generate (according to the instant power demand from the grid) either only electricity (peak times), hydrogen and power (transient times) or only hydrogen for energy storage (when power generation is low). This operational flexibility can be obtained by a simple operational procedure - the gas turbine is gradually turned down to displace a hydrogen stream for purification and then energy storage. To illustrate the ability of hydrogen and power co-generation, Table 3 presents the variation of performance indicators with hydrogen produced (in the range 0 - 200 MW_{th}) for Case 2.

Table 3. Overall plant performance indicators - hydrogen and power co-generation

Main Plant Data	Units	Power	Hydrogen and power	
Coal flowrate as received)	t/h	162.00		
Coal LHV (as received)	MJ/kg	25.353		
Coal thermal energy (A)	MW_{th}	1140.88		
Gas turbine output (M701G2)	MW_e	334.00	294.28	253.10
Steam turbine output	MW_e	200.00	181.01	162.24
Expander power output	MW_e	1.25	1.20	1.15
Gross electric power output (B)	MW_e	535.25	476.49	416.49
Hydrogen output (C)	MW_{th}	0.00	100.00	200.00
Ancillary consumption (D)	MW_e	95.75	94.33	92.84
Net power output (E = B - D)	MW_e	439.50	382.16	323.65
Net efficiency (E/A * 100)	%	38.52	33.49	28.36
Hydrogen efficiency (C/A * 100)	%	0.00	8.76	17.53
Cumulative energy efficiency	%	38.52	42.25	45.89
Carbon capture rate	%	99.00	99.00	99.00
CO_2 specific emissions	kg/MWh	4.10	3.73	3.44

As can be noticed, the hydrogen and power co-generation have a positive influence on overall (cumulative) plant energy efficiency, this indicator increasing with the hydrogen output by about 3.7 net cumulative efficiency point for each 100 MW_{th} hydrogen produced. Other positive changes can be observed: slight decrease of ancillary energy consumption (by about 1.5 MW_e

per each 100 MW_{th} hydrogen) and specific CO_2 emissions (considering the total plant energy produced). In addition to the technical performance indicators, the economic indicators (e.g. specific capital investments, operational & maintenance cost, CO_2 avoidance costs etc.) are also improving with hydrogen co-production [25]. The development of flexible hydrogen production systems with low carbon emissions (as evaluated in this work) are of great importance for a sustainable development of key fossil fuel-dependent industrial sectors e.g. heat and power, transport, petro-chemistry, metallurgy etc. [26-27].

CONCLUSIONS

This paper evaluates three water-gas-shift (WGS) process configurations used in connection with a coal-based IGCC power plant with carbon capture as follow: (i) conventional multi-catalytic reactors coupled with reactive gas-liquid absorption; (ii) iron looping cycle and (iii) sorbent enhanced chemical looping cycle. As the results show, the looping cycles have significant advantages compared to conventional design e.g. higher overall plant energy efficiency (by about 0.9 - 1.9 net efficiency points), higher carbon capture rate (96 - 99% vs. 90%) and lower SPECCA values (by about 0.4 - 0.9 MJ/kg). The hydrogen and power co-generation based on IGCC design with carbon capture has also significant operational advantages: better plant flexibility (cycling), higher overall (cumulative) efficiency (3.7 net energy efficiency points per each 100 MW_{th} hydrogen), better techno-economic indicators.

ACKNOWLEDGMENTS

This work was supported by a grant of the Romanian National Authority for Scientific Research, CNCS – UEFISCDI, project ID PN-III-P4-ID-PCE-2016-0031: "*Developing innovative low carbon solutions for energy-intensive industrial applications by Carbon Capture, Utilization and Storage (CCUS) technologies*".

REFERENCES

1. European Commission, "A policy framework for climate and energy in the period from 2020 to 2030", COM(2014) 15 final, Brussels, Belgium, **2014**.
2. B. Metz, O. Davidson, H. de Coninck, M. Loos, L. Meyer, "Carbon Dioxide Capture and Storage", Intergovernmental Panel on Climate Change (IPCC), Geneva, Switzerland, **2005**.
3. A. M. Cormos, C. Dinca, C. C. Cormos, *Applied Thermal Engineering*, **2015**, *74*, 20.
4. R. Segurado, S. Pereira, D. Correia, M. Costa, *Renewable and Sustainable Energy Reviews*, **2019**, *103*, 501.

5. T. A. Adams, P. I. Barton, *Fuel Processing Technology*, **2011**, *92*, Issue 3, 639.
6. A. I. Papadopoulos, P. Seferlis, "Process systems and materials for CO_2 capture - Modelling, design, control and integration", John Wiley & Sons Ltd., **2017**, chapter 11.
7. S. Saeidi, F. Fazlollahi, S. Najari, D. Iranshahi, J. J. Klemeš, L. Baxter, *Journal of Industrial and Engineering Chemistry*, **2017**, *49*, 1.
8. K. Liu, C. Song, V. Subramani, "Hydrogen and syngas production and purification technologies", AIChE - Wiley, Inc., **2010**, chapter 6.
9. C. C. Cormos, A. M. Cormos, L. Petrescu, *Chemical Engineering Research and Design*, **2014**, *92*, 741.
10. L. S. Fan, "Chemical looping systems for fossil energy conversions", AIChE - Wiley, Inc. **2010**, chapter 1.
11. C. Higman, M. van der Burgt, "Gasification", second ed., Gulf Professional Publishing, Elsevier Science, **2008**.
12. B. Shi, W. Xu, E. Wu, W. Wu, P. C. Kuo, *Journal of Cleaner Production*, **2018**, *195*, 176.
13. C. C. Cormos, *Energy*, **2012**, *42*, 434.
14. International Energy Agency - Greenhouse gas R&D programme (IEAGHG), "Potential for improvement in gasification combined cycle power generation with CO_2 capture", Report PH4/19, Cheltenham, UK, **2003**.
15. W. Wu, F. Wen, J. R. Chen, P. C. Kuo, B. Shi, *Journal of the Taiwan Institute of Chemical Engineers*, **2019**, *96*, 193.
16. D. P. Hanak, S. Michalski, V. Manovic, *Energy Conversion and Management*, **2018**, *177*, 428.
17. U. Ahmed, U. Zahid, Y. Lee, *International Journal of Hydrogen Energy*, **2019**, *44*, 7137.
18. A. M. Cormos, C. C. Cormos, *International Journal of Hydrogen Energy*, **2014**, *39*, 2067.
19. W. Xu, B. Shi, W. Wu, *Energy Procedia*, **2018**, *152*, 1248.
20. J. A. R. Diamante, R. Tan, D. C..Y. Foo, D. K. S. Ng, K. B. Aviso, S. Bandyopadhyay, *Journal of Cleaner Production*, **2014**, *71*, 67.
21. A. M. Cormos, C. Dinca, L. Petrescu, D. A. Chisalita, S. Szima, C.C. Cormos, *Fuel*, **2018**, *211*, 883.
22. National Energy Technology Laboratory (NETL), "Cost and performance baseline for fossil energy plants - Volume 1: Bituminous coal and natural gas to electricity", Report 2010/1397, Albany, USA, **2010**.
23. A. Zohrabian, M. M. Majoumerd, M. Soltanieh, S. Sattari, *International Journal of Greenhouse Gas Control*, **2016**, *44*, 94.
24. M. van der Spek, S. Roussanaly, E. S. Rubin, *International Journal of Greenhouse Gas Control*, **2019**, *83*, 91.
25. A. M. Cormos, C. C. Cormos, *Applied Thermal Engineering*, **2019**, *147*, 29.
26. A. Chapman, K. Itaoka, K. Hirose, F. T. Davidson, K. Nagasawa, A. C. Lloyd, M. E. Webber, Z. Kurban, S. Managi, T. Tamaki, M. C. Lewis, R. E. Hebner, Y. Fujii, *International Journal of Hydrogen Energy*, **2019**, *44*, 6371.
27. A. Ozawa, Y. Kudoh, A. Murata, T. Honda, I. Saita, H. Takagi, *International Journal of Hydrogen Energy*, **2018**, *43*, 18083.

STUDIA UBB CHEMIA, LXIV, 2, Tom II, 2019 (p. 383-392)
(RECOMMENDED CITATION)
DOI:10.24193/subbchem.2019.2.32

Dedicated to Professor Ioan Bâldea on the Occasion of His 80th Anniversary

SINTERING AND CHARACTERIZATION OF NEW FORSTERITE CERAMICS

MARIA GOREA[a], MARIETA-ADRIANA NAGHIU[a], ALEXANDRA AVRAM[a,*], IOAN PETEAN[a], MARIA TOMOAIA-COTISEL[a,b]

ABSTRACT. This study presents the sintering of new forsterite ceramics (FCs) using nano forsterite powder, obtained by a sol-gel method. The forsterite ceramics were sintered between 1200 and 1450 °C. The resulted forsterite ceramics, namely FC at sintering temperature, T, written as FC(T), were characterized by various methods, XRD, AFM, apparent density, porosity and shrinkage. Mechanical properties were determined for FC(1400), with a Young elastic modulus at about 43.84 GPa and nano-indentation hardness at around 3.07 GPa. Furthermore, the *in vitro* biocompatibility of FC(1200) was evaluated using cell staining with fluorescein diacetate, FDA, assay. The cell viability results confirmed that forsterite ceramic, FC(1200), promotes cell adhesion and proliferation in cell culture, with no significant cytotoxic effects. These findings strongly recommend the new forsterite ceramics, as potential biomaterials for biomedical applications.

Keywords: *forsterite ceramics, porosity, density, biocompatibility*

INTRODUCTION

In recent years, both forsterite ceramics [1-7] and forsterite composites [8-10] were found of vital interest due to their potential applications in biomedicine. Therefore, various techniques were developed to synthesize nano-crystalline forsterite powder of high purity [11-20] for various applications,

[a] *Babes-Bolyai University, Faculty of Chemistry and Chemical Engineering, Department of Chemical Engineering, Physical Chemistry Center, 11 Arany Janos Str., 400028 Cluj-Napoca, Romania*
[b] *Academy of Romanian Scientists, 54 Splaiul Independentei, 050085, Bucharest, Romania*
**Corresponding author: aavram@chem.ubbcluj.ro*

as bone substitutes and implants [16, 17] as well as for drug delivery [19, 20], particularly due to its high bioactivity, good mechanical properties and biocompatibility [3, 5-10,15].

In this work, the sintering of new forsterite ceramics (FCs) is reported via nano forsterite powder, synthesized by using a sol-gel method. The forsterite ceramics were fired between 1200 and 1450 °C and were characterized by various methods including, porosity and mechanical properties. Also, the forsterite ceramic sintered at 1200 °C, FC(1200), was investigated in cell culture and demonstrated an excellent biocompatibility.

RESULTS AND DISCUSSION

New forsterite ceramics

The forsterite ceramics (FCs) underwent some changes depending on their structural characteristics, like apparent porosity, apparent density, and linear shrinkage as function of the sintering temperatures, 1200, 1300, 1400 and 1450 °C used in the fabrication process for the obtained FCs, noted FC(1200), FC(1300), FC(1400), and FC(1450).

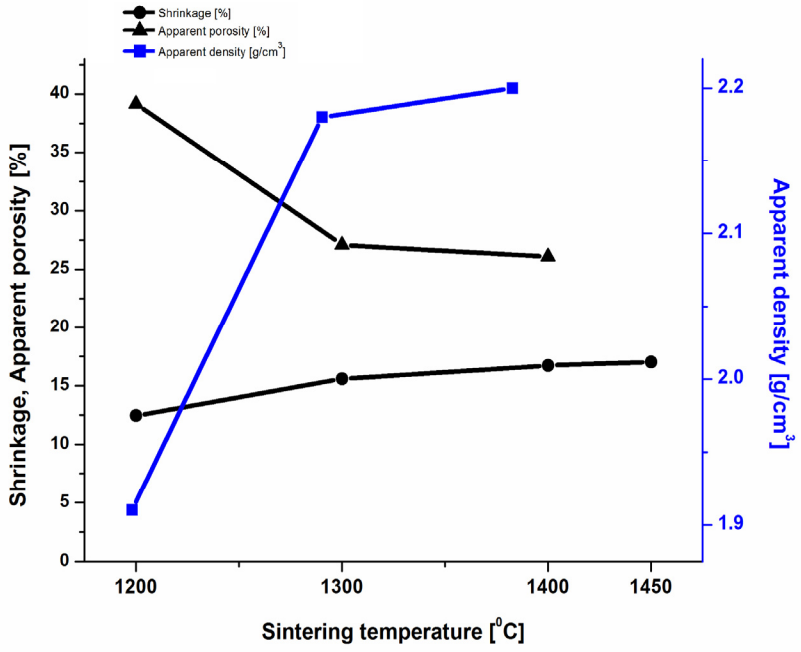

Figure 1. Apparent density, apparent porosity and linear shrinkage determined for forsterite ceramics in function of sintering temperature.

As shown in Figure 1, the linear shrinkage of the sintered forsterite ceramics displayed a steady increase from 12.46±0.16% to 17.03±0.15%, with an increase in sintering temperature from 1200 to 1450 ^{o}C. Apparent density increased from 1.91 ±0.02 to 2.33±0.01 (g/cm^3), while the corresponding porosity decreased from 39.15±0.16 to 25.05±0.14 %.

Statistical analysis evaluated with GraphPad Prism program showed that increasing the sintering temperature induced an increase in linear shrinkage. Statistically significant differences ($p< 0.05$) evaluated by one-way ANOVA and Bonferroni's multiple comparison test were observed between forsterite ceramics sintered at 1200 ^{o}C versus all the others forsterite ceramics sintered at chosen temperatures. Strong differences were also identified between forsterite ceramics sintered at 1300 ^{o}C versus both ceramics sintered at 1400 ^{o}C and 1450 ^{o}C. No significant differences were found between ceramics sintered at 1400 ^{o}C and 1450 ^{o}C. The order among forsterite ceramics (FC) is: FC(1200) <FC(1300)< FC(1400)≈ FC(1450). This data, shown in Figure 1, revealed that FC(1400) is apparently the best regarding high compactness of particles in the forsterite ceramic with potential application for bone repair defects.

Statistically strong differences were also identified between apparent density for forsterite ceramic sintered at 1200 ^{o}C versus all the other forsterite ceramics, $p<0.05$; no significant differences were found among forsterite ceramics sintered at 1300 ^{o}C, 1400 ^{o}C and 1450 ^{o}C ($p>0.05$). Therefore, the corresponding value at the highest sintering temperature is not shown in Figure 1. Statistically significant differences ($p< 0.05$) were observed between apparent porosity for forsterite ceramic sintered at 1200 ^{o}C versus the other forsterite ceramics, but without a statistically significant difference between forsterite ceramic fired at 1400 ^{o}C compared to FC-1450, $p>0.05$; the last value corresponding to 1450 ^{o}C is not shown in Figure 1.

Results obtained for the new forsterite ceramics, fired at temperatures ranging from 1200 to 1450 ºC, are comparable with those previously reported [3] for similar forsterite ceramics, fired at higher temperature from 1350 to 1550 °C. Our new forsterite ceramics present the advantage that they were obtained at lower sintering temperatures and demonstrated a unique phase of forsterite structure without a secondary phase of MgO, as revealed by XRD spectra. Also, it is important to emphasize that the forsterite ceramic, FC(1200), obtained at the lowest sintering temperature, presents the highest porosity and is selected for *in vitro* biocompatibility evaluation of its scaffolds by using FDA assay in HFL culture.

Mechanical properties of forsterite ceramic, FC(1400)

A novelty in the methodological investigation is represented by nanoindentation, used directly for the first time on forsterite ceramic, FC(1400). The AFM images on FC(1400) fired at 1400 ºC are presented in Figure 2. The surface topographies revealed a sintered ceramic having square shaped crystal aggregates stacked together into a compact microstructure, Figures 2a and 2b. The square sides of the aggregates vary from 2 to 4 μm and their thickness is around 500 nm.

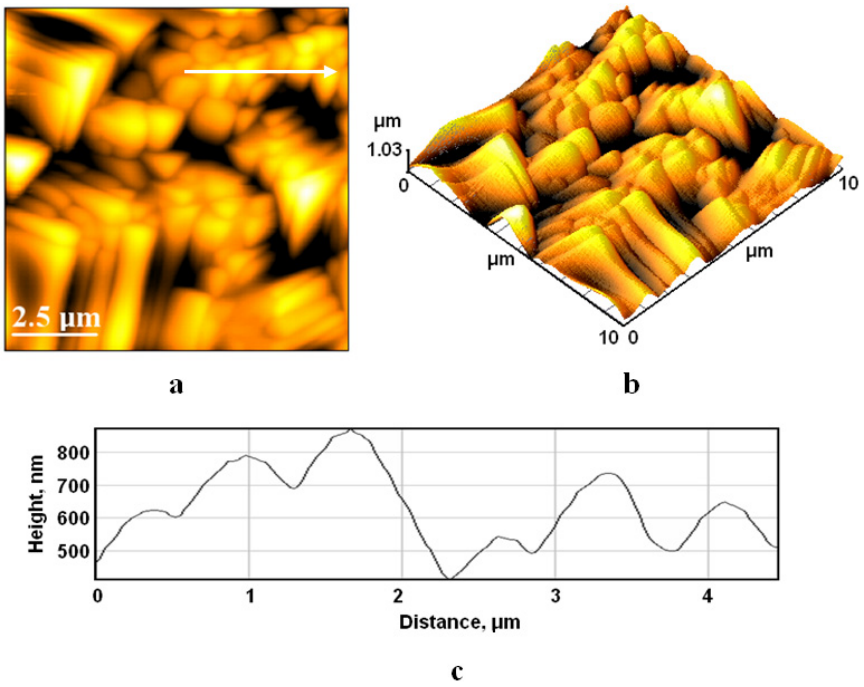

Figure 2. AFM images of forsterite ceramic fired at 1400 ºC, scanning area 10 μm x 10 μm; a) 2D-topography image; b) 3D-topography image; c) cross section on the arrow in panel (a).

Several superficial pores occur due to the close packing of the crystals, visualized in Figure 2b. They have polyhedral shape with a length situated between 2 - 3 μm and a width of about 1 μm. The depth of pores depends on their position related to the top of the surface and could achieve about 1.03 μm. The profile, in Figure 2c, shows the size of crystals with a thickness situated at around 500 nm.

The hardness, 3.07 ± 0.11 GPa and Young elastic modulus, 43.84 ± 3.29 GPa, for forsterite ceramics fired at 1400 ºC temperature were measured

by means of nanoindentation on the scanned area indicated in Figure 2. The Young elastic modulus is higher than the corresponding values found by others for cortical bone [30]. Therefore, it is reasonable to consider FC(1400) as a good candidate for orthopedic and dental implants.

Cell staining with FDA

Cell viability in presence of forsterite ceramics fired at 1200 ºC was estimated by FDA assay at 1, 3 and 7 days in cell culture. The results are a measure of cell proliferation rate.

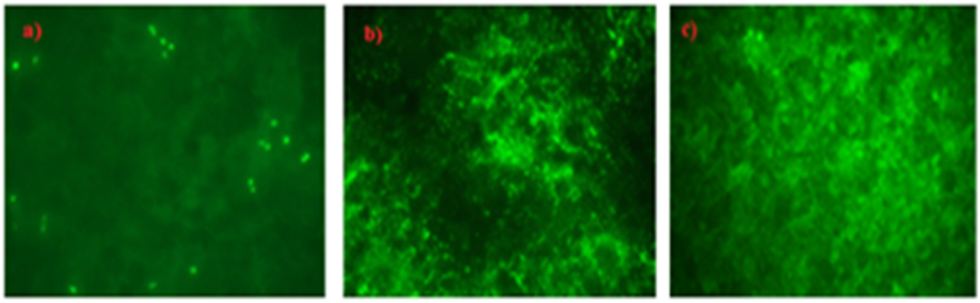

a b c

Figure 3. Optical microscopy images of FDA stained (in green) HFL after different incubation time, a) 1 day (1d), b) 3d, and c) 7d, on the surface of forsterite ceramic scaffolds, fired at 1200 ºC.

Following staining with FDA, living cells appear in fluorescent green (Figure 3). By increasing the time of maintaining the forsterite ceramic, FC(1200), scaffolds in the culture medium, from 1 to 3 and 7 days, the number of living cells also increased.

The cell proliferation on forsterite ceramic scaffolds confirms that forsterite ceramic promotes the proliferation of human fibroblast cells without a significant cytotoxic effect. So, the forsterite ceramic, FC(1200), scaffolds are thought beneficial for adhesion, growth and proliferation of cells with great impact on biomedical applications

AFM on forsterite ceramic scaffolds

The AFM images obtained on the forsterite ceramic fired at 1200 °C are presented in Figure 4. The surface topography is irregular (Figure 4a) due to the presence of pores. The surface of forsterite ceramic, FC(1200), is rather compact, particles being well sintered to one another. This fact is also observed in the phase image where the particles appear in the same shade of brown (Figure 4b). The pores between particles are better evidenced

in the 3D representation in Figure 4c. The local surface roughness, expressed as RMS [24, 25], of the FC surface is situated at 63 ± 10 nm, depending on pore size, on a scanned area of 1μm x 1μm.

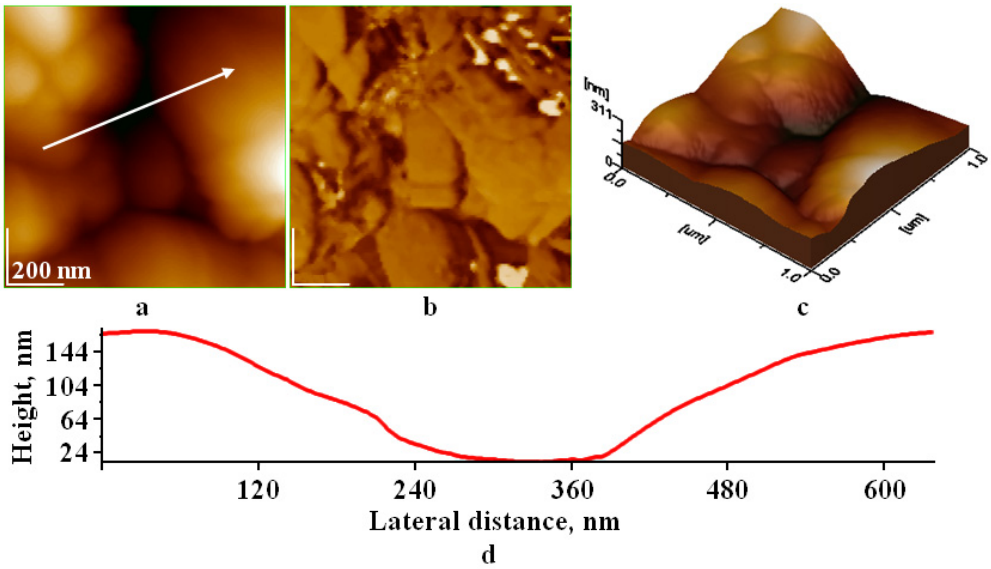

Figure 4. The AFM image of forsterite ceramic, FC(1200), a) 2D-topography; b) phase image; c) 3D-topography; d) cross section along the arrow given in panel a)

The size of surface pore is investigated by the surface profile illustrated in Figure 4d. The average depth of the identified pore is around 164 nm. The pore shape is rounded. Therefore, the equivalent diameter of this pore is about 400 nm.

Definitely, the porous surface of scaffolds can promote cell attachment and movement and thus, can support the excellent biocompatibility of forsterite ceramics, FC(1200), as evidenced by FDA staining of fibroblasts (Figure 3).

CONCLUSIONS

New porous forsterite ceramics were obtained by sintering at 1200, 1300, 1400 and 1450 ºC from nano forsterite powder synthesized by an original sol-gel method, using magnesium nitrate and TEOS as raw materials. The apparent porosity of the four forsterite ceramics, decreased gradually with the increase in sintering temperature from about 39 % at 1200 °C to 25 % at 1450 °C. The FC(1400) revealed a rather high hardness of about 3 GPa, which recommend this material for biomedical applications as porous implants.

However, mechanical properties need to be better investigated to determine the specificity of these ceramics for clinical applications. Additionally, fosterite ceramics FC(1200), revealed excellent biocompatibility in HFL culture, as judged by cells staining FDA assay.

Taking into account that nano forsterite structure possesses antimicrobial activity, the new porous forsterite ceramics developed in this work are suitable for antimicrobial applications, serving as carrier for antibiotics. These findings recommend the new porous forsterite ceramics as a good choice for bone repair simultaneously protecting the bone against microbial infections, which are produced especially by staphylococcus aureus.

EXPERIMENTAL SECTION

Preparation of forsterite ceramics

Nano forsterite powder was synthesized using 99.5% pure magnesium nitrate hexahydrate ($Mg(NO_3)_2 \cdot 6H_2O$, Merck) and tetraethyl orthosilicate ($C_8H_{20}O_4Si$ - TEOS, Merck) as precursors, following a Mg:Si molar ratio of 2:1. Magnesium nitrate was dissolved in 200 mL ultrapure water. TEOS was then added. A quantity of sucrose 4 times the previously added amount of TEOS was dissolved in 400 mL ultrapure water. The dissolved sucrose was added drop by drop into the precursor mixture. The final solution was then homogenized on a magnetic stirrer for 2 hours. Polyvinyl alcohol (PVA) at a ratio of 0.8:1 to the previously used sucrose was added to the homogenized solution. The pH of the solution was brought to 1 using nitric acid (65%, Merck) followed by a second homogenization period of 2 hours at room temperature and a third one for another 2 hours at 80^0C. The final mixture was aged for 24 hours at room temperature to allow for gel formation. The formed gel was dried at 100^0C in an air atmosphere until complete dehydration, resulting in a black, thick gel that was finally thermally treated at 900^0C for 2 h with a heating rate of 5^0C/min.

To obtain forsterite ceramics, the nano forsterite powder was mixed with a aqueous solution of 6% poly vinyl alcohol (PVA, from Sigma-Aldrich), leading to a granulated mixture, which was pressed into compact pellets, with a diameter of about 6 mm and a thickness of around 2 mm at a specific pressure of 500 kgf/cm^2 (49 MPa).

Then, the forsterite samples were fired in air at temperatures of 1200, 1300, 1400 and 1450 °C in a laboratory kiln at a heating rate of 2°C/min, for 3 h plateau, at each sintering temperature. Every experiment was repeated for four times and the data are given as average values ± SD (standard deviations). For biocompatibility study in cell culture, the same FC pellets were used as FC scaffolds.

Characterization of forsterite ceramics

Phase composition. *X-Ray Diffraction (XRD).* The phase composition of forsterite ceramics was determined using a Bruker D8 Advance diffractometer, with Co, $K\alpha_1$ = 1.79026 Å, operated at 35 kV and 40 mA. The pattern was collected for 2ϑ range from 5° and 65°, with a step size of 0.02 °/ sec (*unpublished results*). Phase composition of forsterite ceramics fired from 1200 to 1450 °C was determined and a unique forsterite phase was detected at all sintering temperatures,

Morphology of FC thin layer. Atomic force microscopy (AFM) imaging was performed in tapping mode, on a Jeol JSPM 4210 scanning probe microscope using a specific cantilever NSC 15 hard produced by Micromasch Co., having a spring constant of 40 N/m and a resonant frequency of 325 kHz. Different macroscopic areas were investigated at different scanning areas ranging from 5 μm x 5 μm to 1 μm x 1 μm. The AFM images were obtained on layers of ceramics prepared similarly as already reported for biomaterials [21-23] and surface roughness was determined by root mean square, RMS, [24, 25].

Compactness characteristics. The compactness characteristics, like apparent density, apparent porosity and shrinkage, were determined by a hydrostatic method, weighing the FC samples in both air and water according to Archimedes' principle [4].

Mechanical properties of forsterite ceramics. Mechanical properties, as Young elastic modulus and hardness, of forsterite ceramic, FC-1400 fired at 1400°C, were performed by means of a Triboindenter Hysitron TI900 nano-indenter coupled with an atomic force microscope.

Biocompatibility of FC-1200 scaffolds. Biocompatibility of forsterite ceramic scaffolds was determined by cells viability assay [26-29]. Forsterite ceramic, FC(1200), scaffolds (pellets) were subjected to *in vitro* biocompatibility investigation using fluorescein diacetate, FDA, assay [28] to detect cell adhesion and proliferation in human fibroblast from lung, HFL culture. HFL cells were cultured in standard DMEM medium supplemented with nutrient mixture F-12 HAM medium with 10% fetal calf serum (FCS) and proper amount of penicillin and streptomycin.

The FDA is an indicator of cell viability, and is the substrate for the intracellular nonspecific esterase. The FDA diffuses freely into cells and is rapidly hydrolysed to fluorescein once it enters within a viable cell. The intensity of fluorescence is dependent on membrane integrity and enzymatic activity of the cells, so the fluorescent signals are proportional with the number of viable cells.

Briefly, the $2x10^5$ HFL cells were seeded in each well of the 24-well plates, namely in complete DMEM medium/well on the surface of each FC(1200) scaffold. After 1d, 3d and 7d, the cell viability (adhesion and proliferation of cells) was analysed using FDA assay. Cells were incubated 5 min in dark at 37°C with 1mL / well of FDA solution (at a final concentration of 2.4 mM in phosphate buffer saline, PBS) supplemented with Ca^{2+} and Mg^{2+}. After incubation the wells were washed twice with PBS, and viable fluorescent cells adhered on scaffolds were visualized with the Zeiss Axio Observer D1 inverted fluorescence microscope with 200x magnification lens, using a 488 nm excitation filter. Images were captured with a CCD camera (Axiocam MRM) and analyzed using Axiovision Release 4.6.3 software.

Cell adhesion and proliferation were evaluated after cell seeding at 1d, 3d and 7 days, by FDA assay. The results from fluorescein diacetate staining were also validated by MTT assay. At 14 days in cell culture, the cells viability was high but not significant higher than the cells activity at 7 days in cells culture, indicating that an optimal viability is reached already at 7 days.

Statistical analysis. GraphPad Prism 5 was used for statistical analysis. All data are given as the mean value ± standard deviation (SD) of at least four independent experiments. Significant differences were identified using the one-way ANOVA and Bonferroni's multiple comparison test. Differences among samples were considered statistically significant if $p<0.05$, or otherwise stated.

ACKNOWLEDGEMENTS

One of the authors, Alexandra Avram would like to thank the Executive Agency for Higher Education, Research, Development and Innovation Funding (UEFISCDI) for financial support through grant no. 83. All authors would like to thank D. Frankel for assistance with nanoindentation used to determine mechanical properties of forsterite ceramics.

REFERENCES

1. F. Tavangarian; R. Emadi; *Mater.Lett.,* **2011,** *65(4)*, 740–743.
2. S. Oh; N. Oh; M. Appleford; J. L. Ong; *Am. J. Biochem. Biotechnol.,* **2006**, *2(2),* 49–56.
3. S. Ni; L. Chou; J. Chang; *Ceram. Int.*, **2007**, *33(1),* 83–88.
4. K. Y. S. Lee; K. M. C. Chin; S. Ramesh; J. Purbolaksono; M. A., Hassan; M. Hamdi; W. D. Teng; *J. Ceram. Process. Res.*, **2013**, *14(1),* 131-133.
5. M. Kharaziha; M. H. Fathi; *J. Mech. Behav. Biomed. Mater.,* **2010**, *3(7),* 530–537.
6. M. Saqaei; M. Fathi; H. Edris; V. Mortazavi; N. Hosseini; *Adv. Powder Technol.*, **2016**, *27(5),* 1922-1932.
7. A. Krajewski; A. Ravaglioli; E. Roncari; P. Pinasco; L. Montanari; *J. Mater. Sci.: Mater. Med.*, **2000**, *11(12),* 763–771.
8. M. Saqaei; M. Fathi; H. Edris; V. Mortazavi; *Mat. Sci. Eng. C*, **2015**, *56*, 409-416.

9. G. Furtos; M. A. Naghiu; H. Declercq; M. Gorea; C. Prejmerean; O. Pana; M. Tomoaia-Cotisel; *J. Biomed. Mater. Res. Part B*, Appl. Biomat., **2016**, *104(7),* 1290-1301.
10. S. Naghieh; E. Foroozmehr; M. Badrossamay; M. Kharaziha; *Mater. Des.*, **2017**, *133*, 128-135.
11. R. Choudhary; P. Manohar; J. Vecstaudza; M .J. Yáñez-Gascón; H. Pérez Sánchez; R. Nachimuthu; J. Locs; S. Swamiappan; *Mater. Sci. Eng. C*, **2017**, *77*, 811-822.
12. M. Zabihi; M. R. Ayatollahi; H.R.Rezaie; *Theor. Appl. Fract. Mech*., **2018**, *94*, 173-180.
13. H. Ghomi; M. Jaberzadeh; M. H. Fathi; *J. Alloys Compd., **2011**, 509(5*), L63-L68.
14. S. M. Mirhadi; A. Forghani; F. Tavangarian; *Ceram. Int.,* **2016**, *42(7),* 7974-7979.
15. M. A. Naghiu; M. Gorea; E. Mutch; F. Kristaly; M. Tomoaia-Cotisel, *J. Mater. Sci. Techol.,* **2013**, *29(7),* 628-632.
16. M. A. Naghiu; M. Gorea; F. Kristaly; M. Tomoaia-Cotisel; *Ceram-Silikaty*, **2014**, *58(4),* 303-307.
17. M. Gorea; M. A. Naghiu; M. Tomoaia-Cotisel; G. Borodi; *Ceram-Silikaty*, **2013**, *57(2),* 87-91.
18. Y. Xie; W. Zhai; L. Chen; J. Chang; X. Zheng; C. Ding; *Acta Biomater*., **2009**, *5(6),* 2331-2337.
19. R. Choudhary; A. Chatterjee; S. K. Venkatraman; S. Koppala; J. Abraham; S. Swamiappan; *Bioact. Mater.*, **2018**, *3(3)*, 218-224.
20. A. Danistean; M. Gorea; A. Avram; S. Rapuntean; Gh. Tomoaia; A. Mocanu; C. Garbo; O. Horovitz; M. Tomoaia-Cotisel; *Studia Chem*., **2016**, *61(3),* 275-283.
21. F. Goga; E. Forizs; A. Avram; A. Rotaru; A. Lucian; I. Petean; A. Mocanu; M. Tomoaia-Cotisel; *Rev. Chim. (Bucharest),* **2017**, *68(6),* 1193-1200.
22. F. Goga; E. Forizs; G. Borodi; Gh. Tomoaia; A. Avram; R. Balint; A. Mocanu; O. Horovitz; M. Tomoaia-Cotisel; *Rev. Chim. (Bucharest),* **2017**, *68(12),* 2907-2913.
23. Gh. Tomoaia; M. Tomoaia-Cotisel; L. B. Pop; A. Pop; O. Horovitz; A. Mocanu; N. Jumate; L. D. Bobos; *Rev. Roum. Chim.,* **2011***, 56(10-11),* 1039-1046.
24. P. T. Frangopol; D. A. Cadenhead; Gh. Tomoaia; A. Mocanu; M. Tomoaia-Cotisel; *Rev. Roum.Chim.,* **2015***, 60(2-3),* 265-273.
25. U. V. Zdrenghea; Gh. Tomoaia; D.-V. Pop-Toader; A. Mocanu; O. Horovitz; M. Tomoaia-Cotisel; *Comb. Chem. High Throughput Screen*., **2011**, *14(4),* 237-247.
26. Gh. Tomoaia; O. Soritau; M. Tomoaia-Cotisel; L. B. Pop; A. Pop; A. Mocanu; O. Horovitz; L. D. Bobos; *Powder Technol.,* **2013**, 238, 99-107.
27. Gh. Tomoaia; A. Mocanu; I. Vida-Simiti; N. Jumate; L. D. Bobos; O. Soritau; M. Tomoaia-Cotisel; *Mat.Sci. Eng. C*, **2014**, *37*, 37–47.
28. S. Rapuntean; P. T. Frangopol; I. Hodisan; Gh. Tomoaia; D. Oltean-Dan; A. Mocanu; C. Prejmerean; O. Soritau; L. Z. Racz; M. Tomoaia-Cotisel; *Rev. Chim. (Bucharest),* **2018**, *69(12),* 3537-3544.
29. D. Dufrane; C. Delloye; I. J. Mckay; P. N. De Aza; S. De Aza; Y. J. Schneider; M. Anseau; *J. Mater. Sci. Mater. Med*., **2003**, *14(1),* 33–38.
30. J. Y. Rho; R. B. Ashman; C. H. Turner; *J. Biomech*., **1993**, *26(2),*111-119.

STUDIA UBB CHEMIA, LXIV, 2, Tom II, 2019 (p. 393-400)
(RECOMMENDED CITATION)
DOI:10.24193/subbchem.2019.2.33

Dedicated to Professor Ioan Bâldea on the Occasion of His 80th Anniversary

PHARMACOKINETIC PROOFS ON INTERACTION BETWEEN ZOLPIDEM AND PHENYTOIN: A TWO-TREATMENT, TWO-PERIOD STUDY IN HEALTHY MALE SUBJECTS

DANA MARIA MUNTEAN[a], MARIA ADRIANA NEAG[b], DANIELA PETRUTA PRIMEJDIE[c*], ADINA POPA[c], MARCELA ACHIM[a], LAURIAN VLASE[a]

ABSTRACT. In clinical practice, the simultaneous use of zolpidem and phenytoin cannot always be avoided, although it can be associated with additive depressants effects on the central nervous system. Considering the common metabolic pathways involving CYP3A and CYP2C, a pharmacokinetic interaction between phenytoin and zolpidem is possible, although not previously quantified. The study was designed as a non-randomized, two-period preclinical trial. Twenty male subjects were included in a study consisting of two periods. Between these, subjects were treated for 6 days with a single daily dose of 150 mg phenytoin. For each treatment period, pharmacokinetic parameters of zolpidem were determined. The multiple-dose administration of phenytoin influenced zolpidem's pharmacokinetics in healthy volunteers, decreasing its exposure through enzymatic induction.

Keywords: *zolpidem; phenytoin; drug interaction; enzymatic induction*

INTRODUCTION

Insomnia is a prevalent and undertreated sleep disorder, having diverse and interrelated consequences, with Z-drugs among the preferred therapeutic options [1]. Zolpidem (Fig. 1) is indicated for the short-term treatment

[a] *"Iuliu Haţieganu" University of Medicine and Pharmacy, Faculty of Pharmacy, Department of Pharmaceutical Technology and Biopharmaceutics, 41 Victor Babes Street, RO-400012, Cluj-Napoca, Romania*
[b] *"Iuliu Haţieganu" University of Medicine and Pharmacy, Faculty of Medicine, Department of Pharmacology, Toxicology and Clinical Pharmacology, 41 Victor Babes Street, RO-400012, Cluj-Napoca, Romania*
[c] *Iuliu Haţieganu" University of Medicine and Pharmacy, Faculty of Pharmacy, Department of Clinical Pharmacy, 12 Ion Creanga Street, RO-400010, Cluj-Napoca, Romania*
** Corresponding author: danaprimejdie@umfcluj.ro*

of insomnia, characterized by difficulties with sleep initiation or by difficulty returning to sleep after middle-of-the-night awakening [2]. Available clinical experience confirmed its positive effect on subjective and objective measures of sleep, in both acute and chronic insomnia as well as the absence of rebound insomnia in situations of intermittent administration [3,4]. It is also under investigation for several other indications as the management of restless legs syndrome, various disorders of consciousness or persistent pain [5,6,7].

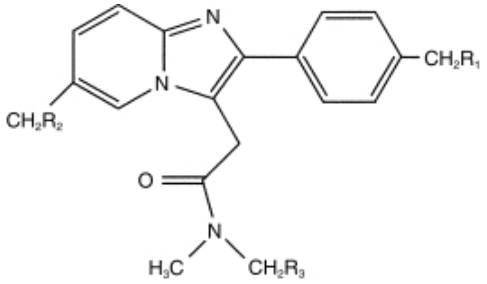

Figure 1. Chemical structure of zolpidem

Zolpidem activates the α1-containing GABAA (BZ1) receptor, with a reduced influence on the α2, α3 or α5 subunits [8]. Its selectivity explains the reduced myorelaxant or anticonvulsant effects and the preservation of deep sleep (stages 3 and 4) at hypnotic doses [9]. Zolpidem has an approximately 70% bioavailability. The elimination half-life is about 2.5 - 2.6 hours [2]. CYP3A4 is mainly involved in its metabolism (61% of the net intrinsic clearance), with a more reduced contribution of CYP1A2, 2C9, 2D6, and 2C19, respectively [10].

Given their multiple and complex mechanisms of action, antiepileptic drugs are used for the treatment and prevention of seizures, and for the management of various nonepileptic neurologic or psychiatric disorders [11]. Phenytoin is labeled for the treatment and prophylaxis of seizures during and following neurosurgery or secondary to traumatic brain injuries, as a treatment of generalized tonic-clonic and complex partial seizures and for the management of trigeminal neuralgia [12]. It can also be recommended for the management of the peripheral nervous system disorders secondary to brain tumors or HIV / AIDS infection [13,14,15].

Phenytoin slows the rate of reactivation of voltage-dependent sodium channels after depolarization. The anticonvulsant activity does not cause general depression of the central nervous system and the therapeutic drug levels in the cerebrospinal fluid correlate with the free plasmatic concentration (the anticonvulsant activity is usually obtained at levels of 10-20 μg/mL) [16]. It presents an oral bioavailability of 20% - 90% and it is highly protein-bound (88 - 93%). It is metabolized by a saturable and genetically polymorphic, hepatic process *via* the CYP2C9 and CYP2C19 isoenzymes [17]. One population

pharmacokinetic analysis conducted in various patients groups, suggested a linear two-compartment model for phenytoin [18]. The average half-life of phenytoin is about 24 hours for most patients in the low to mid therapeutic range, showing large age-dependent interindividual variations (12-60 hours) [19]. Pharmacokinetic drug interactions could be related to impaired absorption, to plasmatic protein displacement or to altered metabolism, as phenytoin is a CYP2C9 and CYP2C19 substrate and a strong inducer for CYP3A4, CYP2C9, CYP2C19 and CYP2B6 [20,21], respectively. Therefore, the therapeutic drug monitoring of phenytoin remains a challenging aspect of its therapeutic use, considering its non-linear pharmacokinetics, zero-order elimination and multilevel drug-drug interactions [22].

In clinical practice, the simultaneous use of multiple drugs acting on the central nervous system is frequent, although it is associated with potential additive depressant effects [9]. Moreover, considering the common metabolic pathways involving CYP3A and CYP2C, a pharmacokinetic interaction between phenytoin and zolpidem is possible, although not previously quantified. Therefore, the aim of this study was to evaluate the magnitude of such a pharmacokinetic interaction in healthy volunteers.

RESULTS AND DISCUSSION

The mean plasma concentrations for zolpidem when administered alone, or in combination with phenytoin after 6 days of treatment with phenytoin are shown in Figure 2.

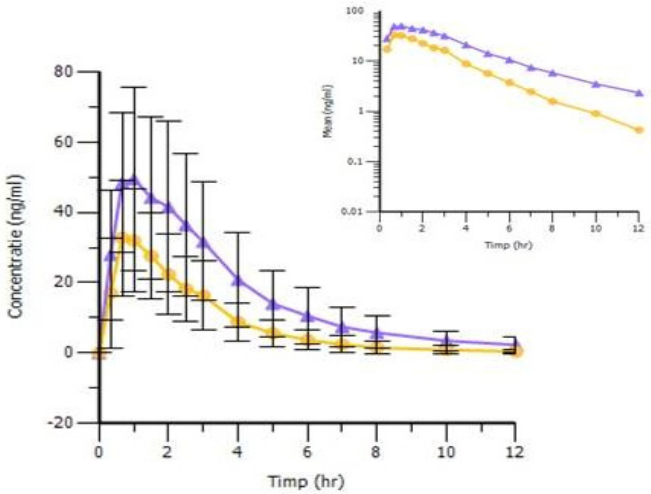

Figure 2. Mean ± SD plasma concentration–time curves of zolpidem (single dose 5 mg p.o.) administered alone (▲) or in combination with phenytoin (150 mg, p.o.), after pre-treatment with phenytoin during 6 days (●), n=20. In the insert a logarithmic scale is employed.

The mean values of pharmacokinetic parameters [16] of zolpidem administered alone, or in combination with phenytoin, as well as statistical ANOVA test results are given in Table 1.

Table1. Pharmacokinetic parameters of zolpidem administered alone or after treatment with phenytoin and the result of statistical ANOVA test (in form of *p* values) used for comparison

Parameter (±SD)	**Zolpidem** (Reference)	**Zolpidem + Phenytoin** (Test)	***p** value**
C_{max} (ng/mL)	56.6±25.4	36.0±14.6	0.0005, S
t_{max} (hr)	0.8±0.3	0.8±0.4	0.816, NS
$AUC_{0-\infty}$ (ng.hr/mL)	211.5±119.6	103.5±54.0	0.0009, S
k_{el} (1/hr)	0.3±0.1	0.4±0.1	0.0411, S
$t_{½}$ (hr)	2.5±0.9	1.7±0.5	0.0411, S
Cl (mL/hr)	34290.4±27007.8	61587.0±32764.4	0.0009, S

* Statistically significant (symbolized S) when $p<0.05$; NS stands for non-significant

The present study showed that phenytoin had an important influence on the pharmacokinetics of zolpidem. A systemic metabolic drug-drug interaction was observed since the half-life of zolpidem was significantly decreased. This may due to the phenytoin's enzymatic induction of hepatic CYP3A4, CYP2C9 and CYP2C19. However, zolpidem's exposure (C_{max} and $AUC_{0-\infty}$) was also significantly reduced by the pre-treatment/co-administration of phenytoin; this indicated a pre-systemic metabolic drug-drug interaction. The metabolism of zolpidem occurs predominantly through CYP3A4, CYP2C9 and CYP1A2 isoenzymes [10]; the CYP3A4 isoenzymes are the predominant ones at both the intestinal and hepatic levels, whereas the others are mainly present in the liver [23]. Phenytoin induces CYP3A4 at both the intestinal and hepatic level and consequently, the first-pass metabolism of zolpidem was increased [24]. As an effect of a pre-systemic pharmacokinetic drug-drug interaction, the exposure of zolpidem was significantly lowered.

This study offers a first perspective on the magnitude of the pharmacokinetic interaction between zolpidem and phenytoin administered to human subjects. Results may contribute to the establishment of effective dosing intervals or treatment regimens [25]. For example, insomnia is common in epilepsy and it was associated with short term poor seizure control and worse quality of life [26]. Sleep disorders are frequently associated with various neurologic conditions, including persistent neuropathic pain, for which phenytoin has an on-label indication. Therefore, such clinical settings might require the co-prescription of phenytoin and zolpidem, in spite of their additive central nervous system depressant effect [27]. If such association is implemented, then the pharmacokinetic interaction should be taken into consideration in situations when a long-term phenytoin treatment is to be stopped. This scenario favors an

increased risk for zolpidem overdose and side-effects, including daytime residual effects on cognitive and psychomotor performance [28]. On the other hand, the initiation of phenytoin in a patient exposed to a chronic therapy with zolpidem could trigger signs and symptoms of zolpidem withdrawal that can complicate the patient's clinical state [29].

We identified a single previous investigation analyzing the simultaneous use of zolpidem and phenytoin, which focused on a pharmacodynamic aspect of their interaction, suggesting an increased antiepileptic effect. It was demonstrated on Wistar rats; it was supposed to be mediated through hyper-polarization, secondary to membrane stabilizing activity through sodium channel blockade by phenytoin and to reinforced GABA mimetic action of zolpidem [30].

Therefore, these results bring new information referring to the pharmacokinetic interactions previously confirmed for both zolpidem and phenytoin [31-34].

CONCLUSIONS

Administration of multiple-dose phenytoin influenced zolpidem pharmacokinetics in healthy volunteers, decreasing its exposure due to enzymatic induction.

EXPERIMENTAL SECTION

Subjects

Twenty healthy adult male subjects aged 22 to 30 years were eligible for the study. The health status of each volunteer was assessed using the individual medical history, the results of physical examinations, vital signs, electrocardiogram evaluation, and laboratory test results. Exclusion criteria included: use of any non-prescription drug products within 14 days before initiation of the study; use of prescription drugs during the 30-day period before the start of the study; use of other investigational drugs within 60 days before initiation of the study; donations or transfusions of blood or blood products during the 60-day period before the start of the study; smoking of more than 10 cigarettes per day; history of drug abuse; sitting systolic blood pressure ≥ 140 mm Hg or ≤ 90 mm Hg; or sitting diastolic blood pressure ≥ 90 mm Hg or ≤ 50 mm Hg.

The study was conducted according to the principles of Declaration of Helsinki (1964) and its amendments (Tokyo 1975, Venice 1983, Hong Kong 1989) and Good Clinical Practice (GCP) rules. The clinical protocol was reviewed and approved by the Ethics Committee of the University of Medicine and Pharmacy "Iuliu Hatieganu", Cluj-Napoca, Romania.

Study design and blood sampling

The study design was one sequence cross-over and consisted in 2 periods: Period 1 (Reference), when each volunteer received a single dose of 5 mg zolpidem and Period 2 (Test), when each volunteer received a single dose of 5 mg zolpidem and 150 mg phenytoin. Between the two periods, the subjects were treated for 6 days with a single daily dose of 150 mg phenytoin. All drugs were administered in the morning, in fasted state. The pharmaceutical products used were Sanval® (5 mg coated tablets, LEK Pharmaceuticals D.D. - Slovenia) and Fenitoin® (phenytoin 100 mg scored tablets, Gedeon Richter Romania, Târgu-Mures, Romania). Serial blood samples (5 mL each) were collected from an indwelling IV catheter immediately before drug administration and at 0.5, 1, 1,5, 2, 2,5, 3, 4, 5, 6, 7, 8, 10 and 12 hours, respectively, after drug administration and for each treatment period. Blood samples were collected in heparinized tubes. Samples were centrifuged at 1800 g for 5 min and harvested plasma samples were stored at -20 ºC until analysis.

Analysis of plasma samples

Zolpidem plasma concentrations were determined by a validated high throughput liquid chromatography-mass spectrometry method, by using citalopram as an internal standard. The HPLC system was an Agilent 1100 series (Agilent Technologies, USA) and was coupled with a Brucker Ion Trap SL (Brucker Daltonics GmbH, Germany). A Zorbax SB-C18 chromatographic column (100 mm x 3.0 mm i.d., 3.5 µm) (Agilent Technologies) was used. The mobile phase consisted of 62:38 (V/V) 1 mM ammonium acetate in water:methanol. The flow rate was 1 mL/min and the thermostat temperature set at 45 ˚C. The mass spectrometry detection was in multiple reaction monitoring mode (MRM), positive ions, using an electrospray ionization source. The ion transitions monitored were m/z 308→(m/z 235+ m/z 263) for zolpidem and m/z 325→m/z 262 for the internal standard.

0.6 mL of methanol (containing internal standard, 10 ng/mL) were added to 0.2 mL of plasma in an Eppendorf tube. The tube was vortex-mixed for 20 seconds, and then centrifuged for 3 min at 12000 rpm. The supernatant was transferred to an autosampler vial and 1 µL was injected into the LC/MS system. The calibration curve of zolpidem was linear at a concentration range of 2 - 208 ng/mL plasma, with a correlation coefficient of 0.996. At quantification limit (2 ng/mL), accuracy and precision were: 3.9% and 7.4% (intra-day) and 9.2% and 10.5% (inter-day), respectively.

Pharmacokinetic analysis

Non-compartmental pharmacokinetic analysis was employed to estimate the pharmacokinetic parameters of zolpidem when administered alone or in combination with phenytoin. The maximum plasma concentration

(C_{max}, ng/mL) and the time to reach the peak concentration (t_{max}, hr) were obtained directly by visual inspection of each subject's plasma concentration-time profile. The area under the concentration-time curve (AUC_{0-t}) was estimated by integration. The area was extrapolated to infinity ($AUC_{0-\infty}$) by addition of C_t/k_{el} to AUC_{0-t} (*t* in the index indicates the time resolved value). The elimination rate constant k_{el} was estimated by the least-square regression of plasma concentration-time data points lying in the terminal region, by using a semi-logarithmic dependence that corresponds to first-order kinetics. The half-life ($t_{½}$) was calculated as the ratio $0.693/k_{el}$. The pharmacokinetic analysis was performed using Kinetica 4.2 (Thermo Labsystems, U.S.A.).

Statistical analysis

Analysis of variance (ANOVA testing) was used to compare the calculated pharmacokinetic parameters of zolpidem for the two periods, using general linear model procedures, in which sources of variation were subject and period. In order to identify possibly clinically significant differences in pharmacokinetic parameters, 90% confidence intervals of the test/reference period ratios for C_{max}, AUC_{0-t} and $AUC_{0-\infty}$ (*log* transformed) were determined by the Schuirmann's two one-sided *t*-test. The equivalence between zolpidem administered alone or in combination with phenytoin was inferred if the 90% confidence intervals for these pharmacokinetic parameters were within the range 0.8-1.25. For t_{max}, the equivalence range was expressed as untransformed data, and significance tested using the nonparametric Friedman test. All statistical analysis were performed using the Kinetica 4.2 software.

ACKNOWLEDGMENTS

This work was supported by a PNII-IDEI project, code 462, contract 229/2007 financed by CNCS Romania, for which the authors gratefully acknowledge.

REFERENCES

1. J. MacFarlane, C. M. Morin, J. Montplaisir, *Clin Ther.*, **2014**, *36(11)*, 1676.
2. Truven Health Analytics. Micromedex® 2.0. Zolpidem. DRUGDEX® Evaluations. Available at: http://www.micromedexsolutions.com/home/dispatch. Accessed February 2017.
3. E.L. Sutton, *Med. Clin. N. Am.*, **2014**, *98*, 565.
4. A. Qaseem, D. Kansagara, M.A. Forciea, *et al., Ann. Intern. Med.,* **2016**, *165(2).*
5. J.A. Generali, D.J. Cada, *Hosp. Pharm.,* **2011**, *46(2)*, 101.
6. R. Ciurleo, P. Bramanti, R.S. Calabrò, *Drugs,* **2013**, *73(17)*, 1849.
7. M. Puthiyathu, H. Greenspan, W. Levitt, *et al.*, *Psychiatric Annals*, **2013**, *43(3)*, 96.
8. A.C. Fitzgerald, B.T. Wright, S.A. Heldt, *Psychopharmacology,* **2014**, *231*, 1865.

9. Ambien®- zolpidem tartrate tablet, film coated. Sanofi-Aventis U.S. LLC. Drug label information. US National Library of Medicine. DailyMed - official provider of FDA label information. Available at: http://dailymed.nlm.nih.gov/dailymed/drugInfo.cfm?setid=c36cadf4-65a4-4466-b409-c82020b42452. Accessed November 2015.
10. L.L. von Moltke, D.J. Greenblatt, B.W. Granda, *et al*., *Br. J. Clin. Pharmacol.,* **1999**, *48(1)*, 89.
11. M. Bialer, *Epilepsia,* **2012**, *53(7)*, 26.
12. Agence nationale de sécurité du médicament et des produits de santé. Résumé des caractéristiques du produit Di-Hydan® 100 mg, comprimé sécable. Available at: http://base-donnees-publique.medicaments.gouv.fr/affichageDoc.php?specid=66303560&typedoc=R. Accessed February 2017.
13. H. Torbic, A.A. Forni, K.E. Anger, *et al.*, *Am. J. Health. Syst. Pharm*., **2013**, *70(9)*, 759.
14. R. Bauer, M. Ortler, M. Seiz-Rosenhagen, *et al*., *Neurosurg. Rev.,* **2014**, *37(3)*, 381.
15. G.L. Birbeck, J.A. French, E Perucca, *et al.*, *Epilepsia*, 2012, 53(1), 207.
16. J.O. McNamara, Pharmacotherapy of the Epilepsies. In L. Brunton, J. Lazo, K. Parker, Eds. Goodman & Gilman's *The pharmacological basis of therapeutics. 11th ed*. New York: The McGraw-Hill Companies, Inc; **2005**. Chapter 19.
17. Truven Health Analytics. Micromedex® 2.0. Phenytoin. DRUGDEX® Evaluations. Available at: http://www.micromedexsolutions.com/home/dispatch. Accessed February 2017.
18. J. Tanaka, H. Kasai, K. Shimizu, *et al*., *Eur. J. Clin. Pharmacol*., **2013**, *69(3)*, 489.
19. P.N. Patsalos, D.J. Berry, B.F. Bourgeois, *et al.*, *Epilepsia,* **2008**, *49(7)*, 1239.
20. R.J. Porter, B.S. Meldrum, Antiseizure Drugs. In B.G. Katzung, S.B. Masters, A.J.Trevor *Basic & Clinical Pharmacology*, *12th ed*. New York: The McGraw-Hill Companies, Inc; **2012**. Chapter 24.
21. C. Hiemke, P. Baumann, N. Bergemann, *et al*., *Pharmacopsychiatry,* **2011**, *44(6)*, 195.
22. M.D. Krasowski, L.E. Penrod, *BMC Medical Informatics and Decision Making*, **2012**, *12*, 7.
23. A. Galetin, M. Gertz, J.B.Houston, *Drug. Metab. Pharmacokinet*., **2010**, *25(1),* 28.
24. I. Cascorbi, *Dtsch. Arztebl. Int*., **2012**, *109(33–34)*, 546.
25. T. Roehrs, T. Roth, *Neurotherapeutics,* **2012**, *9*, 728.
26. M. Quigg, S. Gharai, J. Ruland, *et al*., *Epilepsy Res.,* **2016**, *122*, 91.
27. M.D. Cheatle, S. Foster, A. Pinkett, *et al*., *Anesthesiology Clin.* **2016**, *34*, 379.
28. N. Gunja, *J. Med. Toxicol*., **2013**, *9*, 155.
29. M.J. Brodie, S. Mintzer, A.M. Pack, et al., *Epilepsia*, **2013**, *54(1)*, 11.
30. C. Gurudeva, P.A. Patil, S.V. Hiremath, *et al*., *Pharmacologyonline,* **2008**, *3*, 978.
31. K. Villikka, K.T. Kivistö, H. Luurila, *et al.*, *Clin Pharmacol. Ther*., **1997**, *62(6)*, 629.
32. Y. Hojo, M. Echizenya, T. Ohkubo, *et al.*, *J Clin Pharm Ther.,* **2011**, *36(6)*, 711.
33. J.F. Okulicz, G.A. Grandits, J.A. French, *et al*., *Epilepsy Res*., **2013**, *103(2-3)*, 245.
34. W.K. Kennedy, M.W. Jann, E.C. Kutscher, *CNS Drugs*, **2013**, *27(12)*, 1021.

STUDIA UBB CHEMIA, LXIV, 2, Tom II, 2019 (p. 401-410)
(RECOMMENDED CITATION)
DOI:10.24193/subbchem.2019.2.34

Dedicated to Professor Ioan Bâldea on the Occasion of His 80th Anniversary

DEGRADATION KINETICS OF ANTHOCYANINS DURING HEAT TREATMENT OF WILD BLACKTHORN (*Prunus spinosa* L.) FRUITS EXTRACT

BIANCA MOLDOVAN[a], ANAMARIA ARDELEAN[a], LUMINIŢA DAVID[a*]

ABSTRACT. The blackthorn (*Prunus spinosa* L.) fruits are known as a valuable source of anthocyanins and for their high antioxidant capacity. The aim of the present study was to investigate the thermal stability of anthocyanins from blackthorn fruits, at different temperatures (2°C, 20°C and 75°C) and to determine the kinetic and thermodynamic parameters of their degradation reactions. Data analysis indicated a first-order reaction kinetics for the degradation of blackthorn anthocyanins at various temperatures. Kinetic parameters, such as reaction rate constant k, half-life $t_{1/2}$, and activation energy Ea values were determined. The obtained results indicated that blackthorn anthocyanins stored at 2°C exhibited the highest stability, the degradation constant rate being $5.0 \cdot 10^{-4}$ h^{-1}. The activation energy of the thermal degradation was also determined and was found to be 53.96 kJ/mol. The activation enthalpy $\Delta H^{\neq}$, Gibbs free energy $\Delta G^{\neq}$ and activation entropy $\Delta S^{\neq}$ for the degradation process were also determined.

Keywords: *Prunus spinosa* L.*,* anthocyanins, degradation kinetics

INTRODUCTION

At the present, there is a growing trend and interest in the nutrition quality of the consumed food, especially in the developed societies. Consumers do more and more regard food in relation to its health benefits, increasing their attention on food nutraceutical components. Fruits and vegetables are consumed as sources of bioactive compounds with a particularly positive

[a] *Babeş-Bolyai University, Faculty of Chemistry and Chemical Engineering, 11 Arany Janos str., RO-400028, Cluj-Napoca, Romania*
**Corresponding author: muntean@chem.ubbcluj.ro*

health impact. Berries, such as blackberry, blueberry, cranberry, strawberry, raspberry, are largely consumed for their delicious taste but also as rich sources of various disease-fighting compounds such as phenolics, flavonoids, anthocyanins, carotenoids, vitamins and minerals [1-3]. Extracts of most berries possess high antioxidant activity, acting effectively as free radical scavengers [4, 5]. Among phytocompounds which contribute to protection against degenerative diseases and against ageing processes, effects attributed to their antioxidant activity, anthocyanins play a significant role. These compounds are water soluble pigments, belonging to the flavonoids group, produced by plants as secondary metabolites, playing an important role in plant defence against different stress factors, such as UV radiation, pathogens, or plague [6].

Blackthorn (*Prunus spinosa* L.) is a perennial plant belonging to rose family (*Rosaceae*) which grows as a shrub and is native to Europe, western Asia and north-west Africa. Its fruits are bitter and astringent, with a poor commercial value, being less consumed raw but usually processed into jams, marmalades, juice, tea or macerated with sugar and alcohol to obtain a type of liquor [7]. Blackthorn (*Prunus spinosa* L.) has been used in ethno-botanic medicine for treatment of hypertension, of cough, as antispastic, diuretic, antiseptic, laxative or anti-inflammatory agent [8, 9].

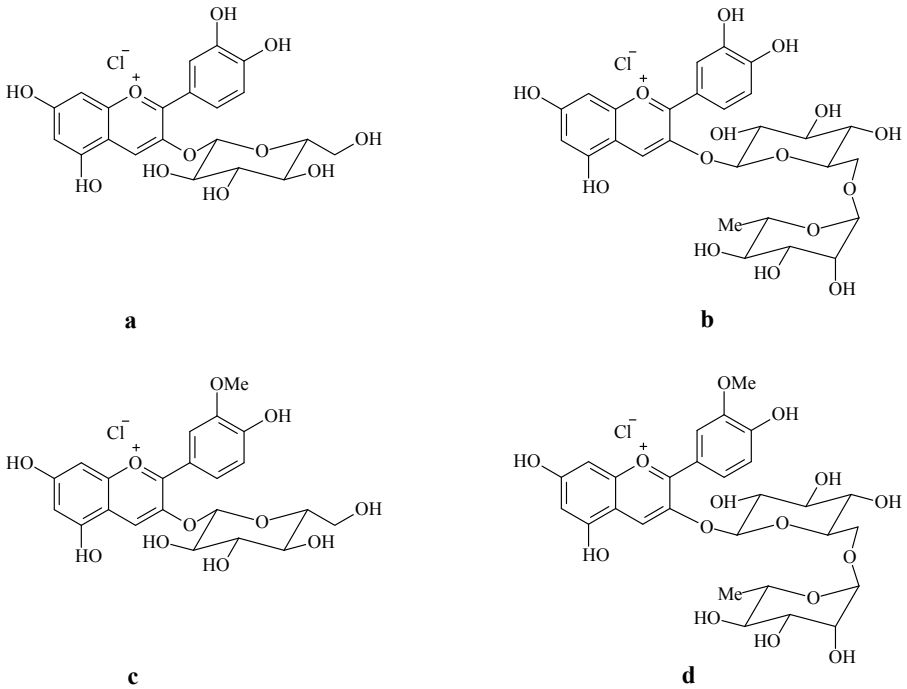

Figure 1. Chemical structures of blackthorn anthocyanins: a) cyanidin-3-glucoside; b) cyanidin-3-rutinoside; c) peonidin-3-glucoside; d) peonidin-3-rutinoside.

Apart from phytotherapy, blackthorn could also be an important source of colour compounds useful in the food industry. The anthocyanins from *Prunus spinosa* L. fruits could be a healthy alternative to the toxic red dyes usually employed to colour food products. Deineka *et al.* [10] identified four anthocyanic compounds in blackthorn fruits, namely cyanidin-3-glucoside, cyanidin-3-rutinoside, peonidin-3-glucoside and peonidin-3-rutinoside (Figure 1).

However, anthocyanins are not very stable compounds as they easily degrade during thermal processing, light exposure and storage, causing colour fainting or colour change of anthocyanin coloured foods. Thus, investigating the stability of these compounds in order to use them as health beneficial natural colorants is a matter of great concern. As a consequence, kinetic studies of anthocyanins degradation in various conditions, such as thermal exposure and storage, are very important for the food industry.

The aim of the present study was to investigate the thermal stability of anthocyanins isolated from blackthorn and to determine the kinetic and thermodynamic parameters of the degradation process of these compounds at various temperatures.

RESULTS AND DISCUSSION

The fruit extract obtained from *Prunus spinosa* L. fruits was investigated in order to determine its TAC (total anthocyanin content). The assessment of this parameter was realised by using a well known and widely applied method: the pH differential method of Giusti and Wrolstad [11]. It is based on the spectrophotometric determination of anthocyanin concentrations in a fruit extract at two different pH values (1 and 4.5, respectively), by taking into account the structural dependence of anthocyanins molecules from the solution pH value. The red coloured flavylium cation is the predominant structural form of anthocyanins at pH=1, while at pH=4.5, the colourless carbinol predominates.

The TAC of the blackthorn fruit extract was calculated using equation (1) and the results were expressed as mg of cyanidine-3-glucoside (Cy-3-Glu) equivalents/ litre of extract:

$$TAC = \frac{A \cdot MW \cdot DF \cdot 1000}{\varepsilon \cdot l} \quad (1)$$

where: A = absorbance, calculated as: (equation 2)
MW = 449.2 g/mol (molecular weight of Cy-3-Glu)
DF = dilution factor

l = path length (1 cm)
ε = 26900 L/mol/cm (molar extinction coefficient of Cy-3-Glu)
1000 = conversion factor from gram to milligram

$$A = (A_{pH1.0} - A_{pH4.5})_{517nm} - A_{pH1.0} - A_{pH4.5})_{700nm} \quad (2)$$

The initial TAC of the blackthorn fruit extract was found to be 44.75 mg Cy-3-Glu equivalents/ litre of extract.

The degradation of blackthorn anthocyanins over time was investigated at several temperatures (2°C, 20°C and 75°C) by isothermal exposure of the fruit extract in darkness at these temperatures.

The anthocyanins' concentration decreased with exposure time at all investigated temperatures, indicating the degradation of these compounds. The loss of anthocyanins was more drastic at higher temperatures. After 24 h at 75°C, only 22.68% of the original content of anthocyanins was present in the extract, while at 20°C after 12 days of storage 62.66 % of the anthocyanins were still present in solution.

The kinetic parameters of the thermal degradation process of Blackthorn anthocyanins were determined using the linear regression of the natural logarithm (ln) of the concentration at different process times (see Figures 2-4).

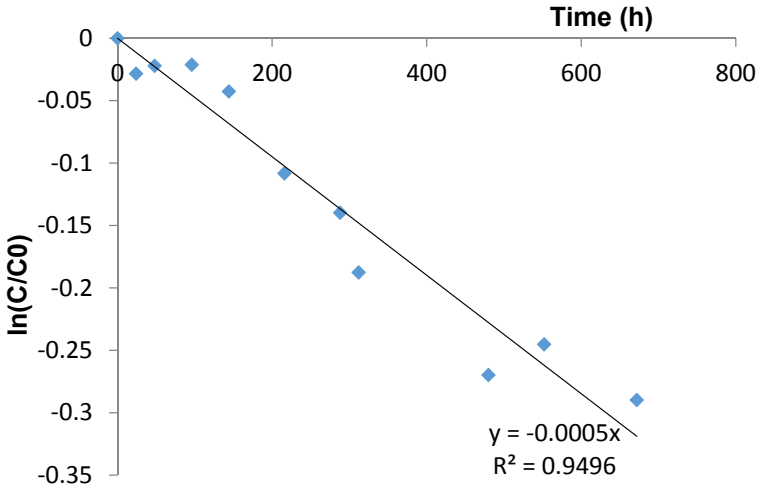

Figure 2. The degradation process of anthocyanins from Blackthorn fruits extract at 2°C.

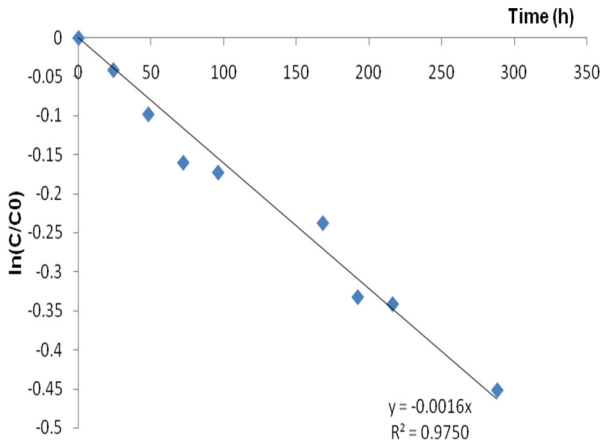

Figure 3. The degradation process of anthocyanins from Blackthorn fruits extract at 20°C.

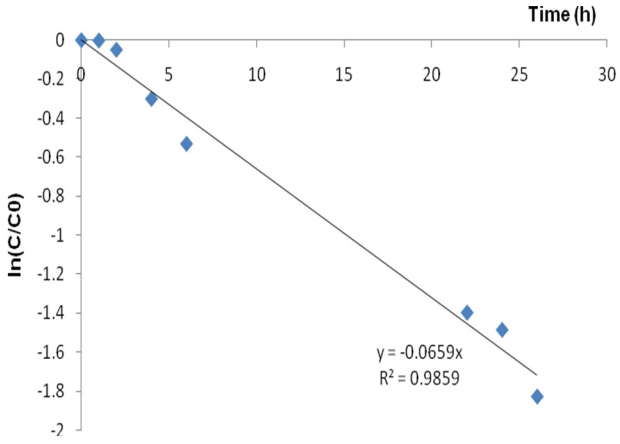

Figure 4. The degradation process of anthocyanins from Blackthorn fruits extract at 75°C.

The obtained plots indicated a first order degradation kinetics at all temperatures, results in agreement with previous studies of anthocyanins thermal degradation in various extracts [12-16].

The first-order rate constants k and the half-life $t_{1/2}$ values obtained for the degradation reactions of anthocyanins at each temperature are given in Table 1.

Table 1. Kinetic parameters of the degradation process of blackthorn anthocyanins

Temp. (°C)	$k \cdot 10^4$ (h^{-1}) ±SD*	$t_{1/2}$ (h) ± SD*
2	5±0.23	1386±63.75
20	16±0.76	433.1±20.57
75	659±26.09	10.5±0.42

*SD = Standard deviation

The high values of R^2 (>0.94) obtained for all cases indicated a good fit to the proposed first order reaction kinetics.

The kinetic rate constant values increased with temperature (being 132 fold higher at 75°C than at 2°C, while increasing the temperature from 2°C to 20°C resulted in a 3 fold faster degradation). This confirms the strong influence of temperature on the degradation process of the anthocyanins. The calculated $t_{1/2}$ values obtained for Blackthorn anthocyanins at elevated temperature were higher than those reported for the degradation of anthocyanins from other sources. Kara *et* Erelebi [17] reported a half-life value of mulberry anthocyanins of 4.4 h at 70°C while Wang and Xu [18] obtained 8.8 h for blackberry anthocyanins degradation at the same temperature. Compared to these results, the degradation process of blackthorn anthocyanins was slower than that of mulberry or blackberry anthocyanins, blackthorn pigments presenting a greater heat stability.

In order to determine the effect of the temperature on the degradation process of blackthorn anthocyanins, the kinetic rate constants obtained at 2°C, 22°C and 75°C where fitted to the Arrhenius equation (3):

$$k = K_0 e^{-Ea/RT} \quad (3)$$

where: k = rate constant (h^{-1})
K_0 = frequency factor (h^{-1})
E_a = activation energy (kJ/mol)
R = universal gas constant (8.314 J/mol/K)
T = absolute temperature (K)

The calculated value of the activation energy of anthocyanins' degradation process was 53.96 kJ/mol.

The high Ea value determined for the blackthorn anthocyanins indicates that the investigated compounds are less susceptible to thermal degradation. Previous studies reported comparable Ea values for various fruits anthocyanins degradation: 58.55 kJ/mol for Cornelian cherries [14], 66.37 kJ/mol for blueberries [15] and 65.32 kJ/mol for grape pomace [19].

The thermodynamic parameters of the anthocyanin degradation reaction are also determined, by means of equations (4), (5) and (6):

$$\Delta H^{\neq} = Ea - R \cdot T \tag{4}$$

$$\Delta G^{\neq} = -R \cdot T \cdot \ln\left(\frac{k \cdot h}{k_B \cdot T}\right) \tag{5}$$

$$\Delta S^{\neq} = \frac{\Delta H^{\neq} - \Delta G^{\neq}}{T} \tag{6}$$

where: $\Delta H^{\neq}$ = activation enthalpy (kJ/mol)
Ea = activation energy (kJ/mol)
R = universal gas constant (8.314 J/mol/K)
T = absolute temperature (K)
$\Delta G^{\neq}$ = Gibbs free energy of activation (kJ/mol)
k = rate constant at temperature T
h = $6.6262 \cdot 10^{-34}$ Js (Planck's constant)
k_B = $1.3806 \cdot 10^{-23}$ J/K (Boltzmann's constant)
$\Delta S^{\neq}$ = activation entropy (J/molK)

Table 2 presents the values of the activation enthalpy $\Delta H^{\neq}$, activation entropy $\Delta S^{\neq}$ and Gibbs free energy $\Delta G^{\neq}$ at the investigated temperatures.

Table 2. Thermodynamic parameters of blackthorn anthocyanins' thermal degradation

Temp. (°C)	$\Delta H^{\neq}$ (kJ/mol)	$\Delta S^{\neq}$ (J/mol.K)	$\Delta G^{\neq}$ (kJ/mol)
2	51.67	- 51.45	65.82
20	51.51	- 55.66	67.93
75	51.07	- 53.98	69.85

Relatively small values of activation $\Delta H^{\neq}$ indicate that the formation of the activated complex is favorised as the energy barrier to achieve the transition state is low. As shown in Table 2, the activation enthalpy values were similar for all experimental conditions, varying between 51.07 and 51.67 kJ/mol. The positive sign of $\Delta H^{\neq}$ means that activation of the degradation is endothermic.

The activation $\Delta S^{\neq}$ values determined for the reaction investigated in this study ranged from - 51.45 to - 53.98 J/molK, being all negative. The negative sign of the entropy indicates that the structural freedom of the transition state is lower than that of the reactants [20].

The positive activation $\Delta G^{\neq}$ values suggest that the thermal anthocyanin degradation in the Blackthorn extract is a non-spontaneous reaction [21].

CONCLUSIONS

The present study investigated the thermal degradation of blackthorn anthocyanins, stored at various temperatures. The results clearly indicated that the degradation process followed first-order reaction kinetics. The first order rate constants ranged from $5 \cdot 10^{-4}$ to $6.59 \cdot 10^{-2}$ h^{-1}, the degradation process being faster at elevated temperatures. The activation energy for the degradation process was determined to be of 53.96 kJ/mol. The thermodynamic parameters of the degradation process suggest that its activation is endothermic and non-spontaneous. Overall, blackthorn anthocyanins proved to be rather stable compared to pigments isolated from other sources, and hence may be successfully used as colorants in the food industry.

EXPERIMENTAL SECTION

Chemicals and reagents

All chemicals and reagents were purchased from Merck (Darmstadt, Germany), were of analytical grade and were used without further purification. A TYPDP1500 Water distiller (Techosklo LTD, Držkov, Czech Republic) was used to obtain the distilled water.

Plant material

Blackthorn fruits were harvested in October 2017 from Alba county, Romania.

Extract preparation

The extraction of the anthocyanins was obtained by mixing 20 grams of fresh crushed fruits with 50 mL 96% ethanol and stirred for 1 hour at ambient temperature. The mixture was filtered under reduced pressure and the filtrate was used to determine total anthocyanins concentration.

Determination of anthocyanin content

Anthocyanins were quantified by using the pH differential method. The fruit extract was mixed with a KCl buffer solution (0.025 M, pH = 1) as well as with a CH_3COONa solution (0.4 M, pH = 4.5) at a pre-established dilution factor of 8. After 15 minutes in the dark, the absorbencies of each mixture were measured at 517 and 700 nm using an UV-VIS Perkin Elmer Lambda 25 double beam spectrophotometer. From the obtained absorbencies the total anthocyanins content was calculated and expressed as mg /1 liter extract of cyanidin-3-glucoside. All experiments were carried out in triplicate.

Degradation studies

The thermal degradation experiments were conducted at 2°C, 20°C and 75°C, respectively.

Aliquots of 15 mL of blackthorn fruit extract were transferred in 3 hermetically sealed amber vials previously equilibrated in a thermostatic water bath at the desired temperatures. At different time intervals, samples were removed and rapidly cooled into an ice bath and the total anthocyanin content was determined as previously indicated. Data were fitted to the first-order kinetic equations and the desired kinetic and thermodynamic parameters were calculated for each temperature.

REFERENCES

1. B. Moldovan, O. Ghic, L. David, C. Chişbora, *Revista de Chimie*, **2012**, *63*, 463.
2. B. Moldovan, L. David, *Mini-Reviews in Organic Chemistry*, **2017**, 14(6), 489.
3. B. Moldovan, A. Popa**,** L. David, *Journal of Applied Botany and Food Quality*, **2016**, 89, 208.
4. S. N. Jimenez-Garcia, R. G. Guevara-Gonzalez, R. Miranda-Lopez, A. A. Peregrino-Perez, I. Torres-Pacheco, M. A. Vazquez-Cruz, *Food Research International*, **2013**, *54*, 1195.
5. B. Moldovan, L. David, S. C. Man, *Studia Universitatis "Babeş-Bolyai" Chemia*, **2017**, 62 (2 TOM II), 311.
6. A. Szajdek, E. J. Borowska, *Plant Foods for Human Nutrition*, **2008**, *63*, 147.
7. B. M. Ruiz-Rodriguez, B. de Ancos, C. Sanchez-Morena, V. Fernandez-Ruiz, M. C. Sanchez-Mata, M. Camara, J. Tardio, *Fruits*, **2014**, *69*, 61.
8. J. M. Velickovic, D. A. Costic, G. S. Stojanovic, S. S. Mitic, M. N. Mitic, S. S. Randelovic, A. S. Dordevic, *Hemijska Industrija*, **2014**, *68*, 297.
9. E. Sicora, M. I. Bieniek, B. Borczak, *Acta Scientarum Polonorum*, **2013**, *12*, 365.
10. V. I. Deineka, L. A. Deineka, A. A. Sirotnin, *Chemistry of Natural Compounds*, **2005**, *41*, 230.

11. M.M. Giusti, R.E. Wrolstad, *Current Protocols in Food Analytical Chemistry*, Wiley, New York, **2001**, F.1.2.1-F1.2.13.
12. B. Moldovan, R. Mintău, L. David, *Studia Universitatis "Babeş-Bolyai" Chemia*, **2015**, 60 (1), 139.
13. B. Moldovan, L. David, R. Donca, C. Chişbora, *Studia Universitatis "Babes-Bolyai", Chemia*, **2011**, 56, 189-194.
14. B. Moldovan, L. David, *Molecules*, **2014**, *19*, 8177.
15. A. Martynenko, Y. Chen, *Journal of Food Engineering*, **2016**, *171*, 44.
16. A. Sinela, N. Rawat, C. Mertz, N. Achir, H. Fulcrand, M. Dornier, *Food Chemistry*, **2017**, *214*, 234.
17. S. Kara, E.A. Ercelebi, *Journal of Food Engineering,* **2013***, 116,* 541.
18. W. D. Wang, S.Y. Xu, *Journal of Food Engineering,* **2007***, 82,* 271.
19. D.K. Mishra, K.D. Dolan, L. Yang, *Journal of Food Science,* **2008,** *73*, E9.
20. V.B. Vikram, M.N. Ramesh, S.G. Prapulla, *Journal of Food Engineering,* **2005***, 69,* 31.
21. G.D. Mercali, D.P. Jaeschke, I.C. Tessaro, L.D.F. Marczak, *Food Chemistry*, **2013**, 136, 853.

STUDIA UBB CHEMIA, LXIV, 2, Tom II, 2019 (p. 411-419)
(RECOMMENDED CITATION)
DOI:10.24193/subbchem.2019.2.35

Dedicated to Professor Ioan Bâldea on the Occasion of His 80th Anniversary

RADIOCARBON INVESTIGATION OF THE SUPERLATIVE AFRICAN BAOBABS FROM SAVÉ VALLEY CONSERVANCY, ZIMBABWE

ADRIAN PATRUT[a,*], ROXANA T. PATRUT[a], LASZLO RAKOSY[b], DANIEL A. LOWY[c], DRAGOS MARGINEANU[a], KARL F. VON REDEN[d]

ABSTRACT. The article reports the radiocarbon investigation results of the superlative African baobabs from Savé Valley, Zimbabwe. Several wood samples collected from these baobab were analysed by AMS (accelerator mass spectrometry) radiocarbon dating. The radiocarbon dates of the oldest samples were 1529 ± 14 BP for Matendere Big baobab, 1179 ± 19 BP for Chishakwe Big tree and 1096 ± 35 BP for Mokore Giant baobab. The corresponding calibrated ages are 1430 ± 15, 1090 ± 40 and 1020 ± 25 calendar yr. The oldest tree from Savé Valley, which we described previously, is the Humani Bedford Old baobab. The radiocarbon date of its oldest sample, 1655 ± 14 BP, corresponds to a calibrated age of 1580 ± 30 calendar yr.

***Keywords*:** *AMS radiocarbon dating, Adansonia digitata, tropical trees, dendrochronology, age determination, Zimbabwe.*

INTRODUCTION

The African baobab (*Adansonia digitata* L.), which belongs to the Bombacoideae, a subfamily of Malvaceae, is the best known of the eight or nine *Adansonia* species. The African baobab has a natural distribution in the tropical arid savanna regions of mainland Africa between the latitudes 16º N and 26º S. It can also be found on several African islands and outside Africa, in different areas throughout the tropics, where it has been introduced [1-5].

[a] *Babeş-Bolyai University, Faculty of Chemistry and Chemical Engineering, 11 Arany Janos, RO-400028, Cluj-Napoca, Romania*
[b] *Babeş-Bolyai University, Faculty of Biology and Geology, 44 Republicii, RO-400015, Cluj-Napoca, Romania*
[c] *VALOR HUNGARIAE, Dept. of Science and Innovation, 4 Nagysándor József, 1054 Budapest, Hungary*
[d] *NOSAMS Facility, Dept. of Geology & Geophysics, Woods Hole Oceanographic Institution, Woods Hole, MA 02543, U.S.A.*
** Corresponding author: apatrut@gmail.com*

In 2005, we started an extended research project to elucidate several controversial aspects related to the architecture, growth and age of the African baobab and of other large and/or old baobab species. This research is based on our new approach, which is not limited to fallen specimens, but allows to investigate and date live individuals, as well. Our approach consists of AMS (accelerator mass spectrometry) radiocarbon dating of tiny wood samples collected especially from inner cavities, deep incisions/entrances in the stems, fractured stems and from the outer part/exterior of large baobabs [6-12].

The majority of baobabs start growing as single-stemmed trees. Nevertheless, over time, single-stemmed individuals become multi-stemmed, owing to the baobabs' ability to produce periodically new stems, such as other tree species produce branches. By this special capacity, baobabs develop over time architectures of increasing complexity. Therefore, we focused on the investigation of superlative individuals, i.e., very large and potentially old baobabs. One should emphasize that neither the identification of such very complex architectures nor the accurate age determination of old baobabs are possible via traditional dendrochronological methods based on tree ring investigation [13]. The oldest dated African baobab specimens were found to have ages greater than 2000 yr [13-15]. By these values, the African baobab becomes the longest living angiosperm.

The Savé Valley Conservancy is a large wildlife area (3442 km^2), located in the semi-arid South East Lowveld of Zimbabwe, at an altitude of 480–620 m. It consists of multiple properties owned by private ranchers, local councils, government and a local community [16]. Savé Valley hosts thousands African baobabs, out of which four are superlative specimens. All these very large and old trees are located to the north of Turgwe river, more precisely in the Matendere, Chishakwe, Mokore and Humani ranches.

In a previous article, we presented the AMS radiocarbon dating results of the Humani Bedford Old baobab, which is not only the oldest tree of Zimbabwe, but also the oldest living African baoab [17].

Here we also disclose the results of the radiocarbon investigation of the other three superlative baobabs from the Savé Valley Conservancy.

RESULTS AND DISCUSSION

The superlative baobabs and their areas. The four superlative baobabs are located on four ranches, which belong to the Savé Valley Conservancy, Chiredzi district, Zimbabwe. The mean annual rainfall in these areas is between 360-460 mm.

The northernmost superlative baobab is the Matendere Big baobab, which was discovered in 1994 by Léon Duplessis on the Matendere Ranch. Its GPS coordinates are 20º00.325' S, 032º03.808' E and the altitude is 702 m. It has a height h = 22.5 m, the circumference at breast height (cbh; at 1.30 m above ground level) is cbh = 26.30 m and the overall wood volume (trunk and branches, including the cavity) is around 300 m^3.

The Matendere Big baobab is composed of 7 large units, which correspond to stems. It has a closed ring-shaped structure defined by 5 stems that incorporate a false cavity, with a very tall opening at a height of over 6 m. Its canopy has the horizontal dimensions of 38.3 x 39.4 m.

A second representative baobab of Savé Valley, i.e., the Chishakwe Big tree, can be found on the Chishakwe Ranch. The GPS coordinates are 20º06.656' S, 032º04.991' E and the altitude is 588 m. It has the following dimensions: h = 26.1 m, cbh = 26.56 m, V = ca. 375 m^3 (**Figure 1**). The Chishakwe Big tree consists of 7 fused stems. It has a closed ring-shaped structure, with a ring composed of 5 or 6 stems that completely close a false cavity inside. The cavity has only a tall opening at a height of 7-8 m, which is inaccessible. The large canopy has the horizontal dimensions of 38.5 x 36.1 m.

The Humani Bedford Old baobab, that we previously dated [17], is located on the Bedford Block of the Humani Ranch. It was discovered only in 2011 by Roger and Anne Whittall. The GPS coordinates are 20º24.474' S, 032º14.135' E and the altitude is 432 m. Its dimensions are: h =18.2 m, cbh = 23.65 m, V = 240 m^3. The big trunk has a closed ring-shaped structure which consists now of three fused stems (one stem is missing) that partially close a false cavity with the walls covered by bark. The Humani baobab has huge branches, with diametres up to 2.2 m, which form a canopy with the horizontal dimensions of 27.2 x 24.7 m.

The best-known baobab of Savé Valley, the Mokore Giant baobab, is located on the Mokore Ranch. It has the following GPS coordinates: 20º23.950' S, 036º06.836' E and the altitude is 462 m. Its dimensions are: h = 23.2 m, cbh = 28.11 m and V = ca. 320 m^3 (**Figure 2**). The Mokore Giant baobab possesses 7 stems of different sizes and ages and a large false stem, which acts as a structural support/anchor. The false stem is mainly empty and fissured; this might have dramatic consequences on the survival of this specimen in the near future. The Mokore baobab has a closed ring-shaped structure, with a ring of 4 stems that close a false cavity. The cavity has an opening only in the upper part, at a height of over 5 m. The horizontal dimensions of the very large canopy are 42.3 x 35.1 m.

The Matendere Big baobab and the Humani Bedford Old baobab are basically unknown in the literature, as well as outside Savé Valley; they are not included in the registers of the Tree Society of Zimbabwe.

Wood samples. Several samples were collected from the walls of the inner cavity (Humani Bedford), as well as from deep incisions in the exterior/ outer part (Matendere, Chishakwe, Mokore) of the four baobabs. The heights of the sampling points were between 1.36 and 2.05 m. A number of tiny pieces/ segments, each 0.1 cm long, were extracted from determined positions of each sample.

Figure 1. The Chishakwe Big tree is the tallest and largest African baobab of Zimbabwe (26.1 m, 375 m^3).

Figure 2. The Mokore Giant baobab has the biggest circumference (28.11 m) of all trees of Zimbabwe.

AMS results and calibrated ages. Radiocarbon dates of the two oldest samples/segments extracted from each baobab are listed in Table 1. Radiocarbon dates and errors were rounded to the nearest year. The radiocarbon dates are expressed in ^{14}C yr BP (radiocarbon years before present, i.e., before the reference year AD 1950).

Calibrated (cal) ages, expressed in calendar years, are also presented in Table 1. The 1-σ probability distribution was selected to derive calibrated age ranges. For four samples, the 1-σ distribution is consistent with only one range of calendar years, while for the other four samples the 1-σ distribution corresponds to two or three ranges of calendar years. For these segments, the confidence interval of one range is considerably greater than that of the other(s); therefore, it was selected as the cal AD range of the segment for the purpose of this discussion. For obtaining single calendar age values of sample segments, we derived a mean calendar age of each segment from the selected range (marked in bold). Calendar ages of samples represent the difference between AD 2019 and the mean value of the selected range, with the corresponding error. Calendar ages and errors were rounded to the nearest 5 yr.

Table 1. AMS Radiocarbon dating results and calibrated calendar ages of samples collected from superlative baobabs from Savé Valley Conservancy

Tree	Sample/ segment code	Radiocarbon date of oldest sample(s) [error] (^{14}C yr BP)	Cal AD range 1-σ [confidence interval]	Sample age [error] (cal yr)
Matendere Big baobab	MAT-1	1529 [± 14]	552-556 [3.3%] **572-604 [56.3%]** 618-627 [8.6%]	1430 [± 15]
	MAT-2	1305 [± 19]	**684-738 [59.3%]** 762-771 [8.9%]	1310 [± 25]
Chishakwe Big tree	CH-1	1179 [± 34]	**888-970 [68.2%]**	1090 [± 40]
	CH-2	1065 [± 24]	**994-1026 [68.2%]**	1010 [± 15]
Humani Bedford Old baobab	HB-1	1655 [± 14]	**410-469 [68.2%]**	1580 [± 30]
	HB-2	1375 [± 20]	**658-682 [50.2%]** 746-757 [18.0%]	1350 [± 10]
Mokore Giant baobab	MOK-1	1096 [± 35]	**972-1026 [68.2%]**	1020 [± 25]
	MOK-2	990 [± 18]	1042-1050 [7.7%] **1080-1145 [60.5%]**	910 [± 30]

Dating results of oldest samples (segments). The two oldest samples originating from the Matendere Big baobab, labelled MAT-1 and MAT-2, were found to have radiocarbon dates of 1529 ± 14 and 1305 ± 19 BP (before present, i.e., before the reference year AD 1950). These values correspond to old calibrated ages, namely 1430 ± 15 and 1310 ± 25 calendar yr.

The two oldest samples extracted from the Chishakwe Big tree, i.e., CH-1 and CH-2, had radiocarbon dates of 1179 ± 19 and 1065 ± 24 BP. These dates correspond to calibrated ages of 1090 ± 40 and 1010 ± 15 calendar yr.

For the Mokore Giant baobab, the oldest samples MOK-1 and MOK-2 have radiocarbon dates of 1096 ± 35 and 990 ± 18 BP. These values correspond to calibrated ages of 1020 ± 25 and 910 ± 30 calendar yr.

We previously disclosed the radiocarbon dating results of samples collected from the Humani Bedford Old baobab. The two oldest samples HB-1 and HB-2 were found to have radiocarbon dates of 1655 ± 14 and 1375 ± 20 BP. These dates correspond to calibrated ages of 1580 ± 30 and 1350 ± 10 calendar yr [17].

Architecture of the superlative baobabs. All four superlative baobabs of the Savé Valley Conservancy possess a closed ring-shaped structure with a false cavity inside. This special type of architecture enables baobabs to reach large sizes and old ages. We remind that false cavities, which have the walls covered by bark, are in fact natural empty spaces between several fused stems disposed in a closed ring-shaped structure. Over time, false cavities close progressively. Several false cavities have closed completely over time, retaining only one or several small openings. The thickness of the cavity walls, i.e., of the fused stems that define the false cavity, is of only 1-2 m. For wood samples collected from the false cavity walls toward the exterior, as well as in the case of samples collected from the exterior toward the false cavity, the age sequence shows a continuous increase from the sampling point up to a certain distance into the wood, after which it decreases in the opposite direction. The oldest part of the fused stems is located between the false cavity walls and the exterior of each stem, always closer to the cavity, in an area that would be accessible to the increment borer and allows to collect very old samples [12,13,15,18].

Three superlative baobabs (Matendere, Chishakwe, Mokore) have their false cavity completely closed, with the exception of a high opening positioned at 5-8 m above the ground. Their false cavity can be observed only by climbing the trunk of the baobab or with the help of a drone. The fourth superlative baobab (Humani Bedford) also had its false cavity quasi-completely closed several centuries ago. The cavity has now a large opening after the collapse of a fourth stem of the ring.

Ages of the superlative baobabs. The oldest dated samples/segments originate from the false cavity only for the Humani Bedford Old baobab. In this direction, the distance from the false cavity to the exterior/outer part, i.e., the width of the cavity walls, was found to be 1.20 m. We also evinced the presence of the growth stop phenomenon. Radiocarbon dating results demonstrated that the oldest dated stem stopped growing toward the false cavity 600 yr ago, while it has continued its growth toward the exterior for almost 250 yr.

By considering the sample/segment positions and ages, the growth stop and the width of the cavity walls, we estimated that the investigated stem of the Humani-Bedford baobab has an age of 1800 ± 100 yr. By this value, it becomes the oldest living African baobab [17].

For the other three superlative baobabs, the oldest samples/segments were collected from the exterior toward the false cavity. In these cases, we cannot determine the width of the cavity walls and we have no concrete evidence about the growth stop. We can only state that the age of the oldest part of each tree is certainly older than the oldest dated sample/segment. In a conservative estimate, we assume that their ages would be: 1500 ± 100 yr for the Matendere Big baobab, 1200 ± 100 yr for the Chishakwe Big tree and also for the Mokore Giant baobab.

CONCLUSIONS

Our research discloses the AMS radiocarbon dating results of the four superlative African baobabs from the Savé Valley Conservancy, Zimbabwe. These baobabs are: the Matendere Big baobab, the Chishakwe Big tree, the Humani Bedford Old baobab and the Mokore Giant baobab. The main aim of the research was to establish the architectures and the ages of these trees.

All four baobabs exhibit a closed ring-shaped structure with a false cavity inside. This architecture consists of several fused stems around a natural empty space, which we named false cavity.

Several wood samples collected from the baobabs were radiocarbon dated. The radiocarbon dates of the oldest samples were found to be 1529 ± 14 BP for the Matendere Big baobab, 1179 ± 19 BP for the Chishakwe Big tree and 1096 ± 35 BP for the Mokore Giant baobab. These values correspond to calibrated ages of 1430 ± 15, 1090 ± 40 and 1020 ± 25 calendar yr.

However, the oldest tree from Savé Valley, which we have previously described, is the Humani Bedford Old baobab. The radiocarbon date of its oldest sample, i.e., 1655 ± 14 BP, corresponds to a calibrated age of 1580 ± 30 calendar yr.

EXPERIMENTAL SECTION

Sample collection. The wood samples were collected with a Haglöf CH 800 increment borer (80 cm long, 0.54 cm inner diametre). A number of tiny pieces/segments of the length of 0.1 cm were extracted from predetermined positions along the wood samples. The segments were processed and investigated by AMS radiocarbon dating.

Sample preparation. The standard acid-base-acid pretreatment method was used for removing soluble and mobile organic components [19]. The pretreated samples were combusted to CO_2 by using the closed tube combustion method [20]. Then, CO_2 was reduced to graphite on iron catalyst, under hydrogen atmosphere [21]. Finally, the resulting graphite samples were analysed by AMS.

AMS measurements. AMS radiocarbon measurements were performed at the NOSAMS Facility of the Woods Hole Oceanographic Institution (Woods Hole, MA, U.S.A.) by using the Pelletron ® Tandem 500 kV AMS system. The obtained fraction modern values, corrected for isotope fractionation with the normalized $\delta^{13}C$ value of -25 $^{0}/_{00}$, were ultimately converted to a radiocarbon date.

Calibration. Radiocarbon dates were calibrated and converted into calendar ages with the OxCal v4.3 for Windows [22], by using the SHCal13 atmospheric data set [23].

ACKNOWLEDGMENTS

Authors would like to acknowledge Léon and Judy Duplessis, the owners of the Matendere Rach, Lisa-Jane Campbell of Chishakwe Ranch, Roger Whittall, the owner of the Humani Ranch and his wife Anne Whittall, Greg and Melanie Duckworth of Mokore Ranch for granting access in the ranches and for authorising the investigation and sampling of the monumental baobabs. The research was funded by the Romanian Ministry of National Education CNCS-UEFISCDI under grant PN-III-P4-ID-PCE-2016-0776, Nr. 90/2017.

REFERENCES

1. D.A. Baum, *Annals of the Missouri Botanical Garden*, **1995**, *82*, 440-471.
2. G.E. Wickens, P. Lowe, "The Baobabs: Pachycauls of Africa, Madagascar and Australia", Springer, Dordrecht, **2008**, pp. 232-234, 256-257, 295-296.
3. J.D. Pettigrew, L.K. Bell, A. Bhagwandin, E. Grinan, N. Jillani, J. Meyer, E. Wabuyele, C.E. Vickers, *Taxon*, **2013**, *61*, 1240-1250.

4. G.V. Cron, N. Karimi, K.L. Glennon, C.A. Udeh, E.T.F. Witkowski, S.M. Venter, A.E. Assobadjo, D.H. Mayne, D.A. Baum, *Taxon*, **2016**, *65*, 1037-1049.
5. D.A. Baum, R.L. Small, J.F. Wendell, *Systematic Biology*, **1998**, *47*, 181-207.
6. A. Patrut, K.F. von Reden, D.A. Lowy, A.H. Alberts, J.W. Pohlman, R. Wittmann, D. Gerlach, L. Xu, C.S. Mitchell, *Tree Physiology*, **2007**, *27*, 1569-1574.
7. A. Patrut, D.H. Mayne, K.F. von Reden, D.A. Lowy, R. Van Pelt, A.P. McNichol, M.L. Roberts, D. Margineanu, *Radiocarbon*, **2010**, *52(2-3)*, 717-726.
8. A. Patrut, K.F. von Reden, R. Van Pelt, D.H. Mayne, D.A. Lowy, D. Margineanu, *Annals of Forest Science*, **2011**, *68*, 93-103.
9. A. Patrut, K.F. von Reden, P. Danthu, J-M. Leong Pock Tsy, R.T. Patrut, D.A. Lowy, *PLOS One*, **2015**, *10(3): e0121170*.
10. A. Patrut, K.F. von Reden, P. Danthu, J-M. Leong Pock-Tsy, L. Rakosy, R.T. Patrut, D.A. Lowy, D. Margineanu, *Nuclear Instruments and Methods in Physics Research Section B,* **2015**, *361*, 591-598.
11. A. Patrut, R.T. Patrut, P. Danthu, J.-M. Leong Pock-Tsy, L. Rakosy , D.A. Lowy, K.F. von Reden, *PLOS One*, **2016**, *11(1)*, e0146977.
12. A. Patrut, S. Woodborne, K.F. von Reden, G. Hall, M. Hofmeyr, D.A. Lowy, R.T. Patrut, *PLOS One*, **2015**, *10(1): e0117193.*
13. A. Patrut, S. Woodborne, R.T. Patrut, L. Rakosy, D.A. Lowy, G. Hall, K.F. von Reden, *Nature Plants*, **2018**, *4(7)*, 423-426.
14. A. Patrut, K.F. von Reden, D.H. Mayne, D.A. Lowy, R.T. Patrut, *Nuclear Instruments and Methods in Physics Research Section B*, **2013**, *294*, 622-626
15. A. Patrut, S. Woodborne, K.F. von Reden, G. Hall, R.T. Patrut, L. Rakosy, J-M. Leong Pock Tsy, D.A. Lowy, D. Margineanu, *Radiocarbon*, **2017**, *59(2)*, 435-448.
16. P. Lindsay, R. du Toit, A. Pole, S. Romanach, "Savé Valley Conservancy: A Large-Scale African Experiment in Cooperative Wildlife Management." In: H. Suich, B. Child, A. Spenceley, editors, "Evolution and Innovation in Wildlife Conservation", Earthscan, London, Sterling, VA, **2009**, pp.163-186.
17. A. Patrut, L. Rakosy, R.T. Patrut, I.A. Ratiu, E. Forizs, D.A. Lowy, D. Margineanu, K.F. von Reden, *Studia UBB Chemia*, **2016**, *LXI, 4*, 7-20.
18. A. Patrut, S. Woodborne, R.T. Patrut, L. Rakosy, G. Hall, I.A. Ratiu, K.F. von Reden, *Studia UBB Chemia*, **2017**, *LXII, 2*, 347-354,
19. I.U. Olsson, Radiometric Methods. In: B. Berglung, editor "Handbook of Holocene palaeoecolgy and palaeohydrology", Wiley, Chichester, **1986**, pp. 273-312.
20. Z. Sofer, Analytical Chemistry, 1980, 52(8), 1389-1391.
21. J.S. Vogel, J.R. Southon, D.E. Nelson, T.A. Brown, *Nuclear Instruments and Methods in Physics Research Section B*, **1984**, *5*, 289-293.
22. C. Bronk Ramsey, *Radiocarbon*, **2009**, *51*, 337-360.
23. A.G. Hogg, Q. Hua, P.G. Blackwell, M. Niu, C.E. Buck, T.P. Guilderson, T.J. Heaton, J.G. Palmer, P.J. Reimer, R.W. Reimer, C.S.M. Turney, R.H. Zimmerman, *Radiocarbon*, **2013**, *55(4)*, 1889-1903.

STUDIA UBB CHEMIA, LXIV, 2, Tom II, 2019 (p. 421-434)
(RECOMMENDED CITATION)
DOI:10.24193/subbchem.2019.2.36

Dedicated to Professor Ioan Bâldea on the Occasion of His 80th Anniversary

HEMOGLOBIN-ALBUMIN CO-POLYMERS FOR BLOOD SUBSTITUTES: INCREASING THE REPRODUCIBILITY OF THE POLYMERIZATION REACTION

FLORINA SCURTU[a*], BOGDAN TEBREAN[b], MARIANN KINGA ÁRKOSI[a], ADRIAN IONELE[a], RADU SILAGHI-DUMITRESCU[a*]

ABSTRACT. Reticulation/polymerization of proteins using bifunctional reagents, with glutaraldehyde as a typical example, has a wide range of applications – of which HBOC (hemoglobin/hemerythrin based oxygen carriers) are illustrative. Here, the kinetics of the derivatization reaction of hemoglobin and albumin with glutaraldehyde are revisited, in order to establish the optimal conditions such as concentration of protein and derivatization agent for which the final product can be a reasonable candidate for blood substitutes. A purpose-built mixing device is described, which allows automated mixing of up to four reagents in less than 100 milliseconds, allowing for polymers with a more reproducible molecular weight.

Keywords*: hemoglobin, glutaraldehyde, bovine serum albumin, blood substitutes, mixer, polymerization*

INTRODUCTION

Able to transport oxygen outside of the red blood cell, native tetrameric hemoglobin (Hb) would be the first option for a blood substitute [1,2]. However, cell-free Hb appears to be toxic [3,4] because its tetrameric structure is prone to dissociation into dimers, which then undergo rapid extravasation [2,5]. To prevent rapid tetramer elimination in blood substitute candidates, Hb is

[a] *Babeş-Bolyai University, Department of Chemistry and Chemical Engineering, 11 Arany Janos Street, Cluj-Napoca 400028, Romania*
[b] *Technical University of Cluj-Napoca, Electrical Engineering and Measurements Department, 26 G. Baritiu Street, Cluj-Napoca 400027, Romania*
** Corresponding author: rsilaghi@chem.ubbcluj.ro*

typically treated with agent(s) capable of increasing the apparent molecular weight of the protein and/or establishing covalent bonds between the subunits [1, 6-12]. In this respect, one of the most commonly used methods involves reticulation/polymerization with dialdehydes such as glutaraldehyde [7,8,13-15]. This reaction allows intermolecular bonding between the amino groups (-NH2) of lysines (and N-terminal valines) of Hb and the carbonyl groups (-C=O) of glutaraldehyde, with the formation of covalent-bonded dimers, trimers, tetramers and polymers [7,9,16]. Compared to Hb polymers, the Hb-albumin copolymerization strategy has been reported to present key advantages in avoiding oxidative stress side-reactions, with minimal effects in biological tests [9,11,17]. Here, we describe a device for mixing the reactants in order to attain higher molecular weights with better reproducibility in the hemoglobin reticulation/polymerization reactions with glutaraldehyde, as well as for co-polymerization reactions of hemoglobin with bovine serum albumin (BSA). The use of the described mixer allows for more informed and controlled choices in establishing protocols for producing protein-based oxygen carriers in larger quantities.

RESULTS AND DISCUSSION

Mathematical modeling of the mixer

The device employed for the mixing procedures was built in order to obtain a promptly homogeneous reaction mixture, from two to four species, in various concentrations, with the aid of an electromechanically delivery system and a mixing chamber.

The electromechanical system contains a stepper motor, an electronic circuit, the mechanical components, two to four syringes, and elastic connecting tubes. It can be adapted to different types of syringes, offering the possibility to easily modify the volumes of the chemicals that are involved in the reactions. The flow rate variation of the delivered species is also controllable *via* the velocity of the stepper motor, controlled *via* the electronic circuit. Figure 1 illustrates the flow rate through the connecting tubes as being a linear vs the stepper motor's angular velocity (regardless of its value), for a single-syringe case.

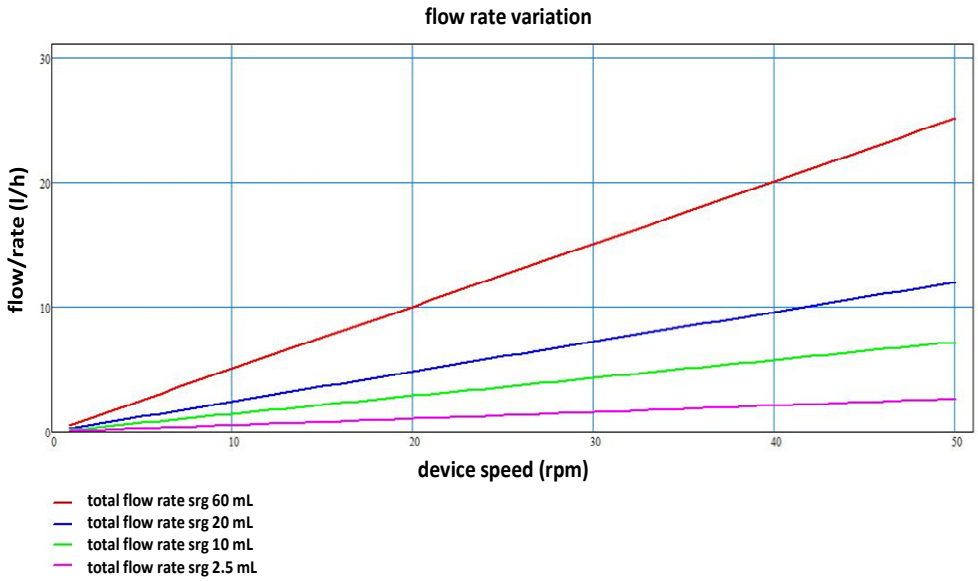

Figure 1. Flow rate variation for different syringe types (2.5 to 60 mL).

The mixing device (cf. Figure 2) that was used for this case consists of a silicone tube and three syringe needles used for the two inlets and the outlet of the mixer. The whole assembly has a coating of elastic silicone in order to protect the mixing tube from external influences, and to avoid variation of internal pressure.

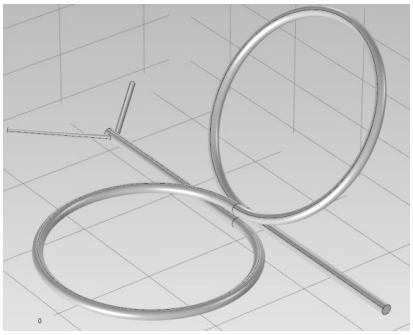

Figure 2. The mixing device and the interior geometry. Schematic representation.

The implementation of the mixing chamber was based on several tests and evaluations through mathematical modeling of the proposed geometry. The CFD modeling was performed for the physical model, with an initial velocity condition presumed at the inlet tubes of 0.5 m/s for each species.

The modeling result presented in Figure 3 shows that at the outlet of the mixing tube, the velocity of the mixture is around 2 m/s, and there are no significant turbulences. This value is sufficient to obtain a residence time, inside the mixer, of around 100 ms.

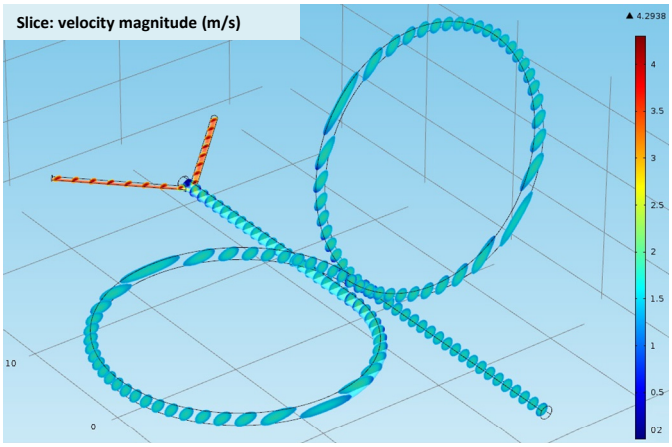

Figure 3. Velocity profile of the species in the mixing tube.

The results in Figure 4 illustrate the evolution of concentration only for the first species; for the second one the results are symmetrical. Thus, the outlet concentration of the substance is at half of its initial/inlet value – suggesting that the species are indeed homogenously mixed and the chosen geometry can be successfully implemented.

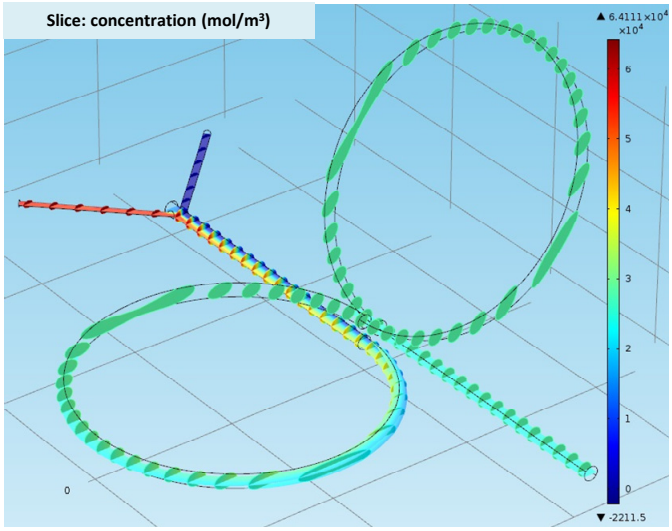

Figure 4. Concentration of the first species through the mixing tube.

FPLC-derived kinetics of the Hb-GL and Hb-BSA-GL reactions

The gel-filtration chromatograms in Figure 5 illustrate the changes in apparent molecular mass of Hb, induced by polymerization with 8 mM glutaraldehyde. The area under the peak corresponding to the derivatized sample (region to the left of the dashed vertical line in Figure 5) increases continuously with derivatization time, up to 120 min. This value was proposed [7] as a reasonable time-point for obtaining suitable for blood substitute molecular weights.

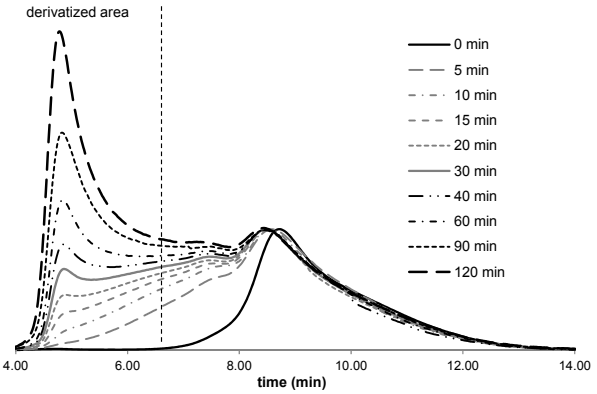

Figure 5. Size-exclusion chromatograms of 1 mM Hb derivatized with 8 mM GL, at different intervals after automated reactant mixing. Conditions: 20 mM Tris pH 7.4, 150 mM NaCl, room temperature.

Figure 6 shows the time evolution of the Hb-BSA-GL ternary reaction mixture. The process appears to follow faster kinetics as compared to the simple Hb-GL mixture, but with distinctly smaller contributions from fractions present near the front of the eluent (i.e., those with molecular weights of 1000 kDa and higher).

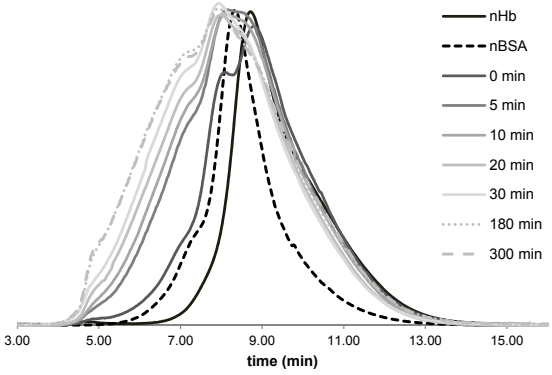

Figure 6. Size-exclusion chromatograms for 1 mM Hb derivatized with 1 mM BSA in the presence of 8 mM GL, at different intervals after reactant mixing. Conditions: 20 mM Tris pH 7.4, 150 mM NaCl, room temperature.

SDS-PAGE-derived kinetics

Figure 7 shows an SDS-PAGE analysis of the influence of glutaraldehyde (Figure 7A) and BSA (Figure 7B) on hemoglobin (co-)polymers, at different intervals after mixing. A clear trend is seen in the band corresponding to the Hb monomer at ~16 kDa, as its intensity decreases constantly with the reaction time. The results are in agreement with those obtained by size exclusion chromatography: for the hemoglobin-only polymer the reaction is not completed after 120 min, while in case of copolymer the reaction is completed after aprox. 30 min, in line with data in Figures 6 and 8B (see below).

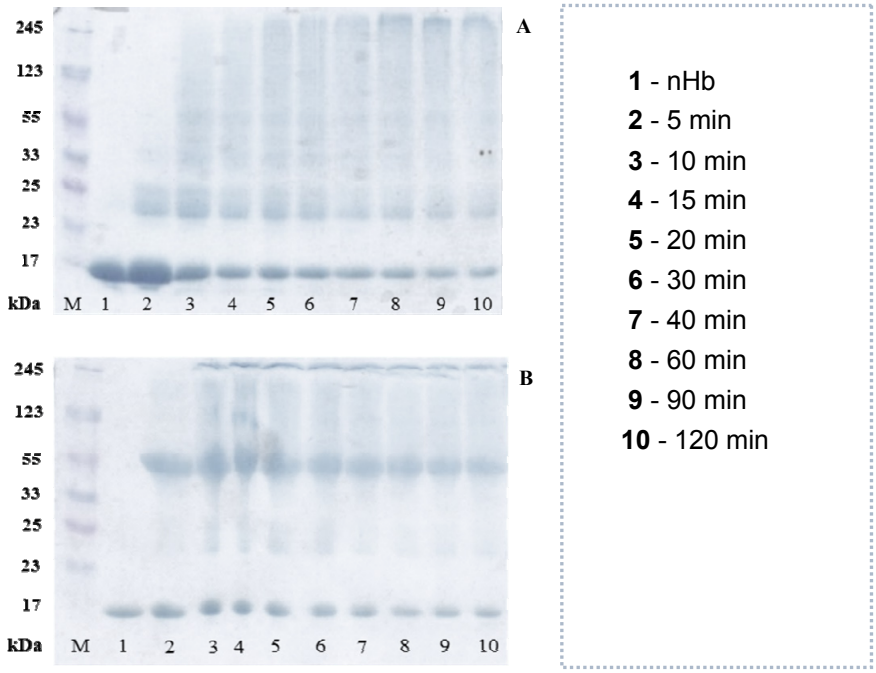

Figure 7. SDS-PAGE illustrating the effect of 8 mM glutaraldehyde (**A**) and 1 mM BSA (**B**) on polymerization degree, at different intervals after reactant mixing: **1**– native Hb, **2**- 5 min, **3**- 10 min, **4**- 15 min, **5**- 20 min, **6**- 30 min, **7**- 40 min, **8**- 60 min, **9**- 90 min, and **10**- 120 min.

Images of the gels were analyzed digitally (by using the specialized software called Thin Layer Chromatography Analyzer). Figure 8A (corresponding to polymerized Hb) shows that the intensity of the monomer band (16 kDa) decreases constantly with the increase of reaction time, while the intensity of the polymer band (245 kDa) increases, demonstrating the evolution of

the polymerization reaction. By contrast, the line corresponding to the Hb copolymerized with BSA, maintains the same intensity as the line corresponding to the copolymerized sample with 120 min reaction time (Figure 8B), demonstrating that the copolymerization is completed after aprox. 30 min.

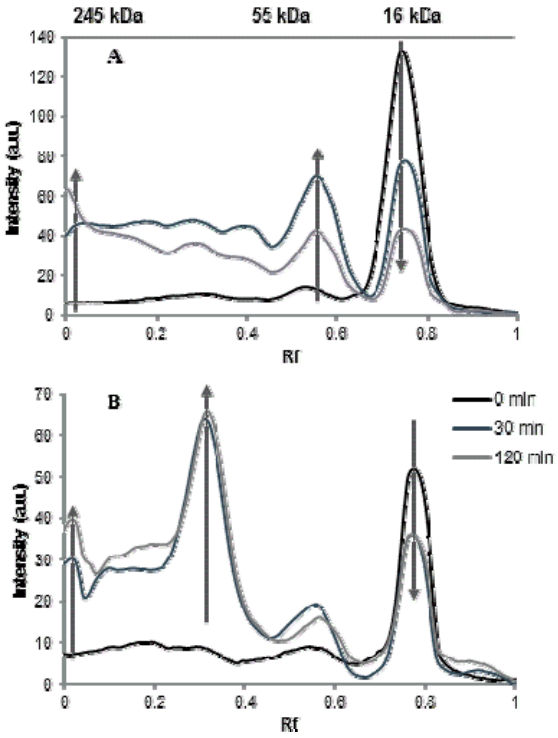

Figure 8. SDS-PAGE image analysis by a specialized software (**A:** 1 mM Hb + 8 mM GL, **B:** 1 mM Hb + 1 mM BSA + 8 mM GL)

UV-vis characterization of the (co)polymers

Figure 9 shows UV-vis spectra of derivatized Hb immediately after the derivatization procedure with or without BSA, when using glutaraldehyde as a cross-linking agent. The increase in absorbance at 630 nm (specific to ferric hemoglobin), coupled with decreases at 540 and 580 nm (specific to ferrous-oxy hemoglobin), indicates that glutaraldehyde induces a slightly enhanced autooxidation tendency (higher concentration of derivatization agent causes higher autooxidation rate) – which, as also seen in Figure 9 (solid dark grey trace), BSA can alleviate. Similarly, higher reaction times increase the autooxidation tendency (Figure 10). Moreover, after approximately 4 hours the protein precipitates.

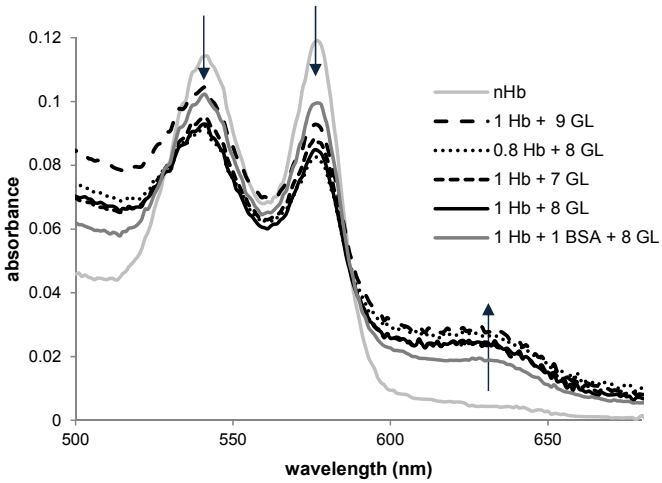

Figure 9. UV-VIS spectra of native and (BSA co)polymerized hemoglobin, measured after derivatization with glutaraldehyde at various concentrations (mM). Conditions: PBS, room temperature.

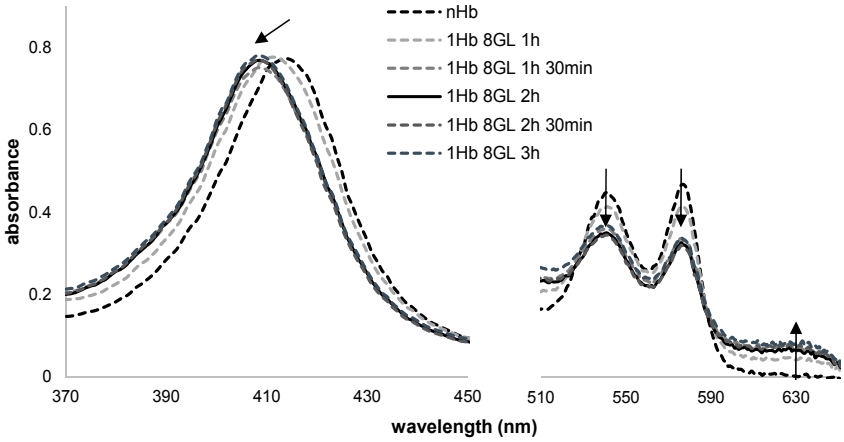

Figure 10. UV-VIS spectra of polymerized hemoglobin, measured after derivatization with glutaraldehyde at different time of reaction. Conditions: 1 mM Hb, 8 mM GL, PBS, room temperature.

Influence of reactant concentration

Figure 11 illustrates that the degree of polymerization increases with the concentration of derivatizing agent. Thus, the largest derivatized area was obtained in the sample with the highest concentration of glutaraldehyde

(see Table 1). Again, one may note that the reaction is still incomplete at 120 min after mixing in the Hb-GL cases, while it is essentially completed after 30 min for the Hb-BSA mixtures. Although the derivatized area is higher after 180 minutes, the reaction is optimally quenched at 120 min because at longer times there are also higher autoxidation rates in the product (see Figure 10). Time resolved data in Figure 10 were fitted with the exponential growth function $y = A_1*\exp(x/t_1) + A_2*\exp(x/t_2) + y_0$, in order to obtain the kinetic data in Table 1.

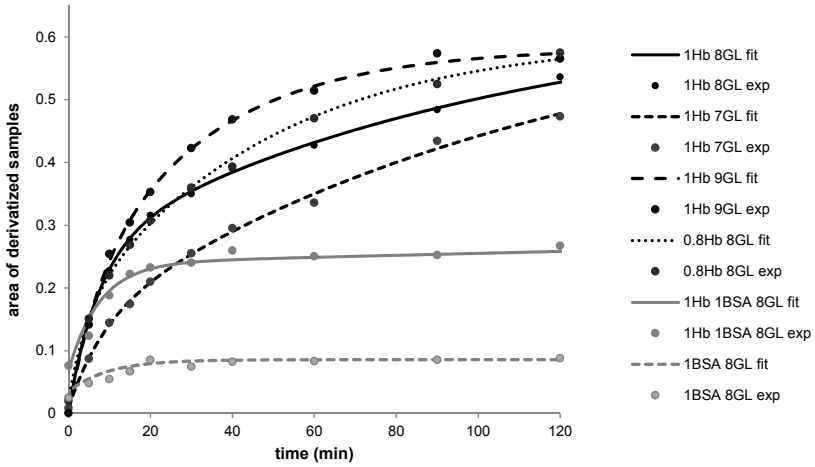

Figure 11. Time course evolution of derivatized Hb at various reactant concentrations.

Table 1. Derivatized area of the analyzed samples and fitted parameter values.

Sample	***Derivatized area after 120 min of reaction (a.u · time.)***	***A_1 (a.u.)***	***t_1 (min)***	***A_2 (a.u.)***	***t_2 (min)***	***R^2***
1 mM Hb + 7 mM GL	114	0.53	117.28	0.13	8.43	0.99
1 mM Hb + 8 mM GL	125 *	0.27	8.08	0.53	188.22	0.99
1 mM Hb + 9 mM GL	140	0.17	6.79	0.41	31.34	0.99
0.8 mM Hb + 8 mM GL	132	0.17	6.28	0.45	66.22	0.99
1 mM Hb + 1 mM BSA + 8 mM GL	129	0.09	10.7	0.09	10.7	0.97
1 mM BSA + 8 mM GL	40	1154.36	2.17	0.06	10.11	0.91

**for this mixture, areas at 180 and 240 min were also recorded; of 198 and 155 a.u. · time, respectively*

Figure 12 compares chromatograms of samples obtained by mixing the reactants manually and when using the mixer, at different time intervals. It is important as well as useful that the derivatized area is larger in the case of automatically mixed reactants. The better homogeneity of the reaction mixture also provides a better uniformity of the resulted aggregates (in terms of molecular weight), and also leads to better reproducibility.

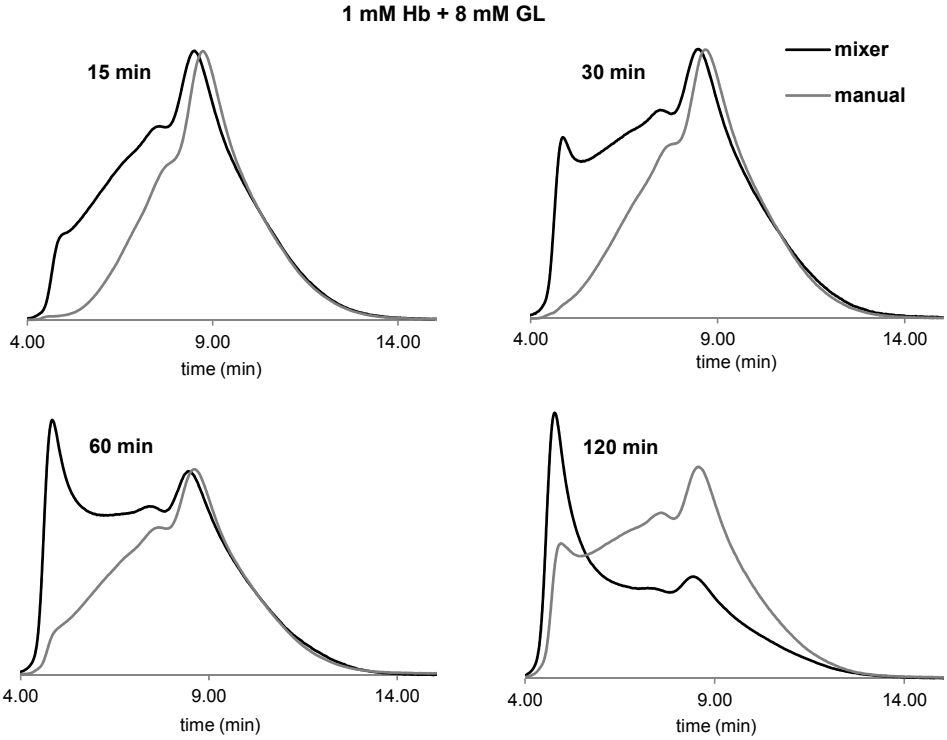

Figure 12. Size-exclusion chromatograms of Hb derivatized with 8 mM GL at different time intervals after mixing the reactants either manually, or with the mixer.

CONCLUSIONS

The kinetics of the derivatization reaction of hemoglobin and albumin with glutaraldehyde have been revisited, in order to establish the optimal conditions (time of reaction, concentration of protein and derivatization agent) for which the final product would be a reasonable candidate for blood substitutes. The use of an automated mixing device (with a tens-of-milliseconds mixing time) allows for polymers with a distinctly more reproducible molecular weight, compared with manual mixing under magnetic stirring. The importance of

dedicated mixing devices for protein derivatization, discussed here for the glutaraldehyde-based reticulation of hemoglobin and albumin, is likely an observation valid more generally for performing relatively fast (bio)chemical reactions.

EXPERIMENTAL SECTION

Mixer. The mixer is built from a nonporous redox-inert material, which may be metal or plastic. Its constraints are: (1) it should be impermeable and (2) should not be oxidized by water and oxygen. In order for the mathematical model to embed the key issues relevant for building a mixer relevant for blood substitute solutions, two aqueous solutions were considered - GL (0.1% glutaraldehyde) and Hb (3.2% hemoglobin), and the initial conditions shown in Table 2 were imposed.

Table 2. Experimental conditions for the mixer building.

Parameters	***Value***
Glutaraldehyde final concentration	0.1 [g/l]
Hemoglobin final concentration	16 [g/l]
Diffusion coefficient (D_{GL-Hb})	$4.5*10^{-9}$ m^2/s
Density (ρ_{GL}, ρ_{Hb})	$\rho_{GL} = \rho_{Hb} = 1$ kg/m^3
Dynamic viscosity (μ_{GL}, μ_{Hb})	$\mu_{GL} = \mu_{Hb} = 1$ mPa*s
Temperature	4˚C
Flow rate (total)	Q = 1l/h (may vary as needed)
Pressure drop	1 atm
Residence time of the mixed substance	100 ms

Hemoglobin purification. Bovine hemoglobin was purified by following the general protocol of Antonini and Brunori [18]. Concentrations in the text are given *per* heme rather than tetramer. Native, non-derivatized hemoglobin or bovine serum albumin is hereafter referred to as “nHb” and “nBSA”, respectively.

Protein derivatization. PolyHb and copolyHb-BSA were obtained by mixing a nHb solution with or without a BSA (fraction V, Sigma, Germany) solution, with glutaraldehyde (Sigma, Germany) at 4ºC, at concentrations indicated in text. The reaction was stopped by addition of NaBH4 in equimolar amount to the glutaraldehyde. The borohydride reduces imine bonds to stable amines and also quenches excess carbonyl groups. After quenching, the reaction mixtures were dialyzed against 20 mM Tris buffer, 150 mM NaCl at pH 7.4, to remove excess $NaBH_4$ and side-products, respectively [7,9].

Mixing procedures. The samples were mixed either manually, using the tip of the automated pipette upon addition of the GL to the protein solution in a 1.5-mL reaction vessel, or by using a purpose-designed mixer. In the latter case, the protein and GL solutions are introduced into two different syringes, the fluids being then directed towards the mixing chamber, through separate tubes driven by a mobile plate with a constant speed. Here, the reactants are mixed in a ratio decided by the diameters of the tubing and syringes (in all experiments this was 1:1), allowing attainment of a homogeneous reaction mixture (see Figure 13).

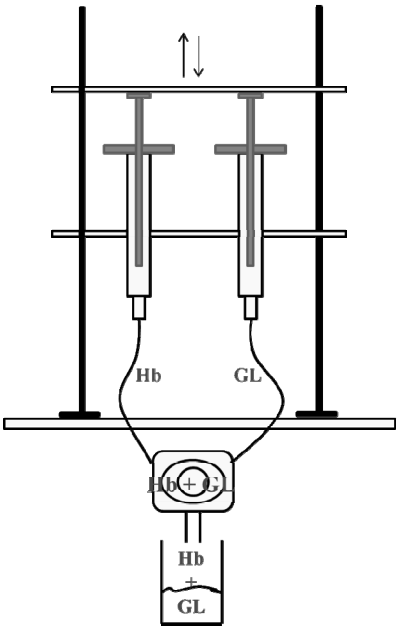

Figure 13. Schematic representation for the mixing device employed for hemoglobin polymerization.

***SDS-PAGE*.** The polymerization yield was assessed using 15% SDS-PAGE (sodium dodecyl sulfate polyacrylamide gel electrophoresis). The gels generally consist of acrylamide, bisacrylamide, SDS, Tris-Cl buffer with adjusted pH, ammonium persulfate and TEMED (N,N,N',N'-Tetramethyl ethylenediamine).

Fast protein liquid chromatography (FPLC, GE Healthcare, Sweden) was employed for determining the percentage of total cross-linked Hb. A Superdex 200 5/150 GL size exclusion column with 0.25 mL/min flow rate was used, with a mobile phase of 20 mM Tris buffer, 150 mM NaCl at pH 7.4. The absorbance was monitored at 280 nm. Samples retrieved from the

reaction mixture at various times in the interval of 0 – 120 minutes, were each analyzed on the analytical gel-filtration column. The areas under the peaks corresponding to derivatized hemoglobin were used as measure of the polymerization degree and apparent molecular weight.

UV-VIS spectra were recorded on a Cary 50 (Varian, Inc) instrument in PBS 7.4.

ACKNOWLEDGMENTS

Financial support from the Romanian Ministry for Education and Research (grant PCE 488/2012) is gratefully acknowledged. Florina Scurtu also thanks the Babeş-Bolyai University of Cluj-Napoca for financial support by means of the Sectoral Operational Programme for Human Resources Development 2007-2013, co-financed by the European Social Fund, under the project POSDRU/159/1.5/S/132400 - "Young successful researchers – professional development in an international and interdisciplinary environment".

REFERENCES

1. A. I. Alayash, *Nature Reviews. Drug Discovery*, **2004**, *3*, 152-159.
2. C. L. Modery-Pawlowski, L. T. Lewis, V. Pan, A. Sengupta, *Biomacromolecules,* **2013**, *14*, 939-948.
3. A. I. Alayash, R. E. Cashon, *Annals of the New York Academiy of Sciences*, **1994**, *738*, 378-381.
4. A. I. Alayash, *Free Radical Biology and Medicine*, **1994**, *16*, 137-138.
5. J. G. Riess, *Chemical Reviews*, **2001**, *101*, 2797-2919.
6. T. M. S. Chang, *Artificial Organs,* **2004**, *28*, 789-794.
7. F. Deac, A. Todea, R. Silaghi-Dumitrescu, "Glutaraldehyde derivatization of hemoglobin: a potential blood substitute", In *Metal Elements in Environment, Medicine and Biology Tome IX* (Silaghi-Dumitrescu, R.; Garban, G., Eds.), pp 165-173, Cluj University Press, Cluj-Napoca, Romania, **2009**.
8. F. Scurtu, A. Mot, R. Silaghi-Dumitrescu, *Pharmaceuticals*, **2013**, *6*, 867-880.
9. F. Scurtu, O. Zolog, B. Iacob, R. Silaghi-Dumitrescu, *Artificial Cells, Blood Substitutes, and Immobilization Biotechnology*, **2014**, *42*, 13-17.
10. F. Deac, B. Iacob, E. Fischer-Fodor, G. Damian, R. Silaghi-Dumitrescu, *Journal of Biochemistry* (Tokyo), **2011**, *149*, 75-82.
11. B. Iacob, F. Deac, D. Cioloboc, G. Damian, R. Silaghi-Dumitrescu, *Artificial Cells, Blood Substitutes, and Immobilization Biotechnololy*, **2011**, *39*, 293-297.
12. O. Zolog, A. Mot, F. Deac, A. Roman, E. Fischer-Fodor, R. Silaghi-Dumitrescu, *The Protein Journal*, **2011**, *30*, 27-31.
13. W. H. Chang, Y. Chang, Y. C. Chen, H. W. Sung, *Artificial Cells, Blood Substitutes, and Immobilization Biotechnology*, **2004**, *32*, 243-262.
14. H.-W. Kim, A. Greenburg, *Artificial Organs*, **2004**, *28*, 813-827.

15. A. I. Alayash, *Clinics in Laboratory Medicine*, **2010**, *106*, 76-85.
16. A. I. Alayash, *Trends in Biotechnology*, **2014**, *32*, 177-185.
17. A. N. Fedorov, V. S. Iarochkin, V. B. Koziner, A. A. Hachaturian, G. I. Rozenberg, *Doklady Akademii Nauk SSSR*, **1978,** *243*, 1324-1326.
18. E. Antonini, M. Brunori, “Hemoglobin and Myoglobin in their Reaction with Ligands”, North-Holland, Amsterdam, **1971**.

STUDIA UBB CHEMIA, LXIV, 2, Tom II, 2019 (p. 435-446)
(RECOMMENDED CITATION)
DOI:10.24193/subbchem.2019.2.37

Dedicated to Professor Ioan Bâldea on the Occasion of His 80th Anniversary

A DFT INVESTIGATION OF A POLYCYCLIC STANNYLENE MODEL; STRUCTURAL CHARACTERIZATION AND STABILITY ASSESSMENT

IONUT-TUDOR MORARU[a], GABRIELA NEMES[a*]

ABSTRACT. The first part of this study aims at evaluating by DFT methods the structural features and the stability of a stannylene derivative, Sn(II) being included into an extended polycyclic framework. Natural Bond Orbital (NBO) analyses are performed in order to understand bonding patterns and also the role of secondary electronic effects on the stability of this unsaturated derivative. In the second part, the coordination of NHC and THF ligands to the Sn(II) atom of the polycyclic stannylene species are investigated. The strength of these interactions and the nature of the chemical bonds formed are also discussed.

Keywords: *stannylene, stilbene, DFT calculations, NBO analyses.*

INTRODUCTION

Metallylenes, the heavier analogues of carbenes, have gained an increased attention in the last period, due to their possible applications in catalysis or as precursors in the synthesis of new polymers with controlled properties.

Starting with the first transient metallylene, these compounds also attracted interest from the fundamental point of view, since they display several contrasting features compared to those of carbenes. Previous studies performed on this class of compounds featured their characteristic electronic configuration involving an inert lone pair (LP) situated in the n*s* orbital and a vacant *p* orbital on the E (Si, Ge, Sn) atom [1-5]. Therefore, they can in principle act as both Lewis acids and Lewis bases. As a result of their amphoteric properties, metalylenes are highly reactive, short-lived and difficult to characterize, unless stabilization by steric bulk or electron donating groups is achieved. [6-8]

[a] *Babeş-Bolyai University, Faculty of Chemistry and Chemical Engineering, 11 Arany Janos str., RO-400028, Cluj-Napoca, Romania*
** Corresponding author: gabriela.nemes@ubbcluj.ro*

The singlet-triplet energy differences for H_2E species (E = C, Si, Ge, Sn, Pb) were previously evaluated by *ab-initio* calculations. For all heavier analogues, the singlet state is more stable, with calculated gaps of 16.7 kcal/mol for silylene, 21.8 kcal/mol for germylene, 24.8 kcal/mol for stanylene and 34.8 kcal/mol for plumbylene, while in the case of H_2C: carbene, the singlet-triplet energy difference was estimated as -14.0 kcal/mol. [9] The same study additionally emphasizes that the relative stabilities of the singlet species R_2E: (E = C, Si, Ge, Sn, Pb; R = alkyl or aryl), related to their corresponding dimers, $R_2E=ER_2$, increases in the series: C < Si < Ge < Sn < Pb.

Stabilization of metallylenes can be achieved either thermodynamically and/or kinetically. More precisely, kinetic stabilization can be accomplished by introduction of bulky substituents onto the molecule which can block the highly reactive vacant *p* orbital, while thermodynamic stabilization can be achieved by coordination to different organic, organometallic or inorganic fragments [10, 11].

If the steric hindrance is insufficient, the metallylene will be subjected to self-oligomerization, leading to the corresponding dimer or even polymers. [3]

Starting with the first completely characterized tin(II) derivative stabilized by the tridentate 2,6-bis[(dimethylamino)methyl]phenyl group reported by van Koten in 1989 [12], a new topic, that of pincer ligand stabilized metallylenes, was implemented. The majority of the pincer ligands reported in literature as being used for stabilizing metalylenes consist in N,C,N-pincer type ligands [13-17] while only few examples of O,C,O-pincer ones were successfully reported until now. [18-21]

Since the synthesis of the first N-heterocyclic carbene, 1,3-di-1-adamantyl-imidazol-2-ylidene, noted as NHC throughout the text [22], these species were intensively used in stabilization of metalylenes due to their electronic proprieties, namely the strong N→C(carbene) π-donation. [23] Other carbenes used as stabilizing co-ligand of metallylenes are benzimidazole [24] or acyclic derivatives [25], but the Arduengo type imidazole-based carbenes are much widely used due to their enhanced stability. While NHC–germylenes have numerous examples reported to date [26-29], their reactivity is less investigated, in opposing trends to those of NHC–silylene analogues, for which fewer examples are known. [30-32]. In the case of NHC-stabilized stannylenes, only few examples were reported in the literature [33, 34], their reactivity being less investigated because of their low stability in solution.

In order to increase the thermodynamic and kinetic stabilization of metallylenes, the phosphaalkenyl Mes*P=C< unit was connected to the NHC-germylene and NHC-stanylene derivatives [35, 36]. It is known that in the case of low coordinate species containing a heavy element of groups 14 and 15, with the Mes*P=C-E skeleton, the phosphaalkenyl moiety induces a stabilizing effect [37-40]. The newly stable phosphaalkenyl metalylenes were completely characterized and their reactivity was investigated [41-43].

In order to increase the stability of the heavier analogues of carbene, we have focused our recent research towards systems in which the germanium(II) or the tin(II) atom is included into a cycle, with prospects of aromaticity or *pseudo*-aromaticity. Based on our previous studies [44-46], we consider that the fluorenyl-metallylenes or metallapine derivatives (containing a stilbene group) will be thermodynamically stabilized due to electronic effects induced by extending the conjugation on the heterorganic cycle.

In this work we report a computational chemistry study concerning structural characterization and stability assessment of a polycyclic stannylene (the structure is shown in Figure 1, being further noted as **I**). In addition, possible formation of adducts between **I** and the NHC and THF ligands was also assessed.

RESULTS AND DISCUSSION

The structural features of a stannylene-pine derivative **I** are investigated by DFT calculations. The B3LYP hybrid functional and its long range dispersion corrected form, B3LYP-D3, are employed within this study in order to assess whether dispersion corrections influence the computed data.

The optimized molecular structures of **I**, performed with both B3LYP and B3LYP-D3 functionals, are shown in Figure 1. The flanking fused phenyl rings and the seven membered tin-containing heterocycle are *quasi*-planar in the molecular geometry obtained with the B3LYP functional, a calculated value of about 177.5° being obtained for the C3-C1-C2-C4 dihedral (see Figure 1a and Table 1). On the other hand, the calculation performed with B3LYP-D3 functional reveal a bent molecular structure minimum, the lateral phenyl groups being displaced cis with respect to the central stannepin ring. Nevertheless, both structures depicted in Figure 1 display similar distances for the Sn-C chemical bonds (in-between 2.18 and 2.19 Å), while for the C-Sn-C bonding angle, calculated values are close to 100° in both cases (see Table 1).

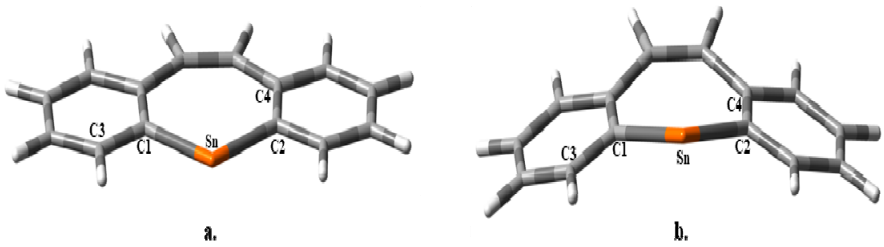

Figure 1. Molecular structures of stannylene **I** optimized at (**a**) B3LYP/Def2-TZVP and (**b**) B3LYP-D3/Def2-TZVP levels of theory.

Energy differences between the planar and the angular geometries of **I** are calculated with both B3LYP and B3LYP-D3 functionals. As in both cases the results are roughly identical in terms of calculated bond lengths and bonding angles, we appreciate that the planar structure achieved at the B3LYP level of theory represents a good approximation for a merely *single-point* energy calculation with B3LYP-D3 functional (without any geometry optimization), in order to determine the magnitude of the planar-angular gap (bending potential) of **I** at B3LYP-D3 level. A similar procedure is also accomplished for the B3LYP functional. Calculated energy gaps between planar and bent structures exhibit low values in both cases (0.1 kcal/mol at both B3LYP and B3LYP-D3 levels), underlining the ability of the Sn atom towards flipping between the two sides of the stilbene moiety.

Table 1. Selected geometrical parameters for stannylene **I**

Parameter	**B3LYP**	**B3LYP-D3**
Sn-C1 (Å)	2.181	2.185
Sn-C2 (Å)	2.181	2.185
C1-Sn-C2 (°)	102.8	100.1
C3-C1-C2-C4 (°)	177.4	156.0

*The atom labeling for tabulated parameters is in agreement with the one illustrated in Figure 1.

Natural Bond Orbital (NBO) calculations reveal weak stabilization effects occurring from the stilbene moiety towards the vacant *p* orbital on the Sn atom. Figure 2 depicts the NB orbitals involved in these charge transfer interactions. The overall stabilization energy, consisting in two electronic departures of the type π(C-C)→*p*(Sn) for each of the investigated species illustrated in Figure 2, has calculated values of 12.5 kcal/mol in the case of planar geometry (B3LYP) and of 15.9 kcal/mol for the angular one (B3LYP-D3).

Data presented throughout this study relies on calculations performed on the singlet state of stannylene **I**. In agreement with previous studies, the NBO analyses performed on **I** displays a mainly *s* character (82% *s*, 18% *p*) for the LP on the Sn atom. Nevertheless, the singlet-triplet gap (ΔE_{ST}) is also evaluated. For both functionals the singlet state of **I** is considerably more stable than the triplet one. Calculated ΔE_{ST} amounts are of 37.2 kcal/mol (B3LYP) and respectively 37.3 kcal/mol (B3LYP-D3), zero-point energy corrections (ZPE) being included in the energetic comparisons. However, these values are with about 12.5 kcal/mol higher than previous *ab-initio* data reported for H_2Sn [9]. The enhanced stabilization of the singlet state for the cyclic stannylene **I**, compared to H_2Sn, can be understood in terms of π(C-C)→*p*(Sn)

secondary electronic effects (Figure 2). The increase in ΔE_{ST} for the cyclic species is in line with the calculated amount of the stabilization energy corresponding to the donor-acceptor interactions (12.5-15.9 kcal/mol, see the NBO section above).

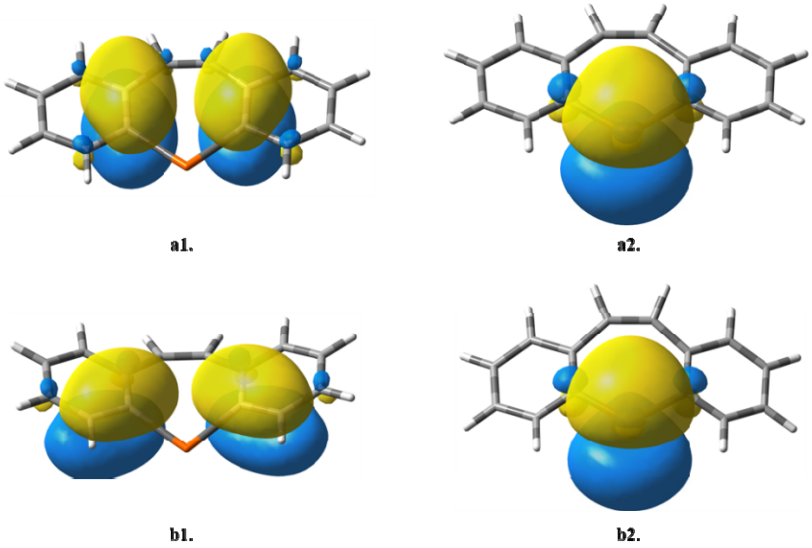

Figure 2. NB orbitals involved in charge transfer interactions in **I** for calculations performed at B3LYP/Def2-TZVP (**a1** and **a2**) and B3LYP-D3/Def2-TZVP (**b1** and **b2**) DFT levels of theory. **a1**) π(C-C) donor NBOs on the planar structure; **a2**) *p*(Sn) acceptor NBO for planar geometry; **b1**) π(C-C) donor NBOs on the angular structure; **b2**) *p*(Sn) acceptor NBO for bent geometry.

Another key aspect to be taken into account when questioning stability of targeted derivatives consists in the assessment of the HOMO-LUMO gap. [47] Large gaps indicate enhanced stabilization, highlighting thus considerable energy separation between the ground and the first excited state. In the case of **I**, calculated HOMO-LUMO separation has values of 3.33 eV (76.8 kcal) at B3LYP level and of 3.27 eV (75.3 kcal) at B3LYP-D3. In order to gain relevant comparisons, the HOMO-LUMO gap for the NHC carbene is additionally calculated at the same levels of theory, NHC serving as a well know example of stable unsaturated species.

The calculated HOMO-LUMO separation for NHC is of 6.18 eV (142.7 kcal) at both B3LYP and B3LYP-D3 levels, value that is noticeably higher than those computed for **I**.

Figure 3 illustrates the frontier MOs computed for **I** with both functionals. In both cases, HOMO is predominantly located on the stilbene moiety, with small contributions from the Sn atom. Within the angular structure, the contribution of the Sn atom to HOMO is noticeably higher than in the case of the planar geometry. Regarding LUMO, it is located to a large extent on the Sn atom for both planar and angular structures, and consists in a vacant *p* orbital.

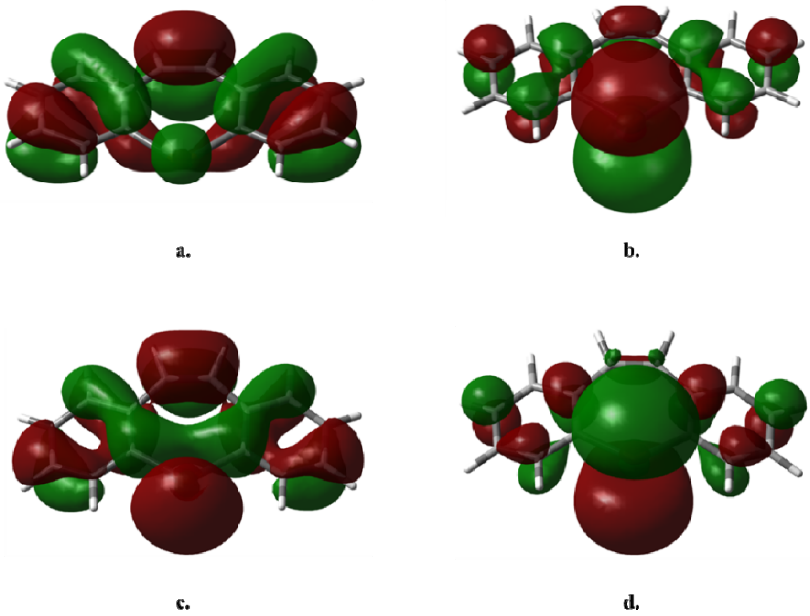

Figure 3. Frontier MOs calculated for **I**: **a)** HOMO for planar structure (B3LYP/Def2-TZVP); **b**) LUMO for planar molecule (B3LYP/Def2-TZVP); **c)** HOMO for bent geometry (B3LYP-D3/Def2-TZVP); **d**) LUMO for angular structure (B3LYP-D3/Def2-TZVP).

Stabilization of stannylene I with NHC and THF ligands

Blocking the unoccupied *p* orbital of metallylenes with strong Lewis bases represents one of the know reactions used to stabilize these species. Owing to the notoriety of the NHC carbene towards stabilizing unsaturated derivatives by enhanced electron donation, intermediates of the type **I-NHC** (Figure 4) were considered within this DFT study.

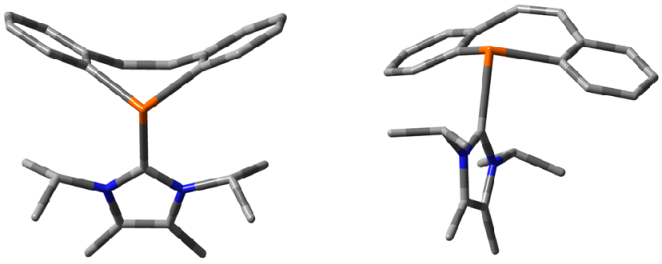

Figure 4. Molecular geometries of **I-NHC** species for: **a)** isomer **Ia–NHC**, the NHC species and the flanking phenyl rings are oriented in *trans*; **b)** isomer **Ib–NHC**, the NHC group and the lateral phenyl rings are disposed in *cis*; hydrogen atoms were omitted for clarity reasons.

In addition, the molecular geometries of **I-THF** adducts (Figure 5) were computed. The reason behind choosing THF as another possible stabilizing ligand was of interest for the actual work because (i) THF represents a widely used solvent in organometallic chemistry and thus it is worth knowing its stabilizing effects on metallylenes, and also (ii) for gaining a broader overview on the bonding pattern in cyclic stannyllenes.

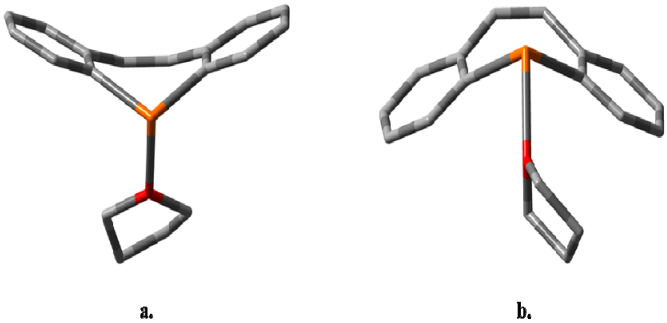

Figure 5. Molecular structures of **I-THF** species for: **a)** isomer **Ia–THF**, the THF ligand and the phenyl rings are oriented in *trans* with respect to the central heterocyle; **b)** isomer **Ib–THF,** the THF ligand and the phenyl groups are oriented in *cis* with respect to the central heterocyle; hydrogen atoms were omitted for enhanced clarity.

For both **I-NHC** and **I-THF** species, two different isomers are considered for each case: one isomer in which the flanking phenyl groups of the polycyclic stannyllene and the NHC/THF ligands are disposed in *trans*, and another one in which they are oriented in *cis* (see Figures 4 and 5). The molecular structures delivered by both B3LYP and B3LYP-D3 functionals are very similar

for each of the **I-NHC** and **I-THF** adducts. Therefore, only one set of structures (one *cis* and one *trans* isomer) are illustrated in each of the cases, and not two different ones as was in the case of **I**, for which the two employed functionals lead to two different geometries.

The calculated energy differences between the investigated isomers are small (ZPE included), with the *trans* isomer being the most stable one in all cases. For instance, for **I-NHC** species, calculated gaps are of 1.6 kcal/mol at B3LYP level and of 1.7 kcal/mol for the dispersion corrected functional, B3LYP-D3. In the case of **I-THF**, calculated *cis-trans* energy differences are of 0.7 kcal/mol for B3LYP and of 1.3 kcal/mol for B3LYP-D3.

Table 2 presents some key structural parameters calculated for **I-NHC** and **I-THF** adducts. As it can be noticed, the values computed with B3LYP are slightly higher than those computed with B3LYP-D3. Nevertheless, differences are negligible for the chemical bonds, their lengths being found to be the same within 1/1000 Å for the Sn-C bonds, and within 1/100 Å in the case of Sn←C and Sn←O coordinate bonds. Angles differ between B3LYP and B3LYP-D3 by at most 0.6° in the case of **I-NHC**, and by at most 1.2° for **I-THF**. In comparison with stannylene **I**, Sn-C bonds formed with the flanking phenyl groups are slightly elongated upon coordination of NHC (up to 0.054 Å at B3LYP level and to 0.052 Å at B3LYP-D3) and of THF (up to 0.037 Å at B3LYP level and to 0.035 Å at B3LYP-D3). A decrease of the C-Sn-C angle is also noticed in all cases (see Tables 1 and 2 for comparisons).

Table 2. Selected geometrical parameters for the calculated systems **I-NHC** and **I-THF**

I-NHC	**B3LYP**		**B3LYP-D3**		**I-THF**	**B3LYP**		**B3LYP-D3**	
	trans	***cis***	***trans***	***cis***		***trans***	***cis***	***trans***	***cis***
Sn←C(NHC)(Å)	2.398	2.418	2.387	2.403	Sn←O(THF)(Å)	2.438	2.434	2.424	2.420
Sn-C (Å)	2.235	2.228	2.237	2.231	Sn-C (Å)	2.210	2.218	2.212	2.220
C-Sn-C (°)	92.9	97.4	92.3	97.6	C-Sn-C (°)	97.0	94.4	95.9	92.2

An energetic index for the Sn←C (NHC) and Sn←O (THF) bonds, based on the second order perturbation analysis of the NBO technique, is presented in Table 3. Note that the second order perturbation energy for the Sn←C (NHC) bonding is not available in the case of the *trans* isomer of **I-NHC** (see Table 3), being regarded by the NBO analyses as rather covalent, and not as a “classical” donor-acceptor interaction usually displayed in the output of the NBO calculations. However, the contribution of Sn to the Sn←C bond is small: ~18% in the case of both B3LYP and B3LYP-D3. According to the computed data, the strength of Sn←C bonding is far higher

than that of Sn←O bonds. However, these trends are in line with previous DFT studies concerning the stabilization of posphaalkenyl germylenes with various Lewis bases (NHC, THF, Et_2O) [42].

Table 3. NBO data for Sn←C (NHC) and Sn←O (THF) chemical bonds of **I-NHC** and **I-THF** adducts

Coordinative Bond	B3LYP		B3LYP-D3	
	trans	***cis***	***trans***	***cis***
Sn←C (NHC) (kcal mol^{-1})	–	117.2	–	120.0
Sn←O (THF) (kcal mol^{-1})	30.3	30.4	30.5	31.0

For the **I-THF** type adducts, NBO calculations also suggest the occurrence of weak intermolecular hyperconjugative interactions of the type p(O)→σ^*(Sn-C). The calculated energies of these effects range in-between 3.7 and 4.4 kcal/mol. Nonetheless, these kinds of hyperconjugative effects were shown to play important roles in molecular stannoxanes [48].

CONCLUSIONS

The structural features and the stability of a stannylene-pine type **I** species were investigated using DFT calculations. NBO analyses revealed that the extended cyclic framework of investigated stannylene assures an increased stabilization compared to acyclic counterparts, due to charge transfer interactions of the type π(C-C)→p(Sn). The enhanced stability is reflected in the singlet-triplet gap which in terms is considerably higher than the one previously reported for H_2Sn species. Concerning the calculated HOMO-LUMO gap, DFT data revealed a separation of about 3.3 eV, which is significantly lower than the one calculated for the reference NHC species, which had a gap of 6.2 eV. Further stabilization can be achieved *via* coordination, the role of NHC and THF ligands being assessed in this respect. The strength of Sn←C (NHC) interaction is significantly higher than that of Sn←O (THF) bond, in line with previous DFT studies on germylenes. Nevertheless, the stabilization with THF is undoubtable, being at the same time of great practical importance, since THF serves as a widely used solvent in metallylene chemistry.

Finally, the present study compared the geometries delivered by B3LYP with its dispersion corrected form, B3LYP-D3. According to the DFT data, a good agreement of both bond length and angles was achieved among the two employed functionals, highlighting thus that the effect of the D3 long-range dispersion corrections on the computed data is negligible in the present case.

EXPERIMENTAL SECTION

Computational Details

Density Functional Theory (DFT) calculations were performed with the *Gaussian 09* software package [49]. Geometries were fully optimized in the gas phase without any symmetry constraints, employing the B3LYP [50] hydrid functional and also its dispersion corrected form, B3LYP-D3 (with D3 standing for Grimme's dispersion corrections [51]), and the valance triple-zeta Def2-TZVP basis set [52]. Stuttgart effective core potentials (ECPs) were used for computing the relativistic core electrons of the Sn atom. The ECPs are included in the implementation of the basis set in *Gaussian 09*. The optimization criteria were set to tight in all cases. Vibrational frequencies were computed in order to characterize the nature of the stationary points, and also used for calculating zero-point energy corrections (ZPE). According to the vibrational analyses, all optimized geometries correspond to minima. For all calculations, the integration grid used was of 99 radial shells and 950 angular points for each shell (99,950), precisely the "ultrafine" grid within *Gaussian 09*. Natural Bond Orbital (NBO) [53] *single-point* calculations were carried out on the optimized molecular structures, in order to shed light on the structural features and on the nature of the chemical bonding in the analyzed species. The *Gaussian 09* implemented version of the *NBO program* was used.

ACKNOWLEDGMENTS

This work was supported by a grant of Ministery of Research and Innovation, CNCS-UEFISCDI, project number PN-III-P4-ID-PCE-2016-0351, within PNCDI III.

REFERENCES

1. W. P. Neumann, *Chem. Rev.,* **1991,** *91*, 311-334.
2. J. Barrau; G. Rima, *Coord. Chem. Rev.,* **1998,** *178-180*, 593-622.
3. Y. Mizuhata; T. Sasamori; N. Tokitoh, *Chem. Rev.,* **2009,** *109*, 3479-3511.
4. F. Lollmahomed; L. A. Huck; C. A. Harrington; S. S. Chitnis; W. J. Leigh, *Organometallics,* **2009,** *28*, 1484-1494.
5. P. A. Rupar; V. N. Staroverov; K. M. Baines, *Science,* **2008,** *322*, 1360-1363.
6. S. Nagendran; H. W. Roesky, *Organometallics,* **2008,** *27*, 457-492.
7. S. K. Mandal; H. W. Roesky, *Chem. Commun.,* **2010**, 6016-6041.
8. M. Asay; C. Jones; M. Driess, *Chem. Rev.,* **2011**, *111*, 354-396.
9. G. J. Trinquier, *Am. Chem. Soc.,* **1990**, *112*, 2130-2131.
10. P. P. Power, *Chem. Re*v., **1999**, *99*, 3463-3504.
11. J. Barrau; J. Escudié; J. Satgé, *Chem. Rev.,* **1990**, *90*, 283-319.
12. J. T. B. H. Jastrzebski; P. A. Van der Schaaf; J. Boersma; G. Van Koten; M. C. Zoutberg; D. Heijdenrijk, *Organometallics,* **1989**, *8*, 1373-1375.

13. M. P. Bigwood; P. J. Corvan; J. J. Zuckerman, *J. Am. Chem. Soc.,* **1981**, *103*, 7643-7646.
14. C. Bibal; S. Mazières; H. Gornitzka; C. Couret, *Angew. Chem. Int. Ed*., **2001**, *40*, 952-954.
15. S.-P. Chia; H.-X. Yeong; C.-W. So, *Inorg. Chem.,* **2012**, *51*, 1002-1010.
16. S. Khan; P. P. Samuel; R. Michel; J. M. Dieterich; R. A. Mata; J.-P. Demers; A. Lange; H. W. Roesky; D. Stalke, *Chem. Commun.,* **2012**, *48*, 4890-4892.
17. B. Kašná; R. Jambor; M. Schürman; K. Jurkschat, *J. Organomet. Chem.,* **2008**, *693*, 3446-3450.
18. M. El Ezzi; R. Lenk; D. Madec; J.-M. Sotiropoulos; S. Mallet-Ladeira; A. Castel, *Angew. Chem. Int. Ed.,* **2015**, *127*, 819-822.
19. N. Deak; P. M. Petrar; S. Mallet-Ladeira; L. Silaghi-Dumitrescu; G. Nemeş; D. Madec, *Chem. - Eur. J.,* **2016**, *22*, 1349-1354.
20. N. Deak; O. Thillaye du Boullay; I.-T. Moraru; S. Mallet-Ladeira; D. Madec; G. Nemes, *Dalton Trans.,* **2019**, *48*, 2399-2406.
21. N. Deak; I.-T. Moraru; N. Saffon-Merceron; D. Madec; G. Nemes, *Eur. J. Inorg. Chem.*, **2017**, *36*, 4214-4220.
22. A. J. Arduengo; R. L. Harlow; M. Kline, *J. Am. Chem. Soc.,* **1991,** *113*, 361-363.
23. D. Nemcsok; K. Wichmann; G. Frenking, *Organometallics,* **2004,** *23*, 3640-3646.
24. F. E. Hahn; L.Wittenbecher; R. Boese; D. Bläser, *Chem. Eur. J.* **1999,** *5*, 1931-1935.
25. R. W. Alder; P. R. Allen; M. Murray; A. G. Orpen, *Angew. Chem. Int. Ed. Engl.,* **1996,** *35*, 1121-1122.
26. A. J. Arduengo; R. H. V. Dias; J. C. Calabrese; F. Davidson, *Inorg. Chem.,* **1993,** *32*, 1541-1542.
27. A. Sidiropoulos; C. Jones; A. Stasch; S. Klein; G. Frenking, *Angew. Chem. Int. Ed.,* **2009,** *48*, 9701-9704.
28. P. A. Rupar; V. N. Staroverov; K. M. Baines, *Organometallics,* **2010,** *29*, 4871-4881.
29. A. C. Filippou; O. Chernov; B. Blom; K. W. Stumpf; G. Schnakenburg, *Chem. Eur. J.,* **2010,** *16*, 2866-2872.
30. R. S. Ghadwal; H. W. Roesky; S. Merkel; J. Henn; D. Stalke, *Angew. Chem. Int. Ed.,* **2009,** *48*, 5683-5686.
31. A. C. Filippou; O. Chernov; G. Schnakenburg, *Chem. Eur. J.,* **2011,** *17*, 13574-13583.
32. H. Cui; C. Cui, *Dalton Trans.,* **2011,** *40*, 11937-11940.
33. K. C. Thimer; I. S. M. Al-Rafia; M. J. Ferguson; R. McDonald; E. Rivard, *Chem. Commun.,* **2009**, 7119-7121.
34. B. Bantu; G. M. Pawar; U. Decker; K. Wurst; A. M. Schmidt; M. R. Buchmeiser, *Chem. Eur. J.,* **2009,** *15*, 3103-3109.
35. D. Matioszek; T.-G. Kocsor; A. Castel; G. Nemes; J. Escudié; N. Saffon*, Chem. Commun.*, **2012**, *48*, 3629-3631.
36. T.-G. Kocsor; G. Nemes; N.Saffon; S. Mallet-Ladeira; D. Mandec; A. Castel; J. Escudié, *Dalton Trans*., **2014**, *43*, 2718-2721.
37. P. M. Petrar; R. Septelean; H. Gornitska; G. Nemes, *J. Organomet. Chem.*, **2015**, *787*, 14-18.
38. R. Septelean; G. Nemes; J. Escudié; I. Silaghi-Dumitrescu; H. Ranaivonjatovo; P. M. Petrar; H. Gornitzka; L. Silaghi-Dumitrescu; N. Saffon*, Eur. J. Inorg. Chem.*, **2009**, 628-634.

39. R. Septelean; H. Ranaivonjatovo; G. Nemes; J. Escudié; I. Silaghi-Dumitrescu; H. Gornitzka; L. Silaghi-Dumitrescu; S. Massou, *Eur. J. Inorg. Chem*., **2006**, 4237-4241.
40. G. Cretiu Nemes; H. Ranaivonjatovo; J. Escudié; I. Silaghi-Dumitrescu; L. Silaghi-Dumitrescu; H. Gornitzka; *Eur. J. Inorg. Chem*., **2005**, 1109-1113.
41. T.-G. Kocsor; D. Matioszek; G. Nemes; A. Castel; J. Escudié; P. Petrar; N. Saffon-Merceron; I. Haiduc, *Inorg. Chem.*, **2012**, 51, 7782−7787.
42. T.-G. Kocsor; P. Petrar; G. Nemeş; A. Castel; J. Escudié; N. Deak; L. Silaghi-Dumitrescu; *Comput. Theor. Chem.,* **2011**, 974, 117-121.
43. R. Septelean, I.-T. Moraru; T. Kocsor; N. Deak; N. Saffon; A. Castel; G. Nemes, *Inorg. Chim. Acta*, **2018**, *475*, 112-119.
44. L. Buta; R. Septelean; I.-T. Moraru; A. Soran; L. Silaghi-Dumitrescu; G. Nemes, *Inorg. Chim. Acta*, **2019**, *486*, 648-653.
45. P. M. Petrar; R. Septelean; H. Gornitska; G. Nemes, *J. Organomet. Chem.*, **2015**, *787*, 14-18.
46. G. Cretiu Nemes; L. Silaghi-Dumitrescu; I. Silaghi-Dumitrescu; J. Escudié; H. Ranaivonjatovo; K. C. Molloy; M. F. Mahon; J. Zukerman-Schpector, *Organometallics*, **2005**, *24*, 1134-1144.
47. R. Hoffmann; P. v. R. Schleyer; H. F. Schaefer, *Angew. Chem. Int. Ed*., **2008**, *47*, 7164 –7167.
48. I.-T. Moraru; P. M. Petrar; G. Nemes, *J. Phys. Chem. A,* **2017**, *121*, 2515-2522.
49. M. J. Frisch, G. W. Trucks, H. B. Schlegel, G. E. Scuseria, M. A. Robb, J. R. Cheeseman, G. Scalmani, V. Barone, G. A. Petersson, H. Nakatsuji, X. Li, M. Caricato, A. Marenich, J. Bloino, B. G. Janesko, R. Gomperts, B. Mennucci, H. P. Hratchian, J. V. Ortiz, A. F. Izmaylov, J. L. Sonnenberg, D. Williams-Young, F. Ding, F. Lipparini, F. Egidi, J. Goings, B. Peng, A. Petrone, T. Henderson, D. Ranasinghe, V. G. Zakrzewski, J. Gao, N. Rega, G. Zheng, W. Liang, M. Hada, M. Ehara, K. Toyota, R. Fukuda, J. Hasegawa, M. Ishida, T. Nakajima, Y. Honda, O. Kitao, H. Nakai, T. Vreven, K. Throssell, J. A. Montgomery, Jr., J. E. Peralta, F. Ogliaro, M. Bearpark, J. J. Heyd, E. Brothers, K. N. Kudin, V. N. Staroverov, T. Keith, R. Kobayashi, J. Normand, K. Raghavachari, A. Rendell, J. C. Burant, S. S. Iyengar, J. Tomasi, M. Cossi, J. M. Millam, M. Klene, C. Adamo, R. Cammi, J. W. Ochterski, R. L. Martin, K. Morokuma, O. Farkas, J. B. Foresman, D. J. Fox, *Gaussian 09*, revision *E.01*; Gaussian, Inc.: Wallingford, CT, 2009.
50. a) C. Lee, W. Yang, R. G. Parr. *Phys. Rev. B: Condens. Matter Mater. Phys*. **1988**, *37*, 785. b) A. D. Becke. *J. Chem. Phys.* **1993**, *98*, 5648-5652.
51. S. Grimme, J. Antony, S. Ehrlich, H. Krieg. *J. Chem. Phys*. **2010**, *132*, 154104.
52. a) A. Schafer, C. Huber, R. Ahlrichs, *J. Chem. Phys*. **1994**, *100*, 5829; b) D. Rappoport, F. Furche. *J. Chem. Phys.* **2010**, *133*, 134105.
53. a) F. Weinhold, C. R. Landis, *Valency and Bonding: A Natural Bond Orbital Donor-Acceptor Perspective*; Cambridge Univ. Press: Cambridge, U.K., **2005**. b) F. Weinhold, C. R. Landis, *Discovering Chemistry with Natural Bond Orbitals*; Wiley-Interscience: Hoboken, NJ., **2012**. c) F. Weinhold, C. R. Landis, E. G. Glendening, *Int. Rev. Phys. Chem.* **2016**, *35*, 399

STUDIA UBB CHEMIA, LXIV, 2, Tom II, 2019 (p. 447-456)
(RECOMMENDED CITATION)
DOI:10.24193/subbchem.2019.2.38

Dedicated to Professor Ioan Bâldea on the Occasion of His 80th Anniversary

INFLUENCE OF THE BALL MILLING PROCESS AND AIR SINTERING CONDITIONS ON THE SYNTHESIS OF $La_{0.7}Sr_{0.3}MnO_3$ CERAMICS

ENIKŐ BITAY[a*], ANA-MARIA PILBAT[b], EMIL INDREA[c], IRÉN KACSÓ[c], MÁRTON MÁTÉ[a], ATTILA LEVENTE GERGELY[a], ERZSÉBET VERESS[d*]

ABSTRACT. Conventional solid-state synthesis was used to produce mixed valence manganite $La_{0.7}Ca_{0.3}MnO_3$ (LCMO) from the mechanochemically activated mixture of the corresponding metal oxides. Prepared samples were characterized by XRD and SEM measurements. The results showed that it is possible to produce single phase LCMO perovskite after at least 2h of ball milling of the reaction mixture, followed by 1400 ºC sintering of the dry-pressed sample pellets. The prolonged milling time as well as the higher sintering temperature leads to further stabilization of crystal structure.

Keywords: *perovskite manganites, LCMO, mechanochemical synthesis, XRD, SEM, microstructural characterization*

INTRODUCTION

Due the practical significance of their outstanding magneto-electric properties (high temperature superconductivity, huge magneto-resistance, magneto-caloric and magneto-optical effect, spin-glass state), there is an ever growing interest towards the mixed oxidic ceramic systems containing transition

[a] *Sapientia Hungarian University of Transylvania, Faculty of Technical and Human Sciences, OP 9 CP 4, RO-540485 Targu-Mures, Romania*
[b] *Institute of Biochemistry, Biological Research Centre of the Hungarian Academy of Sciences, Temesvári krt. 62, H-6726 Szeged, Hungary*
[c] *National Institute for Research and Developement of Isotopic and Molecular Technologies, Donath Str. 65-103, RO-400293 Cluj, Romania*
[d] *Transylvanian Museum Society, Napoca Str. 2-4, RO-400750 Cluj, Romania*
** Corresponding authors: ebitay@ms.sapientia.ro; veresserzsebet@gmail.com*

metals and/or REE (perovskites, spinels, pyrochlores) [1]. The peculiar properties of these materials result from local micro-structural electric and magnetic phase transitions. The colossal magnetic resistant (CMR) behavior of perovskites, e.g., can be associated to the paramagnetic-ferromagnetic phase transition taking place when the temperature decreases below a critical value (the Curie point, T_C) [2].

Nowadays, study is mainly focused on CMR manganite perovskites of the general formula $A_{1-x}A'_xMnO_3$ (A - Me^{3+}, e.g. La and A' = Me^{2+}, e.g. Ca, Sr, Ba), where $La_{1-x}A'_xMnO_3$ ($0<x<1$) mixed manganites (parent compound: $LaMnO_3$) are the representative ("prototype") CMR ceramic family. Replacement of La with divalent cations oxidizes Mn^{3+} to Mn^{4+}, introduces holes in the Mn 3d band and induces the metallic and/or ferromagnetic behavior ("oxidative nonstoichiometry"). Considering the ease of the oxidation process $Mn^{3+} \rightarrow Mn^{4+} + 1\ e^-$, such a defective material is formed also by annealing $LaMnO_3$ in air or O_2 atmosphere. As insertion of excess oxygen is not possible in the perovskite structure, the global composition resulted due to the non-stoichiometric incorporation, *via* cation vacancies, will be $LaMnO_{3+\delta}$ [2]. In fact, the mixed manganites' general but correct crystallographic formula is $La_{1-x}Mn_{1-x}O_3$, $x = \delta/(3 + \delta)$.

The presence of mixed Mn^{3+} - Mn^{4+} valences gives rise to a double-exchange mechanism which, together with the charge ordering and the strong electron-phonon coupling (of a type of dynamic extended system version of the Jahn-Teller effect), are at the origins of: the sharp increasing of the electrical conductivity, the ferromagnetic-like behavior with reentrant spin-glass character, the large magnetoresistance, as well as the unusual magneto-caloric and magneto-elastic effects observed near the phase transition temperature. Divalent cation substitution for La is particularly effective in the doping range of $x \approx 0.2–0.4$ (20 - 40% holes/Mn ion), with the phase transition temperature exceeding room temperature in some cases (in the $La_{1-x}Ca_xMnO_3$ system T_C varies between 182 and 278 K) [3].

The special phase transition related magneto-electric properties of the manganites can be controlled through their synthesis method (and conditions), chemical composition, temperature, pressure, external magnetic field strength, hence offering them a great variety of applications.

This paper presents a preliminary XRD and SEM study of $La_{0.7}Ca_{0.3}MnO_{3+\delta}$ samples, prepared by the standard ceramic technology, with the aim of establishing the influence of the mechanical activation (the ball milling time) and the firing conditions (time and temperature) on the phase composition and the microstructural characteristics of the obtained ceramic material.

RESULTS AND DISCUSSION

$La_{0.7}Ca_{0.3}MnO_{3+\delta}$ synthesis and characterization

Mixed-valence manganites destined for practical applications are prepared most frequently as *thin films* (mostly by sol-gel dip coating, spray pyrolysis or electrochemical deposition; sputtering, PLD from ceramic targets, MOCVD or MBE) and *nanoparticles* (by sol-gel route, combustion – auto-combustion, precipitation from aqueous or non-aqueous solution, from reversal microemulsions). *Single crystals*, obtained usually by the flux melt technique, floating zone melting, hydrothermal synthesis, sol-gel method, etc. are used generally for research purposes [1, 4].

Bulk polycrystalline ceramics are most easily prepared by the standard ceramic method: repeated grinding, compaction and firing of the stoichiometric mixture of the oxide components, until a single-phase material is achieved. To obtain $La_{1-x}Ca_xMnO_3$, a mixture of La_2O_3, CaO and MnO_2 has to be grinded together, pelleted and fired in air for several hours. The process has to be repeated as many times as necessary, until the uniform single phase material is obtained. Since the method depends on the solid-state interdiffusion between the oxides, a finely powdered, well-compacted starting mixture has to be used. A variant of the method uses previously dried precursors (typically carbonates or oxalates) which decompose into highly reactive, ultrafine-grained oxides during a preliminary calcination. The starting oxide mixture can be obtained also in form of a precursor gel by wet chemical methods (co-precipitation), or from a citrate gel, by dissolving La_2O_3, $CaCO_3$ and $MnCO_3$ in HNO_3, then adding citric acid and ethylene glycol [4].

The present study investigates the ball milling time and firing conditions influence on reaction completion for the standard solid state synthesis of polycrystalline $La_{0.7}Ca_{0.3}MnO_{3+\delta}$ ceramics (LCMO).

For this purpose, four series of LCMO ceramics were prepared starting from the stoichiometric mixture of high purity of dried La_2O_3, MnO_2 and $CaCO_3$ (Table 1). Starting mixtures of identical composition were homogenized, pulverized and mechanically activated by 1, 2 and 3 hours of ball milling, then pelletized, and fired during 2 h at 1200ºC (samples 12.1, 12.2 and 12.3); 2 h at 1200ºC then 2 h at 1300ºC (samples 13.1, 13.2 and 13.3); and 2 h at 1200ºC, 2 h at 1300ºC, then 2 h at 1400ºC (samples 14.1, 14.2, 14.3, and respectively 14.1.L, 14.2.L, 14.3.L). In the end, excepting samples 14.1.L, 14.2.L and 14.3.L which were left in the oven to self-cool up to room temperature, all others were rapidly cooled by quenching.

Table 1. The list of prepared LCMO ceramics

Sample coding	Milling time (h)	Firing time (h)			
		1200^{0}C	1300^{0}C	1400^{0}C	1400^{0}C
12.1	1	2			
12.2	2	2			
12.3	3	2			
13.1	1	2	2		
13.2	2	2	2		
13.3	3	2	2		
14.1	1	2	2	2	
14.2	2	2	2	2	
14.3	3	2	2	2	
14.1.L*	1	2	2		2
14.2.L*	2	2	2		2
14.3.L*	3	2	2		2

*self-cooled

The LCMO phase formation for syntheses carried out according to the conditions presented in Table 1 was determined by XRD analysis. Phase purity of the ceramic samples (regarded as reaction efficiency) was estimated on the basis of the recorded diffractograms. The one corresponding to the 14.3.L sample is presented in Figure 1.

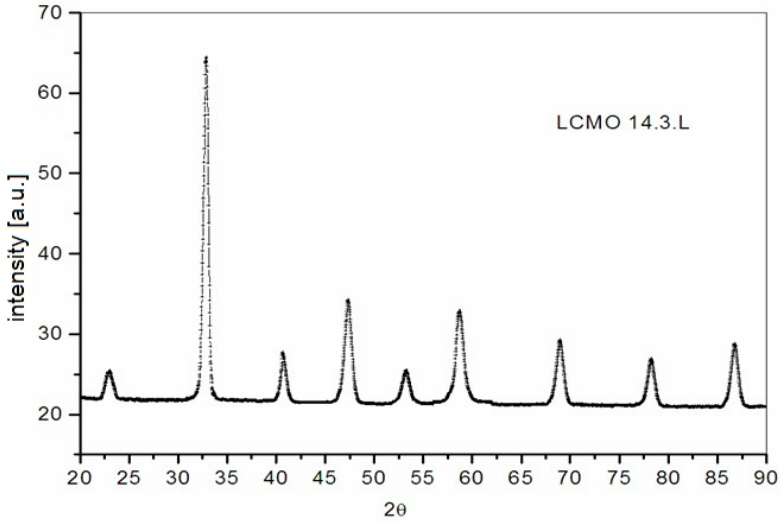

Figure 1. Experimental X-ray pattern of LCMO sample 14.3.L.

The microstructural data (lattice constants, unit cell volumes, density) were calculated by assuming an orthorombic crystal structure (space group *Pnma*, RGNR 62); Rietveld analysis was performed by using the PowderCell 2.4 program and the data set presented in Table 2 [5-8].

Table 2. Data set used for the Rietveld refinement*
(reference unit cell constants of LCMO and the atomic positions)

CELL	5.4650	7.7231	5.4798	90.000	90.000	90.000
La	57	1.0000	0.2500	1.0000	0.7000	(4c)
Ca	20	1.0000	0.2500	1.0000	0.3000	(*4c*)
Mn	25	0.0000	0.0000	0.5000		(*4b*)
O1	8	0.5000	0.2500	1.0000		(*4c*)
O2	8	0.7524	0.0000	0.3000		(*8d*)

(*orthorombic system, RGNR 62 *Pnma*).

XRD patterns recorded for the ceramic samples did in neither case reveal impurity phases. Thus, it may be concluded that the synthesis was fairly completed even for the mildest employed reaction conditions (2 hours of firing at 1200ºC after only 1 hour of milling). However, it must be taken into account that XRD evidences only mineral phases over 2-3 wt%.

In order to compute the microstructural parameters, experimental XRD data were considered only in the 2θ intervals 28 to 35 and 55 to 62, respectively, in the domain of most intensive peaks (Table 3). Possible changes of the lattice parameters were also taken into account.

Table 3. Parameters of the main XRD peaks for sample 14.3.L.

H	K	L	2θ [º]	d [Å]	I_{abs}	F(hkl)|	Mu	FWHM
0	0	2	32.657	2.73990	264.51	211.37	2	0.2236
1	2	1	32.737	2.73336	967.48	202.42	8	0.2236
2	0	0	32.748	2.73250	241.26	202.21	2	0.2236
2	1	0	34.798	2.57602	0.00	0.00	4	0.2236
1	2	3	58.332	1.58062	309.87	166.28	8	0.2236
0	4	2	58.427	1.57827	166.31	172.46	4	0.2236
3	2	1	58.447	1.57777	308.34	166.09	8	0.2236
2	4	0	58.485	1.57685	154.78	166.49	4	0.2236
2	3	2	59.741	1.54667	0.00	0.00	8	0.2236
2	0	3	60.963	1.51856	0.00	0.53	4	0.2236
3	0	2	61.033	1.51698	1.61	17.47	4	0.2236
1	4	2	61.063	1.51630	3.22	17.48	8	0.2236
2	4	1	61.105	1.51536	0.01	0.85	8	0.2236

Microstructural parameters calculated for the samples 14.3 and 14.3.L are presented in Table 4. Agreement among the unit cell edge values was obtained, and the reference values confirm the orthorombic lattice structure.

Table 4. Microstructural parameters of samples 14.3 and 14.3.L.

Sample	**a** Å	**b** Å	**c** Å	**V** Å^3	**ρ** g/cm^3
14.3.L	5.46(1)	5.48(1)	7.72(7)	231.283	6.032
14.3.	5.45(6)	5.47(4)	7.71(4)	230.387	6.179
Reference value*	5.4650	5.4798	7.7231		

* RGNR 62 *Pnma* [9]

The microstructural data of Table 4 are also in agreement with the similar values published in the literature, the differences being generally within the permitted experimental errors interval (Table 5).

Table 5. Lattice parameters of LCMO ceramics obtained by different methods

Sample type	**a** Å	**b** Å	**c** Å	Observations	Ref.
Self-combustion	5.445	5.475	7.720	SHS	[10]
Sol-gel	5.3761	5.3739	7.5715	$La_{0.3}Ca_{0.7}MnO_3$	[11]
Epitaxial thin film	5.433	5.446	7.842	Carrier:: LAO	[12]
	5.461	5.495	7.798	Carrier:: YAO	
	5.488	5.553	7.690	Carrier:: STO	
Conventionally sintered	5.458	5.458	15.44	Pseudocubic double perovskite structure	[13]

Even if the $La_{0.7}Ca_{0.3}MnO_3$ phase is present starting with ceramic samples fired at 1200 ºC, the materials sintered below 1400 ºC are quite pulverulent, and the fit of the calculated diffractograms is totally satisfying for samples 14.2., 14.3. and 14.3.L only (Figure 2). In conclusion, in order to obtain a qualitatively adequate end-product, at least 2 hours milling time and at least 1400 ºC firing temperature is required.

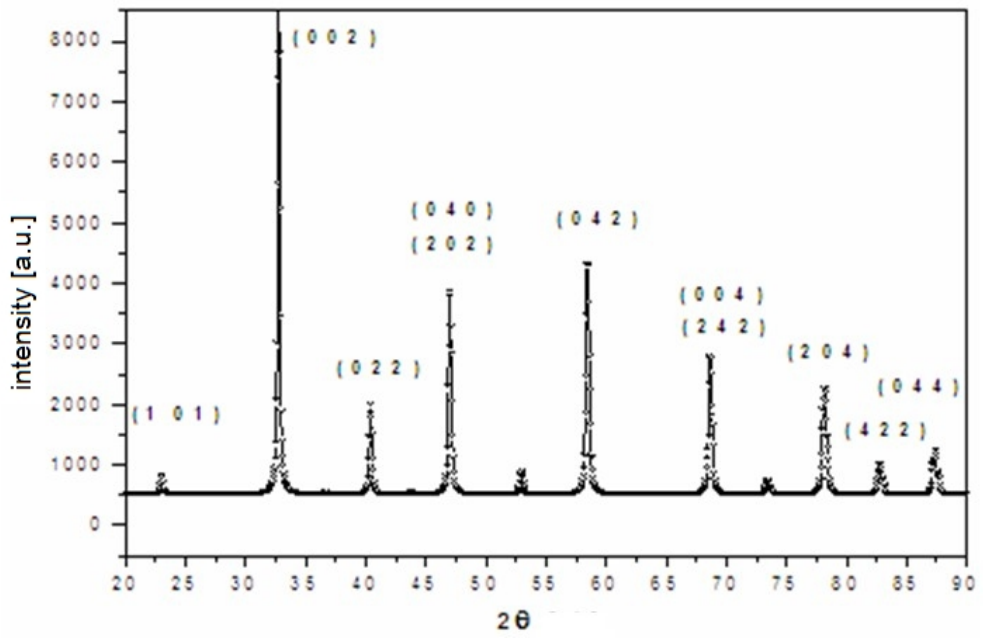

Figure 2. Calculated X-ray pattern of LCMO sample 14.3.L.

Due to their pulverulency, an adequate SEM investigation of the synthesized ceramics was possible only in case of the samples fired at 1400 ºC.

As shown by the microphotos registered at 1k magnification, the general morphology is very similar, although the structure of the quenched samples shows a more crystalline character (Figure 3).

The differently colored, lighter and darker zones probably correspond to the differently ordered magnetic phases.

At larger (50k) magnification the microphotos evidence that whereas the structure of the quenched sample (14.2) is constituted of regular perovskite crystals, the corresponding slowly cooled 14.2.L crystalline structure is already partly melted (Figure 4).

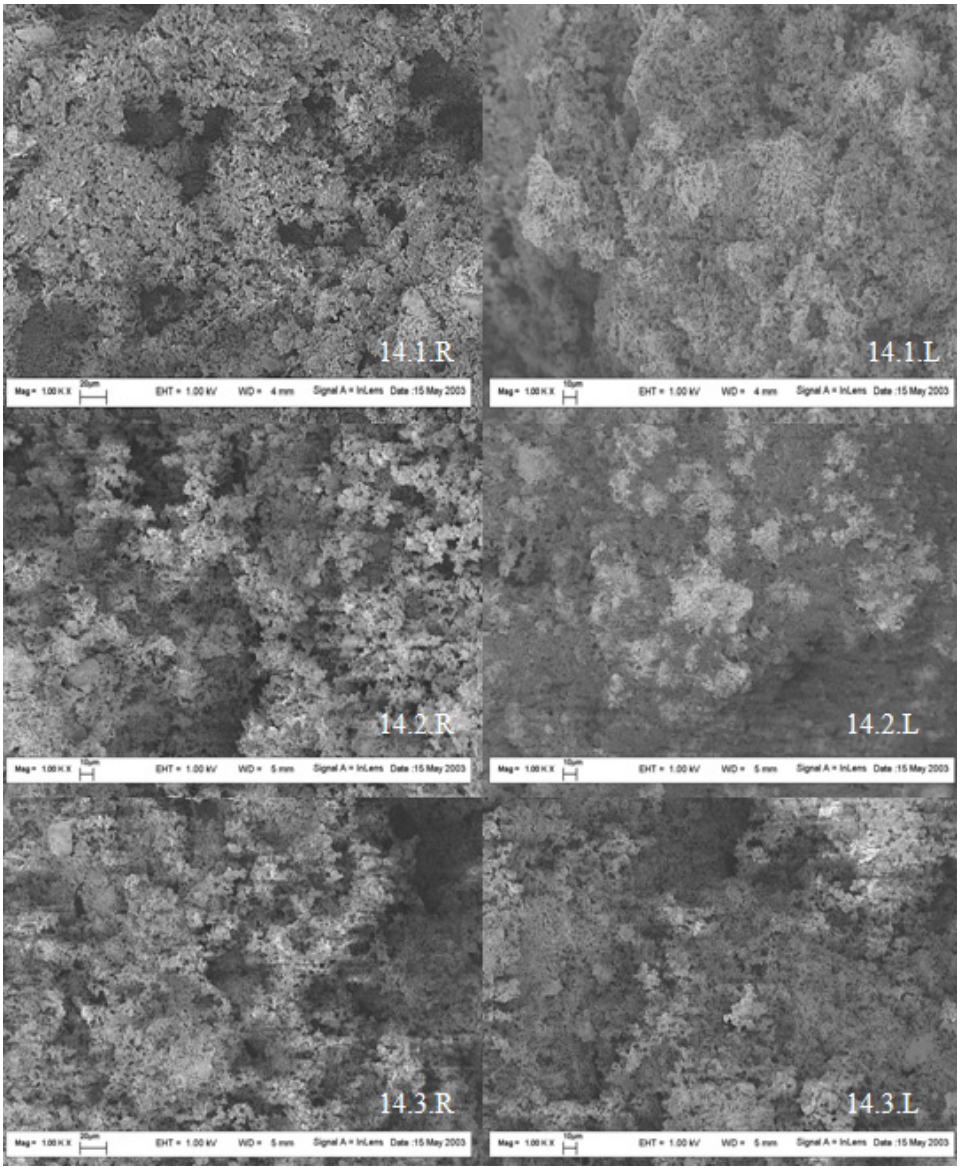

Figure 3. Milling time influence on the structure of the LCMO ceramics sintered at 1400 ºC (magnification: 1k).

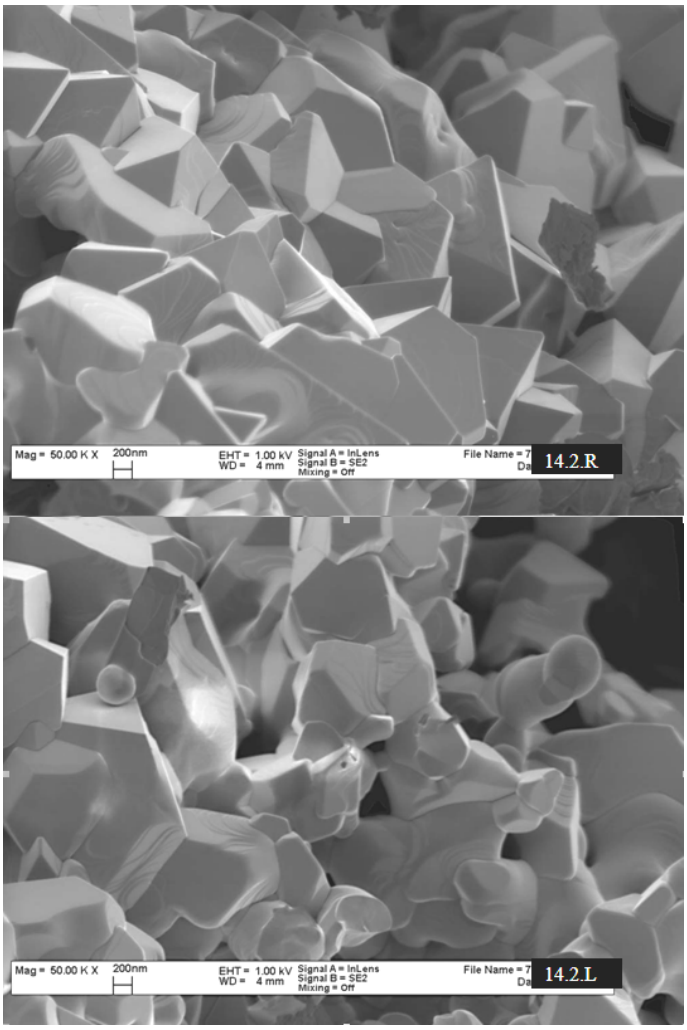

Figure 4. Perovskite crystals in the quenched (here noted as 14.2.R) and the slowly cooled (14.2.L) LCMO manganite.

CONCLUSIONS

X-ray diffractograms prove that the $La_{0.7}Ca_{0.3}MnO_3$ phase is present starting with ceramic samples fired at 1200 ºC. However, the materials sintered below 1400 ºC are pulverulent, and the fit of the calculated diffractograms is totally satisfying for the samples 14.2., 14.3. and 14.3.L only. A qualitatively adequate end-product necessitates at least 2 hours milling time and at least 1400 ºC firing temperature.

The calculated microstructural parameters agree well with previously published values, as well as with the generally accepted reference values, confirming together with the 50k magnification SEM images, the occurence of the orthorombic lattice structure.

EXPERIMENTAL

XRD analysis was performed using a BRUKER D8 Advance diffractometer (working parameters: 45 kV, 45mA, Ni filtered Cu K_α radiation collimated with Soller slits, step-scanning mode with $\Delta 2\theta$ of 0.01º steps, spectral pure Al_2O_3 as internal standard). The sample support was uniformly coated with the finely pulverized ceramic sample (agate ball mill, mean particle diameter < 63 μm, PVC-based adhesive). The *crystalline phase composition* was determined be means of the MATCH! phase identification software and the IUCr/COD/AMCSD reference database.

SEM investigations were carried out by using a LEO 1540 XB (Gemini) microscope, on samples covered with a vacuum evaporated gold film of ≈10 nm thickness.

REFERENCES

1. J. Alonso, J.M. Barandiarán, L.F. Barquín, A. García-Arribas, *Magnetic Nanoparticles, Synthesis, Properties, and Applications*, In Magnetic Nanostructured Materials: From Lab to Fab, A.A., El Gendy, J.M. Barandiarán, R.L. Hadimani, Eds., Elsevier, **2018**, 1-40.
2. A.P. Ramirez, *Journal of Physics: Condensed Matter*, **1997**, *9*, 8171.
3. J.A. Alonso, D. Khomskii, J.M.D. Coey, G.A. Gehring, M. Blamire, S.W. Cheong, P.C. Riedi, N.D. Mathur, D.M. Edwards, J.P. Attfield, P. Battle, *Philosophical Transactions: Mathematical, Physical and Engineering Sciences*, **1998**, 1617.
4. J.M.D. Coey, M. Viret, S. Von Molnar, *Advances in physics*, **1999**, *48*, 167.
5. H. Rietveld, *Journal of applied Crystallography*, **1969**, *2*, 65.
6. P.R. Sagdeo, S. Anwar, N.P. Lalla, *Powder diffraction*, **2006**, *21*, 40.
7. W. Kraus, G. Nolze, *PowderCell. Version 2.4*. Federal Institute for Materials Research and Testing, Berlin, **1999**.
8. G. Nolze, *PowderCell: A mixture between crystal structure visualizer, simulation and refinement tool*. In Powder Diffraction: Proceedings of the II International School on Powder Diffraction*,* **2002***,* 146*.*
9. T. Sudyoadsuk, R. Suryanarayanan, P. Winotai, L.E. Wenger, *Journal of magnetism and magnetic materials*, **2004**, *278*, 96.
10. A.V. Boris, N.N. Kovaleva, A.V. Bazhenov, A.V. Samoilov, N.C. Yeh, R.P. Vasquez, *Journal of applied physics*, **1997**, *81*, 5756.
11. Y.H. Li, F. Damay, L.F. Cohen, K.A. Thomas, A.K. Hossain, J.L. MacManus-Driscoll, *Journal of the American Ceramic Society*, **2001**, *84*, 747.
12. G. Ceder, K. Persson, *The Materials Project: A Materials Genome Approach to accelerating materials innovation,* **2010**, APL Materials, **2013**, *1*, 011002.
13. A. Gómez, E. Chavarriaga, I. Supelano, C.A. Parra, O. Morán, *AIP Advances*, **2018**, *8*, 056430.

STUDIA UBB CHEMIA, LXIV, 2, Tom II, 2019 (p. 457-469)
(RECOMMENDED CITATION)
DOI:10.24193/subbchem.2019.2.39

Dedicated to Professor Ioan Bâldea on the Occasion of His 80th Anniversary

HEAVY METALS ACCUMULATION IN RIPARIAN VEGETATION IN BAIUT METALLOGENIC AREA, MARAMURES COUNTY (ROMANIA)

GIANA POPA[a], TANIA MIHAIESCU[a,*], ANTONIA ODAGIU[a], RADU MIHAIESCU[b], CLAUDIA BALINT[a], ION OLTEAN[a]

ABSTRACT. The present study was focused on evaluating the manner in which heavy metals, originated from natural and anthropic sources (former mining activity in Baiut metallogenic area), in the upper basin of the Lapus River, transferred into sediments and accumulated in the riparian vegetation. Total concentrations ofPb, Ni, and Cd, classified as priority hazardous substances in the WFD, were measured in samples of water, sediments and some emergent flora species (*Equisetum fluviatile*, *Myosotonaquaticum*, *Carexaquatilis*, *Salix fragilis*, *Mentha aquatica*, *Juncus* spp.), in 4 selected sections of the Lapus River, including a reference section (a pollution free area). The heavy metal concentration in collected samples were determined by atomic adsorption spectrometry. In all the monitored sections the heavy metals concentrations were higher in plants than in sediments or water samples. The highest concentrations were recorded for Pb, then for Ni and lastly for Cd in the genus *Carex* and *Salix* in the most contaminated river section. The results of the study show that the ability to accumulate heavy metals differs between species, and affinity for a particular metal depends on its bioavailability.

Keywords: *heavymetals, riparian vegetation, surface water, mining activity, Lapus River*

[a] *University of Agricultural Sciences and Veterinary Medicine, Faculty of Agriculture, 3-5 Manastur str., RO-400372, Cluj-Napoca, Romania*
[b] *Babeş-Bolyai University, Faculty of Environmental Science and Engineering, 30 Fantanele str., RO-400294, Cluj-Napoca, Romania*
** Corresponding author: tania.mihaiescu@usamvcluj.ro*

INTRODUCTION

The presence of heavy metals in the aquatic environment, in a variety of complex chemical forms, continues to cause concern on account of the changes it generates to the biodiversity of aquatic communities and implicitly due the risk that some organisms may develop resistance to the new environmental conditions.

The reaction of aquatic organisms to growing concentrations of heavy metal corresponds to the responsiveness of each species, to the intensity and length of the exposure and to the toxicity level and form of the metal in question [1].

Resistance to heavy metals can be obtained through either of two ways: avoidance, through which a plant is externally protected from stress and tolerance, through which a plant survives internal stress effects [2].

From the physiological point of view the survival of a plant in its specific environment is based on its requirements of chemical elements needed for a normal metabolism (macronutrients, micronutrients and the benefit elements) [3] and/or on the tolerance to theexcess of essential and metaboliccally nonessential elements [4]. Therefore, plantsneed to adopt their physiological process to the environment in which they germinate, and their beneficial metabolic charactersneed to be transferred to next generation by changing the genetic structure of the local population [5].

In most cases metallogenetic environments are contaminated with more than one type of metal, in potentially toxic concentrations, consequently plants develop multiple tolerances. In some cases, plants develop low-level co-tolerance, for metals with low concentration in their environment [6].

The dividing line between tolerance and non-tolerance for aquatic organisms is their ability to root, survive and reproduce in soil substrates contaminated with heavy metals [1].

Consequently, ecosystems tend to adapt to the new conditions, either with species tolerant to heavy metal contamination, or with the appearance of dominant species to the detriment of diversity. The occurrence of such species can constitute an indicator for the contamination level and for bad ecological conditions.

Heavy metal pollution can determine severe phytotoxic actions on plant species, with implications on their genotype, guiding their development selectively towards greater heavy metal tolerance [1].

Aquatic plants are fundamental for the structure and functioning of aquatic habitats [7]. Additionally, high degrees of visibility for aquatic plants indicate a less polluted environment [8].

“Chemical pollution” has a chronic and acute effect on aquatic organisms. The accumulation of polluting substances in ecosystems and the disappearance of biodiversity and habitats are the result of pollution with some heavy metals (Cd, Hg, Ni and Pb). These heavy metals are considered

priority contaminants, with proven significant risks to the water environment. According to Water Framework Directive [9] and to the Environmental Quality StandardsDirective [10], these substances relate to different environmental objectives set for them and to their particular definition in differentiated legislative contexts.

Taking into account that some species have developed such a high degree of tolerance that they can survive and thrive in environments with metallogenic substrates, the determination of the bioavailability of metals and of the bioaccumulation and concentration of heavy metals in plants is very relevant today. The first sign of bioavailability is bioaccumulation, when an organism absorbs a part of the polluting substance [11].

The study focuses on the water body Lapus - "Izvoare - Suciu and the tributaries" RORW2.1.66_B1, analyzing the section between the Izvorul Alb-Negru (the reference) section and the Lapusul Romanesc section, which conforms to the RO 01 typology (according to the WFD) and which captures the significant impact of mining activity in Băiuț metallogenic area. Its chemical state risks not reaching the target of the Water Framework Directive [9] and constitutes an exception to the general good status of the river.

In 2006, prior to the cessation of waste depositing and implicity of mining activity (obligation included in the EU Ascension Treaty of Romania), the water quality of the Lapus River showed an evident impact of heavy metal presence. In all sections (Izvorul Alb Negru, Lapusel, Razoare and Bucsag) monitored by the basin water authority, the measured values for Pb and Cd determined the fifth grade, the most unfavorable, for the Lapus River (referred to the Order no.161 / 2006[12]). If the measured values for 2006 are related to the EQS limits provided by the current EU legislation[10], they exceed the allowed limits for cadmium in all sections and for lead in the Lapusel and Bucsag sections.

Based on the evaluation data on the water quality status and, more precisely, the chemical status of the Lapus River (owned by the water basin authority), taking into account all the conformations, it is found that this body of water has a chemical state classified as "bad".

The aim of this study is to evaluate the bioaccumulation level (Bioaccumulation factor, BAF) in riparian vegetation, of those heavy metals which are defined by the EQS Directive as priority substances (Cd, Ni, Pb).

RESULTS AND DISCUSSION

A first assessment of the concentration levels of heavy metals (Cd, Ni, Pb) of sediment and plant samples was undertaken in September 2016, through the sampling of the sedimentary layer surface (4 sections) and helophyte plants sampling (same 4 sections).

Sediments

In each section an instanter sediment sample was collected from the minor riverbed of the Lapus River, along with a pH measurement conducted at the same location.

The results obtained from the determination of heavy metals concentrations are presented in Table 1.

The dates submitted in Table 1 include water results from the surveillance monitoring sets by the water basin authority for Pb, Ni and Cd, in two sections on the Lapus River (Izvorul Alb Negru, Lapusul Romanesc) for chemical status evaluation on “Izvoare - Suciu and the tributaries” water body. The values refer to the annual mediate of monthly determinations for Pb, Ni and Cd. The difference of concentrations between the two sections, upstream and downstream along the Lapus River, indicates the existence of significant pressures with heavy metals.

Table 1. Levels of heavy metal concentration
in the studied sections of the Lapus River

Sampling point	Sample code	Sample type	Cd	Ni	Pb	pHon water
Lapus River upstream from Băiuțsettlement (background reference section)	S1	Sediment [mg/kg]	1.6	19.2	42.5	7.3
Lapus River downstream from the mineshaft	S2	Sediment [mg/kg]	7.7	60.6	670.7	3.1
Lapus River downstream from Bloaja pond impact area	S3	Sediment [mg/kg]	2.0	50.8	651.8	3.2
Lapus River downstream 2 km from Bloaja pond impact area	S4	Sediment [mg/kg]	2.6	47.9	618.2	3.4
Lapus River – Izvorul Alb Negru	SA	Water [mg/l]	0.1	0.8	0.4	7.2
Lapus River - LapusulRomanesc	SB	Water [mg/l]	2.6	13.9	0.5	7.2

The following aspects are noticeable. The sediment load of Cd, Ni and Pb at the recorded concentrations in the reference area indicate the metallogenic area of the natural background, especially Cd concentrations where the determined value is greater than the 0.8 mg/kg limit [Order 161/2006]. All Cd, Ni and Pb concentrations are higher than the allowed limits (0.8 mg/kg, 35 mg/kg, 85 mg/kg) in the next 3 sections, with the maximum amount being present in the second section (downstream from the mineshaft). The inflow of uncontaminated water from the Strambu Baiut tributary, located right after section 2, diminishes the heavy metal concentration level of the

sediment in section 3, to 2.46 times the allowed limit. In section S4 the Cd amounts are 3.22 times the allowed limit, due to the cumulative effect of the acid mining waters and the tailing pond.

Based on the basins authority data for the year 2016, the highest level of water contamination in the studied sector of the Lapus River was recorded in September, when concentrations of Cd, Ni and Pb were 33, 16 and 2.3 times greater than the EQS parameters for a pH of 6.17. The analysis and processing of data recorded throughout 2016 determined the classification of the entire “Lapus-Izvoare cf. Suciu and tributaries” body of water as having a poor chemical state based on the criteria in the “Water Framework Directive” (WFD)[9].

Compared with the Cd, Ni and Pb concentrations measured in water, those found in sediments are much higher, especially for Ni and Pb. Based on pH, one of the factors known as being a determinant for the solubility and availability of plants for metals, and taking into account that the rivers pH value at the inflow of mine water and tailings (measured during sediment sampling) is around 3.2, the solubility of metals is growing. The absorption process is more important than the precipitation of solids in the decrease of the concentration of metal ions in acidic conditions, while the reverse is true for alkaline conditions [13]. As such, absorption for Pb becomes significant at pH 3-5, and for Cd at pH 5-6.5 [14], this phenomenon is confirmed by the results of the studied sections.

The water basin authority highlighted this specific behavior of metal absorbtion through the monitoring regime established across 2016, for the water evacuated out of the mineshaft (Breiner) in the Lapus River.The average flow of the evacuated waters was approx. 3 l/s and a pH between 2.9 and 5.6, the pollutants were found at the following levels: sulphates: 680 - 1160 mg/l / 600 mg/l allowed [HG 352/2005]; Cd: 3,73 - 67,34 µg/l / 0,2 mg/l allowed; Fe: 5,46 - 121,3 mg/l / 5 mg/l allowed; Ni: 6,5 - 269,6 µg/l / 0,5 mg/l allowed; Zn: 0,973 - 32,95 mg/l / 0,5 mg/l allowed; Hg: 0,006 - 0,042 µg/l / 0,05 mg/l allowed; Pb: 3,992 - 262 µg/l / 0,2 mg/l allowed.

If for the mine waters the concentrations are known, for the pond, being a diffuse pollution source, we can only observe the visual effect it has on the Lapus River and estimate the ponds contamination level. The eroded and active layer of the ponds surface, disperses acid and high salt-content particles towards the river area, generating substantial qualitative changes on it.

From the same sections were collected plant species anchored in the soil, depending on representativity and abundance so as to be relevant for the study. The species diversity was lower, even in section S1 (only metallogenetic background) at the final vegetative period. The plants were washed by the periphyton (all the bodies that live submerged on aquatic plants organisms) and the sediment, being preserved in plastic bags.

In Table 2 the identified species from the monitoring sections and the results of phytotoxicologic determinations for Ni, Pb, Cd and Zn are presented.

The diversity of plants and their abundance is limited and decreases from one section to another, and along the crossing of highly contaminated sections the plants change not only their coloration but also their terrestrial structure, much less developed, while the structure of the roots is more branched and filamentous. With the exception of the Carex species which is present in all sections, the diversity of the rest of the identified plants changes, with the most contaminated section 3 having only Carex and Salix species present.

As for the concentrations of metals measured in plants the highest was found in section S3, followed by section S4 and section S1. Section S2 was poorly represented by the relevant plants.

Table 2. Heavy metal concentrations in identified plant species

Sampling point	Examinated species	Ni	Pb	Cd	Zn
		[mg/kg dry wt.]			
S1 - Lapus River upstream from Baiut settlement	*Equisetum fluviatile* L.	43.0	295.9	26.9	6.8
	Carexacuta L.	39.4	507.8	36.1	2.7
	Alismalanceolatum With.	74.4	1008.1	52.3	28.2
	Alismalanceolatum With.	113.6	1582.5	41.7	33.3
	CarexaquatilisWahlenb	66.9	251.5	9.9	2.6
	Myosotonaquaticum(L.) Moench	72.0	1365.6	124.4	14.1
S3 - Lapus River downstream from Bloaja pond	*CarexhumilisLeyss.*	242.4	1864.6	27.4	33.1
	Salix exigua Nutt.	183.5	1671.0	43.4	17.4
	Carexacuta L.	129.3	2063.9	6.5	10.2
	CarexaquatilisWahlenb	240.1	2557.1	41.6	30.3
	Salix fragilis	251.5	594.0	54.2	27.5
S4 - Lapus River downstream 2 km from Bloaja pond	*Salix exigua Nutt.*	121.3	321.4	98.1	10.0
	Menthaaquatica L.	205.9	463.8	113.9	24.9
	Carexelata All.	117.5	306.3	16.6	5.4
	Juncuseffusus L.	135.0	1068.8	35.5	6.6

The data provided by the toxicological analysis of the riparian vegetation shows that in the reference unpolluted section, plants from the Alismataceae family accumulate heavy metals, determined concentration in plants showing the pattern Pb>Ni>Cd. Additionally, with regards to metal concentration in different species, Pb is bioaccumulated in the following order Alismataceae> Myosotonaquaticum>Carexacuta> Equisetum fluviatile >Carexaquatilis.

The most contaminated, section 3, also records the highest concentrations of Pb and Ni. In the identified Carex species the lead concentration was the highest, namely 1864.6 to 2557.1 mg/kg dry wt., but

also in the two Salix species 594.0 to 1671.0mg/kg dry wt., the nickel followed in the same species in the same order, i.e. Carex> Salix. Also, some species of the Carex family have a higher affinity for Pb and Ni than others. For Pb, the critical toxicity level is reached at 0.6-28 mg/kg dry wt. and for nickel at 10-50 mg/kg dry wt., while the hyperaccumulation level is reached for both metals at concentrations higher than 1000 mg/kg dry wt. [15]. As a result, all plants identified in section 3 may be hyperaccumulators for metals.

For cadmium, the identified concentrations are kept within the same limits for all monitored sections with a higher bioaccumulation for *Myosotonaquaticum* of 124.4mg/kg dry wt. in Section 1 and *Mentha aquatica* of 113.9 mg/kg dry wt. in Section 4, sections upstream and downstream from sources of heavy metal contamination.

Relative to the level of the metal concentrations in the structure of the plant, there are highlighted plants that are at the same time accumulators and “hyperaccumulators”, the latter being characterized by the possibility of taking concentrations for Cd> 100 mg [16]. It is difficult to determine the critical level of toxicity for the chemical elements since usually small quantities are transported into the stem and the relevant toxic effect is sensed in the roots [15]. Under these circumstances it is possible that the two above-mentioned species have the characteristic of cadmium hyperaccumulators.

The bioconcentration rate heavy metals in riparian plants (the concentration of heavy metal in plant reported to the concentration of the same metal in sediments), in the studied sections is presented in Table 3.

Table 3. Bioconcentration rate for Ni, Pb, Cd in identified species

Sampling point	Examinated species	Ni	Pb	Cd
S1 - Lapus River upstream Baiut settlement	*Equisetum fluviatile* L.	2.2	7.0	16.8
	Carexacuta L.	2.1	11.9	22.6
	Alismalanceolatum With.	3.9	23.7	32.7
	Alismalanceolatum With.	5.9	37.2	26.1
	CarexaquatilisWahlenb	3.4	5.9	6.2
	Myosotonaquaticum(L.) Moench	3.7	32.1	77.7
S3 - Lapus River downstream Bloaja pond	*CarexhumilisLeyss.*	4.8	2.7	13.9
	Salix exigua Nutt.	3.6	2.5	22.0
	Carexacuta L.	2.5	3.1	3.3
	CarexaquatilisWahlenb	4.7	3.8	21.1
	Salix fragilis	5.0	0.9	24.5
S4 - Lapus River - 2 km downstream Bloaja pond	*Salix exigua Nutt.*	2.5	0.5	38.0
	Menthaaquatica L.	4.3	0.8	47.8
	Carexelata All.	2.5	0.5	6.4
	Juncuseffusus L.	2.8	1.7	13.8

For Cd, the rate of bioconcentration was highest in section 1 for the *Myosotonaquaticum* species and decreasing as follows *Asteraceae*<*Carex*< *Equisetumfluviatile*<*Carex*aquatilis. In sections 3 and 4 where the Cd concentration was similar with that in section 1, the rate of bioconcentration was lower for the *Carex* species.In section S1, the Cd concentration measured in sedimentswas at a low level and constituted the metallogenetic background, so plants needed to adapt and developed different kinds of tolerance.

ForPb the rate of bioconcentration reported for the sediment load values was in reduced quantities, especially in sections 3 and 4, even if identified plants have high registered concentrations. A much larger bioconcentration rate value was found in section 1 for all identified species, except *Carex* and *Equisetumfluviatile*.

For Ni the rate of bioconcentration remained in the 2.4-4.7 interval, with the exception of Asteraceae whose value was 5.9, even though the heavy metal load values of the sediment and implicitly of the plants differed between the 3 sections. With regards to the genus Carex, which is found in all 3 sections, the highest bioconcentration rate was found in section 3, the most contaminated section.

These results indicate that the metal accumulation ability of plants differs between species, and affinity for one particular metal or another depends on its bioavailability.

The bioavailability of metals can vary seasonally, their toxicity for the benthic community can be maximal in autumn [17], when due to the decomposition of organic matter, anoxia with direct and indirect inhibitive effects can appear (due to the absence of Fe and Mn oxide co-precipitation in heavy metals).

CONCLUSIONS

Even after the cessation of mining activity water pollution is still present due to uncontrolled leaching processes. Is expected that the existent sediment loading will be supplemented with new quantities of heavy metals which are still being released from the polluted area, which is insufficiently protected.

The contamination level of the studied area was reflected in the vegetation that has the ability to take metals in proportion to their concentration in the environment. The plants have accumulated concentrations of Cd, Ni and Pb far above their physiological needs, lacking the ability to distinguish the difference between necessity and excess.

All identified species are co-tolerant because they accumulate high concentrations of one metal (Pb) and to a lesser extent of other metals (Cd), some of them are hyperaccumulators exceeding the “normal” level of concentration.

The survival of plants in this heavily with metals contaminated body of water is owed to their adaptation, some through the bioaccumulation of metals others through the exclusion of concentrations which are greater than their carrying capacity. It can also be sustained through intake of nutrients and organic matter, but as plant diversity and abundance is reduced, for the observed conditions these two parameters are insignificant.

The study once again confirms that sediments can be the “memory” of quality events that occur on rivers and constitute at the same time as a reservoir of metals that they “supply” to aquatic organisms, implicitly to riparian plants.

The lack of measures to minimize the impacts of mining activity will keep the Lapus River, on the studied section, at risk of not satisfying good status as established by the WFD [9].

EXPERIMENTAL SECTION

Study area

The studied area is located in the Herja-Baiut metallogenic area, with an ore deposit with polymetallic mineralization (especially pyrite, galena and chalcopyrite) as well as gold and silver deposits mined until 2007. The Lapus River, which flows through the area, is affected by pollution originated from former mining activities, its chemical state risks not reaching the target of the Water Framework Directive and constitutes an exception to the general good status of the river.

The most important water pollution source is represented by acidic mine water, with a flow rate of about 3 l/s, that is punctually discharged without treatment, through a gallery, the remainder being diffused in Lapus River. Other important pollution sources are represented by Bloaja-Baiut tailings ponds (12.7 ha) and the Bloaja Avarii pond (3.4 ha), which storage sterile(4% pyrite) quantities of 1.027 million tons and 0.15 million tons, respectively. Non-certified Bloaja Avarii pond continues to induce a significant impact on the aquatic environment through the large quantitiesof tailings that are mobilized by rains and driven towards the Lapus River. In dry weather the windalso transports large quantities of fine dust contributing to general pollution of the area.

Sampling and analyzing

Compared to the operational monitoring sections established on the Lapus water body - “Izvorul Alb-Negru - Suciu and the tributaries” by the water basin authority, following “in situ” investigations, to determine the

level of contamination and the transport of contaminants downstream, 4 other sections (located inside this body of water) were established where samples of sediment and riparian vegetation were taken in order to capture the significant impacts of shale mining activity (Fig. 1).

Sediment and riparian vegetation sampling was performed in early autumn, September 2016, from the same sections. The riparian vegetation samples were taken from the soil, which develops in shore areas with depths of less than 1.5 m, depending on their representativeness and abundance, so as to be as relevant as possible for the proposed study.

Samples of the first 5-10 cm of the river deposits were collected in acid rinsed polyethylene bottles. All samples were kept in cooling boxes, at 4°C during transportation, and the analyses were performed immediately after receiving the samples in the laboratory. The collected sediment samples were air-dried, large particles were hand-picked and the rest was ground to powder. The fraction < 50 µm was used for analyzing metals. Dry sediment was digested using aqua-regia in microwave digestion system (Berghof microwave oven). The mineralized mixture was cooled to room temperature, filtered and ultrapure water was added to the filtrate in a volumetric flask up to 100 mL mark.

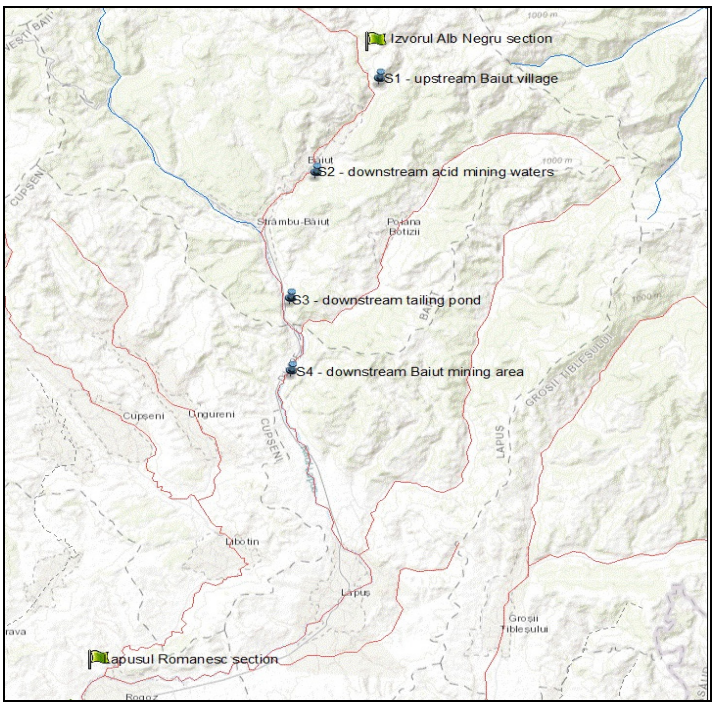

Figure 1. Placement of additional monitoring sections

The sampled plants were washed of periphyton and sediment and stored in plastic bags. The plants were washed with distilled water and dried at room temperature, then in the dryer for 24 hours at 105°C. The dried plants were ground to powder and were digested using a HNO_3 and H_2O_2 mixture in a microwave digestion system (Berghof microwave oven). The mineralized mixture was cooled to room temperature, filtered and ultrapure water was added to the filtrate in a volumetric flask up to 50 mL mark.

The obtained solutions were then analyzed for heavy metal content using atomic absorption spectrophotometry (SHIMADZU AA-6800 spectrometer) in the Somes Tisa water basin laboratory.

The results for sediment and plants analysis were carried outwith anuncertainty interval of ±5%, the determinations being realized in conformity with ISO standards.

The operation conditions were those recommended for each metal in the instrument's method (Table 4).

Table 4. Instrumental parameters for metal determination by AAS

Standard conditions	**Cd**	**Ni**	**Pb**
Wavelength, λ [nm]	228.8	232	283.3
Slit width [nm]	1.0	0.2	1.0
HCL* current (mA)	8	12	10
Background	Deuterium	Deuterium	Deuterium
Flame	C_2H_2/air	C_2H_2/air	C_2H_2/air
fuel flow (N l/h)	1.8	1.6	2.0

*HCL - Hollow-Cathode Lamps

For each type of sample, sediment or plant, the analysis method included the determination of detection and quantification limits, necessary for obtaining validated results. Furthermore, the results validation was certified by the verification methodology on the accreditation standard SR EN ISO/IEC 17025:2018 [18].

The sensitivity of the AAS method was estimated as the limit of detection (LOD) and the limit of quantification (LOQ), which are presented in Table 5.

LOD and LOQ were calculated based on the standard deviation of the response and the slope, using the following equations [19 - 21].

$$LOD = \frac{3 \times \sigma}{S} \; ; \; LOQ = \frac{10 \times \sigma}{S}$$

where, "σ" is the standard deviation of 10 replicate measurements of the blank signal and "S" is the slope of calibration curve.

Regarding pH of water, the measurement in situ was done with a portable pH-metre (Hach analyzer), in each sampling section.

Table 5. LOD and LOQ of the AAS method

Parameter	**Element**		
	Cd	**Ni**	**Pb**
Linear working range [mg/kg]	0 – 50	0 – 150	0 - 200
LOD [mg/kg]	1	6	13
LOQ [mg/kg]	5	20	50

At the time of the sampling, submerged macrophytes were not identified in any of the sections, and the diversity of species was reduced, even in the reference section (the first proposed section, upstream of Baiut settelments). The identification of plant species or families was carried out by the biology laboratory of the basin water authority based on the determinator of plants. The identification of the species was difficult, and in some cases only the family of which the plant belongs could be identified, due to the similarities of the physiological characteristics due to the lack of the elements that differentiate them in the conditions of the end of the vegetation.

REFERENCES

1. A. J. M. Baker, P. L. Walker, *Chemical Speciation & Bioavailability*, **1989**, *1(1)*, 7.
2. A. J. M. Baker, *New Phytologist*, **1987**, *106(1)*, 93.
3. H. Marschner, "Mineral nutrition of higher plants", **1995**, London, Academic Press.
4. W. Larcher, "Physiological plant ecology", **2003**, Berlin, Springer.
5. W. Ernst, *Forest Snow and Landscape Research*, **2006**, *80(3)*, 251.
6. R. G. Turner, Ecological Aspects of the Mineral Nutrition of Plants, British Ecological Society Symposium, **1969**, *9*, 399.
7. S. M. Haslam, "River Plants. The macrophytic vegetation of watercourses", **2006**, Forrest Text.

8. S. M. Haslam, “River pollution: an ecological perspective”, **1990**, London, Belhaven Press.
9. Directive 2000/60/EC of the European Parliament and of the Council of 23 October 2000 establishing a framework for Community action in the field of water policy, published in the Official Journal OJ L 327, 22.12.2000.
10. Directive 2008/105/EC of the European Parliament and of the Council of 16 December 2008 on environmental quality standards in the field of water policy, amending and subsequently repealing Council Directives 82/176/EEC, 83/513/EEC, 84/156/EEC, 84/491/EEC, 86/280/EEC and amending Directive 2000/60/EC of the European Parliament and of the Council OJ L 348, 24.12.2008.
11. M. C. Sandoval, Proceedings of the 25th Annual British Columbia Reclamation Symposium, Campbell River, B.C., **2001**, 67.
12. Order No. 161 of February 16, 2006for the Approval of the Normative on the Classification of Surface Water Quality in order to establish the ecological status of the water bodies (in Romanian). Eminent: Ministry of Waters, Forests and Environmental Protection (Published in: Official Gazette No 511 bis of 13 June 2006).
13. H. A. Elliott, M. R. Liberati, C. P. Chin-pao Huang, *Journal of Environmental Quality*, **1986**, *15(3)*, 214.
14. J. S. Rieuwerts, I. Thornton, M. E. Farago, M. R. Ashmore, *Chemical Speciation and Bioavailability*, **1998**, *10(2)*, 61.
15. M.J. Hodson, *Biochemist*, **2012**, *34(5)*, 28.
16. R. R. Brooks, R. S. Morrison, R. D. Reeves, T. R. Dudley, Y. Akman, *Proceedings of the Royal Society B*, **1979**, *203(1153)*, 387.
17. G. Krantzberg, *Environmental Toxicology and Chemistry*, **1994**, *13(10)*, 1685.
18. SR EN ISO/IEC 17025:2018, General requirements for the competence of testing and calibration laboratories.
19.V. Thomsen, D. Schatzlein, D. Mercuro, *Spectroscopy*, **2003**, *18(12)*,112.
20. C. C. Chan, “*Pharmaceutical Manufacturing Handbook: Regulations and Quality*”, **2008**, edited by Shayne Cox Gad, John Wiley & Sons, Inc., pp 727-742.
21. H. Sun, L. Li, *American Journal of Analytical Chemistry*, **2011**, *2*, 217.

STUDIA UBB CHEMIA, LXIV, 2, Tom II, 2019 (p. 471-481)
(RECOMMENDED CITATION)
DOI:10.24193/subbchem.2019.2.40

Dedicated to Professor Ioan Bâldea on the Occasion of His 80th Anniversary

SOLUBILITY, DUCTILITY AND RESILIENCE OF A PMMA DENTURE RESIN WITH GRAPHENE AND SILVER NANOPARTICLES ADDITION

CECILIA BACALI[a], SMARANDA BUDURU[a], VIVI NASTASE[b], ANTARINIA CRACIUN[a], DOINA PRODAN[c], MARIANA CONSTANTINIUC[a], MANDRA BADEA[a], MARIOARA MOLDOVAN[c], CODRUTA SAROSI[c*]

ABSTRACT: PMMA denture base materials are used for several decades without significant improvements in their composition. The addition of different fillers has been proved to improve some of the acrylic resin's characteristics. Recent studies focused on enhancing PMMA properties using nanoparticles. In our study we assessed the effect of adding graphene and silver nanoparticles on the solubility, ductility and resilience of a commercial denture base acrylic resin.

Keywords: *solubility PMMA, ductility, resilience acrylic resin, graphene, silver nanoparticles*

INTRODUCTION

Acrylic resins have a wide applicability in medicine and among them PMMA are the most used materials in denture fabrication because of their convenient characteristics, such as dimensional stability, ease of handling and processing [1]. However, they are brittle materials with low fracture strength and insufficient surface hardness [2]. Since PMMA resins are relatively brittle

[a] *Iuliu Hatieganu University of Medicine and Pharmacy, Department of Prosthodontics and Dental Materials, 32 Clinicilor str, RO-400006, Cluj-Napoca, Romania*
[b] *Institute for Computational Linguistics, University of Heidelberg, Im Neuenheimerfeld 325, Heidelberg, 69120, Germany*
[c] *Babes Bolyai University – Institute of Chemistry Raluca Ripan, Department of Polymer Composites, 30 Fantanele str., RO-400294, Cluj-Napoca, Romania*
**Corresponding author: codruta.sarosi@gmail.com*

materials and they are subjected to high mastication forces or sometimes to accidental drops, several attempts have been made to improve its mechanical properties by adding fillers of different type and sizes [3]. Inorganic nanofillers have a large surface area which determines a high surface energy at the interface of polymer matrix, improving flexural strength; they improve hardness due to their rigidity and higher stiffness than the matrix [4] and the fracture toughness as well, because of the more uniform distribution compared to micro fillers [5]. Addition of silver nanoparticles to PMMA has several favorable effects: antimicrobial activity, increased monomer conversion, increased flexural strength and elastic modulus, improved thermal stability [6]. Tripathy showed that graphene oxide incorporation into PMMA determines improved mechanical-tensile strength, Young's modulus, strain at break, thermal and electrical properties of the material [7]. The improvement of the characteristics of denture base materials is focused mainly on the mechanical properties and among them on fracture strength. Fractures in composites depend on the heterogeneity, interfacial adhesion between the materials' components, type of fracture and on the brittle or ductile nature of the components [8]. Zhang found that the higher the tensile strain and added fiber concentration the lower the ductility, while a higher break strain is linked to a higher ductility in the studied composites.

Rubberlike materials added to acrylic resins can improve the fracture strength [9]. Muraikami [10] and Alhareb [11] showed that by adding rubber to PMMA enhanced mechanical properties were obtained, while the impact strength was improved as the ceramic fillers acted as impact modifiers, absorbing the energy that resulted consecutive load application and transforming the material behavior from brittle to ductile [11]. Ceramic fillers have also been proved to improve hardness and fracture toughness of dental resins [12]. It also seems there is a synergistic effect between the tendency of fillers to fibrillate and the mechanical behavior of the matrix resin in governing the resulting ductility of the composite [13].

Other authors claim that addition of stiffening reinforcement to dental resins leads to lower ductility values, thus a more brittle material, because the rigid filler hinder the freedom of the polymer to reconfigure its structure after being stressed [13]. As studies showed controversial results regarding ductility, consecutive filler addition to PMMA, their influence on this characteristic of denture base materials is important to be further studied.

Among the researchers that attempted to find correlations between mechanical properties and clinical wear, Peutzfeldt suggested that resilience modulus can be used as a predictor for clinical wear, while resilience was shown to reflect in vivo wear performance [14], so Auer's supposition that resilience could influence polymer resistance to abrasion has been demonstrated [15]. Albers considered that cracks could be responsible of abrasion initiation [16] and his opinion was lately sustained by Peutzfeldt [14].

In dentistry acrylic resins are used inside the oral cavity, so their behavior and properties in the oral environment are of great importance. Although an ideal material should have high chemical and thermal stability, dental resins can absorb substances from the oral medium and release components in the surrounding environment [17, 18]. Solubility of denture base materials results from the leaching out of residual monomer and also water soluble additives into the oral fluids, being a possible cause for tissue irritation, while water sorption affects the mechanical properties (acting as a plasticizer) and as well the dimensional stability and colour [17]. Acrylic resins homogeneity can influence water sorption and solubility [19], the more homogenous resins absorbing less water than the porous ones [20], as porosities permit fluid circulation through the network [21].

In our study we added both silver nanoparticles and graphene to a PMMA denture base resin, in order to improve its mechanical, physical and antibacterial properties.

RESULTS AND DISCUSSION

We computed mean, standard deviation, minimum and maximum values for each set of 10 values for each sample for solubility, ductility and resilience. One way ANOVA was used to analyze the variation in means for the different types of samples. Paired t-test was used to do pairwise comparisons of samples. A “p” value less than 0.05 will indicate statistically significant differences.

For the reinforced material the fracture occurred at slightly lower stress and strain values, indicating that graphene silver nanoparticles addition reduces slightly the ductility of the reinforced resin, compared to the control, but the differences are not statistically significant. The mean values are presented in figure 1. The lowest mean value was found in the sample P1 (0.64) while the highest mean value was found in the control sample M (0.68), while the P2 sample showed intermediate mean values. The measured values ranged between 0.42 and 0.96 mm.

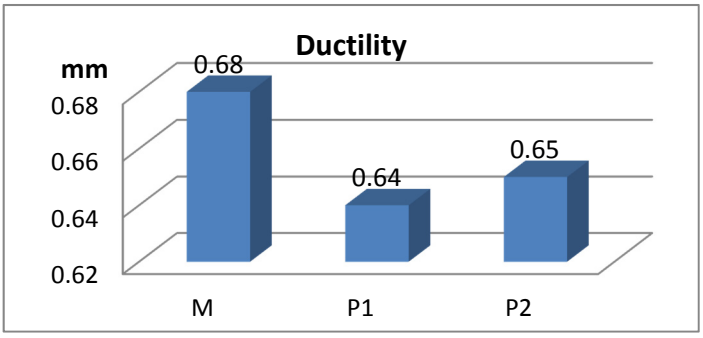

Figure 1. Mean Values of Ductility (mm) for PMMA with graphene samples (P1, P2) and control

Fillers distribution inside the PMMA matrix can be observed in the SEM images, figure 2. No visible pores and bubbles were observed in the polymer when viewed without magnification. The aspect of the fractured surface shows minimal differences between the examined samples. SEM images reveal a smooth surface with rapid cracks (evidenced by the arrows), indicating a brittle fracture.

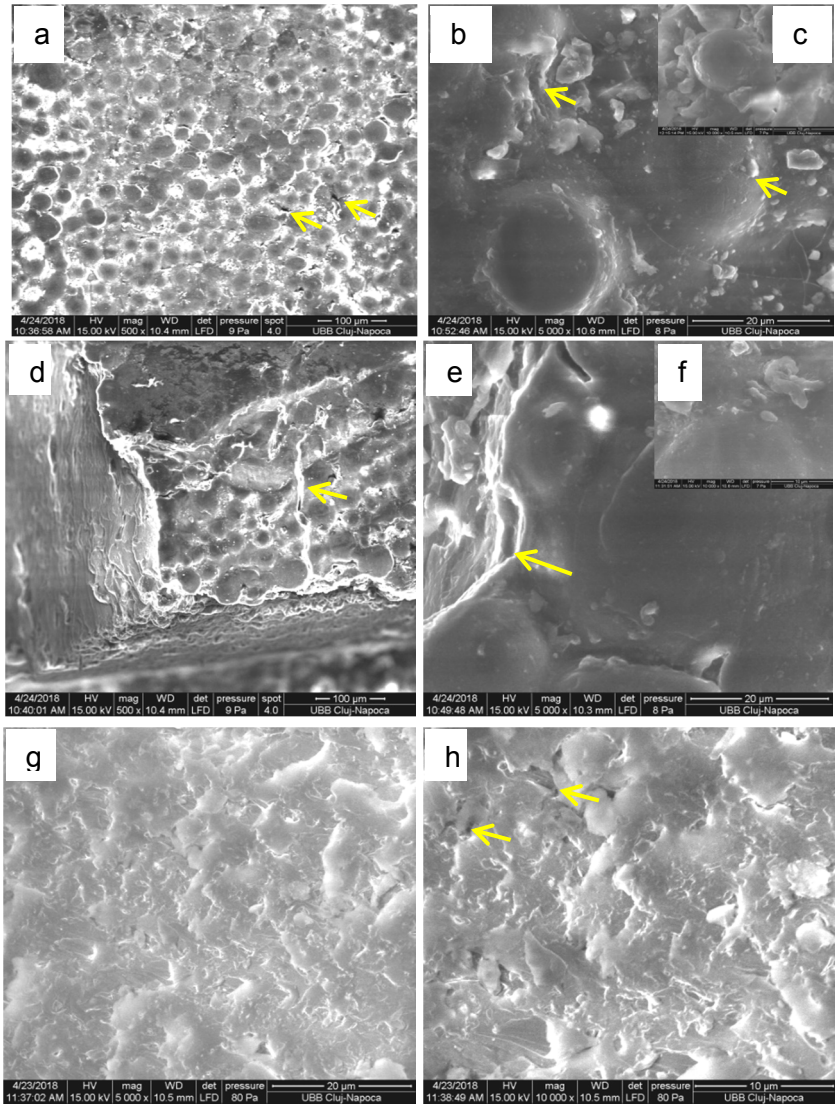

Figure 2. SEM images of the PMMA with graphene (G-Ag) - P1 (a, b, c) and P2 (d, e, f, g, h) samples on the fractured surfaces at different magnification 500x, 5000x and 10000x

The SEM images revealed that the particles with graphene were well distributed and dispersed in the PMMA matrix when 1% and 2% were used in the composition of P1 and P2. Some of the graphene nanoparticles were pulled out from the fractured surfaces of the PMMA - based composite materials during the impact test. There were also some micro-cracks on their fractured surfaces.

Figure 3 shows the mean values for modulus of resilience measured for each group of ten samples (M, P1, P2). The registered values ranged between 1.7 and 6.24 J/m^3. On average, the highest modulus of resilience is achieved for the sample with 1% G-Ag. The variance of mean values within the group is statistically significant (p= 0.00045). In pairwise comparisons, the difference between P1 (PMMA + 1% G-Ag) and P2 (PMMA + 2% G-Ag) has the lowest p value (0.0013), whereas for the other pairs it hovers about 0.05 (0.054 and 0.057 respectively).

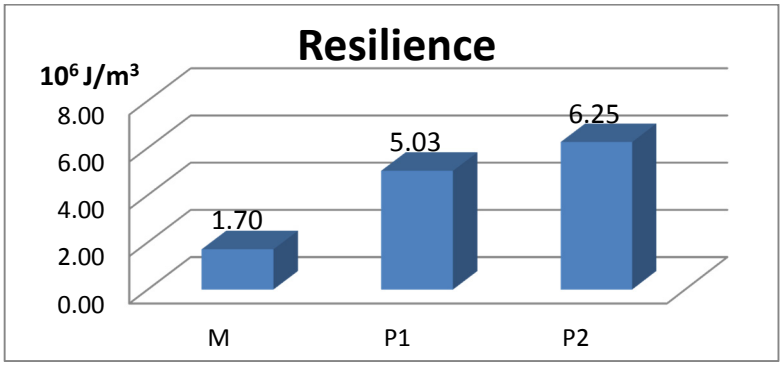

Figure 3. Mean values of modulus of resilience (10^6 J/m^3) for the control and reinforced samples P1 and P2

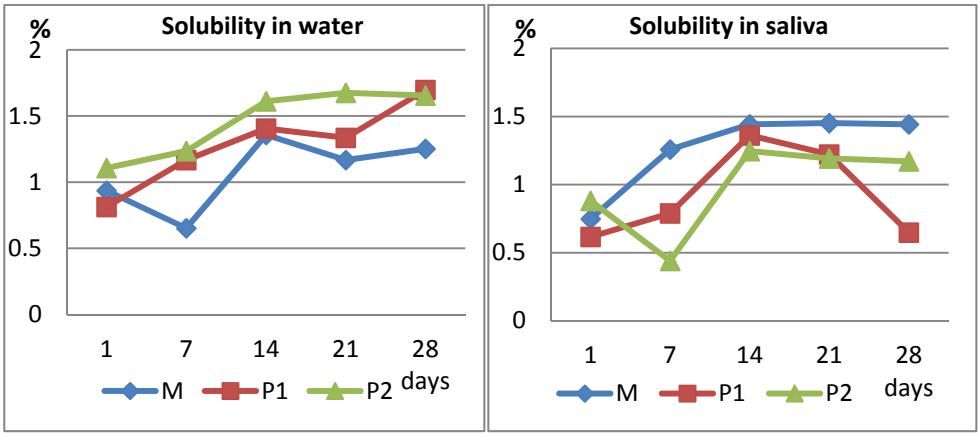

Figure 4. Mean values of solubility in water and saliva (%) for the control (M) and reinforced samples P1 and P2 after 1, 7, 14, 21, 28 days of immersion

The results show that for all three tested materials there are differences in 28 days between the mean values for the two test media, both in terms of absorption and solubility.

Samples reinforced with 1%wt. graphene silver nanoparticles showed higher mean values for the solubility in water and lower values for the solubility in saliva.

Samples reinforced with 2%wt. additives showed increased solubility both in water and saliva compared to control sample.

The lowest value was obtained for the sample P1 in saliva, while the highest value was obtain for the same sample in water.

The mean values for the solubility in water ranged between 0.0078 and 0.0112%, the maximum mean value was found in the sample P1, and the minimum in the control sample. The mean values for the solubility in saliva ranged between 0.0059 and 0.0089%, with a maximum value for the sample P2 and a minimum value for P1.

The P1 sample had the maximum mean value of water solubility, while the minimum values were found in the P2 sample after immersion in saliva.

Many researchers tried to improve denture base acrylic resins' mechanical properties by adding fillers of different type, sizes, shapes, in different proportions, in order to obtain stronger [22-27] and also less brittle materials [28]. Low ductility of dental resins is a key limitation, while increment of both the strength and ductility of matrix composites is still a challenge. Clustering is one of the major problems in nanoparticles reinforced composites [29]. On the other hand, high filler concentrations could decrease mechanical properties, as the lower concentrations permit a better distribution in the PMMA [30, 31]. Fillers addition beyond 1%wt leads to a deterioration of mechanical strength that can be attributed to filler agglomeration [7].

Ductility is a delicate problem in brittle materials, as it is difficult to predict: in low ductility materials it depends on the ultimate tensile strength and fracture energy, while in materials with added ductile second phase it varies with composition. Ductility is decreased by porosities and also by a week interface between phases that lead to low strength and premature failure. High toughness is found when fracture passes through both phases [32].

Addition of elastic and rigid fillers, such as nitrile rubber and ceramic fillers, for example, showed improved values of impact strength and fracture toughness, causing an increment in PMMA ductility [11]. Therefore, addition of materials with high ductility could improve the final ductility of the acrylic resins.

In this study we investigated the effect of adding silver nanoparticles and graphene to a commercial denture base acrylic resin. Silver nanoparticles, rigid structural fillers, were added to the material in order to obtain enhanced mechanical and also antibacterial properties. As the homogenous dispersion

of silver nanoparticles into the PMMA matrix is difficult to be obtained because of the easy agglomeration of the nanoparticles and the high viscosity of the polymer [33], we associated them with graphene, in order to stabilize them.

Graphene is a lightweight and elastic material but also the strongest and stiffest material ever known so far and has remarkable mechanical properties. Although graphene has higher elastic modulus and tensile strength than graphene oxide, graphene oxide hydrophilicity/hydrophilic outer surface are beneficial for the aqueous procession of polymer nanocomposites [34]. While mechanically activated graphene is brittle, the cyclic epoxidic groups on graphene oxide make it ductile by dissipating strain energy and avoiding crack propagation through a covalent epoxide-to-ether functional group transformation [35]. Graphene oxide and its derivates have been lately used for polymer matrices mechanical properties enhancement. Severe internal porosity of the material can favour internal stresses, reducing denture durability [36], while the surface porosity enhances bacterial adhesion [37] and calculus deposition, affecting esthetics [38].

Increased modulus of resilience obtained for both reinforced resins could improve the abrasion resistance and consecutive resins' durability, as the cracks, that initiate abrasion need little energy to break the material and are likely to appear in materials with low modulus of resilience [14,16]. The mean values obtained for the resins with nanoparticle addition (5.02 and 6.24), are higher than those found by Peutzfeld in a study on acrylic resins, 0.67-2.40 MJ/m^3 [14].

Water sorption and solubility still remain a concern regarding dental materials, as they are critical problems that can influence a resin's durability [39]. They cause dimensional changes in the material that can determine internal stresses, favoring cracks and fractures. In our study the tests consisted in sample immersion in distilled water and artificial saliva at 37°C for 28 days, and mass weighting at certain intervals. Higher solubility values were found for the reinforced resins, excepting P1 sample in saliva, which showed a decrease. The higher solubility of the reinforced resins can be explained by the effect of fillers addition to PMMA, that decreases the degree of conversion and consecutive increases the amount of unreacted monomer [4], as the solubility is directly related to residual monomer releasing. Solvent's diffusion in the matrix can also lead to polymer dissolution and dispersion of the particles into the solvent. However, the values we found ranged between the accepted limits. The mean values we obtained were lower than the mean values (0.03-0.13%) found in another study on water solubility of denture base acrylic resins [40].

Addition of 1% graphene silver nanoparticles showed favorable effects on resilience modulus and solubility in saliva, while a concentration of 2% wt increased solubility in water and saliva but also improved the modulus of resilience. Filler incorporation into PMMA was accompanied by a reduction in ductility, although without a statistical significance.

CONCLUSIONS

Different concentrations of graphene-silver nanoparticles, added to PMMA in order to induce antibacterial properties and improve fracture strength, can have different effects on resin's characteristics. We found that a concentration of 1% wt graphene silver nanoparticles has a beneficial effect on the resins' modulus of resilience and solubility in saliva, but it decreases ductility. A concentration of 2% improves resilience and could have good perspectives regarding durability, but increases solubility both in water and saliva and reduces resin's ductility**.**

EXPERIMENTAL SECTION

1. Materials

Castavaria (Vertex Dental, 3769 Soesterberg, The Netherlands), commercial denture base material was used in our tests.

The graphene-silver nanoparticles (G-Ag) composite was synthesized through the Radio-Frequency Catalytic Chemical Vapor Deposition (RF-CCVD) method [41] [Jatania] using silver nanoparticles distributed over magnesium oxide (Agx/MgO, where x = 3 wt %) and graphene oxide, obtained as previously described [42]. Mixing of G-Ag with acrylic denture material was done in 95% ethyl alcoholic solution, at room temperature, under continuous stirring, for 30 minutes. The compounds were then dried in the oven at 40°C. Synthesis was performed using a methane flow rate of 80 mL/min and a reaction time of 60 minutes [43].

2. Sample Preparation

The experimental materials were obtained from a commercial denture base auto-polymerizing acrylic resin, Castavaria (Vertex Dental, 3769 AV Soesterberg, Netherlands). The control sample contains only the commercial material (M), while samples contain also 1% (P1) and 2% (P2) graphene-Ag nanoparticles respectively.

The samples were obtained by mixing Castavaria resin powder with graphene silver nanoparticles (1% and 2%), using a lab vibrator. Acrylic resin, with and without added fillers, was mixed in the recommended ratio (1 ml/0.95 g monomer: 1.7 g polymer) and then poured into a silicone mold. The experimental composites were cured for 30 minutes, at 55°C and 2.5 Barr, as described in

the commercial product specifications and sticks of 150 mm in length and 15 mm diameter were obtained. The sticks were then sectioned using a cutting device (Isomet 1000 Precision Saw, Buehler) in 15x1 mm disks, further used as samples for the solubility tests. For flexural strength assessment, 10 rectangular samples (25x2x2mm) for each material were fabricated using silicone molds in the same processing conditions.

3. Methods

In our study we assessed the water solubility through the loose of mass [19], according to ISO recommended methods [44]. The tests were performed at room temperature; after initial weighting (m_1) using a digital analytical balance (Adventurer AX224M, Ohaus), specimens were immersed in distilled water at 37°C and weighted again – till a constant weight was obtained - at 2, 7, 14 and 28 days after careful drying with an absorbent paper and a 2 hours storing period in a desiccator (m_3).

Solubility, the property of a substance to dissolve in a solvent, is expressed as the reduction in a sample mass following the immersion in a solvent. We assessed solubility by determining the difference between the initial mass of the sample and its mass measured after immersion and then drying in a dessicator.

The water solubility were calculated as: $Wsl=100x((m_1-m_3)/m_1)$.

Ductility represents the amount of energy per unit volume that a material can absorb prior to fracture. Ductility was assessed by determining the fracture stress and strain values. For an unnotched tensile bar, energy to break is related to the area under a stress-strain curve [8]. Modulus of resilience was calculated after determining the flexural strength and the modulus of elasticity using the formula $R=F^2/2E$, where R is the modulus of resilience, F is the flexural strength and E is the modulus of elasticity.

The flexural strength was assessed with a Lloyd universal testing machine (Lloyd Instruments, Ametek, Farham, UK) using a 3-point bending test. The fracture surface of the specimens was examined using Inspect S, FEI Company Scanning Electron Microscope.

ACKNOWLEDGEMENTS

This study was supported through the PCD 7690/76/15.04.2016 grant, funded by the University of Medicine and Pharmacy Iuliu Hatieganu, Cluj-Napoca.

REFERENCES

1. P. SrinivasRao, P. Mahesh, H. C. Kumar, M. Reddi, N. Rao, *Annals and Essences of Dentistry*, **2012**, *4*, 25.
2. Z. Han, B. Zhu, R. Chen, Z. Huang, C. Zhu, X. Zhang, *Materials & Design*, **2015**, *65*, 1245.
3. M. M. Gad, S. W. Fouda, F. A. Al-Harbi, R. Napankangas, A. Raustia, *International Jourmal of Nanomedicine*, **2017**, *12*, 3801.
4. F. Kundie, C. Azhari, A. Muchtar, Z. Ahmad, *Journal of Physical Science*, **2018**, *29*, 141.
5. D. Devaprakasam, P. V. Hatton, G. Möbus, B. J. Inkson, *Journal of Physics: Conference Series*, **2008**, *126*, 012057
6. P. Makvandi, N. Nikfarjam, N. S. Sanjani, N. T. Qazvini, *Bulletin of Materials Science,* **2015**, *38*, 1625.
7. S. Tripathy, P. Saini, D. Gupta, V. Choudhary, *Journal of Materials Science*, **2013**, *48*, 6223
8. Y. Zhang, D. Rodrigue, A. Aït-Kadi, *Polymers and Polymer Composites*, **2014**, *12*, 17.
9. G. Zappini, A. Kammann, W. Wachter, *Journal of Prosthetic Dentistry*, **2003,** *90*, 578.
10. A. Muraikami, J. C. Behiri, W. Bonfield, *Journal of Materials Science*, **1988**, *23,* 2029.
11. A. O. Alhareb, H. M. Akil, Z. A. Ahmad, *The Saudi Journal for Dental Research*, **2017**, *8*, 26.
12. S. O. Alsharif, H. B. M. Akil, N. A. Abbas, N. A. A. El-Aziz, Z. A. B. Ahmad, *Materials and Design*, **2014,** *54*, 430.
13. B. Patham, P. Poornendu, M. Thejaswini, *Journal of Polymers*, **2013**, 424015.
14. A. Peutzfeldt, E. Asmussen, *Dental Materials*, **1992**, *8*, 146.
15. E. E. Auer, "Abrasion resistance. In: Encyclopedia of polymer science and technology", John Wiley&Sons Inc., **1965**. New York. 1, 7.
16. H. F. Albers, "Tooth colored restorations: A text for selection, placement and finishing. 7th Edition", Alto Books **1985** California., USA.
17. B. Agarwal, C. B.S. Patel, B. P. Singh, A. Kumar, M. Singh, N. Singh, *Indian Journal of Applied Research*, **2015,** *5*, 41.
18. A. Picos, A. L. Rachisan, A. Dadarlat, *Materiale Plastice*, **2018**, *55*, 252.
19. V. M. Miettinen, P. K. Vallitu, D. T. Docent, *Journal of Prosthetic Dentistry*, **1997,** 77, 531.
20. L. V. Lassila, P. K. Vallitu, *Journal of Oral Rehabilitation*, **2001,** *28*, 607.
21. J. Malacarne, R. M. Carvalho, M. F. de Goes, N. Svizero, D. H. Pashley, F. R. Tay, C. K. Yiu, M. R. Carrilho, Dental Materials, **2006**, *22*, 973.
22. S. Sava, M. Moldovan, C. Sarosi, A. Mesaros, D. Dudea, C. Alb, *Materiale Plastice*, **2015**, *52*, 90.
23. I. Cojocariu, M. Moldovan, M. Trif, D. Prodan, V. Popescu, I. Constantinescu, *Materiale Plastice*, **2009**, *46*, 383.

24. M. Moldovan, C. Prejmerean, A. Colceriu, C. Tamas, G. Furtos, D. Prodan, M. Trif, C. Alb, S. Neamt, V. Popescu*, Journal of Optoelectronics and Advanced Materials*, **2007**, 11, 3415.
25. S. Sava, C. Sarosi, S. Boboia, A. Tonea, C. Alb, D. Dudea. *Studia UBB Chemia*, **2015**, *2*, 71.
26. G. Furtos, M. Tomoaia-Costisel, C. Garbo, M. Senila, N. Jumate, I. Vida-Simiti, C. Prejmerean, *Particulate Science and Technology*, **2013,** *31*, 392.
27. C. Sarosi, Al. R. Biris, A. Antoniac, S. Boboia, C. Alb, I. Antoniac, M. Moldovan, *Journal of Adhesion Science and Technology*, **2016**, *30*,1779.
28. P. A. Hari, H. S. Mohammed, *Annals of Essences of Dentistry*, **2011**, *3*, 7.
29. J. Liu, Z. Chen, F. Zhang, G. Ji, M. Wang, Y. Ma, S. Zhong, Y. Wu, H. Wang, *Materials Research Letters*, **2018**, *6*, 406.
30. N. V. Asar, H. Albayrak, T. Korkmaz, I. Turilmaz, *The Journal of Advanced Prosthodontics*, **2013,** *5*, 241.
31. A. Sodagar, A. Bahador, S. Khalil, A. S. Shahroudi, M. Z. Kassaee, Journal of Prosthodontic Research, **2013**, *57*, 15.
32. R. M. German, "Particulate composites: Fundamentals and applications", Springer International Publishing, Switzerland, **2016**, chapter 4.
33. E. H. Alsharaeh, *Materials,* **2016**, *9*, 458.
34. S. Kashyap, K. P. Pratihar, S. K. Behera, *Journal of Alloys and Compounds,* **2016,** *684*, 254.
35. X. Wei, L. Mao, R. A. Soler-Crespo, J. T. Paci, J. Huang, S. Nguyen, D. Horacio, *Nature communications*, **2017**, *8*, 14488.
36. J. F. Woofardt, P. Cleaton-Jones, P. Fatti, *Journal of Prosthetic Dentistry*, **1986,** *55*, 393.
37. M. Kattadiyil, R. Jekki, C. Goodacre, N. Baba, *Journal of Prosthetic Dentistry*, **2015**, 114, 818.
38. S. Singh, J. N. Palaskar, S. Mittal, *Contemporary Clinical Dentistry*, **2013,** *4*, 147.
39. J. L. Garcia-Fierro, J. V. Aleman, *Macromolecules*, **1982**, *15*, 4.
40. M. R. S. Figuerôa, B. Conterno, C. A. G. Arrais, C. Y. C. Sugio, V. M. Urban, K. H. Neppelenbroek, *Journal of Applied Oral Science*, **2018**, *26*, e20170383.
41. A. Jatania, B. M. Shivalinga, *European Journal of Dentistry*, **2014**, *8,* 112.
42. D. Olteanu, A. Filip, C. Socaci, A. R. Biris, X. Filip, M. Coros, M. C. Rosu, F. Pogacean, C. Alb, I. Baldea, P. Bolfa, S. Pruneanu, *Colloids and Surface B: Biointerfaces*, **2015,** *136*, 791.
43. B. Zhang, P. Wei, Z. Zhou, T. Wei, *Advanced Drug Delivery Review*, **2016**, *105*, 145.
44. ISO 1567:1999 Dentistry-Denture base Polymers

STUDIA UBB CHEMIA, LXIV, 2, Tom II, 2019 (p. 483-497)
(RECOMMENDED CITATION)
DOI:10.24193/subbchem.2019.2.41

Dedicated to Professor Ioan Bâldea on the Occasion of His 80th Anniversary

PROVENANCE STUDY ON A SMALL SELECTION OF ROMAN POTSHARDS (TĂŞNAD-SERE SITE, SATU MARE COUNTY, ROMANIA). II

ENIKŐ BITAY[a,d], BERNADETH KISS-PATAKI[b], EMIL INDREA[c], IRÉN KACSÓ[c], FERENC TOLVAY-ROŞCA[a], IOAN BRATU[c], ERZSÉBET VERESS[d*]

ABSTRACT. Characterization of five representative archaeological ceramic shards from the Tăşnad-Sere C 52 site by optical microscopy (OM), XRD, and FT-IR spectroscopy [1] was continued by the detailed analysis of the XRD and FT-IR spectroscopic data in order to obtain a deeper insight into the samples microstructure and mineral composition. The XRD investigations were also extended to several clayish soil samples collected in the archaeological site area. The fresh results permit more exact conclusions about the possible local provenance of the raw materials used by the ancient potters.

Keywords: *archaeological ceramics, provenance, XRD microstructure analysis, FT-IR spectra deconvolution*

INTRODUCTION

Earthenware is modelled (both manually or on potter's wheel) from "green" ceramic paste consisting of moist clays or (calcareous or siliceous) clayish soils, usually tempered with different additives. The "green" earthenware, after desiccation, is baked (sintered) in oxidative or reductive conditions. The highest baking (firing) temperatures possibly achieved in the pottering kilns used in the Roman Empire time were around 1100ºC. [2] During the firing, the tempered green clay paste metamorphoses, the mineral components of the

[a] *Sapientia Hungarian University of Transylvania, Faculty of Technical and Human Sciences, OP 9 CP 4, RO-540485 Târgu-Mureş, Romania*
[b] *Bosch Group in Hungary, Postbox 331, H-1475 Budapest Hungary*
[c] *National Institute for Research and Development of Isotopic and Molecular Technologies, Donath Str. 65-103, RO-400293 Cluj, Romania*
[d] *Transylvanian Museum Society, Napoca Str. 2-4, RO-400750 Cluj, Romania*
** Corresponding authors: ebitay@ms.sapientia.ro; veresserzsebet@gmail.com*

clayey matrix and the additives partly decompose, partly structurally rearrange below 950–1050ºC, forming the strengthened fired ceramic body.

Sintering supposes interactions at atomic and/or molecular level between the constituents of the green clay paste (matrix and temper) implying crystal deformation: the grain boundaries of the clay and temper crystallites start melting and/or re-crystallize. The process takes place via phase transition, resulting in the end a more compact material, the hardened bulk ceramic. Detailed data about the sintering processes (phase decomposition and/or transformation, structural changes of the inhomogeneous multiphase ceramic matrix during the firing) together with certain physical and technological parameters help to clarify the manufacturing method used by the ancient potters. [2] Similarities and differences in some properly selected characteristics of the investigated items (mineralogical and elemental composition, macro- and micro-structural issues) can lead to provenance-related conclusions as well. [3-5]

The XRD and FT-IR spectroscopic investigation of the sample selection formerly presented [1] was carried out with the aim to identify, among others, the sintering-induced vitrification and (re)crystallization processes occurred in - and the depositional changes suffered by - the ceramic shards taken for study. However, the capability of the archaeological ceramics' XRD diffractograms and FT-IR spectra to provide reliable information about the findings (their provenance, sintering conditions, the depositional processes suffered) is limited.

As on the XRD patterns appears (Fig. 1), the strong diffraction lines of quartz and feldspar frequently mask the presence of the minor clay minerals (pyroxenes, iron oxides); in addition, some XRD lines could be minimized due to the transformations occurred during firing or the deposition. [6] In fact, the “primary” XRD data allow only the semi-quantitative estimation of the principal mineral components [1] and the qualitative estimation of the structural ordering, and can't be even used to reliably identify all the (minor) mineral components present.

The FT-IR spectra of the samples published before {1} is dominated by the characteristic broad O–H bands of the ancient ceramics around 3400 and 1600 cm^{-1}, and the strong symmetry band centred at 1050 cm^{-1}, defined by the Si–O, Al–O and Si–O–Al units typically present in fired pottery, both constituted by the overlapped closely neighbouring peaks of the component clay minerals. Intensity and shape of the O–H bands depend, besides the firing conditions, on the deposition related rehydration and/or rehydroxylation, the latter being defined, at the same time, by the burial environment, ceramic composition and structure. The intensity and shape of the 1050 cm^{-1} band which characterizes the connectivity of the Si–O, Al–O and Si–O–Al units, is also defined by the ceramic composition and structure.

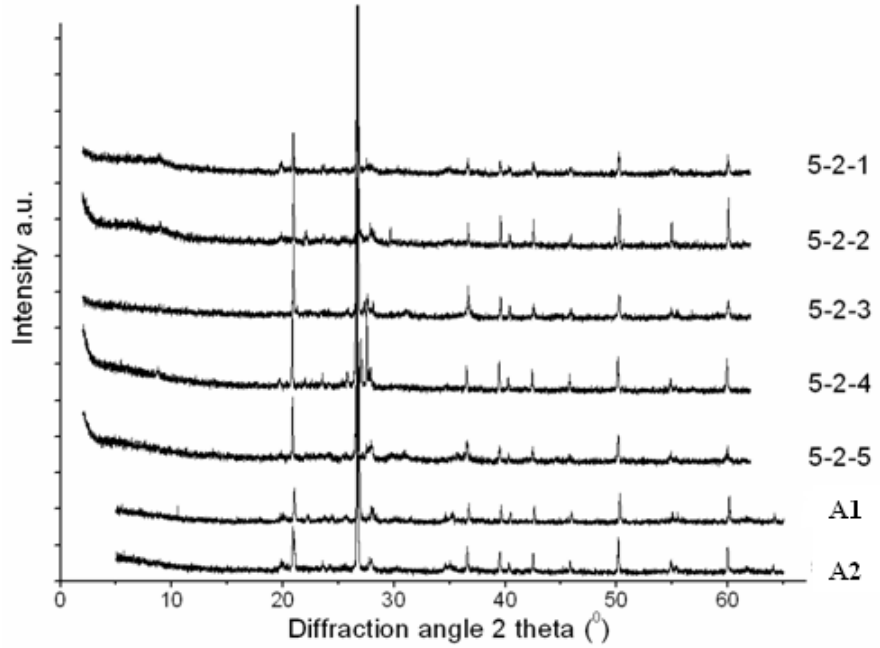

Figure 1. XRD patterns of the studied ceramic samples (5-2-1 to 5-2-5) and of two representative soil samples (A1, A2) (detailed diffractograms of the ceramics presented in [1])

The aim of this study is a more pertinent interpretation of the XRD and FT-IR results, with the aid of additionally derived (small yet significant) similarities or differences of the samples which eventually could lead to a proper classification of the items. This obviously necessitates further micro-structural (XRD) and compositional (XRD, FT-IR) characterization of the samples, starting from (and processing of) the XRD and FT-IR data formerly obtained. In case of multiphase samples, the detailed quantitative XRD crystal phase analysis may be achieved using the crystallites microstructural parameters extracted from the primary diffraction data, applying a Rietveld refinement routine and single X-ray diffraction line profile analysis. [6-8] The broad band generating overlapping FT-IR peaks assigned to the different mineral phases present can be identified by curve fitting deconvolution which mathematically enhances the resolution (without changing the experimental spectra), resolves the overlapped peaks, and allows the identification of the constituting mineral phases, offering a detailed qualitative and quantitative spectrum analysis. [9-12]

RESULTS AND DISCUSSION

Microstructural XRD analysis

XRD is increasingly used for the microstructural characterization of multiphase polycrystalline materials like geological samples or ceramics. [13-16] The position and shape (line broadening) of the experimental diffraction peak are both defined by the microstructure of the material. Peak shifts are related to internal stresses, peak broadenings, apart from that caused by instrumental imperfections, are sample-related: crystallites size distribution and micro-deformations (doping, isotropic or anisotropic micro-strains, stacking faults, etc.).

Microstructural characterization of the ceramic finds and the clayish soil samples collected was performed using the Rietveld method and XRD line profile analysis. [17-20] Experimental data are summarized in Table 1.

Table 1. Microstructural data of the ceramic shards and the soil samples

Sample	Microstructural data								
	V (nm^3)						Q		
	Bt	Mu_2	Mu_3	Orth.	M	Q	Unit-cell edges (nm)		D_{eff} (nm)
							a	c	
5-2-1	0.495	0.921	0.937	0.723	–	0.1126	0.4910	0.5404	124.6
5-2-2	0.492	0.934	0.934	0.725	–	0.1130	0.4914	0.5402	151.6
5-2-3	0.496	0.938	0.929	–	0.164	0.1132	0.4922	0.5396	167.7
5-2-4	0.502	0.938	0.933	–	0.167	0.1122	0.4893	0.5407	43.0
5-2-5	0.494	0.937	0.935	–	0.164	0.1132	0.4915	0.5409	44.1
A1									61.0
A2									63.7
Ref.*	0.498	0.938	0.935	0.725	0.168	0.1130	0.4913	0.5405	

Bt: biotite [3] 1M; Mu2: muscovite 2M(1); Mu3: muscovite [3] 2M(1);
Orth: orthoclase-type K-feldspar; M: mullite; Q: quartz.
*Reference values of AMCSD [21] and mindat.org [22] database.

The predominant mineral components of the ceramic matrix are quartz, (mainly K and some Na feldspars: orthoclase, plagioclase), variable amounts of phyllosilicates (mainly micas: muscovites, biotite) and minor quantities of heavy minerals (pyroxenes, iron oxides). [1] Quartz and feldspars probably play the role of the main temper materials of the clay paste.

Microstructural parameters of the SiO_2 crystallites contained by the ceramic samples were determined considering the α-quartz (100) and (200) XRD line profiles. The experimental unit-cell parameters (edge values *a*, *c*

and unit-cell volumes V) agree well with the AMCSD (American Mineralogist Crystal Structure Database) reference values. Unit-cell volumes for the main mineral components of the ceramic samples were also determined. The differences of the real V values and the mindat.org database reference values are in the experimental error limits in all cases.

Effective mean diameter D_{eff} of the quartz crystallites was determined for the ceramic samples and two of the soil samples collected, A1 and A2. According to the D_{eff} values obtained, the ceramics form three groups: (5-2-1), (5-2-2; 5-2-3), and (5-2-4; 5-2-5), suggesting three different raw material sources. The relative closeness of D_{eff} values found in the soil samples A1, A2 to those of the third ceramic group could indicate (at least in this case) a possible local provenance of the raw materials..

In multiphase samples the phase scattering cross-section for Bragg scattering is proportional to N/V, and N, the number of unit cells which contribute to the scattering, is proportional to I_R. [3] Accordingly, the quantitative phase analysis of the ceramics main mineral components was performed using the corresponding experimental unit-cell volume values, V (Table 1), and the relative peak intensities I_R data published before. [1] Abundance of the main mineral phases (vol%) is summarized in Table 2.

Table 2. Mineral composition of the ceramic samples
(main mineral phases only)

Sample	Mineral phases (vol%)					
	Bt	**Mu_2**	**Mu_3**	**Orth.**	**M**	**Q**
5-2-1	10.99	55.72	–	23.82	–	9.47
5-2-2	8.56	71.45	–	11.81	–	8.18
5-2-3	9.91	56.60	17.38	–	0.51	15.60
5-2-4	1.87	6.57	87.30	–	–	6.26
5-2-5	6.41	71.34	9.40	–	1.30	11.56

Bt: biotite; Mu_2.Mu_3: muscovites; Orth: orthoclase;
M: mullite; Q: quartz.

The values of Table 2 are in general accordance with the semi-quantitative values formerly published [1], with minor differences attributed to the samples overall heterogeneity, determined by the matrix texture, the presence and non-uniform distribution of the pores, of the non-plastic components (clasts) derived from pre-firing residual clay minerals or the applied temper, of newly formed firing minerals, and of post-burial alteration products. Ceramics heterogeneity is influenced, besides the composition of the green clay paste (determined by the raw materials), by the fabrication technology: the paste preparation method (use of levigated clays, with or without temper added), the firing temperature, kiln redox conditions.

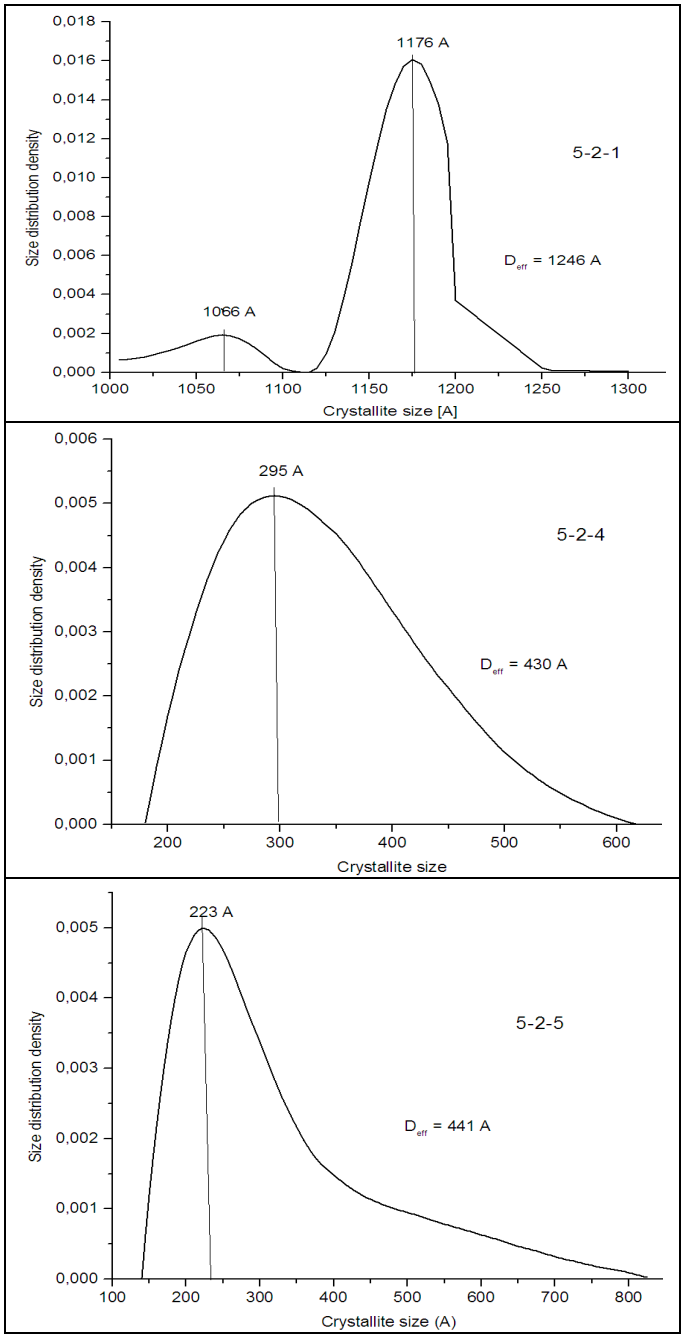

Figure 2. Probability distribution of quartz crystallites size in ceramic samples of hiatal (5-2-1) and serial (5-2-4, 5-2-5) fabric

The size distribution of the crystalline non-plastics characterize the crystalloclasts, added deliberately to the clay mixture as temper material,,or present a priori in the mixture's clay component(s). Typical crystalloclasts of the studied ceramics are quartz, micas, feldspars, and various heavy minerals, mostly iron oxides. [1] Size distribution probability of the most common (quartz) crystallites was determined with the Warren-Averbach XRD line profile analysis of the (100) and (200) SiO_2 quartz peaks, using the XRLINE computer program. [18] The patterns resulted for the 5-2-1, 5-2-4 and 5-2-5 samples are presented on Fig. 2.

The data obtained led to slightly different conclusions about the serial or hiatal character of the ceramic matrix fabric than the former OM results [1], suggesting that the correct interpretation require the knowledge of the similar data obtained for all the main crystalloclasts present in the ceramic system. However, the quartz crystallites size distribution probability curves (defined mainly by the sand naturally present in the green clay or used deliberately as temper) support the same sample grouping as the OM and respectively the D_{eff} data.

The quartz crystallites size distribution probability curves corresponding to the soil samples A1 and A2 were typical clayish soil grain size distribution diagrams. [21-24]

Table 2 data denotes that the amount of the main crystalline phases differ from sample to sample. Considering this and the fact that according the OM data the ceramics contain different types of heavy minerals [1], results that the raw clay(s) cannot have the same provenance. The type of the firing minerals formed and their XRD peaks relative intensity implies that the ceramics were fired in different conditions as well.

The great I_R values resulted for the quartz phase in every sample leads to the conclusion that the tempering of the clay paste was assured mostly by deliberately added alluvial sand.

FT-IR spectroscopy

Infrared spectroscopy is a sensitive tool to monitor the processes occurred during the firing, everyday use and burial of ancient ceramics, as well as to characterize the mineral composition and the (poorly or well) crystallized, sometimes partially glassy structure.

The broad OH bands appearing on the FT-IR spectra of the clayish materials around 3400 cm^{-1} and 1600 cm^{-1}, and the broad symmetry band centred around 1050 cm^{-1} are characteristic for all (more or less disordered) clay based systems. They are formed by overlapping (convolution) of the adjacent characteristic peaks of the constituting minerals. The OH bands

are frequently weakened, or even absent, as their intensity depends, besides the ceramic composition and structural compactness, on the firing conditions and the re-hydration processes taking place during burial, the later being determined by the environmental conditions,. The band around 1050 cm^{-1} characterizes the connectivity of the Si–O, Al–O and Si–O–Al units, being closely related to the structural ordering of the ceramics. [9-11]

Deconvolution of the broad bands can help to differentiate between the ceramic samples, because the constituting mineral phases can be identified through the relative intensities of the –OH, Si–O, Al–O and Si–O–Al units stretching and bending modes. However, the spectral component set is not unequivocal, and attribution (assignment) makes sense only for parent materials belonging to the same or contiguous families. [10] In conclusion, the component bands positions (given by the parameter w), and intensity (given by A), determined using the Origin 8 software (Fourier Self-Deconvolution, FSD), always imply a certain degree of subjectivity. [25] The overall reliability of the deconvolution process in this specific case, is satisfactory, as the basic criteria necessary to be fulfilled in order to consider an acceptable curve-fitting were accomplished (Table 3). The lowest χ^2 (RMS, root-mean-square) values required for good results were reached. (acceptable RMS values has to be of magnitude 10^{-5} for spectra with maximum absorbance values in the 0.05-0.09 range); the below and above fits converge on the same model; the second derivative of the composite sums overlies the second derivative of the original spectra.

Spectral deconvolution of the main peaks of sample 5-2-2, realized by the Gaussian peak-shape function method, is presented on Fig. 3.

As in this case the best goodness-of-fit, measured by the χ^2 parameter, was obtained with a pure Gaussian function, spectral deconvolution was realized using the Gauss profile, taking into account, based on the literature data, the corresponding number of components for each spectral massif. The deconvoluted peaks' absorption frequencies were assigned considering the literature data corresponding to the most common clay minerals and to the previous data obtained on ancient ceramic samples (Table 4). [9-12, 25-39] Since – as exemplified by Fig. 3 for the sample 5-2-2 - the shape of the spectral patterns modelled by the convolution of the calculated absorption bands fit well the experimental spectra, the model can be accepted as correct.

Infrared spectroscopy closely monitors the thermal processes (dehydroxylation, dehydration, redox transformations) taking place during the firing of clay minerals. [40] In this case the weakness or the absence of OH bands and the presence of broad symmetry band centered around 1050 cm^{-1} means that the samples have been fired above 600^0C and were made of a mixture of at least two disordered clays. The presence of iron oxides also confirms the firing temperature as above 600^0C. Prominent peaks at ≈500 cm^{-1} reveals that even if the sample was fired under reduced

atmosphere, air has been allowed at a higher temperature during the cooling, enabling the oxidation of iron components (allowing air during cooling being a common practice for coloration in red of the baked clays). Sandwich structure also indicates firing under reduced atmosphere and admission of the air only at the lower temperature of the cooling.

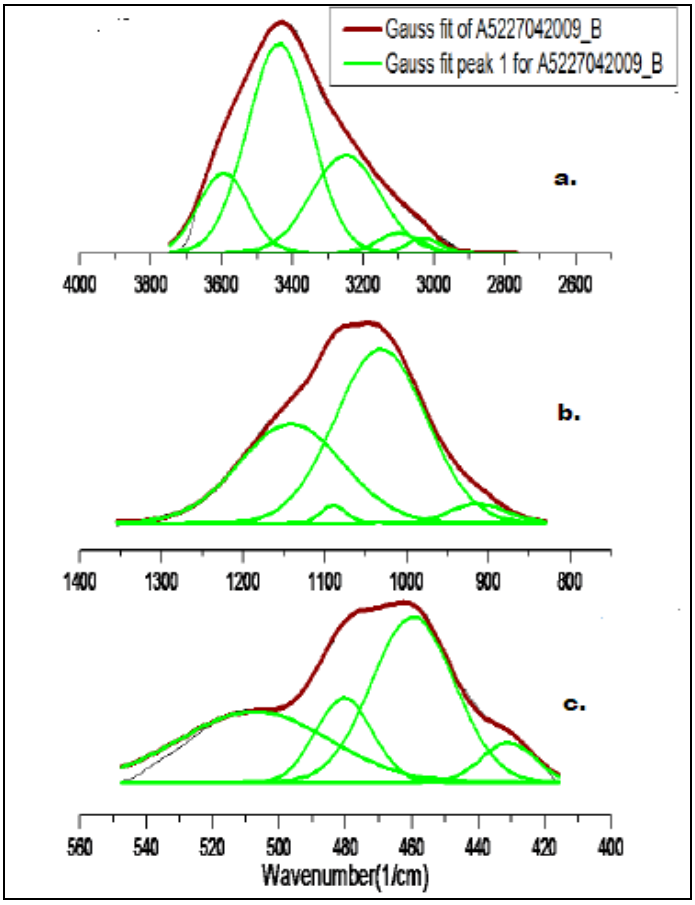

Figure 3. FT-IR spectrum deconvolution for the sample 5-2-2.
Spectral regions: (a) 3800-2800 cm^{-1} (b) 1500-800 cm^{-1}, (c) 600-400 cm^{-1}.

Table 3. FT-IR deconvolution data of the ceramic samples. Resolved bands: 3600-3000 cm^{-1} (O-H band); 1300-850 cm^{-1} (main Si-O / Al-O / Si-O-Al band); 600-400 cm^{-1} (Al-O. Si-O-Al. Si-O-Me. Al-O-Me band). w – peak wavenumber (cm^{-1}); A – peak area

Spectral region	Ceramic sample									
	5-2-1		5-2-2		5-2-3		5-2-4		5-2-5	
	w	A	w	A	w	A	w	A	w	A
3600-3000 cm^{-1}			3595	6.9						
	3568	20.0					3568	7.2	3568	6.2
	3435	40.0	3438	30.0			3435	12.0	3435	7.1
	3290	30.0					3291	9.0	3290	7.5
			3250	15.0						
	3103	12.0	3100	1.8			3103	3.3	3103	3.6
			3030	1.0						
	2940	1.8					2940	0.4	2940	0.4
	2850	1.0					2850	0.1	2850	0.1
χ^2	0.00002		0.00002				0.00002		0.000006	
R^2	0.99737		0.99281				0.99746		0.99814	
1300-850 cm^{-1}									1246	10.0
	1164	44.6			1170	43.8			1158	23.0
			1142	61.6						
							1110	122.		
	1090	3.6	1090	2.6	1084	11.4	1086	5.8	1079	32.5
	1043	164.8	1032	95.1	1054	107.7				
							1012	40.2	990	55.0
	911	5.2	913	6.4			916	5.9		
χ^2	0.00004		0.00003		0.00005		0.0001		0.00013	
R^2	0.9997		0.99957		0.99937		0.99847		0.99487	
600-400 cm^{-1}									513	0.4
	501	12.5	508	6.0	509	7.2	505	4.5		
	481	3.8	480	2.7	483	2.5	478	3.8	483	4.0
	461	10.0	460	7.8	461	16.0	460	2.7	457	5.5
							448	10.0		
	433	4.0	431	1.2	428	2.5			427	1.2
χ^2	0.00003		0.00006		0.00004		0.00006		0.00001	
R^2	0.99847		0.99207		0.99799		0.99397		0.99605	

Table 4. FT-IR deconvolution data of the ceramic samples.
The resolved bands attribution [[9, 10, 27-39].

Wavenumber cm^{-1}	Tentative assignment	Species associated
Spectral domain 3600-3000 cm^{-1}		
3595	O–H str	mica (Na-vermiculite)
3568		mica (Mg-vermiculite)
3438-3435	adsorbed water	montmorillonite, chlorite
3290-3291	N–H str	organic matter remains
3250		
3103-3100	C-H str	organic remains (methyl and methylene sym. and asym. stretching)
3030		
2950		
2840		
Spectral domain 1300-850 cm^{-1}		
1246	C–O str asym. phosphate str	CO_3^{2-} (sample weathering) bone remains (?)
1170-1158	Si–O str	quartz
1142	Si–O/Al–O–Si/O–Si–O str.	quartz, aluminosilicates (kaolinite, illite, smectite, metasmectite)
1110		
1090-1079		
1054-1032		
1012-990	Si-O str.; O–H deform.	kaolinite
918-911	Al–O–H str.; O–H deform.	
Spectral domain 600-400 cm^{-1}		
509-501	Si-O-Al / Fe-O bending	octahedral Al, hematite
483-478	Si–O–Si bending	silicates
461-457		
448	Si–O deform	
433-427		

FT-IR absorption results confirm the mineralogical data obtained by polarized light microscopy and by XRD. The deconvolution results of the 3400 cm^{-1} centered large O-H absorption band, of that of the 1100 cm^{-1} centered Si-O-Si band, and that of the 460 cm^{-1} centered Si-O / Al-O / Si-O-Al band indicate – in concordance with the XRD data - the distinct raw material source (different provenance) of the ceramic samples, as well as their different firing conditions (different fabrication technologies).

CONCLUSIONS

The experimental unit-cell parameters of the SiO_2 crystallites determined by the α-quartz (100) and (200) XRD line profile analysis agree well with the AMCSD (American Mineralogist Crystal Structure Database) reference values. The differences of the real V unit-cell volumes' values determined for the main mineral components of the ceramic samples and the mindat.org database reference values are in the experimental error limits in all cases.

According the effective mean diameter D_{eff} values obtained, the ceramic samples form three groups: (5-2-1), (5-2-2; 5-2-3), and (5-2-4; 5-2-5), suggesting three different raw material sources. The relative closeness of the D_{eff} values of the soil samples A1 and A2 (recolted nearby the archaeological site) to those of the third ceramic group, could suggest a possible local provenance of the raw materials in this case.

The quantitative phase abundance of the ceramics' main mineral components determined using the experimental unit-cell volume values V and the relative peak intensities I_R data published before [1] is in general accordance with the former semi-quantitative values [1], with minor differences which can be attributed to the samples overall heterogeneity, characteristic for archaeological ceramics.

The size distribution data of the quartz crystallites (the most common crystalloclasts) led to slightly different conclusions about the serial or hiatal character of the ceramic matrix fabric than the former OM results [1], suggesting the necessity of the knowledge of the similar data for all the main crystalloclasts present in the ceramic system. However, the size distribution probability patterns confirm the sample grouping resulted from OM and D_{eff} data.

Considering that the amount of the main crystalline phases and the heavy minerals contained by the different samples [1] differ, the raw clay(s) cannot have the same provenance. As the type and abundance of the firing minerals formed also differ, the ceramic technology (firing conditions) differ as well, excepting that (as results from the great I_R values of the quartz phase in every sample) the tempering of the clay paste might be assured by deliberately added alluvial sand.

The weakness or the absence of OH bands and the presence of broad symmetry band centered around 1050 cm^{-1} means that the ceramic samples, made from the mixture of at least two disordered clays, have been fired above 600^0C. The presence of iron oxides also confirms the firing temperature as above 600^0C. Prominent peaks at ≈500 cm^{-1} reveals that even if the sample was fired under reduced atmosphere, air has been allowed at a relatively higher temperature during the cooling, enabling the oxidation of iron components. Sandwich structure observed in the case of sample 5-2-2 [1] also indicates firing under reduced atmosphere and admission of the air during the cooling.

FT-IR absorption results confirm the mineralogical data obtained by other methods. The deconvolution results indicate, in concordance with the microstructural XRD data, different raw material sources and different fabrication technologies (firing conditions) of the ceramic samples.

EXPERIMENTAL SECTION

The powder XRD patterns were obtained as presented before. [1] Unit cell parameters were calculated through Rietveld refinement using the PowderCell software [17-19, 41]. The crystalline phase composition was determined using the MATCH! Phase Identification from Powder Diffraction software together with the "IUCr/COD/AMCSD" reference database [42, 43]. Microstructural informations referring to the SiO_2 crystallites contained in the samples were obtained by Warren-Averbach single X-ray profile analysis [17-19] of the (100) and (200) SiO_2 quartz peak profiles processed by the XRLINE computer program [18].

FT-IR sample preparation and spectra recording were as described in [1]. Deconvolution of the IR absorption bands corresponding to the OH and the SiO (AlO) regions, respectively, was performed using the Origin 8 Pro data analysis software.

ACKNOWLEDGEMENTS

The presented work is partly supported by the research project entitled "Transylvanian technical and cultural legacy. Industrial archaeology, archaeometallurgy and archaeometry" started by the Science and Engineering Department of the Research Institute of the Transylvanian Museum Society.

Our special thanks to Dr. Viorel Ciubotă and Róbert Gindele from the Satu Mare County Historical Museum for entrusting the samples.

REFERENCES

1. E. Bitay, B. Kiss-Pataki, Gy. Szakmány, E. Indrea, I. Kacsó, I. Bratu, E. Veress, *Studia UBB Chemia*, **2017**, *62*, 4/1, 155.
2. G. Eramo, M. Maggetti, *Applied Clay Science* **2013**, *82*, 16-23.
3. M. Emami, Y. Sakali, C. Pritzel, R. Trettin, *Journal of Microscopy and Ultrastructure* **2016**, *4*, 1, 11.
4. C. Rathossi, V. Pontikes, *Journal of the European Ceramic Society*, **2010**; *30*, 9, 1841-1851

5. M.I Dias, A.C Valera, M.I. Prudêncio, *Proceedings of EMAC'03 "Understanding People through their Pottery",* A. Marques de Faria, Ed., *Trabalhos de Arqueologia*, **2005**, *42*, 41.
6. C.T. Kniess, J.C. de Lima, P.B. Prates, *Sintering-Methods and Products*., V. Shatokha, Ed., ISBN: 978-953-51-0371-4, InTech, **2012**, 293
7. R. Martineau, A.V. Walter-Simonnet, B. Grobéty, M. Buatier, *Archaeometry,* **2007**, *49*, 1, 23.
8. G. Barone, L. Bartoli, C.M. Belfiore, V. Crupi, F. Longo, D. Majolino, P. Mazzoleni, V. Venuti, *Journal of Analytical Atomic Spectrometry*, **2011**, *26*, 5, 1060.
9. D. Barilaro, V. Crupi, S. Interdonato, F. Longo, G. Maisano, D. Majolino, V. Venuti, G. Barone, P. Mazzoleni, G. Tigano, S. Imberti, *Il Nuovo cimento della Società italiana di fisica. C*, 31(3), **2008**, 371.
10. S. Shoval, Y. Paz, *Periodico di Mineralogia*, **2015**, *84*, 213.
11. C.I. Fialips, D. Huo, L. Yan, J. Wu, J.W. Stucki, *Clays and Clay minerals*, **2002**, *50*, 4, 455-469.
12. Ph. Colomban, *RSC Analytical Spectroscopy Monographs Vol. 9*, H.G. Edwards and J.M. Chalmers, Eds., Royal Society of Chemistry, **2005**, 192.
13. V. Simić, P. Uhlík, *Geoloski anali Balkanskoga poluostrva*, **2006**, *67*, 109.
14. T. Ungár, P. Martinetto, G. Ribárik, E. Dooryhee, P. Walter, M. Anne, *Molecular and Structural Archaeology: Cosmetic and Therapeutic Chemicals*, G. Tsoucaris, J. Lipkowski, J., Eds., Springer, Dordrecht, **2003**, 211.
15. E. Schafler, M. Zehetbauer, *Reviews on Advanced Materials Science*, **2005**, *10*, 28.
16. T. Ungár, J. Gubicza, *Zeitschrift für Kristallographie-Crystalline Materials*, **2007**, *222*, 3-4, 114.
17. H. Rietveld, *Journal of Applied Crystallography*, **1969**, *2*, 2, 65.
18. N. Aldea E. Indrea, *Computer Physics Communications*, **1990**, *60,* 1, 155.
19. J.G. Van Berkum. A.C. Vermeulen, R. Delhez, T.H. de Keijser, E.J. Mittemeijer, *Journal of applied crystallography*. **1994**, 27, *3,* 345.
20. G.M. Hansford, S.M.R. Turner, P. Degryse, A.J. Shortland, *Acta Crystallographica, A: Foundations and Advances*, **2017**, *73*, 4, 293.
21. R.T. Downs, M. Hall-Wallace, *American Mineralogist*, **2003**, *88*, 1, 247.
22. The Hudson Institute of Mineralogy Database (Mindat.org).
23. G. Cultrone, C. Rodriguez-Navarro, E. Sebastian, O. Cazalla, M.J. De La Torre, *European Journal of Mineralogy*, **2001**, *13*, 3, 621.
24. D.P. Braun, *Journal of Field Archaeology*, **1982**, *9*, 2, 183.
25. S. Roberta, R. Gaetano, J.H. Robin, A.M. De Francesco, *Mediterranean Archaeology & Archaeometry*, **2017**, *17*, 2, 1.
26. M. Hardy, *Clay Minerals*, **1992**, *27*, 1, 47.
27. A. Tinti, V. Tugnoli, S. Bonora, O. Francioso, *Journal of Central European Agriculture*, **2015**, *16*, 1, 1.
28. P. Djomgoue, D. Njopwouo, FT-IR spectroscopy applied for surface clays characterization. *Journal of Surface Engineered Materials and Advanced Technology*, **2013**, *3*, 04, 275.
29. D. Seetha, G. Velraj, *Journal of applied research and technology*, **2016**, *14*, 5, 345.

30. R. Palanivel, U.R. Kumar, *Romanian Journal of Physics*, **2011**, *56*, 1-2, 195.
31. P. Sathya, G. Velraj, *Journal of Experimental* Sciences, **2011**, *2*, 5, 04.
32. T.F.M. Oudemans, J.J. Boon, R.E. Botto, *Archaeometry*, **2007**, *49*, 3, 571.
33. A. Dazzi, C.B. Prater, *Chemical reviews*, **2016**, *117*, 7, 5146.
34. S. Dallongeville, N. Garnier, C. Rolando, C. Tokarski, *Chemical reviews*, **2015**, *116*, 1, 2.
35. L. Bachmann, R. Diebolder, R. Hibst, D.M. Zezell, *Spectrochimica Acta, A: Molecular and Biomolecular Spectroscopy*, **2005**, *61*, 11-12, 2634.
36. G. Ricci, L. Caneve, D. Pedron, N. Holesch, E. Zendri, *Microchemical Journal*, **2016**, *126*, 104.
37. M. Diko, G. Ekosse, J. Ogola, *Acta Geodynamica and Geomaterialia*, **2016**, *13*, 2, 149.
38. P. Sathya, G. Velraj, S. Meyvel, *Advances in Applied Science Research*, **2012**, *3*, 2, 776.
39. L. Vaculikova, E. Plevova, S. Vallova, I. Koutnik, *Acta Geodynamica et Geomaterialia*, **2011**, *8*, 1, 59.
40. G.E. De Benedetto, R. Laviano, L. Sabbatini, P.G Zambonin, *Journal of Cultural Heritage*, **2002**, *3*, 3, 177.
41. G. Nolze, PowderCell: A mixture between crystal structure visualizer, simulation and refinement tool. *Powder Diffraction: Proceedings of the II International School on Powder Diffraction*, **2002**, 146.
42. http://www.crystalimpact.com/match/
43. T.T. Downs, M. Hall-Wallace, *American Mineralogist* **2003**, *88*, 247.

STUDIA UBB CHEMIA, LXIV, 2, Tom II, 2019 (p. 499-508)
(RECOMMENDED CITATION)
DOI:10.24193/subbchem.2019.2.42

Dedicated to Professor Ioan Bâldea on the Occasion of His 80th Anniversary

A PREDICTIVE TOXICITY STUDY OF PEIs, PAMAM AND ZAC DENDRIMERS

CLAUDIU N. LUNGU[a*], CSABA PAIZS[a], MELINDA E. FÜSTÖS[a], ANAMARIA ORZA[a], MIRCEA V. DIUDEA[a], IRENEUSZ P. GRUDZINSKI[b]

ABSTRACT. Polyethyleneimines (PEIs) and polyamidoamine dendrimers (PAMAM) are widely used as non-biological transporters in modern gene therapies. In this study, several zero-generation aromatic core "ZAC" dendrimers were computationally studied for predictive toxicity assessment. The chemical synthesis of the ZAC dendrimers was carried out using three different bromomethylbenzene derivatives as aromatic core and dialkanolamines as branching units with different carbon chain length. Quantitative structure-activity relationships (QSAR) and virtual high throughput toxicity screening (vHTTS) assays were applied on the synthesized zero generation dendrimers to evaluate their toxicities.

Keywords: *molecular descriptors, pharmacophore, QSAR, continuous structures, toxicity, maximum recommended daily dose, dendrimers.*

INTRODUCTION

Quantum structure activity relationship (QSAR) methods are widely used in toxicity prediction [1]. A QSAR model is used to predict accurately compounds properties that belong to the same chemical space as the compounds used in training set [2]. Small molecules or molecular fragments

[a] *Department of Chemistry, Faculty of Chemistry and Chemical Engineering, Babeș-Bolyai University, Arany János Str 11, 400028, Cluj, Romania*
[b] *Department of Applied Toxicology, Faculty of Pharmacy, Medical University of Warsaw, Banacha 1, 02-097 Warsaw, Poland*
** Corresponding author: lunguclaudiu5555@gmail.com*

are ideal tools of exploring a chemical space. In case of macromolecular compounds (*e.g.*, polymers, dendrimers) building regression models based on parts of these molecules is not an accurate approach mainly because in the materials science parts of a structure don't preserve a proportional properties amount (in comparison to ligand-receptor systems, where the fragment-based concept is well known).

Testing toxicity especially in case of nanostructures is expensive mostly because toxicity properties are not additive. Being applied on a series of compounds (or molecular fragments) with similar chemical structure, these methods not always return correct data. Errors are due to both non-additive properties and degeneration of variables (*i.e.*, descriptors) used in building QSAR models. The back trucking may be avoided using virtual High Throughput Toxicity Screening (vHTTS) [3]. This method provides a large amount of unique/specific data for building a QSAR toxicity model.

Selecting small compounds with known toxicities, one covers a large region of the chemical toxicity space, making the model more powerful in terms of prediction.

RESULTS AND DISCUSSIONS

PAMAM and PEI properties were analyzed. Figure1 illustrates their QSAR property space [4]. Chemical space shapes are relatively the same for all PEI, PAMAM and ZAC dendrimers, respectively.

All PAMAM and PEIs herein analyzed for genotoxic and carcinogenic properties do not have such effects due to computation studies. The computational studies for the Ames test (*Salmonella typhimurium*) also turned the negative results for all the compounds studied here. The *in silico* structure biodegrability test predicted a class 2 persistent chemical (tertiary amine) for all compounds. Computation tests performed for biotransformation processes due to cytochrome P450 evidenced for PAMAM both N-dealkylation and N-oxidation, respectively. *In vitro* micronucleus assay based on QSAR showed a H acceptor path 3 h acceptor class 1 for PAMAM series. A multiple linear regression model was computed using PEI and PAMAM. The computed pharmacophores are shown in Figure 2.

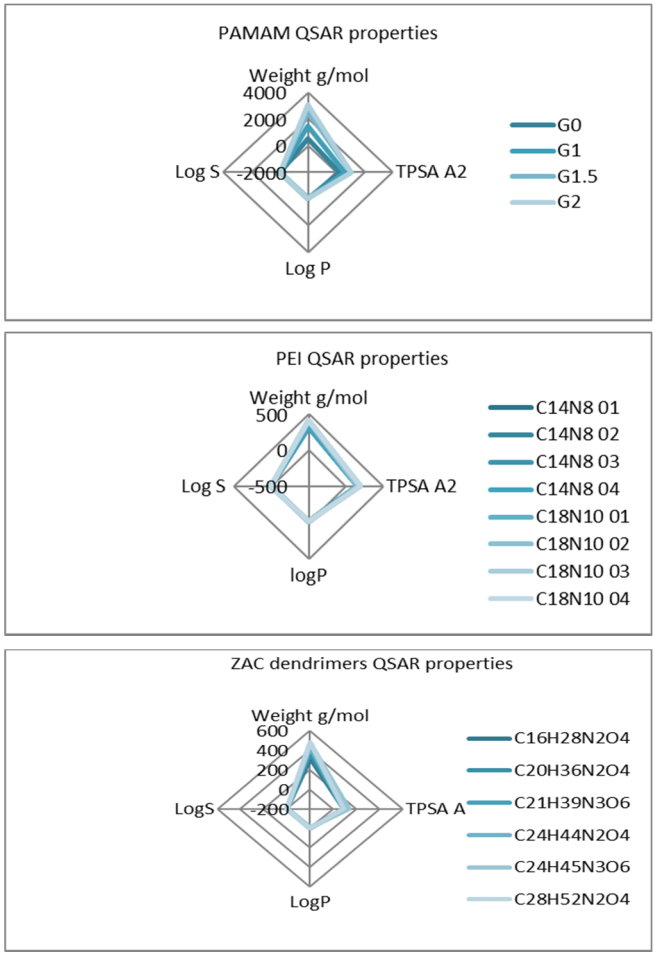

Figure 1. PAMAM/PEI and ZAC dendrimers QSAR properties

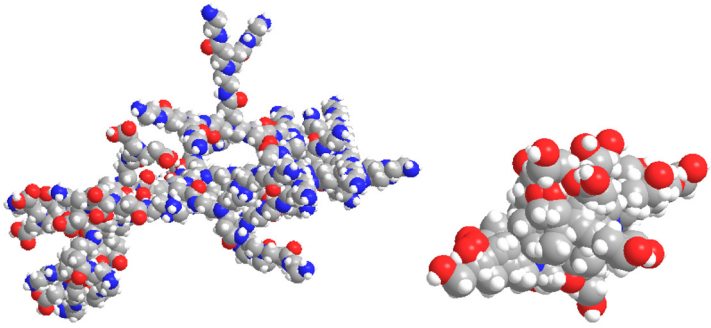

Figure 2. Pharmacophore structures form left to right: PEI/PAMAM and ZAC pharmacophore, respectively

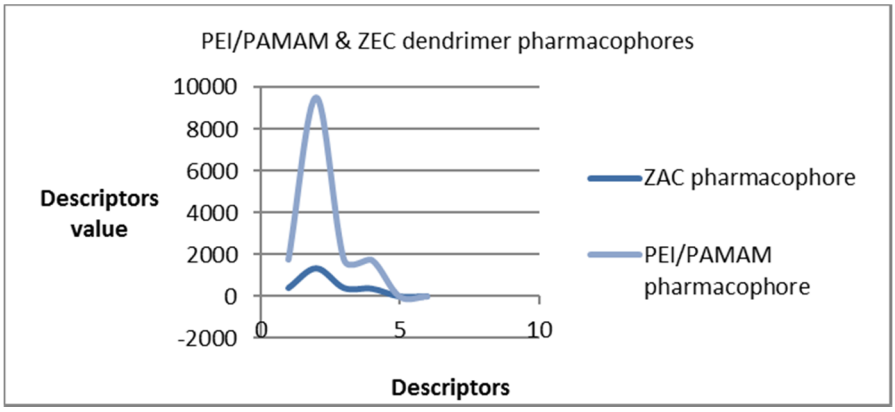

Figure 3. Topological properties of PEI/PAMAM and ZAC dendrimers. Topological properties are represented (from left to right) as follows: 1 cluster count; 2 polar surface area A^2 (PSA); 3 shape attribute; 4 sum of valence degrees; 5 total connectivity; 6total valence connectivity

After minimization of the two pharmacophores (for PEI/PAMAM and ZAC) and consecutively hydrogen bond forming, continuous structures resulted, as shown in Figure 4.

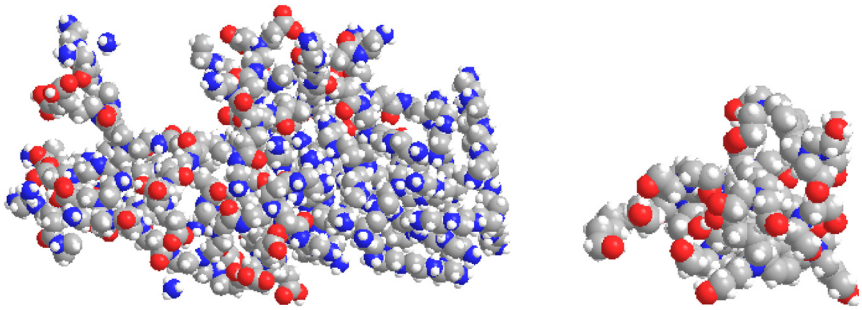

Figure 4. PEI/PAMAM and ZAC dendrimers pharmacophore molecules

Topological properties for the newly resulted molecules (derived from PEI/PAMAM and ZAC pharmacophores) and for the corresponding pharmacophores are shown in Figure 5.

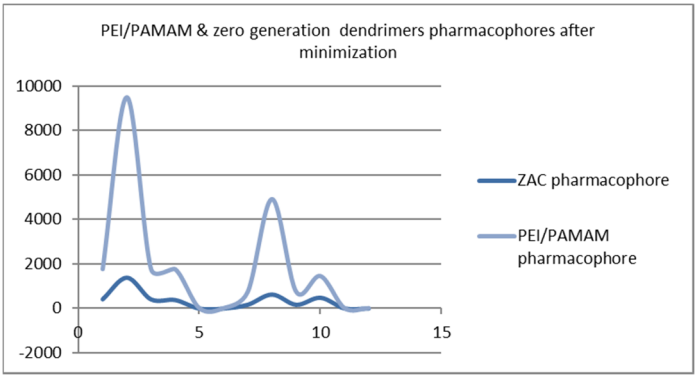

Figure 5. Topological properties of PEI/PAMAM and ZAC dendrimers, newly resulted molecules. Topological properties are represented (from left to right) as follows: 1 cluster count; 2 polar surface area A^2 (PSA); 3 shape attribute; 4 sum of valence degrees; 5 total connectivity; 6total valence connectivity; 7 cluster count minimized; 8 polar surface area minimized A^2 (PSA); 9 shape attribute minimized; 10 sum of valence degrees minimized; 11 total connectivity minimized; 12 total valence connectivity minimized.

Multiple linear regression model [5, 6, 7] was obtained having as independent variable the acute toxicity and as dependent variables the number of H,C, N atoms, molecular weight, total number of atoms, number of heavy atoms, rotation degree, number of hydrogen accepting and donor groups, Anderson charges, minimum distance between two hydrogen distinct donor groups, minimum distance between an H-donor and an H-accepting group, mean distance between two H-donor groups, mean distance between an H-donor and an H-accepting group, Wiener index, logP. All data were used on the training set, resulted in a Pearson correlation of R^2=0.996 with y=0.00165321+ 0.991084x; the cross validated square was 0.991084 (Figure 6).

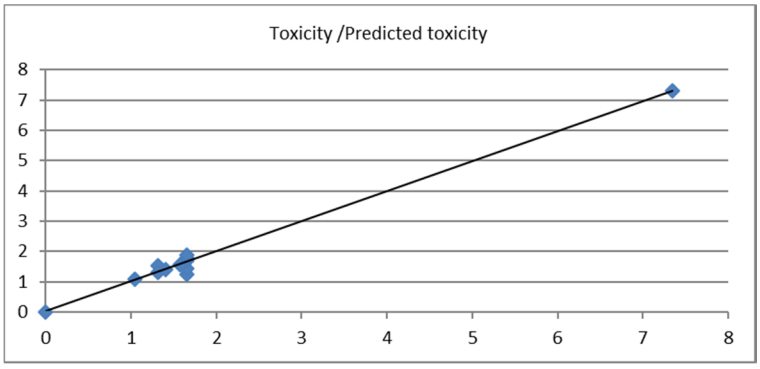

Figure 6. Correlation between toxicity doses used to model the data and the predicted toxicity doses

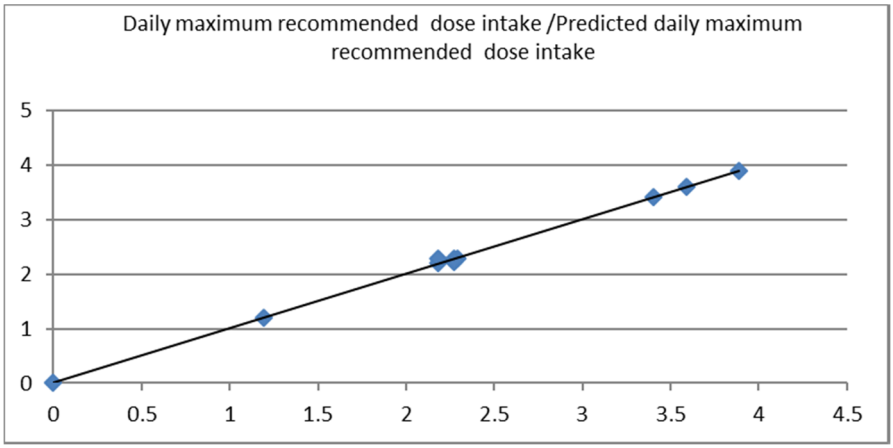

Figure 7. Correlation between daily maximum dose intake used to model data and predicted dose intake.

A model was computed for the prediction of daily dose intake using the maximum daily dose intake as the independent variable [8,9,10]; Person correlation value was R^2=0.999 with y=0.00274498+0.998815x, with cross validated square of Q^2=0.998815 (Figure 7). The K test was applied for the model in Figures 7-9 and no out layers were detected. Models were validated using leave one out technique.

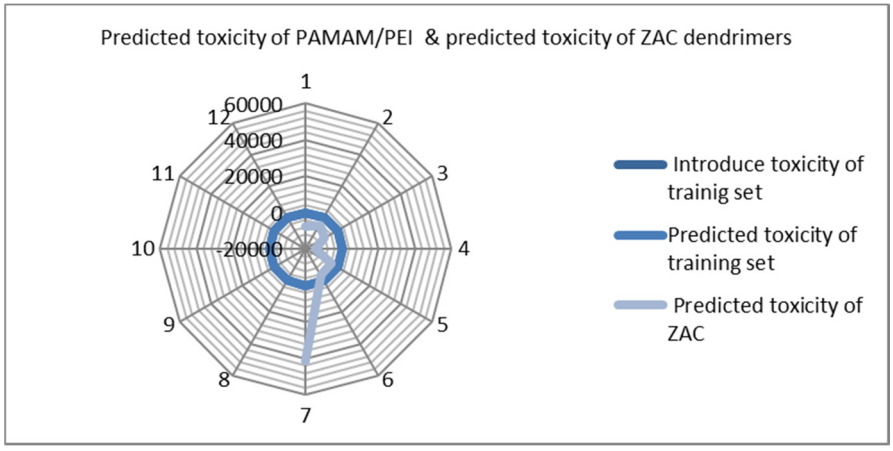

Figure 8. Toxicity values obtained for the studied series using the QSAR model.

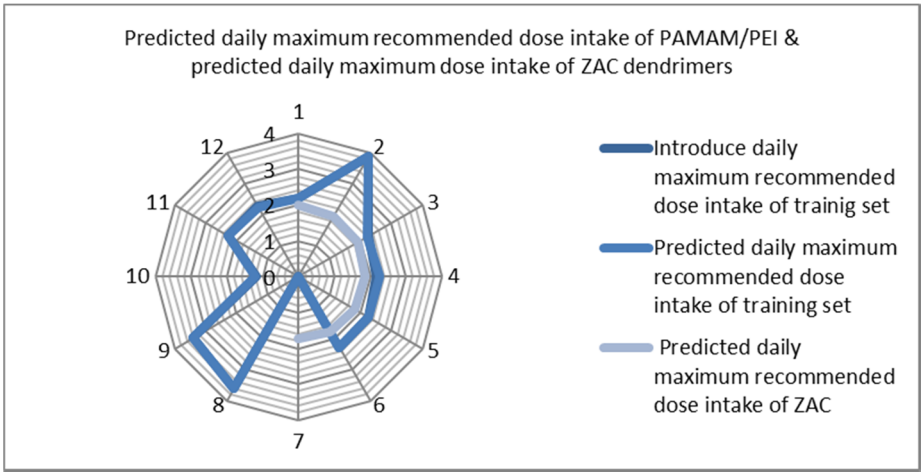

Figure 9. Daily maximum recommended doses for the dendrimer series using the QSAR model.

Data show that ZAC dendrimers are less recommended than the PAMAM/PEI compounds.

CONCLUSIONS

PEIs and PAMAM dendrimers have no evidences on genotoxic effect based on computational models established for the AMES test. All these polymers are classified as the class 2 persistent chemical (tertiary amine). *In silico* tests for cytochrome P450-based biotransformation processes evidence for PAMAM some N-dealkylation and N-oxidation biotransformation pathways having possible interaction with drugs metabolized by the same CYP isoforms. *In silico* computational micronucleus assay has shown a H-acceptor path 3 H-acceptor class 1 for PAMAM series expressing its potential interaction with the genetic material. The synthesized ZAC dendrimers are found to be 1000 times more toxic than PAMAM and PEIs in terms of acute toxicity and maximum daily intake dose as predicted by the QSAR model, which showed a decrease in doses of the ZAC dendrimers comparative to PEI and PAMAM, respectively.

The chemical space of QSAR properties of the model and of the ZAC compounds (see Figure 1) have the same shape and thus the prediction of the model is presumably accurate.

Furthermore, by computed topological properties of both pharmacophores, it was suggested that there is a slight overlap of the training (PAMAM/PEI) pharmacophore and the pharmacophore of ZAC dendrimers. By this reason, the correlation of these properties with the total connectivity and total valence connectivity is less predictive.

Having the same QSAR space, respectively the same topological variation of properties as the training (PAMAM/PEI) set and also high Pearson correlation (R^2=0.996 and 0.999, respectively) it is expected that ZAC dendrimers will have reduced doses than PEI/PAMAM (i.e., the acute dose for ZAC is 1000 smaller than for PEI/PAMAM).

EXPERIMENTAL SECTION

The studied ZAC dendrimers were chemically synthesized according to the literature procedure described by Füstös *et al*. [11]. To data, 1,4-bis(bromomethyl)benzene, 1,3,5-tris(bromomethyl) benzene and 1,3,5-tris(bromomethyl)-2,4,6-trimethylbenzene were used as the aromatic core. Derivatization was performed with the commercially available diethanolamine (DEA) and the “ad-hoc” prepared dipropanolamine, dibutanolamine and dipentanolamine, respectively. General procedure of preparation for ZAC compounds # 1-6 is shown in Figure 10. To a solution of bromomethylbenzene in acetonitrile, the corresponding dialkanolamine was added under continuous stirring.

In order to avoid the dialkanolamine hydrobromide salt formation due to the resulting hydrobromic acid, potassium carbonate was added in excess. The reaction mixture was refluxed for 24 hours, being monitored on thin layer chromatography (eluent hexane:toluene 7:3). The resulted precipitate was separated by vacuum filtration, while the filtrate was evaporated at reduced pressure to give the crude product. After purification the dendrimers were obtained as viscous lightly yellowish liquids. Their structure was confirmed by NMR (^{1}H, ^{13}C) spectroscopy and mass spectrometry [12]. A polyamidoamine (PAMAM)/polyethylenimines (PEI) database was generated in order to perform a vHTTS.

A pharmacophore model (see below) was developed for the 6 ZAC compounds listed in Figure 10. A vHTTS screening was performed on this database (6 aromatic core dendrimers + 8 PEI + 4 PAMAM structures) and the results were sent to the QSAR procedure (5). PAMAM (of generation 0; 1; 1.5 and 2) and PEI ($C_{14}N_8$ and $C_{18}N_{10}$) were computed, in order to establish their chemical space and finally their own toxicity. The toxicity

assessment due to QSAR model was computed using a decision tree software [13]. In order to establish the reliability of the model, pharmacophores used for generating the model (PEI/PAMAM pharmacophore) and the pharmacophore of ZAC dendrimers were studied topologically.

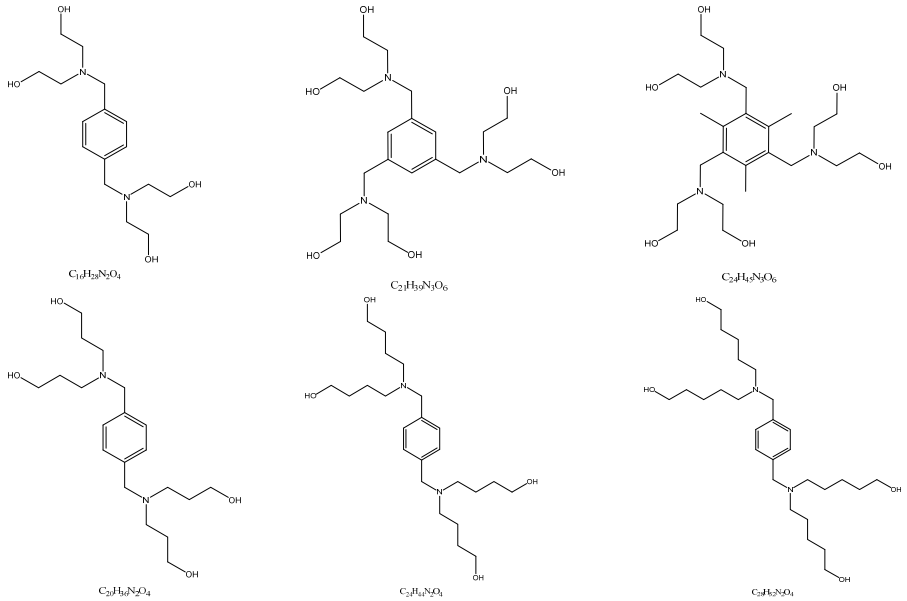

Figure 10. Synthesized ZAC dendrimers-target for vHTTS.

ACKNOWLEDGMENTS

This work was supported by GEMNS project granted in the European Union's Seventh Framework Program under ERA-NET EuroNanoMed II (European Innovative Research and Technological Development Projects in Nanomedicine).

REFERENCES

1. R. Hood, *Developmental and reproductive toxicology*: *a practical approach*, 3rd ed., CRC, Boca Raton, FL, **2011**.
2. V.C. Arena; N.B. Sussman; S. Mazumdar; S. Yu; O.T. Macina; *SAR QSAR Environ. Res.*, **2004**,*15*, 1-18.
3. C. Hansch; A. Leo; S.B. Mekapati; A. Kurup; *Biorg. Med. Chem.,* **2004**, *12*, 3391-3400.
4. T. Langer; G. Wolber; *Pure. App. Chem.*, **2004**, *76*, 991-996.

5. M.E. Füstös; T.A. Sipos; M.V. Diudea; G. Katona; *Croat. Chem. Acta*, **2015**, *88,* 129-132.
6. M.V. Diudea; C.N. Lungu; C.L. Nagy; *Molecules*, **2018**, *23*, 2533.
7. C.N. Lungu; S. Ersali; B. Szefler; A. Pirvan-Moldovan; S. Basak; M.V. Diudea; *Studia UBB, Chemia*, **2017**, *62*, 197-204.
8. A. Vedani; M. Dobler; M. Smieško; *Toxicol. Appl. Pharmacol.,* **2012**, *261*, 142-153.
9. A.J. Leo; C. Hansch; *Perspect. Drug. Discov. Design,* **1999**,*17*, 1-25.
10. C.N. Lungu; M.V. Diudea; M.V. Putz; *Int. J. Mol. Sci.*, **2017**, *18*, 1377.
11. S. Kim; E.E. Bolton; S.H. Bryant; *J. Cheminform.,* **2011**, *3*, 26.
12. R. Perkins; H. Fang; W.D. Tong; W.J. Welsh; *Environ. Toxicol. Chem.,* **2003**, *22*, 1666-1679.
13. C.N. Lungu; B.I. Bratanovici; M.M. Grigore; V. Antoci; I. Mangalagiu; *Curr. Med. Chem.*, **2018**, doi: 10.2174/0929867326666181220094229.

STUDIA UBB CHEMIA, LXIV, 2, Tom II, 2019 (p. 509-516)
(RECOMMENDED CITATION)
DOI:10.24193/subbchem.2019.2.43

Dedicated to Professor Ioan Bâldea on the Occasion of His 80th Anniversary

SYNTHESIS AND ANTIOXIDANT CAPACITY OF (CHLOROBENZYLIDENE)HYDRAZINYL-THIAZOLES

ADRIANA GROZAV[a], DANIELA HANGANU[a*], OVIDIU CRISAN[a], DAN PORUMB[b] AND CASTELIA CRISTEA[b]

ABSTRACT. 2-(chlorobenzilidene)hydrazinyl-thiazole derivatives were conveniently prepared by Hantzsch reaction protocol, starting with thiosemicarbazone and ethyl 2-bromo-3-oxo-3-phenylpropanoate. Their antioxidant capacity was screened by electron transfer based assays. The results of both DPPH (1,1-Diphenyl-2-picrylhydrazyl) free radical scavenging, as well as Ferric Ion Reducing Antioxidant Power (FRAP) assay, indicated antioxidant capacity for the tested hydrazone derivatives. At the concentration of 9.5 μg/mL, the DPPH radical scavenging activity of ethyl 2-(2-(3-chlorobenzylidene)hydrazinyl)-4-phenylthiazole-5-carboxylate was found to be more than 93%.

Keywords: *synthesis, thiazoles, antioxidant capacity, DPPH, FRAP*

INTRODUCTION

The literature data designate the thiazole derivatives as an important class of heterocyclic compounds exhibiting remarkable pharmacological activities. The thiazole core can be often recognized in the structure of commonly used antimicrobial, antifungal or antiretroviral agents, as well as nonsteroidal anti-inflammatory drugs. [1.].

[a] *Faculty of Pharmacy, "Iuliu Haţieganu" University of Medicine and Pharmacy, RO-400012, Victor Babes 41, Cluj-Napoca, Romania*
[b] *"Babeş-Bolyai" University, Faculty of Chemistry and Chemical Engineering, RO-400028, Cluj-Napoca, Romania*
** Corresponding author: dhanganu@umfcluj.ro*

Our previous results in the synthesis and characterization of biologically active novel thiazole derivatives described several 2-hydrazinyl-thiazole derivatives which displayed antibacterial, analgesic, or anti-inflammatory activities [2-5]. Various heterocyclic systems containing thiazole units joint or fused to other aromatic moieties were synthesized and several aspects of their biological activities were described; thus, some benzothiazolo-phenothiazine derivatives exhibited antimicrobial activity [6-9], while *bis*(thiazolyl)-, phenothiazinyl- and indolyl-thiazolylhydrazine derivatives were screened for their anticancer potential [10-19] in search for new antitumour agents producing less hypersensitivity side reactions (which might occur due to platinum complexes which are currently employed in the cancer therapy. [20]). Two ((1*H*-indol-5yl)methylene)-hydrazinyl)-thiazole derivatives were found to be promising antioxidant agents based on DPPH (1,1-Diphenyl-2-picrylhydrazyl) radical scavenging assay; the chemoselectivity of radicals formation was supported by theoretical computational data indicating the extraction of the hydrogen atom from the NH group located in the hydrazinyl bridge rather than in the indole heterocyclic unit. [19]

In this work, we present an extension of our investigations in the area of thiazole derivatives by describing the synthesis and antioxidant capacity of two additional 2-((chlorobenzylidene)hydrazinyl)-thiazole derivatives. A comparison of the antioxidant capacity of thiazole derivatives with their thiosemicarbazone synthetic precursors and typical control compounds (Trolox and Ascorbic acid) was enabled by the results displayed in DPPH radical scavenging activity and ferric reducing antioxidant power (FRAP) assays.

RESULTS AND DISCUSSION

Synthesis of 2-(chlorobenzylidene)hydrazinyl)-thiazole derivatives

The synthetic route towards the 2-(chlorobenzylidene)-hydrazinylthiazoles **3a,b** was designed by taking advantage from the broad scope of the Hantzsch reaction [21]. Thus, thiosemicarbazone precursor **2a,b** (previously prepared by the condensation of chloro-benzaldehyde derivatives **1a,b** [2]) and ethyl 2-bromo-3-oxo-3-phenylpropanoate were subjected to the cyclocondensation reaction as shown in Scheme 1.

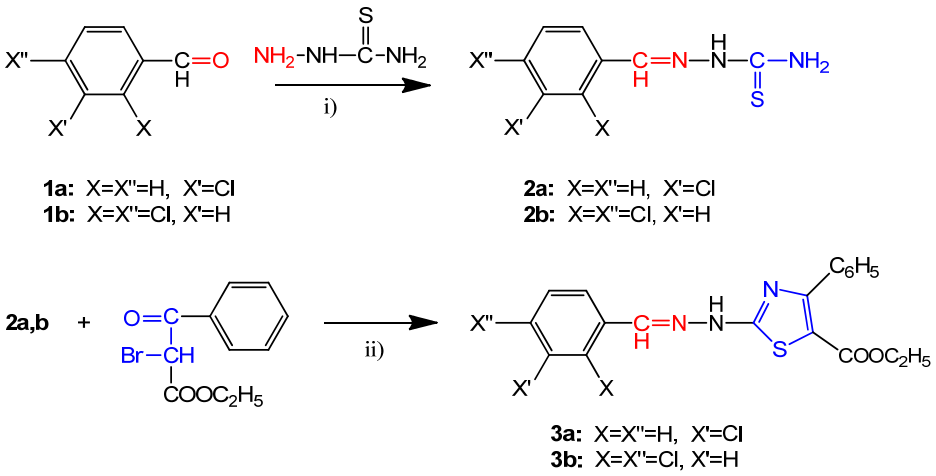

1a: X=X''=H, X'=Cl
1b: X=X''=Cl, X'=H

2a: X=X''=H, X'=Cl
2b: X=X''=Cl, X'=H

3a: X=X''=H, X'=Cl
3b: X=X''=Cl, X'=H

Scheme 1. Synthesis of 2-(chlorobenzylidene)hydrazinyl-thiazole derivatives; conditions: *i) ethanol, 2h, reflux, ii) Acetone/DMF (v/v): 1/0.2, 24h, r.t.*

The structures of thiosemicarbazone intermediates **2a,b** and 2-(chlorobenzylidene)-hydrazinylthiazole derivatives **3a,b** were confirmed by NMR spectroscopic data.

Antioxidant capacity

The antioxidant ability of chemical compounds might be due to free radicals scavenging, metal ions chelating and hydrogen atoms or electrons transferring [22]. In our study, the antioxidant capacity of the synthesized series of hydrazone derivatives was screened by using electron transfer based assays measuring the capacity of an antioxidant in the reduction of an oxidant which changes colour upon reduction. The UV-Vis spectrophotometric monitoring of the reaction offered the possibility of correlating the degree of colour change with the antioxidant concentration. As it may be seen from table 1, thiosemicarbazones **2a,b** and 2-(chlorobenzylidene)hydrazinyl-thiazole derivatives **3a,b** displayed antioxidant capacity determined by DPPH radical scavenging and FRAP assays.

Table 1. The antioxidant capacity of synthesized hydrazone derivatives

Compound	Methods		
	DPPH		FRAP
	IC 50 [μg/mL]	I%	[μM ET/g]
2a	13.64 ± 0.52	65.50 ± 0.64	229.04 ± 1.2
2b	15.57 ± 0.72	56.52 ± 0.53	312.86 ± 0.9
3a	9.55 ± 0.61	93.88 ± 0.72	1710.38 ± 1.5
3b	16.45 ± 0.37	60.70 ± 0.67	11.62 ± 0.6

In the reaction with DPPH radical, both semicarbazone derivatives **2a,b** and 2-(chlorobenzylidene)hydrazinyl-thiazoles **3a,b** determined the colour change of DPPH radical solution from purple to yellow. The reaction was monitored by the decrease of absorbance intensity at λ_{max} = 517 nm, measured after a reaction time of 30 minutes. The DPPH free radicals scavenging potential of the tested compounds was expressed by:

a) the concentration of tested hydrazone derivative that causes a decrease in the initial DPPH concentration by 50% (IC_{50})
b) the percent DPPH scavenging ability (I%) was calculated as:

$$I\% = (A_{control} - A_{sample}/A_{control}) \times 100$$

where $A_{control}$ is the absorbance of DPPH radical in methanol solution
A_{sample} is the absorbance of DPPH radical in solution in the presence of the tested hydrazone derivative.

According to the results presented in Table 1, the DPPH free radicals scavenging potential of the tested hydrazones decreased in the following order: **3a**>**2a**>**2b≈3b**. At the concentration of 9.5 μg/mL, the DPPH radical scavenging activity of hydrazinyl-thiazole **3a** was found to be more than 93%. In terms of concentration that causes a decrease in the initial DPPH concentration by 50%, the antioxidant capacity of **3a** appears comparable to the phenolic standard Trolox (IC_{50} = 9.74 μg/mL), but lower than the ascorbic acid standard (IC_{50} = 2.46 μg/mL).

The reducing capacity of hydrazones **2a, 2b, 3a** and **3b** has been assed using the FRAP assay, which is based on another electron transfer reaction where a ferric salt, is used as an oxidant ($Fe(III)(TPTZ)_2Cl_3$ where TPTZ 2,4,6-tripyridyls-triazine). The reduction of Fe^{3+} to Fe^{2+} and thus the formation of the blue coloured $Fe(TPTZ)^{2+}$ complex depends on the electron donating capacity of the tested compounds, which was quantified by the UV-Vis spectrophotometric method. The reducing ability of the hydrazones decreases in the following order: **3a** > **2b** > **2a >3b** (see Table 1 where the results are quantified as μM Trolox equivalents/g).

The results of both electron transfer assay (the DPPH and FRAP), indicate **3a** as the most efficient antioxidant in the tested series. A structure-activity correlation points towards a superior electron donor ability of **3a,** explainable by the presence of the pi-electron-excessive heterocycle thiazole.

The electron withdrawing effect induced by the second chlorine atom introduced as a substituent of the benzylidene aromatic ring, decreased the overall electron donor ability of **2b** and **3b** and thus their overall antioxidant capacity.

CONCLUSIONS

The results of two electron transfer assays (the DPPH assay and FRAP assay) applied in this study, indicate monochlorobenzylidenehydrazinyl-thiazole **3a** as the most efficient antioxidant in the tested series containing the chlorobenzylidene-hydrazinyl-thiazole and the similarly mono and dicloro substituted thiosemicarbazones.

EXPERIMENTAL SECTION

Materials and Methods

The starting materials and solvents were obtained from commercial sources from Sigma-Aldrich. Melting points were measured with an Electrothermal IA 9200 apparatus (Bibby Scientific Limited (Group HQ), Stone, UK).

NMR spectra were recorded at room temperature on 400 MHz Bruker Avance instruments. Chemical shifts are expressed in δ (ppm) relative to standard tetramethylsilane (TMS).

Compounds **2a,b** were prepared according to the previously reported procedure [2].

General procedure for the synthesis of 2-(chlorobenzylidene)hydrazinyl-thiazole derivative ***3a,b***

A mixture of arylidene-hydrazine-carbothioamide **2a/b** (10 mmol) and ethyl-2-bromo-3-oxo-3-phenylpropanoate (10 mmol) in acetone/DMF (15 mL, *v/v*: 1/0.2) was stirred at room temperature for 20–24h. The reaction mixture was neutralized at pH 7 with $NaHCO_3$ aqueous solution (10%). The precipitate was filtered and recrystallized from ethanol.

Ethyl 2-(2-(3-chlorobenzylidene)hydrazinyl)-4-phenylthiazole-5-carboxylate **3a**

White crystals, yield 82%, m.p. 193–194 °C,

^{1}H-NMR (400MHz, $CDCl_3$) *δ*ppm: 1.33 (*t*, 3H, CH_3), 4.3 (*q*, 2H, O-CH_2), 6.59 (*s*, 1H, CH=N), 7.18 (*d*, 1H) 7.3 (*m*, 3H), 7.41 (*t,* 1H), 7.48 (*t*, 2H), 7.85 (*m*, 2H), 10.5 (*broad*, 1H, NH)

Ethyl 2-(2-(2,4-dichlorobenzylidene)hydrazinyl)-4-phenylthiazole-5-carboxylate **3b**

Light yellow crystals, yield 91%, m.p. 208–209 °C,

^{1}H-NMR (400MHz, $CDCl_3$) *δ*ppm: 1.32 (*t*, 3H, CH_3), 4.28 (*q*, 2H, O-CH_2), 7.22 (*s*, 1H, CH=N), 7.3 (*m*, 5H), 7.8 (*m,* 3H), 9.9 (*broad*, 1H, NH)

Antioxidant capacity

a) DPPH Free Radical Scavenging Activity

A DPPH solution (0.1g/L) in methanol was prepared and 2.0 mL of this solution was added to 2.0 ml of tested compound solution (or standard) in methanol at different concentrations (3.125-25.0 µg/mL for **2a, 2b, 3a** and 9.375-37.5 µg/mL for **3b**). After 30 minutes of incubation at 40°C in a thermostatic bath, the decrease in the absorbance (n = 3) was measured at 517 nm. The percent DPPH scavenging ability (I%) was calculated as: I% = ($A_{control}$ – A_{sample}/$A_{control}$) × 100, where $A_{control}$ is the absorbance of DPPH radical + methanol (containing all reagents except the sample) and A_{sample} is the absorbance of DPPH radical + sample/standard. The antiradical activity (three replicates per treatment) was expressed as IC_{50} (µg/mL), the concentration of compound required to cause a 50% DPPH inhibition. The scavenging activity of Trolox and ascorbic acid were measured and compared with the one of the tested compounds.

b) Reducing Power by Ferric Reducing Antioxidant Power (FRAP) Test

The solutions of the tested compounds **2a,b** and **3a,b** have been prepared in 50 µg/mL concentration

The FRAP reagent consists in a mixture of 2.5 ml 10 mM TPTZ solution in 40 mM hydrochloric acid to which 2.5 ml 20 mM ferric chloride solution and 25 ml acetate buffer at pH = 3.6 is added. At 0.4 mL of diluted sample (50 µg/mL), 6mL the FRAP reagent was added and absorbance was measured at 595 nm after 10 min. Blank consisted in the similar mixture without the sample. Results are expressed as mM Trolox equivalents/g compound, using a calibration curve (R^2 = 0.989) constructed with 10-40 mg/L Trolox standard.

ACKNOWLEDGMENTS

Financial support from the Romanian Ministry of Education and Research (PN-II-ID-PCE-2012-4-0488) is greatly acknowledged. This work was supported also by the Swiss Enlargement Contribution in the framework of the Romanian-Swiss Research Program, project number IZERZO-142198/1. This paper was published under the frame of European Social Found, Human Resources Development Operational Programme 2007–2013, project no. POSDRU/159/1.5/S/136893".

REFERENCES

1. R. Mishra, P. K. Sharma, P. K. Verma, I. Tomer, G. Mathur, P. K. Dhakad, *J. Heterocycl. Chem.,* **2017**, *54(4)*, 2103.
2. A. Grozav, L. I. Găină, V. Pileczki, O. Crisan, L. Silaghi-Dumitrescu, B. Therrien, V. Zaharia, I. Berindan-Neagoe, *Int. J. Mol. Sci.,* **2014**,*15*(12), 22059.
3. A. Grozav, B. Stancu, C. Boari, F. Chirila, N. Fit, C. Cristea, *Studia UBB Chemia*, **2017**, *62(2)*, 365.
4. A.C. Cosma, A. Ignat, I.C. Tarca, V. Zaharia, S. D. Bolboaca, L. Jantschi, *Rev.Chim*., **2018**, *69 (4)*, 777.
5. B. Brem, E.Gal, L. Găină, L.Silaghi-Dumitrescu, E. Fischer-Fodor, C. I. Tomuleasa, A. Grozav, V. Zaharia, L. Filip, C. Cristea, *Int. J. Mol. Sci.*, **2017**, *18*(7), 1365.
6. A.T. Mbaveng, A. Grozav Ignat, B. Ngameni, V. Zaharia, B.T. Ngadjui, V. Kuete; *BMC Pharmcol. Toxicol.*, **2016**, *17 (3)*.
7. M. Sabou, A. Grozav, L. M. Junie, M. Flota, V. Zaharia, C. Cristea, *Studia UBB Chemia*, **2016**, *61(3),*117.
8. A. Grozav, V. Zaharia, C. Cristea, N. I. Fit, *Studia UBB Chemia*, **2015**, *60(3)*, 283.
9. B. Bream, E. Gal, C. Cristea, L. Gaina, A. Grozav, V. Zaharia, L. Silaghi-Dumitrescu, *Studia UBB Chemia*, **2015**, *60*(2), 371.
10. M. A. Pop, T. C. Drugan, A. Grozav, B. Domokos, A. Urda, C. M. Pop, *Studia UBB Chemia*, **2014**, *59(3)*, 119.
11. A. Ignat (Grozav), L. Gaina, V. Kuete, L. Silaghi-Dumitrescu, T. Efferth, V. Zaharia, *Molecules*, **2013**, *18(4)*, 4679.
12. V. Zaharia, A. Ignat (Grozav), B. Ngameni, V. Kuete, M. L. Moungang, C. N. Fokunang, M. Vasilescu, N. Palibroda, C. Cristea, L. Silaghi-Dumitrescu, B. T. Ngadju, *Med. Chem. Res.*, **2013**, *22*, 5670.
13. A. Ignat (Grozav), T. Lovasz, M. Vasilescu, E. F. Fodor, C. B. Tatomir, C. Cristea, L. Silaghi-Dumitrescu, V. Zaharia, *Archiv Der Pharmazie*, **2012**, *345* (7), 574.
14. A. Cozma, L. Vlase, A. Ignat (Grozav), V. Zaharia, S. Gocan, C. Marutoiu, A. Fodor, *Rev. Chim.,* **2012**, *63(7)*, 651.
15. A. Cozma, L. Vlase, A. Ignat, (Grozav), V. Zaharia, S. Gocan, N. Grinberg, *J. L. Chromatogr. Relat. Technol.*, **2012**, *35(1-4)*, 590.
16. V. Zaharia, A. Ignat (Grozav), N. Palibrod, B. Ngameni, V.Kuete, C. N. Fokunang, M. L. Moungang, B. T. Ngadjui, *Eur. J. Med. Chem.*, **2010**, *45(11)*, 5080.

17. A. Ignat (Grozav), V. Zaharia, C. Mogoşan, N. Palibroda, C. Cristea, L. Silaghi-Dumitrescu, *Farmacia*, **2010**, *58* (3), 290.
18. M. Abdel-Maksouda, U.M. Usama, O. Chang-Hyun, *Bioorg. Med. Chem.*, **2019**, *27(10)*, 20141.
19. A. Grozav, I. D. Porumb, L. I. Găină, L. Filip, D. Hanganu, *Molecules,* **2017**, 22(2), 260.
20. S. Cetean, T. Ciuleanu, D. C. Leucuta, C. Cainap, A. M. Constanti, I. Cazacu, S. Cainap, A. Gherman, L. Oprean, A. Hangan, R. Oprean, *J. BUON*, **2015**, *20(6)*,1623.
21. Yong-Jin Wu, Five-Membered Ring Systems: With N and S Atom in *Progress in heterocyclic chemistry*, Ed. G. W. Gribble, J. A. Joule, ISHC Elsevier, **2015**, Vol. 27, chapter 5.5, pp. 287-303.
22. D. Huang, B. Ou, R. L. Prior, *J. Agric. Food Chem.*, **2005**, *53*, 1841-1856.

STUDIA UBB CHEMIA, LXIV, 2, Tom II, 2019 (p. 517-526)
(RECOMMENDED CITATION)
DOI:10.24193/subbchem.2019.2.44

Dedicated to Professor Ioan Bâldea on the Occasion of His 80th Anniversary

VALIDATED LC-MS/MS METHOD FOR THE DETERMINATION OF TADALAFIL – A COMPETITIVE PHOSPHODIESTERASE 5 INHIBITOR (PDE5) – FROM HUMAN PLASMA

RÓBERT TŐTŐS[a*], JÓZSEF BALÁZSI[b]

ABSTRACT. The purpose of this study was the development and validation of an LC-MS/MS method, for the determination of tadalafil from human plasma. The sample workup involved a simple protein precipitation procedure. A core/shell type analytical column (50×2,1 mm, 2.6 Å) was used with C18 stationary phase. The mobile phase consisting of 30% acetonitril and 70% water provided good peak shape, accuracy and precision (stable ionization). The mass spectrometer was operated in positive electrospray ionization mode for analyte and internal standard. The following parameters were evaluated for validation purpose: selectivity, sensitivity, matrix effect, anticoagulant effect, linearity, precision and accuracy, recovery, short and long term analyte/IS stability in solvent/matrix and carryover. The validated calibration range was 22.2-1111.3 ng/ml. The correlation coefficient R^2 was at least 0.9995 in all validation batches. The validated method has been successfully used for the evaluation of bioequivalence of generic tadalafil 20 mg formulations.

Keywords: *tadalafil, phosphodiesterase 5 inhibitor, method validation, bioequivalence trial, LC-MS/MS*

INTRODUCTION

Tadalafil, (6R,12aR)-6-(1,3-benzodioxol-5-yl)-2,3,6,7,12,12a-hexa-hydro-2-methylpyrazino[1′,2′:1,6]pyrido[3,4-b]indole-1,4-dione with the empirical formula $C_{22}H_{19}N_3O_4$ (Figure 1) is a reversible cyclic guanosine

[a] *Babeş-Bolyai University, Faculty of Chemistry and Chemical Engineering, Biocatalysis and Biotransformation Research Centre, 11 Arany János str., RO-400028, Cluj-Napoca, Romania*
[b] *PharmacoKinetics SRL, 373 E/4 Corunca, RO-547367, Mures county, Romania*
** Corresponding author: totosr@chem.ubbcluj.ro*

monophosphate(cGMP)-specific phosphodiesterase Type 5 inhibitor indicated for the treatment pulmonary arterial hypertension, benign prostatic hyperplasia but mainly used for the treatment of erectile dysfunction (impotence) [1, 2, 13]. Tadalafil acts as a muscle relaxant of blood vessels, increasing blood flow to particular part of the human body.

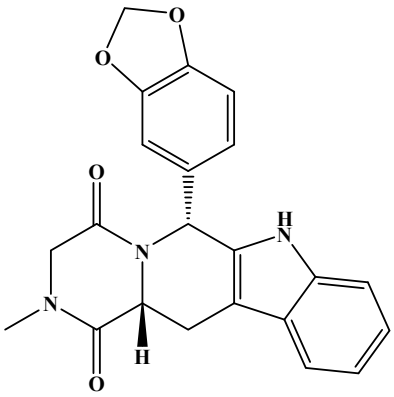

Figure 1. Structure of tadalafil

RESULTS AND DISCUSSION

Determination of acquisition parameters

There are various methods known in the literature for the determination of tadalafil in human blood, plasma or urine [3, 4, 7-9], animal plasma [5] or pharmaceutical formulations/dietary supplements [11], using LC-MS/MS methods.

The m/z transitions used for multiple reaction monitoring (MRM) [6, 10, 12] were chosen based on the spectra from Figures 2 and 3. The monitored transitions should not interfere in their m/z value, specific for a given analyte. Their intensity should be convenient for the qualifiers, and the qualifier/ quantifier ratio should remain stable over the whole calibration range and in time. Taking into account the considerations above the following transitions were chosen for the quantitative assay method:

Tadalafil: m/z 390.2→268.1, (390.2→135.0 qualifier ion) CE 15V,

Losartan (IS): m/z 423.2→207.1 (423.2→377.2 qualifier ion) CE 15V.
(CE – Collision Energy)

For analyte and IS (Internal Standard) the single charged molecular ions were used as precursors.

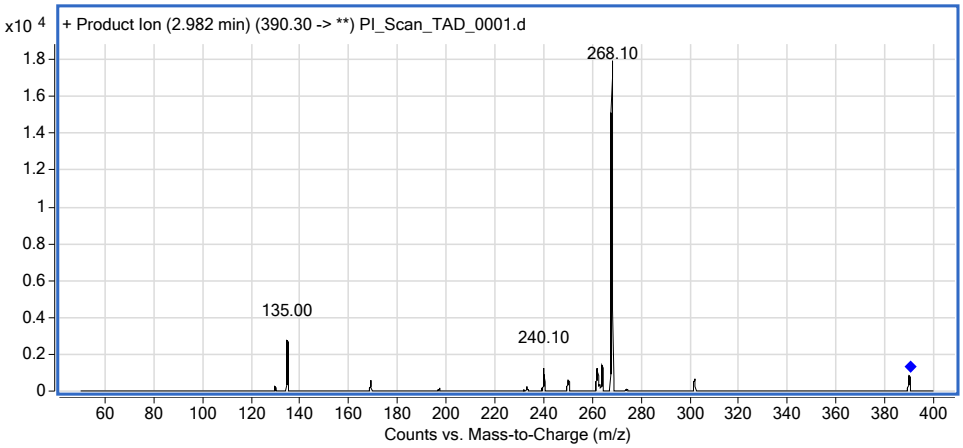

Figure 2. ESI (+) Spectrum of Tadalafil

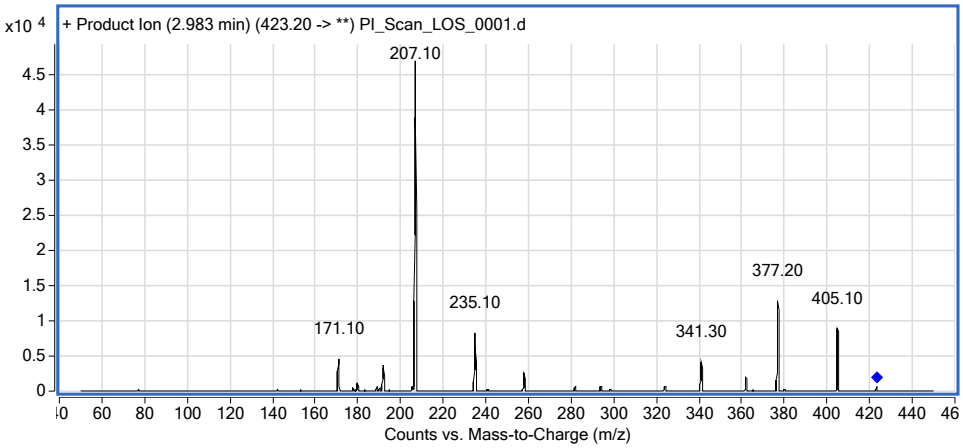

Figure 3. ESI (+) Spectrum Losartan (IS)

Figure 4 shows a typical MRM total ion chromatogram for an ULOQ (upper limit of calibration) sample. The analyte and IS are practically co-eluting at 3.0 min. Values are back calculated concentrations for each analyte.

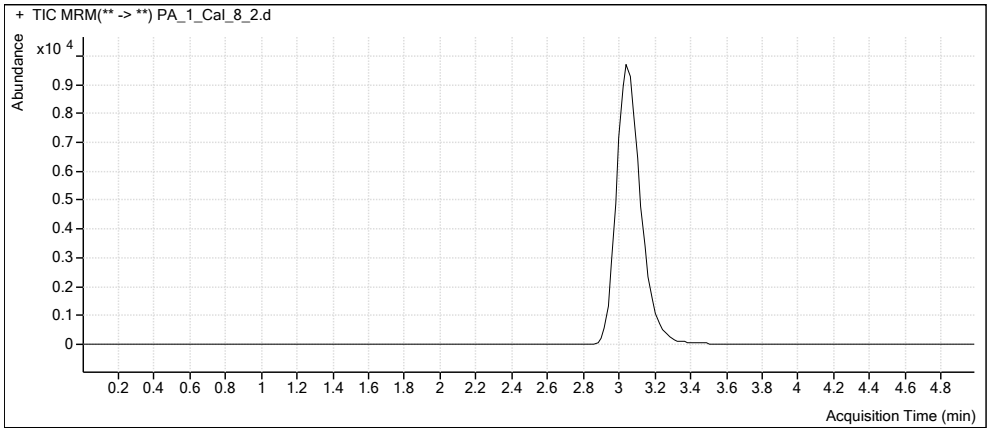

Figure 4. MRM chromatogram of Cal8 (tadalafil 1111.3 ng/ml, Losartan 39.9 ng/ml)

The use of the co-eluting internal standard leads to a minimization of the matrix effect, and it's a convenient alternative to the stable isotope labeled tadalafil. Moreover, it is easily soluble in the sample solvent resulting after plasma protein precipitation (methanol:water 4:1).

It's noticeable, that no significant spectral response has been observed at the retention time of the analyte/IS in matrix blank samples (Figure 5).

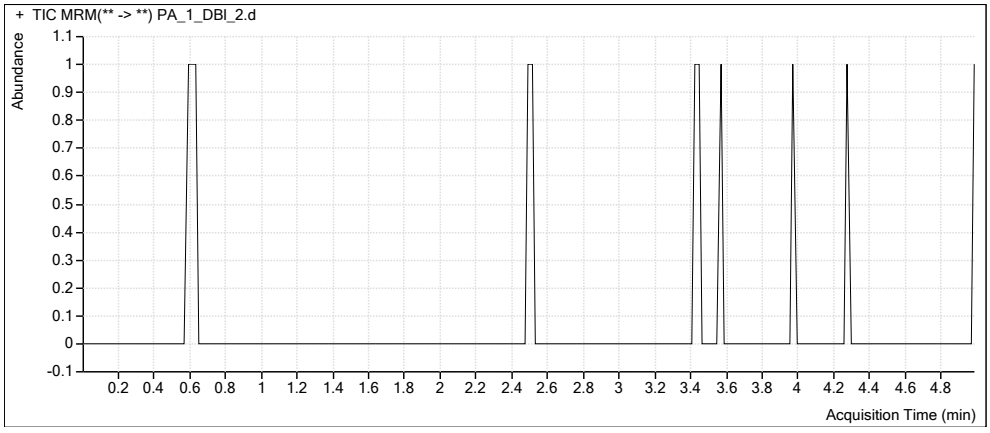

Figure 5. MRM chromatogram of DBl2 (matrix blank 0 ng/ml analyte/IS)

Bioanalytical method validation

The analytical method was validated according to the EMEA/CHMP/EWP/192217/2009 Guideline on validation of bioanalytical methods [14].

The tested parameters were: selectivity, sensitivity, matrix effect, anticoagulant effect, intra/interbatch precision and accuracy, recovery, short/long term stability of stock solutions of analyte, short term stability of working solutions of analyte, tabletop stability in biological matrix, freeze thaw stability in biological matrix, injector/autosampler stability of the processed samples, stability during delayed processing (worst case scenario), dilution qualification, analyte and internal standard carryover. All tests were performed using 6 replicates at the mentioned QC (Quality Control) concentration levels.

The calibration curve range is established according to literature data about plasma concentrations of the analyte. $C_{max\ average\ from\ literature}$ for Tadalafil was found to be ~ 450-500 ng/ml, after administration of a 20 mg dose [2-4, 8].

A summary of main results of validation batches is presented in Table 1.

The validated calibration range was 22.2-1111.3 ng/ml. The calibration curves were obtained using a linear weighted (1/x) regression analysis of the peak area ratio (analyte/internal standard) versus the nominal concentration of the calibration standards. The lower limit of quantitation was set smaller than 5% of expected average C_{max} values.

Linearity summary results for tadalafil are presented in Table 2. The limit of quantitation was 22.2 ng/ml and the linear dynamic range of the curve was from 22.2 to 1111.3 ng/ml.

Summary of method validation

Table 1. Bioanalytical method validation summary for tadalafil

Calibration concentrations (ng/ml)	22.23, 22.23, 44.45, 83.35, 166.70, 333.40, 611.23, 833.50, 1111.33, 1111.33 (ng/ml)
Lower limit of quantitation (ng/ml)	LLOQ, 22.23ng/ml, Accuracy 97.91%, RSD 2.98
QC Concentrations (ng/ml)	LLOQ-QC, LQC, MQC, HQC 22.23, 44.45, 333.40, 833.50 (ng/ml)
Between-run accuracy (%)	LLOQ-QC, LQC, MQC, HQC 99.74, 99.50, 99.11, 99.30
Between-run precision (RSD)	LLOQ-QC, LQC, MQC, HQC 2.18, 2.82, 3.76, 3.97
IS normalized Matrix factor (MF) RSD	0.96 (1.32)

Recovery (%)	LQC, MQC, HQC 100.38, 98.29, 97.14
Long term stability of stock solution and working solutions (Observed change %)	Confirmed up to 20 days at + 4 °C LQC Stab. 111.86, change +11.86% HQC Stab. 105.35 change +5.35%
Short term stability in biological matrix at room temperature or at sample processing temperature. (Observed change %)	Confirmed up to 23.58(3) h LQC Stab. 106.13, change +6.13% HQC Stab. 106.66, change +6.66%
Long term stability in biological matrix (Observed change %)	Confirmed up to 134 days at -50 °C LQC Stab. 106.38, change +6.38% HQC Stab. 103.23 change +3.23%
Autosampler storage stability (Observed change %)	Confirmed up to 73.38(3) h LQC Stab. 103.53, change +3.53% HQC Stab. 100.59, change +0.59%
Freeze and thaw stability (Observed change %)	-50 °C , 3 cycles LQC Stab. 100.77, change +0.77% HQC Stab. 99.01, change –0.99%
Dilution integrity	Concentration diluted (2-fold) 99.97%; RSD 1.91% Concentration diluted (4-fold) 97.73%; RSD 4.35%

PA – Precision and Accuracy batch
LLOQ-QC/LQC/MQC/HQC – Lower Limit of Quantitation/Low/Medium/High Quality Control sample

Table 2. Linearity summary results for tadalafil

Calibration level	Nominal conc. (ng/ml)	Mean conc.±S.D. (ng/ml) n=6	RSD %	Accuracy %
Cal_1_1	22.23	22.21±0.60	2.70	99.92
Cal_1_2	22.23	22.15±0.54	2.43	99.64
Cal_2	44.45	45.24±0.55	1.22	101.78
Cal_3	83.35	83.94±0.77	0.92	100.70
Cal_4	166.70	162.58±3.25	2.00	97.53
Cal_5	333.40	335.99±4.30	1.28	100.78
Cal_6	611.23	603.09±8.76	1.45	98.67
Cal_7	833.50	841.03±2.53	0.30	100.90
Cal_8_1	1,111.33	1103.99±6.81	0.62	99.34
Cal_8_2	1,111.33	1119.52±8.15	0.73	100.74

CONCLUSIONS

A rapid and robust method has been developed and validated for the determination of tadalafil in human plasma. The quantitation was performed on an Agilent 1200 series HPLC system, coupled to an Agilent 6410 triple quadrupole mass spectrometer, using electrospray ionization technique. The components were detected in positive ionization mode. The method was successfully used for the evaluation of bioequivalence of a generic formulation of tadalafil 20 mg film-coated tablets versus *Cialis*® 20 mg film-coated tablets, Eli Lilly, in 26 healthy Caucasian male subjects.

EXPERIMENTAL SECTION

Solvents and reference materials used

All used solvents are of HPLC grade. Acetonitril and Methanol were purchased from VWR, formic acid from Merck KGaA, HPLC water was obtained using a Millipore Simplicity UV water purification system. Certified reference materials of Tadalafil and Losartan potassium (internal standard-IS) were obtained from European Pharmacopoeia (Ph.Eur.), respectively Fluka and are of analytical standard grade. Blank human plasma was obtained from the regional blood transfusion center (CRTS) Cluj.

Instrumentation and working parameters

An Agilent 1200 series HPLC system with a Phenomenex Kynetex C18 column (50 × 2.10 mm) equipped with Phenomenex Security Guard (4 ×2.0 mm) was used for separation. The used mobile phase was an isocratic mixture of 30:70 acetonitrile:water (containing 0.1% formic acid). The used flow rate was 0.3 ml/min, the column temperature was set to 45 ºC. An Agilent 6410 triple Quadrupole Mass Spectrometer (Agilent Technologies, USA), equipped with electrospray ion source was used for the LC-MS/MS analyses. The runtime was 5 min/sample. The data acquisition and processing were carried out using MassHunter software. The whole system (software and hardware) was validated. The mass spectrometer was operated in positive ionization mode for analyte and IS. Nitrogen was used as nebulizing gas and collision cell gas. The temperature of the ESI source was set to 350 ºC, and the needle voltage to 4000V.

The quantitation was performed using MRM (multiple reaction monitoring) of the transitions: m/z 390.2→268.1, (390.2→135.0 qualifier ion) collision energy 15V, for tadalafil and 423.2→207.1 (423.2→377.2 qualifier ion) collision energy 15V for losartan (IS).

The mass spectrometer was operated at unit resolution with a dwell time of 300 ms per transition.

Stock and working solutions preparation

Stock solutions of tadalafil (1.0 mg/ml) were prepared in methanol dissolving accurately weighed amounts of reference material. Stock solutions of losartan-K (1.0 mg/ml) were prepared in methanol/water 50/50 (w/w) dissolving accurately weighed amounts of losartan-K. They were stored at 2-8 °C. Correction factors were applied to the weighed amounts of reference materials to calculate the content of the pure substance (Table 3). Correction factors are derived from the purity and the chemical form (salt, etc.).

Table 3. Correction factors for reference materials

Reference material	**Tadalafil**	**Losartan potassium**
Purity (%)	99.9	99.6
Chemical form correction factor	1.0000	0.9152
Correction factor	**0.9990**	**0.9115**

Working solutions of analyte and internal standard were prepared freshly before use by successive dilutions from stock solutions to appropriate levels, using methanol/water 50/50 (w/w) as solvent. They were used for spiking human plasma used for calibrators and QC samples preparation.

Calibrators and QC samples preparation

To 400 µl of blank human plasma, 50 µl of spiking solution of analyte and 50 µl of spiking solution of internal standard were added in polypropylene tubes, to yield final concentrations of 22.23, 44.45, 83.35, 166.70, 333.40, 611.23, 833.50, 1111.33 ng/ml for tadalafil.

Sample preparation (workup)

To precipitate plasma proteins, 2 ml of methanol was added to the spiked samples, then vortexed for 20 minutes at 1500 rpm. Further the samples were centrifuged at 4 °C for 20 minutes at 4000 rpm. 450 µl of supernatant was transferred to HPLC autosampler vials diluted with 450 µl of water and injected into the analytical system (15 µl/sample).

Calibration curve parameters

The linearity of the method was evaluated using spiked plasma samples in the concentration range mentioned above using the method of least squares. Two identical validated analytical systems has been used, three linearity curves were analyzed on each system.

Each calibration batch (curve) consisted of: blank samples in duplicate, zero samples (blank with IS) in duplicate and eight non-zero concentration levels, of which the lower and upper limit of quantitation samples were in duplicate. The calibration curves were obtained by using a linear weighted (1/x) regression analysis of the peak area ratio (analyte/internal standard) versus the nominal concentration of the calibration standards. Study samples concentrations were obtained by interpolation from the calibration curve.

The linearity results are summarized in Table 2 in the 'Results and Discussion' section.

ACKNOWLEDGMENTS

This work was performed using private funding of S.C KYNETYX HT SRL.

REFERENCES

1. *https://www.rxlist.com/cialis-drug.htm:* ***CIALIS*** *(tadalafil) Tablets; Viewed: 14.03.2019)*
2. S. T. Forgue, B. E. Patterson, A. W. Bedding, C. D. Payne, D. L. Phillips, R. E. Wrishko, M. I. Mitchell, *Br. J. Clin. Pharmacol.,* **2005**, *61*, 280.
3. N.V.S. Ramakrishna, K.N. Vishwottam, S. Puran, M. Koteshwara, S. Manoj, M. Santosh, J. Chidambara, S. Wishu, B. Sumatha, *J. Chromatogr. B.*, **2004**, *809***,** 243.
4. Bo Ma, Xuejun Shang, Qi Zhang, Jing Li, Yinhui Liu, Xiaomei Cao, Qiuyu Xu, *J. Pharm. Biomed. Anal.*, **2013**, *77*, 149.
5. J. H. Lee, J.-H. Oh, Y.-J. Lee, *Arch. Pharm. Res*., **2013**, *77*, 457.
6. J.-M. Lee, J. Hong, H. B. Oh, B. Moon, *Bull. Korean Chem. Soc*., **2017**, *39*, 190.
7. K. Hasegawa, O. Suzuki, K. Gonmori, I. Yamagishi, H. Nozawa, K. Watanabe, *Forensic Toxicol*., **2012**, *30*, 25.
8. A. Bhadoriya, B. Dasandi, D. Parmar, P. A. Shah, P. S. Shrivastav, *J. Pharm. Anal.,* **2018**, *8*, 271.
9. P. Nagaraju, B. Kodali, P. V. Datla, *J. Pharm. Biomed. Anal.*, **2018**, *152*, 215.
10. L. Wang, Y. Wang, Y. Chai, Y. Kang, C. Suna, S. Zenga, *J. Mass Spectrom*., **2017**, *52*, 411.

11. Y. Zhang, Z. Huang, L. Ding, H. Yan, M. Wang, S. Zhu, *J. Sep. Sci.*, **2010**, *33*, 2109.
12. P. Zou, P. Hou, S. Sze-Yin Oh, M.-Y. Low, H.-L. Koh, *Rapid Commun. Mass Spectrom.,* **2006**, *20*, 3488.
13. Fachinformation Cialis, Lilly, Stand. Mar. **2017**, https://www.fachinfo.de
14. EMEA/CHMP/EWP/192217/2009 Rev. 1 Corr. 2** Guideline on validation of bioanalytical method, 21 July 2011 (Updated 03/06/2015).

STUDIA UBB CHEMIA, LXIV, 2, Tom II, 2019 (p. 527-537)
(RECOMMENDED CITATION)
DOI:10.24193/subbchem.2019.2.45

Dedicated to Professor Ioan Bâldea on the Occasion of His 80th Anniversary

EVALUATION OF BIOCHEMICAL AND MICROBIOLOGICAL CHANGES OCCURRING IN FRESH CHEESE WITH ESSENTIAL OILS DURING STORAGE TIME

MELINDA FOGARASI[a], SONIA A. SOCACI[b], SZABOLCS FOGARASI[c]*, MIRELA JIMBOREAN[a], CARMEN POP[b], MARIA TOFANĂ[b], ANCA ROTAR[b], DORIN TIBULCA[a], DAN SALAGEAN[a], LIANA SALANTA[b]

ABSTRACT. The current study aimed to determine the chemical composition and antibacterial activity of two essential oils extracted from herbs belonging to the family *Lamiaceae* (mint and oregano), and their beneficial impact on the biochemical and microbiological changes occurring in fresh cheese during storage time. Based on the essential oils results three types of fresh cheese were formulated and the consumer prefer sample were sensory evaluated using the 9-point hedonic test. In order to determine the stability during storage, the selected sample and the essential oil free control sample were sampled initially, after 6 and 12 days of storage than subjected to physicochemical (protein, fat, moisture, ash, total carbohydrates, and energy) and microbiological analyses (*S. aureus*, *E. coli*).

Keywords: *Antibacterial activity*, *Biochemical changes, essential oils, microbiologic, sensory evaluation, storage, volatile profile*

INTRODUCTION

In the recent years, cheese manufacturing and processing has transitioned from traditional art to science. Many of the cheese varieties have been developed and tested for different environmental conditions in order to meet the highly pretentious customer standards [1]. Fresh cheeses

[a] *Department of Food Engineering, University of Agricultural Sciences and Veterinary Medicine of Cluj-Napoca, Cluj-Napoca, Romania, Calea Mănăştur 3-5, 400372 Cluj-Napoca, Romania*
[b] *Department of Food Science, University of Agricultural Sciences and Veterinary Medicine of Cluj-Napoca, Cluj-Napoca, Romania, Calea Mănăştur 3-5, 400372 Cluj-Napoca, Romania*
[c] *Babeş-Bolyai University, Faculty of Chemistry and Chemical Engineering, 11 Arany Janos Str., Cluj-Napoca, RO-400028, Romania*
** Corresponding author: szfogarasi@chem.ubbcluj.ro*

production involves the enzymatic coagulation of milk with rennet and/or other coagulating enzymes, which in some cases are combined with specific lactic bacteria [2]. It is well known that soft texture, low salt content, high acidity and moisture, which are characteristics of fresh cheeses, favor the growth of spoilage microorganisms, leading to consumer rejection and possible economic losses for the industry. Moreover, fresh cheeses are considered potential vehicles for *Escherichia coli*, a pathogen able to survive and grow even at refrigerate temperature. As a result, the manufacturing of cheeses involves the addition of synthetic preservatives, (e.g., potassium and sodium sorbate) in order to ensure the safety of fresh cheeses [3]. However, many studies revealed the negative effects of synthetic food preservatives on human health and the increasing resistance of microorganisms to these compounds. As a result, researchers are focused on the identification and use of natural preservatives like essential oils (EOs), which are volatile liquids distilled from different aromatic plant materials [4-7]. EOs from *Origanum vulgare L.* (oregano – OrEO) and *Mintha piperita* (mint – MiEO) are effective in inhibiting a range of cheese-related bacteria in vitro systems, making them a key alternatives for cheese preservation [8]. Considering the antioxidant activity and food preserving properties of OrEO and MiEO and the fact that they are natural products [7], which can be produced in organic condition, the selected EO could be used in organic food products with short shelf-life. Therefore, this study aimed to evaluate the physicochemical, microbiological and sensory aspects that characterized a fresh cheese made with the incorporation of OrEO and MiEO and the effects of these EOs on the cheese during refrigerated storage.

RESULTS AND DISCUSSION

Chemical Composition of Essential Oils

The volatile compounds detected by ITEX-GC/MS analysis in the two essential oils with their percentage composition are summarized in Table 1.

According to the results, the MiEO contained 39 constituents and the most important ones were α-pinene (3.57%), β-pinene (4.71%), Sabinene (2.04%), D-limonene (13.06%) and Eucalyptol (17.76%), all of them belonging to the monoterpene hydrocarbons class. The obtained results are similar to the aromatic profile presented by de Sousa Barros et al. [8] regarding essential oils extracted from different Mentha species. Similarly, OrEO included 21 major components among which p-cymene (13.76%), gamma terpinene (11.94%), D-limonene (34%) and thymol (19.38%) had the highest concentration which is also confirmed by the data presented by Sahbaz A. et al. [9]. The thymol belongs to the oxygenated monoterpenes class and the rest of them to monoterpene hydrocarbons.

Table 1. Volatile compounds profile of oregano and mint essential oils

Crt. No.	Compound	MiEO, %	OrEO, %
1.	Furan, 2,5-diethyltetrahydro-	0.14	-
2.	2-Hexenal, (E)-	-	0.29
3.	Origanene	-	2.37
4.	alpha.-Thujene	0.53	-
5.	alpha.-Pinene	**3.57**	1.51
6.	Camphene	0.15	0.39
7.	3-Methyl-cyclohexanone	0.20	-
8.	Sabinene	2.04	-
9.	beta.-Pinene	**4.71**	0.24
10.	beta.-Myrcene	0.67	4.78
11.	n.i.	0.04	-
12.	1-Methylene-4-(1-methylethenyl)- cyclohexane	0.07	-
13.	Octanal	-	0.20
14.	alpha.-Phellandrene	0.05	0.69
15.	3-Carene	0.05	0.24
16.	alpha.-Terpinene	0.27	3.49
17.	*p*-Cymene	0.08	**13.76**
18.	n.i.	2.43	-
19.	D-Limonene	**13.06**	**34.08**
20.	Eucalyptol	**17.76**	-
21.	beta-*trans*-Ocimene	0.13	0.06
22.	beta-*cis*-Ocimene	0.03	0.10
23.	gamma.-Terpinene	0.51	**11.94**
24.	n.i.	0.16	-
25.	Terpinolene	0.13	0.32
26.	Benzene, 2-ethenyl-1,3-dimethyl-	-	0.06
27.	beta.-Linalool	-	0.62
28.	Thymol	-	**19.38**
29.	Carvacrol	-	5.28
30.	Cyclohexanone, 5-methyl-2-(1-methylethyl)-	30.54	-
31.	Menthofuran	2.06	-
32.	Cyclohexanone, 5-methyl-2-(1-methylethyl)-, (2R-cis)-	5.99	-

Crt. No.	Compound	MiEO, %	OrEO, %
33.	Cyclohexanol, 5-methyl-2-(1-methylethyl)-, (1.alpha.,2.alpha.,5.alpha.)	0.86	-
34.	Cyclohexanol, 5-methyl-2-(1-methylethyl)-, (1.alpha.,2.beta.,5.alpha.)-(.+/-.)-	9.63	-
35.	Cyclohexanol, 5-methyl-2-(1-methylethyl)-, [1S-(1.alpha.,2.beta.,5.beta.)]-	0.15	-
36.	alpha.-Terpineol	0.09	-
37.	Pulegone	0.38	-
38.	Piperitone	0.13	-
39.	Cyclohexene, 4-methyl-1-(1-methylethyl)-	0.10	-
40.	Menthol, acetate	2.14	-
41.	Cyclohexane, 1-ethenyl-1-methyl-2-(1-methylethenyl)-4-(1-methylethylidene)-	0.07	-
42.	n.i.	0.06	-
43.	Caryophyllene	0.88	0.17
44.	alpha.-Caryophyllene	0.02	-
45.	Germacrene D	0.07	-
46.	n.i.	0.02	-
TOTAL		100	100

MiEO- mint essential oil, OrEO – oregano essential oil

Antibacterial Activity of Essential Oils

In order to evaluate the antibacterial activity, minimum inhibitory concentration tests of the studied essential oils were performed. According to the results shown in Table 2, minimum inhibitory concentrations values differ significantly between the two essential oils.

Table 2. Minimum inhibitory concentrations (MIC) of essential oils

Essential Oil	*E. coli* ATCC 25922	*S. aureus* ATCC 25923	*S. enteritidis* ATCC 13076	*L. monocytogenes* ATCC 19114
	µl/ml			
MiEO	0.56 ± 0.0	2.45 ± 0.0	1.59 ± 0.0	5.14 ± 0.0
OrEO	0.22 ± 0.0	0.13 ± 0.0	0.27 ± 0.0	0.13 ± 0.0

MiEO- mint essential oil, OrEO – oregano essential oil, *E. coli* - *Escherichia coli*, *S. aureus* - *Staphylococcus aureus*, *S. enteritidis* - *Salmonella enteritidis*, *L. monocytogenes* - *Listeria monocytogenes*. Values are results of three replicates. Control negativ, were 0.11 ± 0.0 for *E. coli* (ATCC 25922) and 0.05 ± 0.0 µg GE mL^{-1} for *S. aureus* (ATCC 25923), 0,24± 0.0 for *S. enteritidis,* 0.11 ± 0.0 for *L. monocytogenes* .

The results show that OrEO was the most bacteriostatic against all four of the selected bacteria, considering that it had the lowest MIC values. However, in the case of *E. coli*, the antibacterial activity of the two essential oils is comparable while for the other bacteria the differences are more significant. In the case of bacteria *S. aureus* and *L. monocytogenes* OrEO had the same antibacterial activity (0.13 µl/ml). The antibacterial activity of MiEO was also the most bacteriostatic against *E. coli*, followed by *S. enteritidis, S. aureus* and *L. monocytogenes*.

Sensorial Analysis

Considering that the sensorial quality of food products is a key factor in consumer's decision-making process, the Hedonic testing was used to determine consumer's attitude towards all three fresh cheese formulations samples by measuring the degree of acceptance of the new products. It is very important to note that the organoleptic properties of fresh cheese enhanced with essential oils remained acceptable to consumers and the quality level similar to the current commercially available products. This is also confirmed by the results shown in the Table 3 for sensorial evaluation of fresh cheese samples containing different type and level of essential oils compared to the control sample (without EOs).

Table 3. Results of sensorial evaluation

Sample	Appearance	Color	Texture	Odor	Taste	Overall acceptability
C.S.	7.1	7.0	6.2	7.2	7.1	6.9
CH. 0.03% MiEO	7.5	7.6	8.2	7.6	8	7.8
CH. 0.02% OrEO	7.0	7.0	6.4	6	7	6.6

C.S. – control sample, CH. 0.03% MiEO- cheese with 0.03% mint essential oil, CH. 0.02% OrEO – cheese with 0.02% oregano essential oil

It was found that the acceptability of the fresh cheese with 0.02% oregano essential oil was the lowest which can be attributed to the taste and the intense smell of OrEO. In contrast, the sample with 0.03% MiEO had the highest acceptability score (7.8) as well as for the other organoleptic characteristics. The mint essential oil has given a fresh taste and smell to the product and it reduces the fatty taste of the product. Moreover, the sensorial evaluation revealed that fresh cheese with 0.03% MiEO achieved higher score than the control cheese sample.

The biochemical analysis of the fresh cheese

The results of the biochemical analysis presented in Table 4 revealed that the physicochemical parameters for the cheese samples with and without MiEO were approximately the same during storage. It was observed that the gradual reduction in of cheeses moisture content during the storage led to an increase in total lipids, protein, and ash. According to the literature, this can be explained by the curd shrinkage, as a consequence of the acid production by starter culture, which helps to drain the whey from the cheese mass [3].

Table 4. The compositional parameters percentage values according to the ripening stages

Sample	Control sample			Fresh cheese with 0.03% MiEO		
Storage time, day	1	6	12	1	6	12
Fat, g/100 g	27.5 ± 0.1	28.63 ± 0.3	30.17 ± 0.1	28 ± 0.07	29.04±0.04	30.39 ± 0.09
Protein, g/100 g	17.98 ± 0.08	19.11± 0.1	21.07 ± 0.5	18.14 ± 0.1	19.28± 0.3	20.97 ± 0.2
Moisture, g/100 g	44.87 ± 0.2	43.08±0.06	41.93 ± 0.1	45.48 ± 0.05	44.17± 0.4	42.96 ± 0.03
Ash, g/100 g	2.6 ± 0.04	2.71 ± 0.07	2.85 ± 0.01	2.73 ± 0.06	2.8±0.02	2.97 ± 0.1
Total carbohydrates, g/100 g	7.05 ± 0.01	6.47 ± 0.2	3.98 ± 0.03	5.65 ± 0.02	4.71 ± 0.1	2.71 ± 0.08
Energy, kcal/100 g	347.62±0.09	359.99±0.1	371.73±0.2	347.16±0.07	357.32±0.1	368.23±0.06

MiEO- mint essential oil

The biochemical analysis of the fresh cheese with and without MiEO has revealed that the fat percentage shows a consistent upper trend during the ripening stages, from 28.0 ± 0.76 g/100 g within first day of ripening to 30.39 ±0.09 in the last stage (day 12).

Microbiological evaluation of cheese during storage

Quantitative detection of *Escherichia coli* (*E. coli*) and Staphylococcus *aureus* (*S.aureus*) was performed to establish the contribution of essential oil to the fresh cheese microbial load and to evaluate their safety. The European regulations on microbiological criteria for cheese preparations (European Union, 2005) contain limits for *E. coli* and *S. aureus* only. The results of fresh cheese microbiological examination, Table 5, indicate that MiEO has an important antimicrobial effect on the finished product in comparison to the control sample.

Table 5. Microbiological characteristics of cheese formulations

Sample	Storage time	*E. coli*	*S. aureus*
	day	log CFU/g	
Control sample	1	ABS	2.14
	6	ABS	2.34
	12	ABS	2.57
Fresh cheese with 0.03% MiEO	1	ABS	ABS
	6	ABS	ABS
	12	ABS	ABS

In the case of the fresh cheese with 0.03% MiEO, it can be seen that *S. aureus* is absent during storage which sustains the inhibitory effect of the MiEO. Moreover in the control sample *S. aureus* grow in the product during storage from 2.14-2.57 [log CFU/g. These findings clearly underline the beneficial impact of the addition of 0.03% MiEO on the biochemical and microbiological changes occurring in fresh cheese during storage time.

CONCLUSIONS

The present work proved that the incorporation of OrEO and MiEO can enhance the antimicrobial properties of fresh cheese during storage time, leading to the natural preservation of the product. Based on the results it can be concluded that OrEO was the most bacteriostatic against all four of the selected bacteria, due to the lowest MIC values, being followed by MiEO. On the other hand, sensory analysis revealed that the acceptability of the fresh cheese with 0.02% OrEO was the lowest while the sample with 0.03% MiEO had the highest acceptability score (7.8) due to the fresh taste and smell, which is related to the distinctive volatile profile of MiEO. As an overall conclusion it can be stated, the addition of 0.03% MiEO to the fresh cheese improves significantly its sensorial quality and stability during storage time, but without modifying the physicochemical parameters of the final product.

EXPERIMENTAL SECTION

Plant Materials and Essential Oils Extraction

The dried mint and oregano leaves were purchased from a company that markets food ingredients (Solina Group, Alba Iulia, Romania). Essential oils were obtained by hydrodistillation using 50 g dried leaves for both plants. The

extraction was performed for 3 h with 750 mL distilled water in a Clevenger-type apparatus (S.C. Energo-Metr S.R.L., Odorheiu Secuiesc, Romania). The essential oils were dried over anhydrous sodium sulphate and stored at 4 °C until analysis.

ITEX/GC-MS Analysis of Volatile Components

The extraction of volatile compounds was performed using the in-tube extraction technique (ITEX) as described in our previous work [10] using 1 µL of sample. The analysis of volatile compounds was carried out on a GCMS QP-2010 (Shimadzu Scientific Instruments, Kyoto, Japan) model gas chromatograph-mass spectrometer which can be used for measurement of various components including hydrogen [11], volatile organic compounds [12]. Next, the volatile compounds were separated on a Zebron ZB-5ms capillary column of 30 m × 0.25 mm i.d. × 0.25 µm film thickness. In all determinations, the carrier gas was He, 1 ml/min and the split ratio 1:20. The temperature program used for the column oven was: from 40 oC (kept at this temperature for 2 min) to 160 °C at 4 °C/min, then raised to 240 °C at 15 °C /min (kept at this temperature for 5 min). The injector, ion source and interface temperatures were set at 250 °C and the MS mode was electron impact (EI) at ionization energy of 70 eV. The scanned mass range was 40–650 m/z. Volatile compounds were tentatively identified using the spectra of reference compounds from NIST27 and NIST147 mass spectra libraries and verified by comparison with retention indices drawn from www.pherobase.com or www.flavornet.org (for columns with a similar stationary phase to the ZB-5ms column). Compounds were considered “tentatively identified” only in the case in which their mass spectra similarity value was above 85%. All peaks found in at least two of the three total ion chromatograms (TIC) were considered when calculating the total area of peaks (100%) and the relative areas of the volatile compounds.

Bacterial Strains

The following microorganisms were tested: *Escherichia coli* (ATCC 25922), *Staphylococcus aureus* (ATCC 25923), *Salmonella enteritidis* (ATCC 13076) and *Listeria monocytogenes* (ATCC 19114). All strains were grown into a test tube containing 10 mL sterile nutrient broth (Oxoid Ltd., Basingstoke, Hampshire, England) at 37 °C for 24 h in the case of *E. coli*, *S. aureus* and *S. enteritidis*, while *L. monocytogenes* at 37 °C for 30 h. The purity of the inoculums was confirmed by plating on appropriate selective media and microscopic examination of the Gram-stained smear (Optika microscope, B-252, M.A.D. Apparecchiature Scientifiche, Milan, Italy). A loopful of inoculums was transferred by streaking onto a selective medium: TBX for *E. coli*, BP (baird

parker) for *S. aureus*, XLD agar (Oxoid Ltd., Basingstoke, Hampshire, England) for *S. enteritidis* and Palcam agar base (Oxoid Ltd., Basingstoke, Hampshire, England) with added Palcam selective supplement for *L. monocytogenes*. Plates were incubated at 44 ◦C for 24 h *E. coli*, at 37 ◦C for 24 h in the case of *S. Aureus*, and *S. enteritidis* and at 37 ◦C for 30 h in the case of *L. monocytogenes*. Bacterial morphology was confirmed by optical microscopy. Several colonies were collected with a sterile inoculating loop, transferred into sterile saline solution (8.5 g L^{-1}), and adjusted to match the turbidity of a McFarland 0.5 standard (1.5×108 CFUmL^{-1}) [31]. Then, three serial 10-fold dilutions (107, 106, and 105 CFU mL^{-1}) were prepared using the sterile saline solution as diluent.

Fresh Cheese Manufacture

All cheese samples were elaborated in the Experimental Laboratory of Dairy Products (pilot scale) of the Faculty of Food Science and Technology, Cluj-Napoca (University of Agricultural Sciences and Veterinary Medicine Cluj-Napoca, Romania). The control sample (fresh cheese without EOs) was obtained using 100 l of cow milk with 3.4 % of fat content, which was previously pasteurized at 65˚C/30 min and cooled to 35˚C. Coagulation was performed at 35°C for 60 minutes using calcium chloride and 5 U selected cultures of lactic bacteria *(Lactococcus lactis ssp. lactis, Streptococcus thermophilus and Lactobacillus casei)* and microbial enzyme rennet in form of two cubes [13]. Once the curd was formed, it was smoothly cut into 4-5 cm cubes and shredded with harp up to 6-8 mm. The obtained curd was placed in perforated containers (10 cm diameter) for whey removal for 1 h at 18 °C. The cheese samples were vacuum packaged in sterile polyethylene bags and stored for 12 days in refrigerated storage at 4 °C. The two types of fresh cheese with 0.02% oregano EO and 0.03% mint EO were obtained based on the above steps, like the control sample, with the only difference that the selected EOs were added in the stage of coagulation. The amount of essential oils (mint and oregano) used has been established after the microbiological analyzes results and composition of the EOs.

Sensory evaluation of cheese

Sensory characteristics of cheese samples were evaluated by a panel of 40 untrained assessors, with a mean age of 25, consisted of students and staff members of the department. All samples were coded numerically and supplied in plastic dishes randomly. The 9-point hedonic scale test (1 being “dislike extremely” and 9 being “like extremely”) was used to evaluate all cheese samples. The main sensory attributes used in the assessment of the samples were appearance, color, texture, odor, taste, and overall acceptability.

Physicochemical parameters of cheese

The moisture, ash, total carbohydrates, total sugars, crude fat and crude protein of samples were determined according to AOAC procedures [14]. The cheeses samples moisture content was determined via drying in an oven at 105 °C until constant weight while the ash content was established by incineration at 600±15 °C. The crude protein content of the samples was estimated by the micro-Kjeldahl method, in which the sample was digested with a known quantity of concentrated H_2SO_4 in the Kjeldahl digestion apparatus. The crude fat content was determined in accordance with the Gerber method described by SR ISO 488 [15]. The amount of total carbohydrate resulted as a difference based on the following equation: 100 - (g moisture + g protein + g fat + g ash). The total energy was calculated using the following equation from the literature: energy (kcal) = 4 × (g protein + g carbohydrate) + 9 × (g lipid) [16, 17].

Microbiological evaluation of cheese

Detection of *Escherichia coli* was carried out using the method described in SR EN ISO 16649-2:2007 standard (International Organization for Standardization, 2007, 2007b). *Staphylococcus aureus* was determined using the method described in SR EN ISO 6888-1:2002 standard (International Organization for Standardization, 2002). Total combined yeasts and moulds count (TYMC) was not determined, because the European regulations on microbiological criteria for cheese preparations (European Union, 2005) contain limits only for *E. coli* and *S. aureus*.

ACKNOWLEDGEMENTS

This work was supported by two grants of Ministry of Research and Innovation, CNCS-UEFISCDI, project number PN-III-P1-1.1-TE-2016-0973 and project number PN-III-P2-2.1-CI-2018-0355.

REFERENCES

[1] F.A. Tabaran, S.D. Dan, A. Tabaran, C. Bele, C. Catoi, M. Borzan, G. Valasutean, M. Mihaiu, *Studia UBB Chemia,* **2015**, *60,* 4, 85.
[2] C.M. Asensio, N.R. Grosso, H. Rodolfo Juliani, *LWT - Food Science and Technology,* **2015,** *60,* 2, 664.
[3] H.T. Diniz-Silva, J. Batista de Sousa, J. da Silva Guedes, R.d.C. Ramos do Egypto Queiroga, M.S. Madruga, J.F. Tavares, E. Leite de Souza, M. Magnani, *LWT - Food Science and Technology,* **2019**, 10.1016/j.lwt.2019.01.039

[4] L.-C. Salanta, M. Tofană, S.A. Socaci, E. Mudura, C. Pop, A. Pop, A. Cuceu, M. Nagy, *Hop and Medicinal Plants,* **2014**, *1-2,* 1.
[5] M. Nagy, S.A. Socaci, M. Tofană, C. Pop, C. Mureşan, A.V. Pop Cuceu, L. Salanţă, A.M. Rotar, *Bulletin of University of Agricultural Sciences and Veterinary Medicine Cluj-Napoca. Food Science and Technology,* **2015**, *72,* 1,
[6] C.A. Semeniuc, M.I. Socaciu, S.A. Socaci, V. Muresan, M. Fogarasi, A.M. Rotar, *Molecules,* **2018**, *23,* 9,
[7] N. Khorshidian, M. Yousefi, E. Khanniri, A.M. Mortazavian, Innovative Food Science *& Emerging Technologies,* **2018**, *45,* 62.
[8] A. de Sousa Barros, S.M. de Morais, P.A.T. Ferreira, Í.G.P. Vieira, A.A. Craveiro, R.O. dos Santos Fontenelle, J.E.S.A. de Menezes, F.W.F. da Silva, H.A. de Sousa, *Industrial Crops and Products,* **2015**, *76,* 557.
[9] A. Sahbaz, H. Isik, O. Aynioglu, K. Gungorduk, B.D. Gun, *European journal of obstetrics, gynecology, and reproductive biology,* **2014**, *177,* 44.
[10] S.A. Socaci, C. Socaciu, C. Mureşan, A. Fărcaş, M. Tofană, S. Vicaş, A. Pintea, *Phytochemical Analysis,* **2014**, *25,* 2, 161.
[11] L.-C. Pop, L. Sygellou, V. Dracopoulos, K.S. Andrikopoulos, S. Sfaelou, P. Lianos, *Catalysis Today,* **2015**, *252,* 157-161.
[12] J. Dewulf, H. Van Langenhove, G. Wittmann, **2002**, *21,* 637.
[13] D. Ţibulcă, M. Jimborean, A. Ţibulcă, *Romanian Biotechnological Letters,* **2017**, 10.26327RBL2017.67
[14] Official Methods of Analysis of AOAC INTERNATIONAL, 20th Edition ed., AOAC International; 20 edition.
[15] C.A. Semeniuc, A. Rotar, L. Stan, C.R. Pop, S. Socaci, V. Mireşan, S. Muste, *CyTA - Journal of Food,* **2015**, *14,* 2, 213.
[16] M. Fogarasi, S.A. Socaci, F.V. Dulf, Z.M. Diaconeasa, A.C. Farcas, M. Tofana, C.A. Semeniuc, *Molecules,* **2018**, *23,* 12
[17] M. Nagy, C.A. Semeniuc, S.A. Socaci, C.R. Pop, A.M. Rotar, C.D. Salagean, M. TofanĂ, *Food Science and Technology,* **2017**, *37,* 2, 315.

STUDIA UBB CHEMIA, LXIV, 2, Tom II, 2019 (p. 539-546)
(RECOMMENDED CITATION)
DOI:10.24193/subbchem.2019.2.46

Dedicated to Professor Ioan Bâldea on the Occasion of His 80th Anniversary

A FAST AND SENSITIVE ZYMOGRAPHY METHOD OF PEROXIDASE ACTIVITY DETERMINATION USING SODIUM ACETATE BUFFER

GHEORGHITA MENGHIU[a,b], AMALIA NICOLETA IANCU[a,b] AND VASILE OSTAFE[a,b] *

ABSTRACT. By changing the buffer composition from phosphate to acetate (in both cases, the pH value was 6.0), the sensitivity of the estimation of peroxidase activity in polyacrylamide gels was improved from 4 µg/well to 0.4 µg/well. The optimized method, including electrophoretic separation and zymogram technique realized with guaiacol as substrate, can be performed in only 135 minutes. The improved method was applied to monitor the expression of recombinant peroxidase in a Gram-negative bacterium: the peroxidase activity was detected at 4 h after induction of expression.

Keywords: *zymography, peroxidase, guaiacol, SDS-PAGE*

INTRODUCTION

There are many circumstances when the presence, the purity or even the quantity of a protein in a solution is evaluated by polyacrylamide gel electrophoresis (PAGE) [1-3]. When the analyzed protein is an enzyme, its activity can be estimated combining electrophoretic separation with zymogram [4]. For example, the activity of peroxidase can be analyzed directly on the gel by addition of a suitable substrate, like guaiacol [5]. After the electrophoretic separation, the gels are basically incubated in the substrate solution which will reveal as brownish bands on the translucent gel only those protein bands

[a] *West University of Timisoara, Faculty of Chemistry, Biology, Geography, Department of Biology - Chemistry, 16 Pestalozzi, 300115 Timisoara, Romania*
[b] *West University of Timisoara, Multidisciplinary Research Platform "Nicholas Georgescu - Roengen", Advanced Environmental Research Laboratory,4 Oituz, 300086, Timisoara, Romania*
* *Corresponding author: vasile.ostafe@e-uvt.ro*

that have enzymatic activity. Next, the same gel is colored with Coomassie brilliant blue that will stain all proteins bands separated on that gel [6, 7]. In majority of the cases, the quantity of the enzyme of interest is very low and the sensitivity of the analytical method becomes an important parameter. This can be the case, when the enzyme of interest is heterologous expressed in an appropriate microorganism and the evolution of expression of studied enzyme should be monitored [8, 9]. In this paper we have succeeded to optimize the electrophoretic separation coupled with zymogram identification of peroxidase, performing the analytical method in only 135 min with a detection limit of only 0.4 µg peroxidase/well. As far as we know, the lowest reported sensitivity of a zymogram based on guaiacol for peroxidase was 4 µg peroxidase/well [10].

RESULTS AND DISCUSSION

The 2-methoxyphenol (guaiacol) compound is used in this work as a hydrogen donor substrate in the zymogram assay of the peroxidase. Upon oxidation, it forms tetraguaiacol (Figure 1), a brownish product with maximum absorbance at 470 nm and an extinction coefficient of 26.6 mM^{-1} cm^{-1} [11].

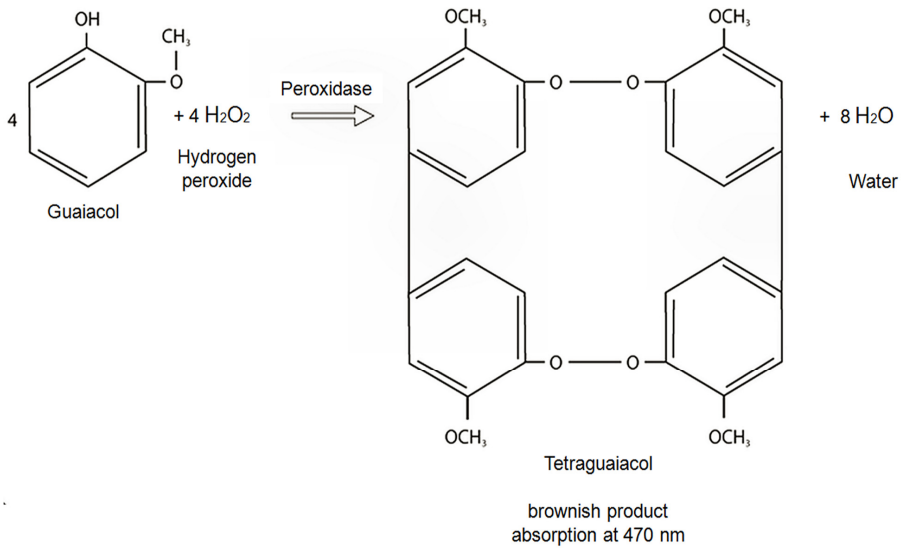

Figure 1. Schematic reaction of peroxidase on H_2O_2 and guaiacol substrates

In Figure 2 is showed the standard SDS-PAGE analysis of different amounts of a commercial horseradish peroxidase (0.05, 0.1, 0.2, 0.4, 0.8, 1.2, 1.6, .2.0, 2.4, 2.8, 3.2, and 3.6 µg/well, under reducing conditions, stained with Coomassie brilliant blue G-250. The sensitivity of the method in the experimental condition is 0.1 µg protein/well (Figure 2, lane 2). To reveal the activity of the peroxidase directly on the polyacrylamide gel a zymogram, using guaiacol as substrate, was realized.

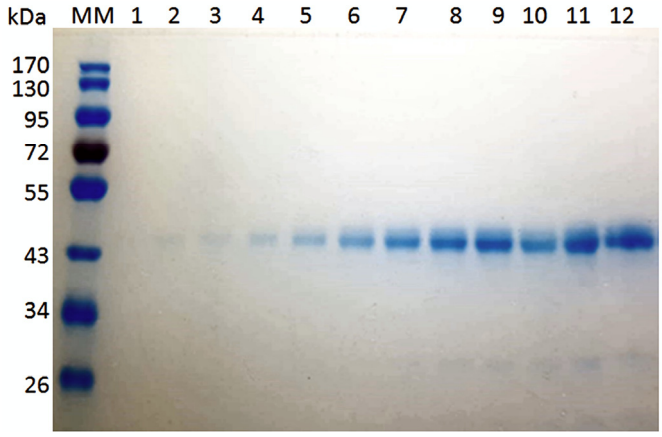

Figure 2. SDS-PAGE analysis (10% gel) of commercial horseradish peroxidase, under reducing conditions. MM = protein molecular marker (kDa). Lanes 1-12, different amounts of commercial peroxidase: lane 1 = 0.05 µg, lane 2 = 0.1 µg, lane 3 = 0.2 µg, lane 4 = 0.4 µg, lane 5 = 0.8 µg, lane 6 = 1.2 µg, lane 7 = 1.6 µg, lane 8 = 2.0 µg, lane 9 = 2.4 µg, lane 10 = 2.8 µg, lane 11 = 3.2 µg, lane 12 = 3.6 µg.

The majority of published techniques for zymogram of peroxidase, using guaiacol as substrate, recommended to use phosphate buffer at pH 7.0 [10]. In these conditions, the sensitivity of the reported method was as low as 4 µg protein/well.

Using phosphate buffer (at three pH values) we have analyzed the sensitivity of methods regarding the identification of peroxidase based on zymogram with guaiacol and identification of protein colored with Coomassie Blue (Figure 3). Although the identification of proteins was as sensitive as 0.1 µg total protein/well, the identification of peroxidase had a sensitivity of only 2 µg total protein/well. It is not the scope of this work to explain why the commercial peroxidase used in these experiments have revealed 3 bands of proteins and 2 bands with peroxidase activity. In the absence of other experiments or information provided by the producer, we can hypothesize that the commercial peroxidase is not a pure product, but contains some

isoenzymes and, perhaps, another protein added as stabilizer (perhaps ovalbumin) [12-14]. What is important to consider from Figure 3 is that the sensitivity of zymogram technique is limited at 2 µg protein/well. Our interest was to study the expression of peroxidase in a bacterial expression system (data presented in another paper) and the needed sensitivity requested by the experiment was at least 0.5 µg peroxidase/well. This is the reason we have considered to change some of the parameters of the zymogram methods.

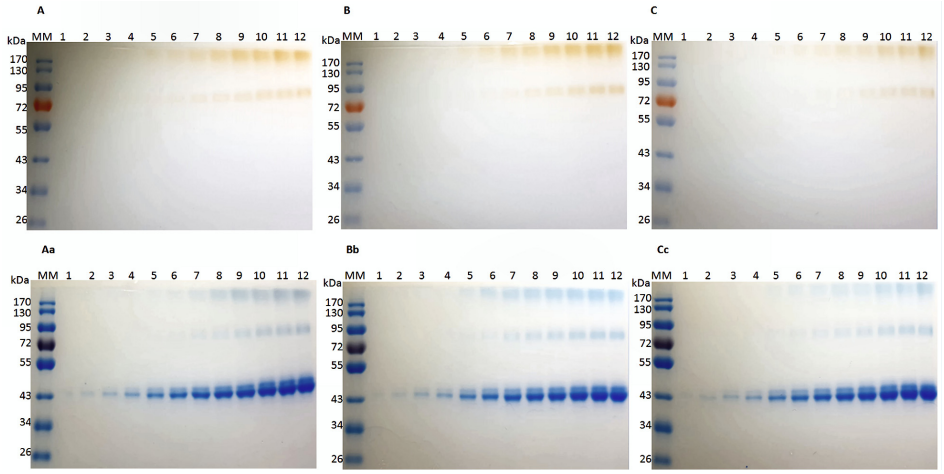

Figure 3. Zymogram analysis of commercial horseradish peroxidase under non-reducing conditions (A, B, C) using 0.1 M sodium phosphate buffer pH 5 (A), pH 6 (B), pH 7 (C), H_2O_2 and guaiacol substrates. SDS-PAGE analysis (10% gel) of commercial horseradish peroxidase, under non-reducing conditions (Aa, Bb, Cc). The gels were stained with guaiacol and after that with Coomassie brilliant blue G-250. MM = protein molecular markers. Lanes 1-12, different amounts of commercial peroxidase: lane 1 = 0.05 µg, lane 2 = 0.1 µg, lane 3 = 0.2 µg, lane 4 = 0.4 µg, lane 5 = 0.8 µg, lane 6 = 1.2 µg, lane 7 = 1.6 µg, lane 8 = 2.0 µg, lane 9 = 2.4 µg, lane 10 = 2.8 µg, lane 11 = 3.2 µg, lane 12 = 3.6 µg.

After testing several buffers compositions, we concluded that the best results are obtained using 0.1 M sodium acetate, pH 6.0 (Figure 4). For the reason of comparison with Figure 3, in Figure 4 are presented the zymograms and protein staining images, realized in acetate buffer at pH 5.0, 6.0 and 7.0 respectively. At pH 5.0 and 6.0, in this buffer, activity of 0.4 µg of peroxidase is visible on the gel (Figure 4 A and B, lane 4). At pH 7.0 only one brownish line of bands can be detected, i.e. only one isoenzyme is active at this pH, and the minimum amount detected was 0.8 µg enzyme/well (Figure 4, C, lane 5).

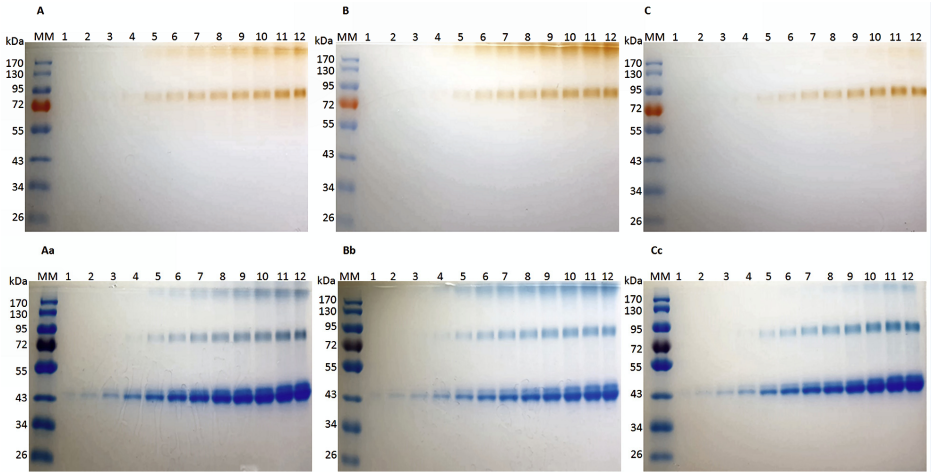

Figure 4. Zymogram analysis of commercial horseradish peroxidase under non-reducing conditions (A, B, C) using 0.1 M sodium acetate buffer pH 5 (A), pH 6 (B), pH 7 (C), H_2O_2 and guaiacol substrate. SDS-PAGE analysis (10% gel) of commercial horseradish peroxidase, under non-reducing conditions (Aa, Bb, Cc). The gels were stained with guaiacol and then with CBB G-250. MM = protein molecular markers. Lanes 1-12, different amounts of commercial peroxidase: lane 1 = 0.05 µg, lane 2 = 0.1 µg, lane 3 = 0.2 µg, lane 4 = 0.4 µg, lane 5 = 0.8 µg, lane 6 = 1.2 µg, lane 7 = 1.6 µg, lane 8 = 2.0 µg, lane 9 = 2.4 µg, lane 10 = 2.8 µg, lane 11 = 3.2 µg, lane 12 = 3.6 µg.

The method for identification of peroxidase using guaiacol as substrate, in acetate buffer, can be realized in only 135 minutes: 90 minutes electrophoretic run, 30 min incubation in reactivation buffer (acetate, containing Triton X100) and 15 min in substrate solution. This improved method of estimation of peroxidase activity in PAGE was very useful for evaluation of peroxidase expression in a Gram-negative bacterium (the experiments will be published in another paper). Figure 5 is presented only as proof that the improved zymogram protocol can be applied to solve some concrete problems from biochemistry laboratories.

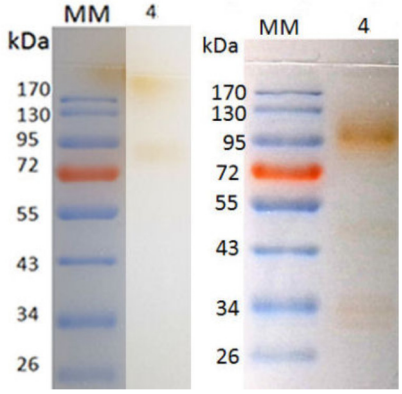

Figure 5. Zymogram analysis of recombinant peroxidase expressed in a Gram-negative bacterium. Left panel – zymogram realized in phosphate buffer, pH 6.0; right panel - zymogram realized in acetate buffer, pH 6.0, in both cases after 4 h after addition of expression inductor.

CONCLUSIONS

An improved method for estimation of peroxidase activity in PAGE capable to reveal quantity of peroxidase activity as low as 0.4 µg/well was realized by performing the enzymatic reaction in acetate buffer, pH 6.0 using guaiacol as substrate. The applicability of the method was tested on real samples.

EXPERIMENTAL SECTION

Chemicals, enzymes and instruments

All chemicals were bought from Carl Roth and Sigma-Aldrich, Germany unless otherwise stated. The horseradish peroxidase was purchased from Sigma-Aldrich, Germany as well. The Mini-Protean electrophoresis system was acquired from Bio-Rad Laboratories, USA.

Buffer solutions

Sodium acetate and sodium phosphate buffers were prepared, both having an ionic strength of 0.1 M and three different pH 5.0, 6.0 and 7.0, respectively. The pH of sodium acetate buffer was adjusted with acetic acid or sodium hydroxide solution. The sodium phosphate buffer was prepared by mixing different volumes of 1 M NaH_2PO_4 and 1 M Na_2HPO_4 stock solutions to obtain three different pH values: 5.0, 6.0 and 7.0, respectively. Phosphoric acid was used to adjust pH to 5.0.

Zymogram analysis solutions

The reactivation solution consisted of 1% Triton X100 dissolved in each buffer solution at each pH value [10]. For substrate solutions, 10 µL of 25% guaiacol (v/v) stock solution were mixed with 1.5 mL of 99.8% ethanol and finally 17.49 mL of each buffer were added. Before use, every substrate solution was supplemented with 1 mL of 0.3% H_2O_2 solution.

Sodium dodecyl sulphate polyacrylamide gel electrophoresis (SDS-PAGE)

SDS-PAGE analysis was modified after Laemmli protocol [15]. Separation gels with 0.75 mm thickness, with 10% acrylamide concentration were prepared.

The samples were prepared under reducing conditions (250 mM Tris-HCl pH 6.8, 25% (v/v) glycerol, 10% (w/v) SDS, 1M 2-mercaptoethanol, 0.05% (w/v) bromphenol blue) and non-reducing conditions (62.5 mM Tris-HCl, pH 6.8, 1% (w/v) bromophenol blue, 25% (v/v) glycerol). A volume of 200 µL of commercial horseradish peroxidase solution (1 mg/mL) was mixed with 200 µL of non-reducing buffer and 100 µL of 50% (v/v) extra glycerol and incubated 10 min at room temperature. Similarly, were processed the samples from expression of peroxidase in Gram-negative

bacteria. The reducing samples were similarly prepared, in a smaller volume, with 10 min boiling. The following amounts of commercial horseradish peroxidase: 0.05, 0.1, 0.2, 0.4, 0.8, 1.2, 1.6, 2.0, 2.4, 2.8, 3.2, and 3.6 µg/well were loaded. The electrophoresis was performed at 120 V in 1x SDS-running buffer (25 mM Tris, 0.19 M glycine, 0.1% (w/v) SDS) at room temperature, for 90 minutes.

Zymogram analysis

After electrophoresis, the gels were washed with distilled water and incubated in reactivation solutions for 30 min, under gentle shaking. The gels were again washed few times and incubated for 15 min, under gentle shaking, in guaiacol substrate solutions containing hydrogen peroxide made in different buffers and different pHs. The gels were photographed and after, the protein bands were colored with Coomassie brilliant blue G-250.

Coomassie brilliant blue (CBB) G-250 gels staining and distaining

Gels were stained, and the proteins were fixed in a solution (A) containing 25% (v/v) 2-propanol, 10% (v/v) acetic acid and 0.05% (w/v) CBB G-250. The mixture was heated until boiling (approx. 30 s) in the microwave oven then the gels were gentle shake for 30 min. The gels were washed with distillated water and immersed in solutions (B) containing 10% (v/v) 2-propanol and 0.05% (w/v) CBB G-250, and (C) containing 10% (v/v) acetic acid and 0.002% (w/v) CBB G-250. In each solution the gels were microwaved 30 s and immediately washed. The destaining step of the gels was performed in 10% (v/v) acetic acid solution and after 1 min of microwaving, a paper towel was added to the reaction vessel, under gentle shaking, for 20 minutes [16].

***A*CKNOWLEDGMENTS**

G. Menghiu acknowledges that this work was supported by the strategic grant POSDRU/159/1.5/S/137750, Project “Doctoral and Postdoctoral programs support for increased competitiveness in Exact Sciences research”. The authors also acknowledge the GRANT PNIII-P3-284, ChitoWound - Biotechnological tools implementation for new wound healing applications of byproducts from the crustacean seafood processing industry.

REFERENCES

1. Rodriguez-Rubio, L., D.M. Donovan, B. Martinez, A. Rodriguez, and P. Garcia, *Methods Mol Biol*, **2019**, *1898*, 107-115.
2. Humer, D. and O. Spadiut, *Int J Mol Sci*, **2019**, 20.
3. Krainer, F.W. and A. Glieder, *Appl Microbiol Biot*, **2015**, *99*, 1611-1625.
4. Leber, T.M. and F.R. Balkwill, *Anal Biochem*, **1997**, *249*, 24-28.
5. Achar, R.R., B.K. Venkatesh, P. Sharanappa, B.S. Priya, and S.N. Swamy, *Appl Biochem Biotech*, **2014**, *173*, 1955-1962.

6. Castro, D., L.M. Contreras, L. Kurz, and J. Wilkesman, *Methods Mol Biol*, **2017**, *1626*, 199-204.
7. Şişecioğlu, M., I. Gülçin, M. Cankaya, A. Atasever, M. Hilal Şehitoğlu, H. Budak Kaya, and H. Özdemir, *J Med Plants Res*, **2010**, *4*, 1187–1196.
8. Pekarsky, A., L. Veiter, V. Rajamanickam, C. Herwig, C. Grunwald-Gruber, F. Altmann, and O. Spadiut, *Microb Cell Fact*, **2018**, *17*, 183.
9. Gundinger, T. and O. Spadiut, *J Biotechnol*, **2017**, *248*, 15-24.
10. Wilkesman, J., D. Castro, L.M. Contreras, and L. Kurz, *Biochem Mol Biol Edu*, **2014**, *42*, 420-426.
11. Uarrota, V.G., R. Moresco, E.C. Schmidt, Z.L. Bouzon, E. Da Costa Nunes, E. De Oliveira Neubert, L.A.M. Peruch, M. Rocha, and M. Maraschin, *Food Chem*, **2016**, *197*, 737-746.
12. Näätsaari, L., F.W. Krainer, M. Schubert, A. Glieder, and G.G. Thallinger, *BMC Genomics*, **2014**, *15*, 227-227.
13. Liu, E.H. and D.M. Gibson, *Anal Biochem*, **1977**, *79*, 597-601.
14. Wang, W., *Protein Sci*, **2015**, *24*, 1031-1039.
15. Laemmli, U.K., *Nature*, **1970**, *227*, 680-685.
16. Guşă, M.E., G. Menghiu, and V. Ostafe, *New Front Chem*, **2016**, *25*, 115-124.

STUDIA UBB CHEMIA, LXIV, 2, Tom II, 2019 (p. 547-553)
(RECOMMENDED CITATION)
DOI:10.24193/subbchem.2019.2.47

Dedicated to Professor Ioan Bâldea on the Occasion of His 80th Anniversary

OPTICAL PROPERTIES MODULATION OF CYANINE DYES IN ORGANIC SOLVENTS AND IN THE CRITICAL INTRACELLULAR pH WINDOW

SISA RICHARD, BREM BALAZS*, GAL EMESE, LUIZA GAINA, DAN PORUMB, CASTELIA CRISTEA AND LUMINITA SILAGHI-DUMITRESCU

ABSTRACT. The synthesis of new 2-(2-(3-formyl-10*H*-phenothiazin-7yl)vinyl)-3*H*-indolium iodide and comparison of the UV–visible absorption/ emission spectral changes for several indolium cyanine dyes upon variation of organic solvents and aqueous solutions with pH in the range between 5–8 pH units were described.

Keywords: *cyanine dyes, phenothiazine, indolium iodide, solvatochromism, pH sensitivity*

INTRODUCTION

In a complex biological material, a pH-sensitive dye can act as a pH-dependent reporter molecule which can be conveniently spotted by using non-invasive spectroscopic absorption/emission detection in the near-infrared region of the electromagnetic spectrum (λ_{max} > 650 nm), where the biological medium is extensively penetrated; thus, labeling of biological macromolecules with a near-infrared chromophore became a documented approach in bioanalytical research [1]

Cyanine dyes is a class of functional dyes of greet interest in many fields due to their high extinction coefficients and tunable optical properties. Trimethine cyanine dyes containing indolium units were reported as displaying observable changes of fluorescent emission within the critical intracellular pH

"*Babes-Bolyai" University, Faculty of Chemistry and Chemical Engineering, RO-400028, Cluj-Napoca, Romania.*
** Corresponding author: bbrem@chem.ubbcluj.ro*

range (6–8) [2]. A near-infrared, pH sensitive colorimetric fluorescent probe containing the dihydro-xanthenes-indolium dimethine cyanine chromofore offered great potential for in vivo bioanalytical applications such as palladium detection and bioimaging [3]

The UV-Vis absorption/emission properties of several dimethinecyanine dyes containing phenothiazine as the core donor and indolium salt as the acceptor previously described, pointed out large bathochromic shifts of the absorption band in halogenated solvents [4] and large Stokes shifts of fluorescence emission, indicative of a great influence of the geometry of the emissive excited state [5]

In this work, we report the synthesis of a new dimethine cyanine dye containing a formyl substituted phenothiazine unit and indolium salt as the acceptor. A comparison of the UV-Vis absorption/emission spectral properties of di-, penta- and heptamethine cyanine dyes containing indolium acceptor moietiy, recorded in solvents of different polarity as well as in aqueous buffer solutions simulating the critical intracellular pH window of 5–8 pH units, is reported.

RESULTS AND DISCUSSION

The synthesis of new 2-(2-(3-formyl-10*H*-phenothiazin-7yl)vinyl)-3*H*-indolium iodide **1** was performed by Knoevenagel condensation of 1,2,3,3-tetramethyl-3*H*-indolium iodide with 10-methyl-10*H*-phenothiazine-3,7-*di*-carbaldehyde as presented in scheme 1.

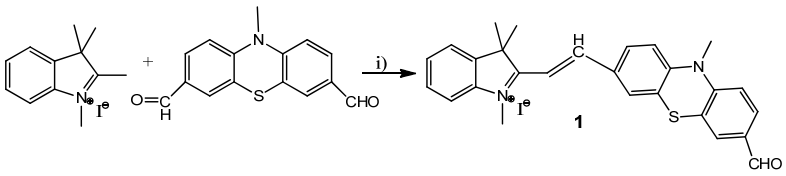

Scheme 1. Synthesis of cyanine dye **1.** *i)* piperidine, ethanol, 12 h, 70 ^{o}C.

The structural assignments of **1** were based on spectroscopic data. The ^{1}H-NMR spectrum displayed the key signals generated by the protons belonging to the vinyl bridge as doublets with vicinal coupling constants of 16.4 Hz pointing the formation of the geometrical *trans*- isomer, while the signal of the CH=O proton was situated downfield at 9.8 ppm.

The electronic absorption and spectra of **1** recorded in different solvents are presented in Figure 1 exhibiting a solvatochromism of the absorption maxima positioned in the visible range (542-592 nm).

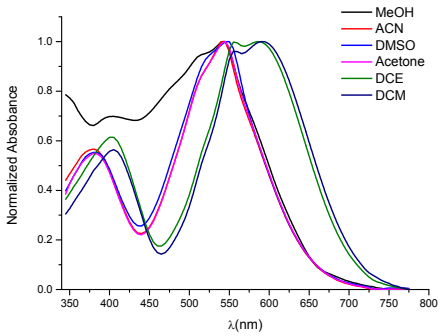

Figure 1. Normalized UV/visible absorption spectra of **1** in various solvents.

Optical properties modulation of cyanine dyes

Several cyanine dyes: chloroheptamethine **2,** cyanine containing the dihidroxanthene heterocyclic unit **3** and bromopentamethine **4** (figure 2) (obtained according to previously reported procedures) were employed in a comparative study of optical properties modulation in the presence of organic solvents of different polarity and aqueous solutions of variable pH, respectively.

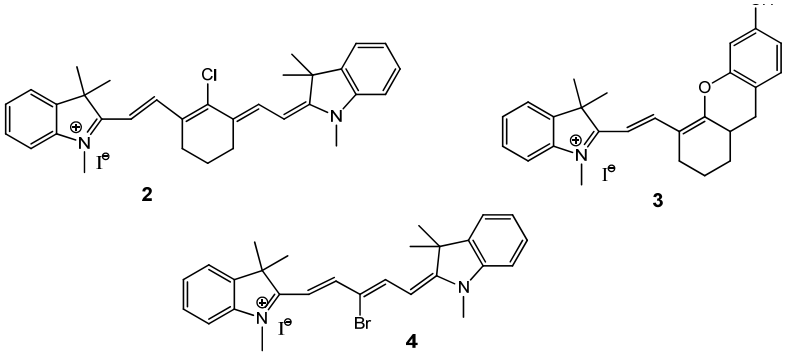

Figure 2. Structure of cyanine dyes employed in the optical properties study

UV-Vis absorption spectra in organic solvents

In figure 3 are displayed the UV-absorption spectra of the cyanine dyes **1-4,** depicting a red shift of the longest wave absorption maxima directly correlated to the length of the pi conjugated system between the donor moiety and the acceptor indolium core.

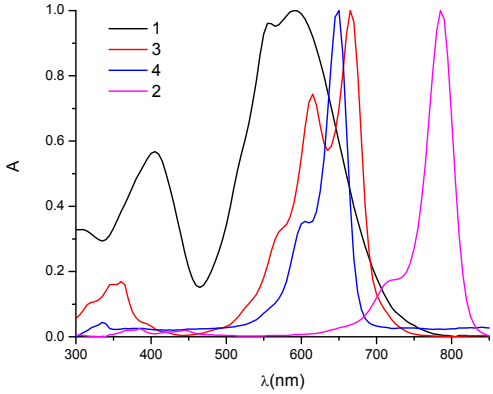

Figure 3. Normalized UV-absorption spectra of the cyanines**1-4**

In Table 1 are summarized the positions of the characteristic absorption maxima recorded in various solvents. A batochromic shift of the absorption maxima can be observed for each cyanine dye when halogenated solvent dichloromethane was used as a solvent. This behavior was also reported for other dyes with donor–pi–acceptor structure and it was rationalized based on halogen–halide interaction responsible for raising the ground state energy level [6]. The hipsochromic shift observed upon increasing solvent polarity can be explained by a better stabilization of the ground state which appears more polar than the excited state. [5]

Table 1. Solvatochromism of UV-Vis longest wave absorption maxima for cyanine dyes **1-4**

Solvent	**1** λ_{max}(nm)	**2** λ_{max}(nm)	**3** λ_{max}(nm)	**4** λ_{max}(nm)
Methanol	542	770	657	633
Acetonitrile	542	771	649	635
Acetone	542	774	655	635
Dimethylsulfoxide	545	784	665	644
Dichloromethane	592	784	665	649

Fluorescence emission spectra in organic solvents.

Upon irradiation with the longest wave absorption maxima, cyanines **2-4** displayed fluorescence emission characterized by larger Stokes shifts in dimethyl sulfoxide solvent as compared to dichloromethane solvent (table 2), pointing towards a better stabilization of the excited stat by polar solvent interactions. For cyanine **1** was not observed any fluorescence emission in solution.

Table 2. Fluorescence emission maxima of cyanine **2-4** in organic solvents

Solvent	**2** λ_{em} (nm)	**3** λ_{em} (nm)	**4** λ_{em} (nm)
Dimethylsulfoxide	812	747	656
Dichloromethane	803	685	654

UV-Vis absorption/emission properties in aqueous solutions of variable pH

The UV-Vis absorption/emission properties of pH sensitive cyanine dyes **2-4** were studied in aqueous buffer solutions of pH 5, 6, 7, and 8 units respectively. In the case of **4** lower pH-values directed the protonation of the tertiary heterocyclic nitrogen atom in the indole free base donor core, determining the hipochrome effect upon absorption and emissions. In figure 4 are presented the UV/visible absorption/emission spectra of cyanine **4** as a function of pH. For the cyanine **3,** solution of higher pH generated the fenoxide auxochrome group which determined a bathochromic shift of the absorption and emission maxima. Table 3 summarizes the shifts of the UV-Vis absorption/ emission maxima upon modulation of pH in aqueous solutions.

Table 3. The UV-Vis absorption/emission properties of pH sensitive cyanine dyes **2-4**

pH	**2**		**3**		**4**	
	λ_{max}(nm)	λ_{em} (nm)	λ_{max}(nm)	λ_{em} (nm)	λ_{max}(nm)	λ_{em} (nm)
5	769	792	649	672	633	650
6	769	778	649	671	633	650
7	769	778	681	704	633	650
8	769	778	681		633	650

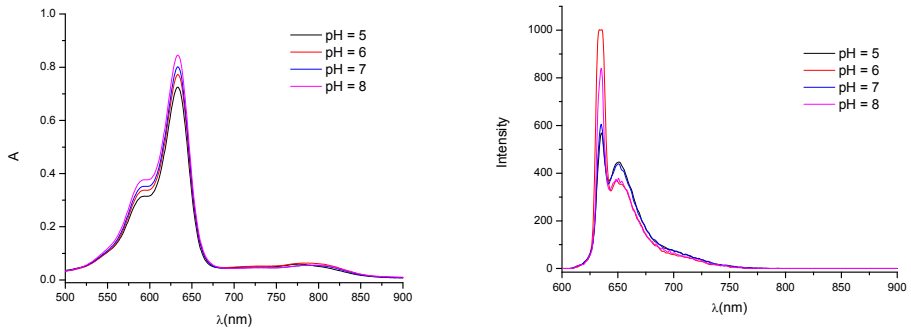

a b

Figure 4. UV-Vis spectra of **4** recorded in aqueous buffer solutions of variable pH a) absorption (C = 10^{-5} M) b) emission (C = 10^{-5} M)

CONCLUSIONS

The optical properties of the cyanine dyes containing indole units can be slightly modulated by using organic solvents of different polarities as well as aqueous solutions of different pH.

EXPERIMENTAL SECTION

Materials and Methods

The starting materials and solvents were obtained from commercial sources from Sigma-Aldrich. NMR spectra were recorded at room temperature on 400 MHz Bruker Avance instruments. Chemical shifts are expressed in δ (ppm) relative to standard tetramethylsilane (TMS).

Compounds **2-4** were prepared according to the previously reported procedure: **2** [1], **3** [3.], **4** [7].

***2-(2-(3-formyl-10H-phenothiazin-7yl)vinyl)-3H-indolium iodide* 1**

10-methyl-3,7-diformyl-phenothiazine (0,4 g, 1,5 mmol) and 1,2,3,3-tetramethyl-indolium iodide were mixed in a Schlenk flask. Then 20 ml of ethanol and catalytic amount of piperidine (100 µl) was added to the mixture under inert atmosphere. The obtained solution was stirred for 12 hours at 70^{o}C. The reaction progress was monitored by thin layer chromatography (TLC, eluent DCM/EtOH = 80:1). After the completion of the reaction the solid product was isolated from the reaction mixture by vacuum filtration. The crude product was then purified using column chromatography (solid phase: silica gel, eluent: gradient solution from DCM/EtOH = 80:1 to DCM/EtOH = 2:1). The pure product was obtained in 55% yield.

MS (*m/z, EI, 70eV*): 425 (M^+)

^{1}H-NMR (400 MHz, DMSO-d_6)**:** δ_{ppm}= 1,77 (s, 6H, 2·CH_3), 3,5 (s, 3H, PtzN-CH_3), 4,12 (s, 3H, N-CH_3), 7,19-7,24 (m, 2H, H_1, H_9), 7,54-7,63 (m, 3H, H_a, H_8, H_{Ar}), 7,69 (d, 1H, H_6), 7,79 (dd, 1H, H_{Ar}), 7,85-7,87 (m, 2H, H_{Ar}), 8,09 (d, 1H, H_{Ar}), 8,15 (d, 1H, H_{Ar}), 8,33 (d, 1H, , H_b,^3J=16,44 Hz), 9,85 (s, 1H, CHO);

^{13}C-NMR (100 MHz, DMSO-d_6): δ_{ppm}= 25,9; 34,7; 36,8; 52,3; 111,6; 115,4; 116,2; 116,3; 122,2; 123,3; 127,8; 128,1; 129,3; 129,5; 130,4; 131,2; 132,2; 133; 142,3; 143,9; 148,4; 149; 152; 181,7; 191,3;

Buffer solutions

Sodium acetate and sodium phosphate buffers were prepared, at three different pH 5.0, 6.0 and 7.0, respectively. The pH of sodium acetate buffer was adjusted with acetic acid or sodium hydroxide solution. The sodium phosphate buffer was prepared by mixing different volumes of 1 M NaH_2PO_4 and 1 M Na_2HPO_4 stock solutions to obtain three different pH values: 5.0, 6.0 and 7.0, respectively. Phosphoric acid was used to adjust pH to 5.0.

ACKNOWLEDGMENTS

This work was supported by a grant of Ministery of Research and Innovation, CNCS-UEFISCDI, project number PN-III-P4-ID-PCCF-2016-0142, within PNCDI III

REFERENCES

1. L. Strekowski, J.C. Mason, H. Lee, M. Say, G. Patonay, *J. Heterocyclic Chem*., **2004**, *41*, 227].
2. R.M. El-Shishtawy, P. Almeida, *Tetrahedron,* **2006**, *62*, 7793.
3. Su W., Gu B., Hu X., Duan X., Zhang Y., Li H., Yao S., *Dyes and Pigments*, **2017**, *137*, 293.
4. B. Brém, Q. Colange, E. Gal, D. Porumb, C. Cristea, L. Găină, T. Lovász, L. Silaghi-Dumitrescu, *Studia UBB Chemia,* **2018***, 63(2),* 117.
5. R.M. El-Shishtawy, F.A.M. Al-Zahrani, S.M. Afzal, M.A.N. Razvi, ZM. Alamshany, A.H. Bakry, AM. Asiria, *RSC Advances*, **2016**, *6*, 91546.
6. Y. Ooyama, Y. Oda, T. Mizumo and J. Ohshita, Tetrahedron, **2013**, *69*, 1755.
7. Hu H., Owens E. A., Su H., Yan L., Levitz A., Zhao X., Henary M., Zheng Y. G., *J. Med. Chem.,* **2015**, *58*(3), 1228.

STUDIA UBB CHEMIA, LXIV, 2, Tom II, 2019 (p. 555-565)
(RECOMMENDED CITATION)
DOI:10.24193/subbchem.2019.2.48

Dedicated to Professor Ioan Bâldea on the Occasion of His 80th Anniversary

SENSORS ARRAY FOR MONITORING AND AUTOMATION OF THE ELECTROCHEMICAL RECOVERY OF METALS FROM WASTE PRINTED CIRCUIT BOARDS

SORIN-AUREL DORNEANU[a, b, c], ENIKO COVACI[a, b], FLORICA IMRE-LUCACI[b], GRAZIELLA LIANA TURDEAN[a, c, *]

ABSTRACT. Nowadays there is increasing interest in using various electrochemical methods as alternative to the energy consuming physico - mechanical, hydrometallurgical and pyrometallurgical techniques for metals recovery from waste printed circuit boards (WPCBs). Thus, cyclic voltammetry (CV) and cyclic square-wave voltammetry (CSWV) methods were used for studying the electrochemistry of some metals (Cu, Sn, Pb, Fe, Zn) on glassy carbon electrode from synthetic leaching solutions containing known concentrations of metallic ions and in real solution obtained from dissolving 10 WPCBs. A good linear correlation was obtained between the parameters evaluated by ICP-OES and cyclic voltammetry. The influence of pH and oxidation/reduction potential (ORP) on the corrosion rate of the mentioned metals was studied gravimetrically. Based on the obtained results, a complex sensors array (amperometric, pH, temperature and ORP) was proposed to assure the accurate monitoring and control of the electrochemical process for metals recovery from WPCBs.

Keywords: *waste printed circuit boards, metals recovery, sensor array, potentiometric and voltammetric sensors*

[a] *Babeş-Bolyai University, Faculty of Chemistry and Chemical Engineering, 11 Arany Janos St., RO-400028, Cluj-Napoca, Romania*
[b] *Interdisciplinary Research Institute on Bio-Nano-Sciences, 42 Treboniu Laurian St., RO-400271, Cluj-Napoca, Romania*
[c] *Research Center of Electrochemistry and Nonconventional Materials, "Babes-Bolyai" University, 11, Arany Janos St., RO-400028, Cluj-Napoca, Romania*
** Corresponding author: gturdean@chem.ubbcluj.ro*

INTRODUCTION

The continuous development and the huge production of electrical and electronic equipment leads to generate great quantities of waste printed circuit boards (WPCBs). Those boards contain an important concentration of heavy metals (like Cu, Sn, Pb, Fe, Zn) and low concentrations of precious and rare metals (Au, Ag, Ga, In) [1-3]. During the leaching process, the metals from WPCBs are transferred into solution, from where metals could be removed and recovered. Due to the high quantities of WPCB and the complex content of the obtained leaching solution, the recovery of even a fraction of metals is becoming a difficult and increasingly important challenge.

Current recycling processes are pyro- [4] and hydro-metallurgical alone [5] or coupled with complementary processes like: electrodeposition, adsorption, ion exchange, extraction, precipitation, membrane separation, solvent extraction and biochemical treatment [6].

It was shown that from environmental and economic points of view, electrochemical recycling of metals from WPCBs have many advantages in comparison to other recovering methods mentioned above [7, 8]. Thus, this technique (i) can operate continuously and yields a metallic form of the product with very high purity which is suitable for rapid reuse or resale and (ii) employs simple electric devices and requires minimal reagent consumption, without additional waste streams [9, 10]. The major challenges for the electrochemical recycling techniques are the increasing of the metals leaching speed and the selectivity improving of the metals electrodeposition of from WPCBs leaching solution by an accurate controlling of the electrochemical operating parameters. Our preliminary results [11] revealed that a model able to predict the behaviour of the chemical and electrochemical reactors and optimize the process parameters must take into consideration some factors. The most important from them are the potential and the concentration profiles at the cathode/electrolyte interface level for the conditions in which the migration and convective diffusion control to overall transport rates.

The aim of the present paper was to find simple and accurate analysis techniques able to evaluate the main process parameters that control the metals leaching rate from WPCBs and the metals selective electrodeposition from the leaching solutions. Consequently, a complex sensor arrays (amperometric, pH, temperature and ORP) was designed for an accurate monitoring and control of the electrochemical process for metals recycling from WPCBs.

RESULTS AND DISCUSSION

Electrochemical behavior in synthetic solutions

The cyclic voltammetry (CV) and cyclic square-wave voltammetry (CSWV) were used to evaluate the electrochemical behaviors of the most abundant metals in WPCBs. The measurements were performed using a glassy carbon (GC) working electrode, an $Ag/AgCl/KCl_{SAT}$ reference electrode (REF) and a Pt wire as counter electrode immersed in synthetic solution samples (SSSs) containing 2 M KBr and 0.5 M HBr and individual metallic ions (i.e., Cu^{2+}, Sn^{2+}, Pb^{2+}, Fe^{2+}, Zn^{2+}) at different concentrations. As it can be seen in Figure 1A, the studied metallic ions are involved either in redox (peaks A1/C1) or in dissolution/ electrodeposition (peaks A2/C2) processes.

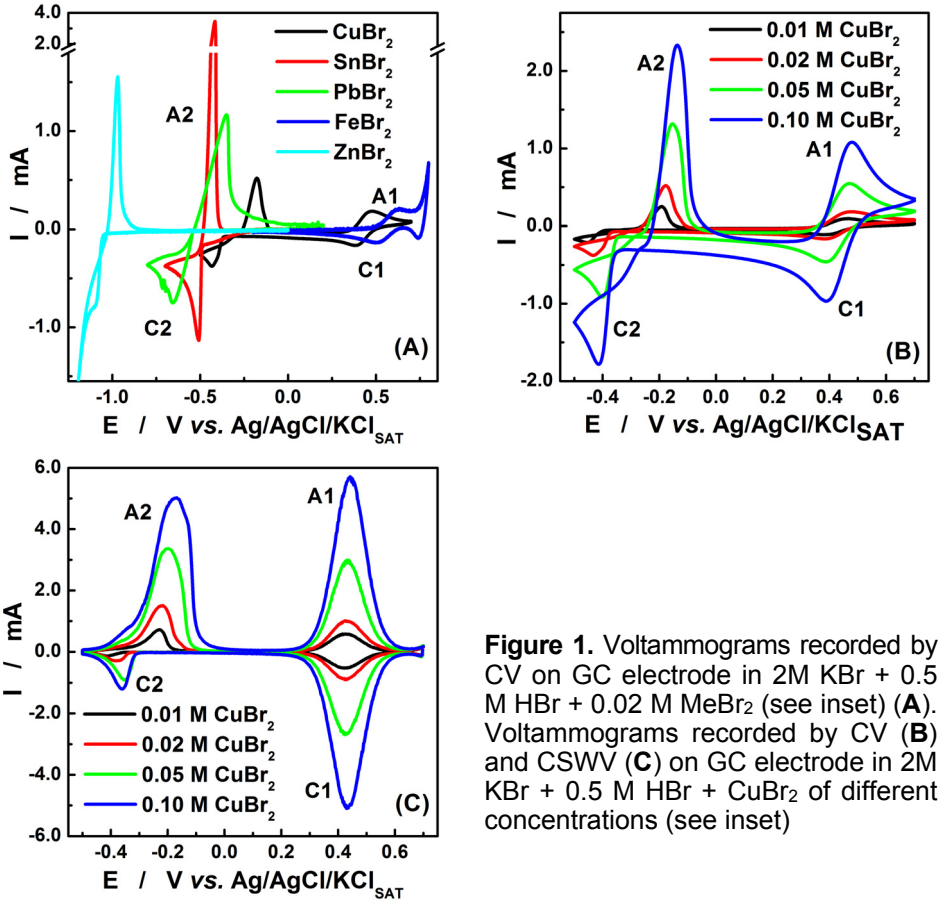

Figure 1. Voltammograms recorded by CV on GC electrode in 2M KBr + 0.5 M HBr + 0.02 M $MeBr_2$ (see inset) (**A**). Voltammograms recorded by CV (**B**) and CSWV (**C**) on GC electrode in 2M KBr + 0.5 M HBr + $CuBr_2$ of different concentrations (see inset)

Accordingly to literature [12], for SSSs containing 2.5 M Br^-, the majority of cuprous bromide species are $CuBr_3^{-2}$, $CuBr_2^-$ and $Cu_3Br_6^{-3}$ and of cupric bromide species are $CuBr_4^{-2}$ and $CuBr_3^-$, respectively. In these conditions, as it can be seen from Table 1, the values of the formal peak potential ($E^{0'}_{calc}$), calculated as the arithmetical mean of the anodic (E_{ap}) and cathodic (E_{cp}) peak potential values, are in good agreement with the theoretical values ($E^{0'}_{theor}$), only minor negative shifts of –10 and – 28 mV being observed for the Fe^{3+}/Fe^{2+} and Cu^{2+}/Cu^+ redox couples, respectively.

Table 1. Peak potential values recorded by CV on GC in 0.1 M Cu^{2+} and Fe^{3+} in SSSs and the corresponding formal and theoretical potentials

Process	**E_{ap} (A1)**	**E_{cp} (C1)**	**$E^{0'}_{calc}$**	**$E^{0'}_{theor}$ ***	**$\triangle E$**
Cu^{2+}/Cu^+	0.480 V	0.390 V	0.435 V	0.463 V	-0.028 V
Fe^{3+}/Fe^{2+}	0.620 V	0.510 V	0.565 V	0.575 V	-0.010 V

*$E^{0'}_{theor}$ (V/REF) = $E^{0'}$ (V/SHE [12, 13]) - E_{REF} (= 0.197 V/SHE)

Even if in the tested solutions the Fe^{3+}/Fe^{2+} and Cu^{2+}/Cu^+ redox couples present a quasi-reversible behavior (the peak-to-peak separation, $\triangle E_p = E_{pa} - E_{pc} > 100$ mV), the amplitude of the corresponding peaks can be used to evaluate the concentration of the two species. The main processes corresponding to the A1/C1 peaks are:

$$Fe^{2+} + e^- \leftrightarrow Fe^{3+} \quad (1)$$

$$[CuBr_4]^{-2} + e^- \leftrightarrow [CuBr_3]^{-2} + Br^- \quad (2)$$

and, for the A2/C2 peaks, the next processes take place:

$$Me^{2+} + 2e^- \leftrightarrow Me^0, \quad \text{where: } Me^0 = Sn, Pb, Zn \quad (3)$$

$$[CuBr_3]^{-2} + e^- \leftrightarrow Cu^0 + 3\ Br^- \quad (4)$$

For all studied metallic ions, the voltamograms recorded by CV and CSWV measurements reveal strength dependence between the ions concentrations and peak current intensities for oxidation/reduction and dissolution/electrodeposition, this fact being exemplified for Cu in the Figures 1B and 1C. As expected, the CSWV is a more sensitive technique, showing higher peak current intensities like those obtained in CV, but peaks limitations appear for Cu concentrations greater than 50 mM.

Also, the peak potentials could be used for the identification of the metallic ions and the intensities of the corresponding peaks can be successfully used for the concentrations monitoring. For example, in Figure 2, the calibration curves, obtained by plotting the peak currents recorded by CV *versus* $MeBr_2$ concentration, are presented for some metals.

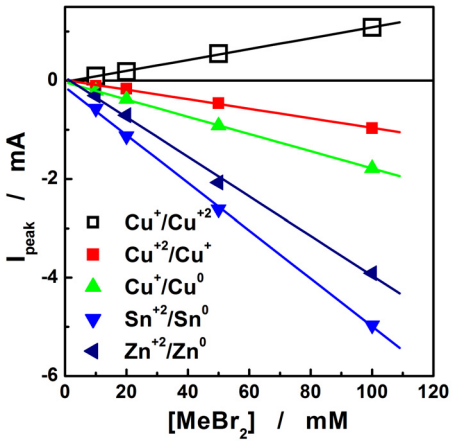

Figure 2. Examples of calibration curves resulted for electrodeposition (C2), reduction (C1), dissolution (A2) and oxidation (A1) peaks recorded by CV in $MeBr_2$ solutions

The parameters of the linear dependencies between the peak current intensities recorded by CV and the metallic ions concentrations, presented in Table 2, reveal a very good correlations (proved by the high values of the correlation coefficient, R) and high sensibilities.

Table 2. Sensibilities and correlation coefficients for some calibration curves

Metallic ion	Peak process	Sensibility (μA / mM)	R / no points
Cu^{2+}	A1	11.1 ± 0.2	0.9995 / 4
	C1	9.7 ± 0.4	0.9987 / 4
Cu^{+}	C2	17.5 ± 0.1	0.9999 / 4
Sn^{2+}	C2	48.6 ± 0.8	0.9997 / 4
Pb^{2+}	C2	43.0 ± 1.4	0.9984 / 4
Fe^{2+}	A1	9.9 ± 0.3	0.9994 / 4
	C1	6.2 ± 0.3	0.9981 / 4
Zn^{2+}	A2	76.7 ± 5.1	0.9956 / 4
	C2	40.2 ± 1.4	0.9988 / 4

The highest sensibilities are recorded by CV in the case of the Sn, Pb and Zn electrodeposition, suggesting an easier electrocrystallization of these metals on the GC surface.

Electrochemical measurements in real sample solutions

Our previous results [14] indicate that, depending on the type of studied WPCBs, the concentrations of the studied metals in the obtained leaching solutions present a significant dispersion, the maximum ($[Me]_{MAX}$), minimum ($[Me]_{MIN}$) and average ($[Me]_{MEAN}$) concentration values and the corresponding standard deviation (SD) being presented in Table 3.

Table 3. Concentration ranges of the more abundant metals in the obtained leaching solutions from 10 WPCBs samples

Metal	Cu	Sn	Zn	Fe	Pb	Al	Ni
$[Me]_{MAX}$ (mM)	598	85	150	145	47	51	18
$[Me]_{MIN}$ (mM)	343	53	34	34	0.2	9	10
$[Me]_{MEAN}$ (mM)	461	71	111	81	26	27	13
SD (mM)	70	12	37	32	15	14	3

As it can seen from Table 3, the concentration ranges for Cu, Zn, Fe and Pb in the real sample solution (RSS) exceed the domains studied by CV and CSWV in SSSs. Moreover, due to the complex composition and the high metals ions concentrations in the undiluted RSSs, the peaks corresponding to the electrodeposition/dissolution (C2/A2) and/or oxidation/reduction (A1/C1) processes, evidenced either by CV or CSWV, are obviously limited and distorted. As a consequence, in order to obtain adequate analytical signals, for all further electrochemical measurements, the RSSs were diluted 10 times using 2M KBr + 0.5 M HBr solution.

In these conditions, CV and CSWV become fast and inexpensive methods to evaluate qualitatively and semi-quantitatively the composition of the leaching solutions. As exemplified in Figure 3.A, the presence of Pb^{2+} in a RSSs is evidenced in CV by the apparition of a peak pair placed at $E_{Pb2+/Pb}$ = -0.565 V/REF and $E_{Pb/Pb2+}$ = -0.480 V/REF. Contrarily, for RSSs resulting from WPCBs released after 2006, when EU RoHS directive [15] took effect, the corresponding Pb electrodeposition and dissolution peaks do not appear (Figure 3A, dashed red line).

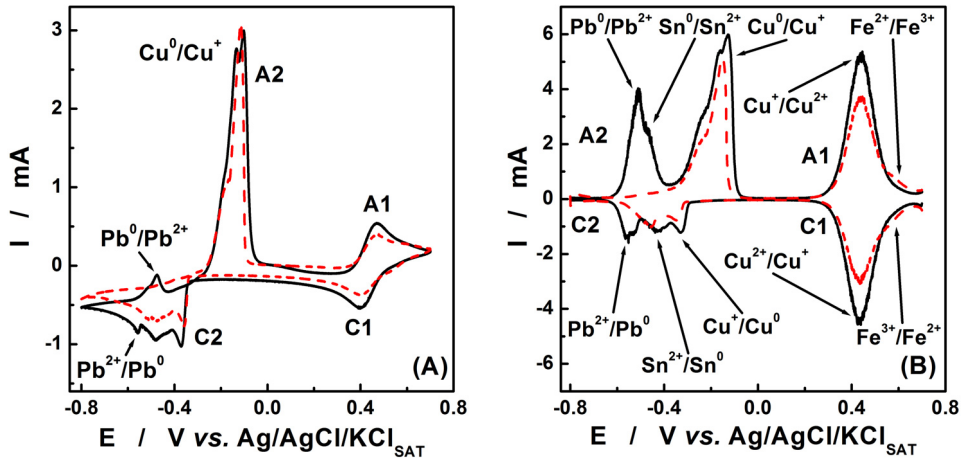

Figure 3. CV (A) and CSWV (B) on GC electrode in 1/10 diluted RSSs containing Pb^{2+} (solid black line) and without Pb^{2+} (dashed red line)

More interestingly, comparing Figures 1A and 3A, we observed that the high amount of Cu present in the RSSs induce a considerable attenuation of the Sn and Pb metals dissolution peaks and a significant distortion of the Cu dissolution peak, suggesting the formation of the Cu-Sn [16] and Cu-Sn-Pb [17] alloys during the electrodeposition step.

From another point of view, a higher Fe concentration in the sample containing Pb^{2+} determines the apparition of the second pair of peaks (of A1/C1 type), associated with the Fe^{3+}/Fe^{2+} redox couple.

As indicated in Figure 3B, all the previous mentioned phenomenon become more evident during the CSWV measurements, better peaks separation and higher amplitudes being recorded.

Correlations of metallic ion concentrations evaluated by ICP-AES and electrochemical methods in real sample solutions

Being an extremely complex matrix, the RSSs obtained by leaching a number of 10 WPCBs were analysed by ICP-AES standardized method. The correlation of the Cu^{2+} concentrations obtained by ICP-AES with those estimated based on CV data recorded in 10 times diluted RSSs is presented in Figure 4.

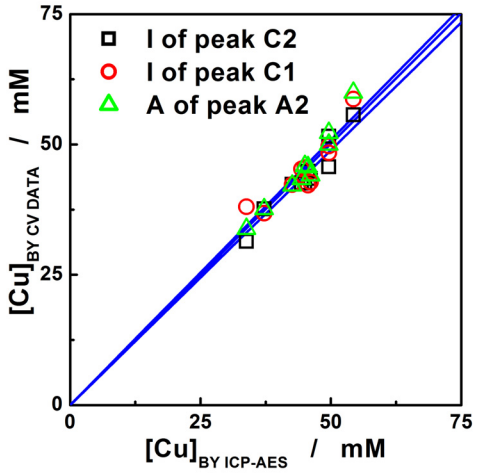

Figure 4. Correlation between Cu^{2+} concentrations obtained by ICP-AES and evaluated from CV data using the electrodeposition C2 peaks intensity (□), the reduction C1 peaks intensity (○), and the area of the dissolution A2 peaks (△) (10 times diluted RSSs)

Three CV data sets (*i.e.*, the intensities of the electrodeposition (C2) and reduction (C1) peaks and the area of the dissolution (A2) peaks) were exemplified. From Figure 4 it can be seen that the concentrations of Cu^{2+} obtained by the two methods are in good agreement, the statistical parameters of the linear correlations being summarized in Table 4.

Table 4. Statistical parameters for the linear correlations between the Cu^{2+} concentration obtained by ICP-AES and evaluated from CV data

Method	Slope (mM/mM)	R	SD	n
C2 peak height	0.979 ± 0.013	0.9608	1.939	10
C1 peak height	1.003 ± 0.019	0.9088	2.642	10
A2 peak area	1.017 ± 0.015	0.9706	2.085	10

As seen from the data presented in Table 4, the slopes of the linear correlations are very close to 1 (between 0.979 and 1.017), with correlation coefficients (R) higher than 90% and standard deviations (SD) not greater than 2.64.

Similar correlations could be obtained using experimental data from CSWV (results not shown). It is important to note that, in the investigated potential range, the Fe electrodeposition/dissolution processes cannot be observed, but the Fe ions concentration can be evaluated based on A1/C1 peak pairs, subtracting the Cu signal. In this purpose, a dedicated algorithm was preliminarily tested with very promising results.

An enhancement of the data accuracy obtained by electrochemical methods (CV and CSWV) can be achieved by restricting the potential scan range, optimizing other experimental parameters (like the scan rate and/or the controlled electrolyte flow), and by recording new calibrations curves in mixed SSSs metals solutions similar to the RSSs.

Influence of pH and oxidation-reduction-potential on the metals leaching rates

It is well known that the pH and oxidation-reduction-potential (ORP) of the leaching solution influence significantly the rate of metals dissolution from WPCBs. In this context, Figure 5 presents the evolutions of pH, ORP and corrosion rate (CR) during the chemical leaching of different pure metallic samples of Fe, Sn, Cu and Zn. As seen, for the tested metals, the dissolution processes are accompanied by the pH increase, simultaneously with the decrease of the OPR and CR.

Consequently, the track of the above parameters, using pH and ORP sensors and dedicated galvanic insulated electrometers, is essential for an adequate control and monitoring of the metals leaching process. Due to the high salinity and acidity, the leaching solutions conductivity is indistinctly affected by the dissolved metals concentrations, making irrelevant their monitoring.

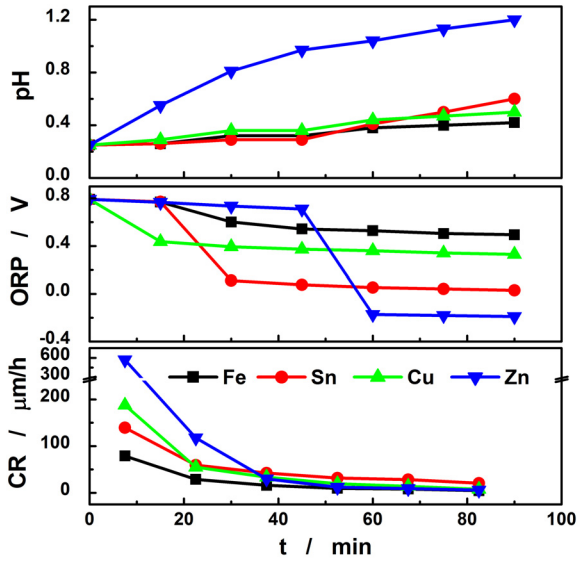

Figure 5. Evolution of pH, OPR and corrosion rate values measured in 100 mL of leaching solution containing 2M KBr + 0.5 M HBr + 0.1 M Br_2 for 8 cm^2 samples of pure Fe (■), Sn (●), Cu (▲), Zn (▼); stirring rate: 480 rpm.

CONCLUSIONS

In order to efficiently monitor and control the process of electrochemical metals recovery from waste printed circuit boards, a complex sensors system, based on pH, OPR, temperature and voltammetric sensors, was designed and the included components were successfully tested in synthetic and real samples using dedicated LabView applications.

The simple and inexpensive voltammetric sensors, exploited by cyclic voltammetry and/or cyclic square wave voltammetry, allow the evaluation of the dissolved metals concentrations (Cu, Sn, Pb, Fe, Zn) with satisfactory accuracy, eliminating the use of complex and expensive traditional analytical equipments and advanced dilutions.

The electric signals delivered by the proposed sensors allow their integration in a complex computerized and/or autonomous control system, simplifying the metals recovery process management and increasing its efficiency.

EXPERIMENTAL SECTION

Chemicals

Reagents as: KBr, HBr, $CuBr_2$, $SnBr_2$, $PbBr_2$, $FeBr_2$ and $ZnBr_2$ are purchased by Fluka and Sigma-Aldrich.

Synthetic samples solutions are prepared by solving appropriate quantities of $CuBr_2$, Sn Br_2, Pb Br_2, Fe Br_2 and Zn Br_2 in 2 M KBr + 0.5 M HBr solution.

Real samples solutions are obtained by leaching the metals from 10 PC motherboards (released between 1998 and 2008), in 2.2 L of 2 M KBr + 0.5 M HBr + 1 M Br_2 solutions [14].

Experimental methods

Cyclic voltammetry and cyclic square wave voltammetry were performed using a computer-controlled multi-channel potentiostat (DXC240, Datronix Computer, România) using dedicated LabView applications. The electrochemical cell was equipped with glassy carbon (GC) disc (ϕ = 3 mm) as working electrode, a $Ag/AgCl/KCl_{sat}$ as reference electrode and a Pt wire (ϕ = 0.5 mm, L = 10 cm) as counter electrode. For all the CV measurements, a scan rate of 50 mV/s was used. The CSWV measurements were performed at a frequency of 20 Hz; a pulse amplitude of ±50 mV and a step potential of 1 mV. Other particular experimental conditions are indicated in the figures captions.

The composition of the real sample solutions were analyzed by the standardized ICP-AES method, using a SPECTRO CIROS CCD spectrometer (SPECTRO Analytical Instruments, Germany).

For the OPR measurements, a combined Pt sensor of SO50X type and a Consort C863 multi-channel-meter, both from Consort, Belgium, were used. The pH measurements were performed using a SenTix® 41 combined glass electrode connected to a pH/Cond 340i pH-meter, both from WTW, Germany.

For the corrosion rate measurements, 2 rectangular samples (20 mm * 20 mm * 2 mm) from each pure metal were immersed in 100 mL of leaching solution containing 2M KBr + 0.5 M HBr + 0.1 M and stirred at 480 rpm. Periodically, the samples were extracted from the leaching solution, washed successively with 2M KBr, distilled water and acetone, dried and weighted. The values of corrosion rate were calculated reporting the weight loss to the sample surface, metal density and dissolution time.

ACKNOWLEDGMENTS

This work was supported by a grant of the Romanian Ministry of Research and Innovation, CCCDI - UEFISCDI, project number PN-III-P1-1.2-PCCDI-2017-0652 / 84PCCDI / 2018, within PNCDI III.

REFERENCES

1. Z. Liu, J. Tang, B.-Yi Li, Z. Wang, *Journal of Cleaner Production*, **2017**, *167*, 97.
2. F. Cucchiella, I. D'Adamo, S.C. Lenny Koh, P. Rosa, *Renewable and Sustainable Energy Reviews*, **2016**, *64*, 749.
3. S. Pinho, M. Ferreira, M. F. Almeida, *Resources, Conservation and Recycling*, **2018**, *132*, 71.
4. H. Wang, S. Zhang, B. Li, D. Pan, Y. Wu, T. Zuo, *Resources, Conservation and Recycling*, **2017**, *126*, 209.
5. H. Li, J. Eksteen, E. Oraby *Resources, Conservation and Recycling*, **2018**, *139*, 122.
6. C. Ning, C. S. K. Lin, D. C. W. Hui, G. McKay, *Topics in Current Chemistry*, **2017**, *375(2),* 1.
7. S. Fogarasi, F. Imre-Lucaci, A. Egedy, Á. Imre-Lucaci, P. Ilea, *Waste Manage.*, **2015**, *40*, 136.
8. L. A. Diaz, T. E. Lister, *Waste Management*, **2018**, *74*, 384.
9. L. J. J. Janssen, L. Koene, *Chemical Engineering Journal*, **2002**, *85*, 137.
10. K. Juttner, U. Galla, H. Schmieder, *Electrochimica Acta*, **2000**, *45*, 2575.
11. S. A. Dorneanu, *Studia UBB Chemia*, **2017**, *62(3)*, 177.
12. E. A. Stricker, K. W. Krueger, R. F. Savinell, J.S. Wainright, *Journal of The Electrochemical Society*, **2018**, *165(9)*, A1797.
13. P. Vanysek, Electrochemical Series, in *CRC Handbook of Chemistry and Physics* (92th ed.), Boca Raton FL, CRC Press, **2011**, pp. 5-80 – 5-89.
14. S. A. Dorneanu, A. A. Avram, A. H. Marincaş, N. Cotolan, T. Frenţiu, P. Ilea, *Studia UBB Chemia*, **2018**, *63(4)*, 147.
15. ***, Directive 2002/95/EC of the European Parliament and of the Council of 27 January 2003 on the restriction of the use of certain hazardous substances in electrical and electronic equipment, *Official Journal L 037, 13/02/2003,* pp. 0019 - 0023
16. Y. Liu, K. Jiang, S. Yang, *Materials,* **2019**, *12*, 603.
17. F. I. Danilov, V. S. Protsenko, E. A. Vasil'eva, O. S. Kabat, *Transactions of the Institute of Metal Finishing*, **2011**, *89(3)*, 151.

STUDIA UBB CHEMIA, LXIV, 2, Tom II, 2019 (p. 567-577)
(RECOMMENDED CITATION)
DOI:10.24193/subbchem.2019.2.49

PHYSIOLOGICAL AND GROWTH RESPONSE OF TOMATO PLANTS AFTER *TRICHODERMA* SPP. SEED TREATMENTS

CRISTINA PETRISOR[a], ALEXANDRU PAICA[b*], FLOAREA BURNICHI[c]

ABSTRACT. Different isolates of *Trichoderma* are able to produce metabolites which induce some morphological and physiological changes in plant such as enhanced plant growth and response to plant pathogens or reduced plant stress. The aim of the present study is to evaluate the effect of some *Trichoderma* isolates on plant growth promoting and physiological parameters of tomato plants. Also, the *Trichoderma* isolates were assessed based on IAA (indole 3-acetic acid) production and ability to solubilize phosphate, traits associated to growth. Tomato seed treatment with *Trichoderma* isolates led to a significant increase in plant height as well as root length and root fresh/ dry weight. However, metabolite production varied among isolates and depends on the isolate. Our data indicated that three of the *Trichoderma* isolates studied increase leaf pigments content and improve the photosynthetic activity of tomato plants.

Keywords: chlorophylls, carotenoids, IAA, root length, fresh weight

INTRODUCTION

Trichoderma spp. are known to interact with plants resulting in beneficial effects such as stimulation of plant defense, development of roots, promotion of plant growth, activation of seed germination, increase of chlorophyll content and photosynthetic efficiency, amelioration of abiotic stress, resistance to membrane pore-forming agents, and enhancement of nutrient uptake [1,2,3].

[a] *Research and Development Institute for Plant Protection, Bdv. Ion Ionescu de la Brad, No.8, District 1, Bucharest, Romania.*
[b] *Institute of Biology, Romanian Academy, Splaiul Independentei, No. 296, Bucharest, Romania.*
[c] *Research and Development Station for Vegetables Buzau, Mesteacanului Street, No.23, Buzau, Romania*
**Corresponding author: e-mail: paicaalexandru@gmail.com*

Trichoderma spp is a genus of fungi that has been reported to be suited for maintaining soil quality and promoting plant growth, by enhancing the availability of nutrients and minerals for plants, producing phytohormones and siderophores even in the absence of pathogens [4,5,6,7,8,9,10,11]. The growth promoting potential of *Trichoderma* spp. has been extensively studied on cucumber, onions, rice, soybeans, tomatoes, radish, bean, chickpea, pepper [7,12, 13, 14, 15, 16, 17, 18, 19]. However, studies of De'Souza et al., (2008) [20] showed that *Trichoderma stromaicum* colonized endophytically cacao seedlings but was unable to induce plant growth.

Studies of Altomare et al., (1999) [21] revealed that *Trichoderma harzianum* strains convert phosphate to a soluble form through chelation mechanisms, thus suggesting a possible mechanism involved in plant growth promotion. Different *Trichoderma strains* have been reported to produce and release indole-3-acetic acid (IAA) and auxin related compounds in the culture medium. These have a positive effect on root morphology and development [6,9,14,22].

Mastouri et al. (2010) [23] found that tomato seed treatment with *Trichoderma harzianum* accelerates germination of seeds and increases seedling vigour. Priming and seed coating with *Trichoderma harzianum* were the most effective treatments in stimulating vegetative growth of pea plants,causing significant increase in early and total green pod yield [24].

This research was conducted in order to investigate the effect of different *Trichoderma* spp. isolates on physiological and growth parameters of tomato plants.

RESULTS AND DISCUSSION

Results revealed changes in plant height, root length, root fresh weight and root dry weight in tomato treated with *Trichoderma* isolates.

Tomato plants obtained from seeds treated with Trichoderma isolates were grown in pots in a growth chamber for 4 weeks. The heights of the plants were measured at the end of the 4-week period.

Application of *Trichoderma* to tomato seeds enhanced the tomato height plant within 4 weeks A pronounced increase in plant height was observed for *Trichoderma* treated tomato plants, which varied between 25.22 cm (M2_14) and 28.28 cm (T85), while the mean height for chemical control (Cropmax) and blank control (no treatment) were recorded at 24.36cm and 22.8cm respectively (table1). The height of tomato plants was noticeably increased when seeds were treated with T85 and T50 compared to the other isolates. These results are in accordance with those of Doni et al. (2014) [7] who obtained an increased height in rice plants treated with *Trichoderma*.

Our findings are also comparable to another study that described the growth improvement of chickpea after treatments with *Trichoderma* [18].

Table 1. Effect of *Trichoderma* treatments on growth parameters of tomato seedlings

Fungal isolates	Plant height (cm)	no. of leaves	Root length (cm)	Root fresh weight (g)	Root dry weight (g)
Blank Control	22.8 ±0.76	15.13 ±0.34	10.05 ±0.04	1.91 ±0.21	0.91 ±0.21
Chemical control	24.36 ±0.65	14.72 ±0.36	10 ± 0.02	2.39 ±0.56	1.78 ±0.12
T85	28.28 ±0.34	15.41 ±0.23	10.45 ±0.04	4.45 ±0.23	2.93 ± 0.09
T50	27 ±0.01	15.5 ±0.21	10.33 ±0.06	3.39 ±0.32	1.9 ±0.18
M14	25.76 ± 0.12	15.84 ±0.04	10.5 ± 0.06	2.21 ±0.05	0.98 ± 0.31
M2_14	25.22 ±0.15	15.88 ±0.05	8 ±0.02	2.08 ±0.12	0.88 ±0.24

The data are expressed as means ±SDV (standard deviation) of three replicates of each experiment

Similar results were reported in radish by Mukhopadhay and Pan (2012) [25]. Also, Hoyos-Carvajal et al. (2009) [9] demonstrated that *Trichoderma* isolates increased the shoot and root length of *Vigna mungo* (black gram) thirty days after sowing.

Tucci et al. (2011) [17] demonstrated that the growth stimulation is dependent on the tomato genotype, suggesting that the response to *Trichoderma* treatment is genetically controlled. Their data show the ability of *Trichoderma harzianum* T22 to increase canopy and stem growth in tomato, and at the same time to modify the root architecture through increasing root length or through development of lateral roots. No significant differeces were found regarding the number of leaves of all tomato plants inoculated with *Trichoderma* isolates in comparison to blank control and chemical control (table 1). These results are in agreement with data of Azarmi et al. (2011) [12], who reported that seed inoculation with *Trichoderma* had no significant effect in leaf number and also in total area of leaf and plant height, root fresh and dry weight. However, their results supported that tomato grown on soil amended with *Trichoderma* sp. had also a marked increase in leaf number, leaf area and chlorophyll content. However, the results of other experiments performed by Ozbay and Newman, (2004) [26] show an increase in leaf number and area and shoot length of tomato plants treated with *Trichoderma* isolates.

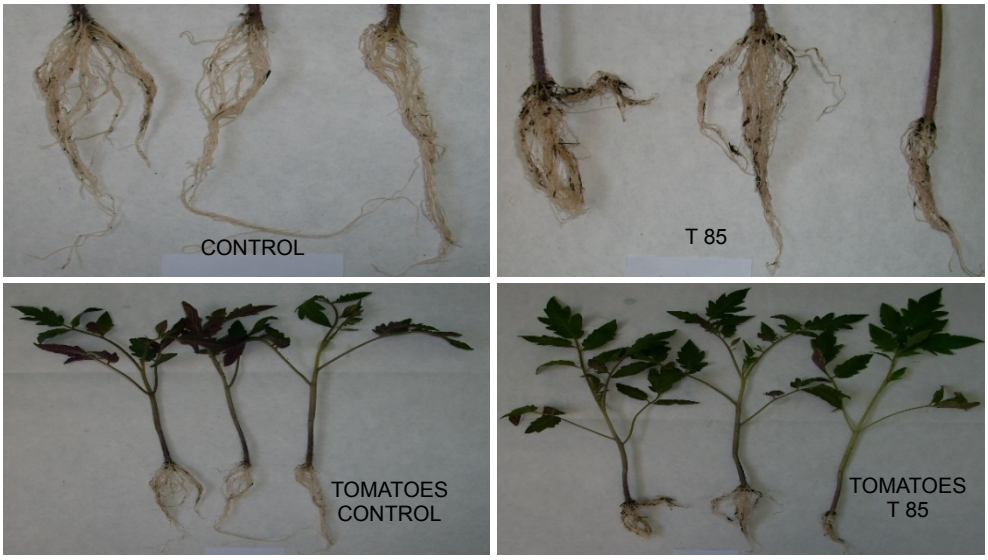

Fig. 1. Effects of Trichoderma treatments on the growth and development of tomato roots and plants

Root development of seedlings was not significantly affected by *Trichoderma* treatments (fig. 1). Root length was increased for the treated tomato plants. Root lengths ranged between 8 cm and 10.45 cm, compared to blank control and chemical treatment control which were recorded at 10 cm. According to the data shown in table 1 the fresh weight and dry weight of tomato roots treated with *Trichoderma* was larger than blank control and treated plants with chemical fertilizer. These results show that *Trichoderma* treatments had a meaningful influence on root mass of tomato plants more so than on root length.

Ozbay& Newman (2004) [26] have shown that some isolates of *Trichoderma harzianum* did not have a significant effect on fresh or dry root mass of tomato plants. Jang et al. (1993) [27] reported that cucumber growth was promoted when seeds were coated with conidia of *Trichoderma* and *Gliocladium* isolates. Also, they describe the growth promoting effect of the two fungal cultures on oat coleoptile segment elongation, which was influenced by filtrate concentration and time of the exposure to the culture filtrate.

The observed increase of plant height and root length in this study may be attributed to the ability of the *Trichoderma* isolates to produce IAA and enhance nutrient uptake. Our data indicate that all *Trichoderma* isolates (fig. 2) used in this work synthesize IAA. However production of IAA varied among the isolates. Isolates T85 and T50 produced the highest amount of IAA ranging between 15.9-19.8 µg/ml (table 2).

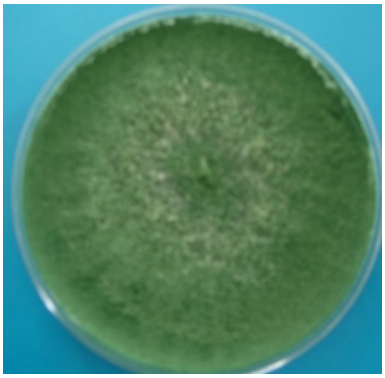

Fig. 2. Characteristic aspects of
Trichoderma Td 85 straincultures

Our results are quantitatively lower than those reported by Kotasthane et al. (2015) [28] and Salas-Marina et al., (2011) [29] which found ranges of 27-30.08 µg/ml for IAA produced by *Trichoderma* isolates. All *Trichoderma* isolates studied cultured in medium without precursor produced low levels of IAA. When L- tryptophan was included in the medium, there was a 13-25-fold increase in production of IAA for T85 and T50 compared to the control without precursor (table 2).

Table 2. Production of IAA and phosphate solubilization by *Trichoderma* isolates

Isolates	IAA(µg/ml)		Phosphate solubilization index	Phosphate solubilization (mg/l)
	With tryptophan	Without tryptophan		
T85	15.9 ±0.02	1.2±0.11	0	0.18±0.01
T50	12.8±0.03	1.0±0.10	0	0.25±0.01
M14	10.1±0.03	0.8±0.03	0	0
M2_14	5.9±0.10	0.7±0.04	0	0

The data are expressed as means ±SDV (standard deviation) of three replicates of each experiment

The capacity of *Trichoderma* to produce phytohormones (IAA) or analogue substance was reported by earlier studies [5,6,9,10,14,22,30] and this is the main mechanism involved in plant growth promotion. Contrary to aforementioned studies, experiments of Sofo et al. (2011) [31] showed that *T harzianum* T22 did not produce phytohormones in growing media, suggesting that T22 is able to induce hormone synthesis *ex novo* in the plants.

Contreras-Cornejo et al. (2009) [6] have shown that strains of *Trichoderma atroviride* and *Trichoderma virens* stimulated lateral root development, increased biomass production and reduced primary root length by producing IAA and auxin like compound in their studies on *Arabidopsis thaliana*. Also, Zhao and Zhang (2015) [19] found that IAA level, root length and fresh root weight of cucumber seedling were increased after treatment with *T. asperellum.* Also, results of Ortega-Garcia et al. (2015) [16] supported that differences in growth stimulation by *T. asperellum* isolates is related to their ability to secrete of IAA like compounds in presence of precursors. Similar results were obtained by Chowdappa et al. (2013) [22] who demonstrated that *Trichoderma harzianum* OTPB3 produced higher quantities of IAA in culture broth.

The importance of phosphate solubilizing fungi consists in increasing phosphate uptake for plant growth. In this study none of the *Trichoderma* isolates tested was able to solubilize the phosphate on Pikovskaya's medium (table 2). Although none of the isolates produced any detectable solubilization zone (halo) in plate PVK agar assay, T85 and T50 shown a slight solubilization between 0.18 and 0.25 mg/l in liquid medium. Thus, plant growth promotion of tomato plants studied in our experiment correlates with IAA production but not with phosphate solubilization. However, some reports indicate the ability of *Trichoderma* spp. to solubilize tricalcium phosphate, suggesting their applicability in crop fields as biofertilizers promoting plant growth [5,12,21]. Production of plant phytohormones by *Trichoderma* might led to higher photosynthetic rates and an enhanced growth response. The leaf chlorophyll a, b, and total chlorophyll contents in tomato treated with *Trichoderma* were increased for all variants with the exception of chemical control and M2_14. This indicates that the treatment with T85 and T50 isolates caused increase assimilation pigments content compared to blank control and chemical control. The content of chlorophyll *a* in tomato inoculated with T85 (194.95 µg/ml) and T50 (190.46 µg/ml) was higher compared to the blank control (182.95 µg/ml) and chemical control (154.96 µg/ml). The results also revealed that plant treated with *Trichoderma* has higher carotenoids content compared to control. All this data supported that plants treated with *Trichoderma* have heightened photosynthetic rates. Similar results were also reported by Fiorini et al. (2016) [30] who indicated that application of *Trichoderma* T6776 on tomatoes seed enhanced the content of all leaf pigments with an increase ranging from 73 to 76.5% compared to control.

Table3. Effects of *Trichoderma* treatments on physiological parameters content of tomato plants

Fungal isolates	Chlorophyll *a* µg/ml	Chlorophyll *b* µg/ml	Carotenoids µg/ml	Chl (*a*+*b*) µg/ml
Control	182.95±0.03	74.65±0.12	43.03±0.07	257.60±0.08
Chemical control	154.96±0.01	58.43±0.10	33.40±0.06	213.39±0.01
T85	194.95±0.02	75.83±0.08	34.82±0.01	270.78±0.13
T50	190.46±0.03	67.95±0.08	45.64±0.05	258.41±0.21
M14	183.04±0.04	79.58±0.09	37.70±0.04	262.62±0.16
M2_14	160.10±0.01	60.47±0.14	32.75±0.06	220.57±0.25

The data are expressed as means ±SDV (standard deviation) of three replicates of each experiment

Our findings are more or less similar to those reported by Alexandru et al. (2013) [32] which show that the differences between the pigments content of tomato plants treated to *Trichoderma* were insignificant but they found an increase of photosynthetic intensity. However, Mastouri et al. (2010) [23] reported no increase in pigment content in tomato seedlings treated with *Trichoderma harzianum* T22. According to the results of Azarmi et al. (2011) [12] chlorophyll content was not significantly increased in the leaves of tomato plants whose seeds have been treated with *Trichoderma harzianum* T969 and T447. Different contradictory results may be due to the use of different *Trichoderma* isolates with characteristic abilities, as well as the different varieties of tomatoes used.

CONCLUSIONS

Trichoderma isolates T85 and T50 are promising beneficial isolates, whose effects consist of growth promotion and an increase in physiological activity.

Plant height of tomatoes inoculated with T85 and T50 was increased compared to control.

Leaf number and root length of *Trichoderma* inoculated plants show no modifications compared to the control.

Three of *Trichoderma* isolates (T85, T50 and M14) tested have a positive influence on photosynthetic pigment content.

EXPERIMENTAL SECTION

Seeds of tomato “Buzau 47” variety were obtained from Research and Development Station for Vegetables Buzau. Isolates of *Trichoderma* which have been used in this experiment were obtained from the collection at the Research and Development Institute for Plant Protection as following: T50 and T85- *Trichoderma asperellum*; M14-*Trichoderma atroviride*; M2_14-*Trichoderma citrinoviride*. Each isolate was grown separately in Potato Dextrose Agar (PDA) plates and incubated for 7 days at 28°C. Spore suspensions of *Trichoderma* spp. were prepared by scraping the spores from cultures. The concentration of *Trichoderma* spore suspension was counted using haemocytometer and was adjusted to 10^7 spores/mL.

Evaluation of tomato plant growth promoting response

Tomato seeds were sterilized by soaking in 1% sodium hypochlorite solution (NaClO) for 5 minutes, then in 70% ethanol for 5 minutes and finally washed for several times with sterile distilled water. The seeds were air dried in a sterile chamber. The sterilized tomato seeds
were immersed in 10 mL *Trichoderma* suspension(10^7 spore/ml) for 1 hour. Control seeds were treated with sterile distilled water. Seeds were sown in plastic pots filled with 250g sterile soil and grown in a culture chamber where the temperature was maintained at 25°C with a relative humidity at 70 % with 12 h light/dark photoperiod. The experiment was conducted using a total of with six variants (four *Trichoderma* isolates, one blank control and one chemical control). Chemical stimulant (Cropmax) was used in accordance to rate application on vegetables. Each treatment consisted of three replicates and the experiment was repeated twice.

Measurement of physiological parameters

Pigments of a known starting weight of leaves was extracted in acetone 100% (v/v) over 24 hours at 4°C. The obtained extracts were filtered through a Whatman No.1 filter paper and centrifuged at 5000 rpm for 15 minutes. The chlorophyll (chla, chlb and total chl) and carotenoids content was quantified according to Lichtenthaler and Welburn, (1985) [33]. The absorbance was determined spectrophotometrically at 663 nm and 645 nm and 470 nm. Concentration of pigments was calculated using Lichtenthaler & Welburn, (1985) [33] equations and values were expressed as (µg/mL).

Qualitative and quantitative estimation of phosphate solubilization in specific medium

Two qualitative assays were used for phosphate solubilizing by *Trichoderma* isolates. For the phosphate solubilisation test, *Trichoderma* isolates were grown in the Pikovskaya’s medium with bromophenol blue (BPB) and

without it as described by Nautiyal, (1999) [34]. The medium contained the following ingredients (g L^{-1}): sucrose (24); $Ca_3(PO_4)$ (22); $MgCl_2$ x $6H_2O$ (22); $MgSO_4$x7 H_2O (0.25); KCl (0.2); $(NH_4)_2SO_4$ (0.1); BPB (0.025); agar (14). pH was adjusted to 7.00.

Tribasic calcium phosphate was used as as phosphate source with BPB included in the Pikovskaya's medium as a pH indicator for acidification. After 72 h incubation at 25 °C isolates turned the media from blue to yellow in zones of acidifications.

Another method used the same Pikovskaya's medium but without BPB. Appearance of cleared zones where calcium phosphate is consumed represented a positive response. The solubilization index was calculated by using the following formula:

Solubilization index =diameter of colony+halo zone /colony diameter

For the quantitative measurement of the phosphorus produced by the fungi cultures, they were grown in Pikovskaya's liquid medium amended with 0.5% insoluble $Ca_3(PO_4)_2$ and incubated for 5 days with shaking (120 rpm) at 28 ±2°C. The supernatant of each culture was centrifuged at 6000rpm for 25 min. The soluble phosphorus was determined using the procedure described by Fiske & Subbarow (1925) [35] and Saravanakumar et al. (2013) [36]. The concentration of soluble phosphorus (P) was calculated by using a standard curve of KH_2PO_4 and expressed in mg/l.

Quantification of indole-3acetic acid (IAA) produced by fungi

Theour isolates belonging to different fungal species were subjected to IAA screening during this investigation. PDB liquid medium with 0.1% L-tryptophan (w/v) was inoculated with two disks of one week old culture of each tested fungus isolates and incubated at 28°C for 6 days as a stationary cultivation. Estimation of IAA-like auxines in the culture filtrate was conducted by using colorimetric technique with Salkowski reagent [37]. Mycelia were removed by centrifugation (5000 rpm, 10 minute), and afterwards by filtration. 1 ml of the supernatant was mixed with 4 ml of Salkowsky reagent (35% perchloric acid; 0.5 M ferric chloride, $FeCl_3$). To determine the amount of IAA produced by the isolates, the mixture was incubated at room temperature for 25 minutes. Pink colouration developed, indicating the presence of IAA, and it was quantified by measuring the absorbance in a spectrophotometer at 535 nm at the end of the incubation. The concentration of IAA was evaluated by comparison with standard curve and expressed as µg/ ml.

Measurement of tomato growth traits

Tomato growth parameters were measured at 30 days after germination.

Plant height (cm) was measured from ground level to the tip of the longest leaf, leaf number were counted for each treatment and controls.

Root length (cm) was measured from the base of stem to the longest root using a ruler. Root dry weight (g) was measured after drying the roots in the oven at 105°C until obtaining a constant weight.

REFERENCES

1. G.E. Harman, *Plant Diseases*, **2000**, *84*, 377
2. R. Hermosa, A. Viterbo, I. Chet, E. Monte, *Microbiology*, **2012**, *158*, 17
3. F. Vinale, K. Sivasithamparam, E.L. Ghisalberti, R. Marra, S.L. Woo, M. Lorito, *Soil Biology and Biochemistry*, **2008**, *40*, 1
4. Y.C. Chang, R. Baker, O. Kleifeld, I Chet, *Plant Diseases*, **1986**, *70*, 145
5. G. Colla, Y. Rouphel, E. Di Mattia, C. El-Nakhel, M. Cardarelli, *Journal of Science Food and Agriculture*, **2015**, *95*, 1706
6. H.A. Contreras-Cornejo, I. Macias-Rodriguez, C. Cortes-Penagos, J. Lopez-Bucio, *Plant Physiology*, **2009**, *149*, 1579
7. F. Doni, A. Isahak, C.R.CM. Zain, W.M.V. Yusoff, *Amb Express*, **2014**, *4(35)*,1
8. G.E. Harman, T. Bjorkman, in Harman & Kubicek (ed): *Trichoderma* and *Gliocladium*. Vol 2, 229-265., Taylor & Francis, London **1998**, cap 11.
9. I. Hoyos-Carvajal, S. Orduz, J.Bissett, *Biological Control*, 2009, *51(3)*, 409.
10. J. Lopez-Bucio, R. Pelagio-Flores, A. Herrera-Estrella, *Scientia Horticulture*, **2015**, 196, 109
11. M.T. Windham, Y. Elad, R. Baker, *Phytopathology*, **1986**, *76*, 518
12. R. Azarmi, B. Hajieghrari, A. Griglou, *African Journal of Biotechnology*, **2011**,*10*, 5850
13. M. Entesari, F. Sharifzadeh, M. Ahmadzadeh, M. Farhangfar, *International Journal of Agronomy Plant Production*, **2013**, *4(4)*, 610
14. V. Gravel, H. Antoun, J. Russell, T. Weddell, *Soil Biology and Biochemistry*, **2007**, *40*, 1
15. B. Nzanza, D. Marais, P. Soundy, *Scientia Horticulture (amst)*, **2012***, 144*, 55
16. J.G. Ortega-Garcia, R. Montes-Belmont, M. Rodriguez-Monroy, J.A.Ramirez-Trujillo, R. Suarez- Rodriguez, G. Sepulveda-Jimenez, *Scientia Horticulture*, **2015**, *195*, 8
17. M. Tucci, M. Rucco, I. De Masi, M. De Palma, M. Lorito, *Molecular Plant Pathology,* **2011**, *12(4)*, 341
18. J. Yadov, J. Verma- Prakash, K. Tiwari-Nath, *Asian Journal Biologic Sciences*, **2011**, *4(3)*, 291
19. I. Zhao, Y.J. Zhang, *Integrative Agriculture*, **2015**, *14(8)*, 1588
20. J.T. De Souza, B.A. Bailey, A.W.V. Pomella, E.F. Erbe, C.A. Murphy, H. Bae, P.K. Hebbar, *Biological Control*, **2008**, *46*, 36
21. C. Altomare, W.A. Norvell, T. Bjorkman, G.B. Harman, *Applied Environmental Microbiology*, **1999**, *65*, 2926
22. P. Chowdappa, S.P. Mohan Kumar, M.J. Lakshami, K.K. Upreti, *Biological Control*, **2013**, *6*, 109

23. F. Mastouri, T. Bojorkman, G.E. Harman, *Phytopatology*, 2010, *100(11)*, 1213
24. R.S.R. El-Mohamedy, M.M.H. Abd El-Baky, *Research Journal of Agriculture and Biological Sciences*, **2008**, *4*, 611
25. R. Mukhopadhay, S.J. Pan, *Plant Protection Science*, **2012**, *4(2)*, 46
26. N. Ozbay, S.E. Newman, W.M. Brown, *Acta Horticulture*, **2004**, *635*,131
27. S.S. Jang, J.K. Han, C.S. Park, K.H. Kim, J. Korean, *Plant Pathology*, **1993**, *9(3)*, 149
28. A. Kotasthane, T. Agrawal, R. Kushwash, O.V. Rahatkar*, European Journal Plant Pathology*, **2015**, *141*, 523
29. M.A. Salas-Marina, M.A. Silva-Flores, E.E. Uresti-Rivera, E. Castro-Longoria, A. Herrera-Estrella, S. Casas-Flores, *European Journal of Plant Pathology*, **2011**, *131*, 15
30. I. Fiorini, I. Guglielminetti, I. Mariotti, M. Curadi, P. Picciarelli, A. Scartazza, S. Sarrocco, G. Vannacci, *Plant Soil*, **2016**, *400*, 351
31. A. Sofo, A. Scopa, M. Manfra, M. De Nisco, G. Tenore, J. Troisi, R. Di Fiori, E. Novellino, *Plant Growth Regulation*, **2011**, *65*, 421
32. M. Alexandru, D. Lazar, M. Ene, T.E. Sesan, *Romanian Biotechnological Letter*, **2013**, *18*, 8499
33. H.K. Lichtenthaler, A.R. Wellburn, *Biochemistry Society Transaction*,**1985**, 11, 591
34. C.S. Nautiyal, *FEMS Microbiology Letters*, **1999**, *170*, 265-270
35. C.H. Fiske, Y.J. Subbarow, *Biological Chemistry*, **1925**, *66*, 375
36. K. Saravanakumar, V.S. Arasu, K. Kathiresan, *Aquatic Botany*, **2013**, *104*, 101
37. S.A. Gordon, R.P. Weber, *Plant Physiology*, **1951**, *26*, 192